Electrons and phonons in graphene : electron-phonon coupling, screening and transport in the field effect setup

Thibault Sohier

THÈSE DE DOCTORAT
DE L'UNIVERSITÉ PIERRE ET MARIE CURIE

Spécialité : Physique

École doctorale : "Physique en Île-de-France"

réalisée

à l'Institut de Minéralogie, de Physique des Matériaux et de Cosmochimie (IMPMC)

présentée par

Thibault SOHIER

pour obtenir le grade de :

DOCTEUR DE L'UNIVERSITÉ PIERRE ET MARIE CURIE

Sujet de la thèse :

Électrons et phonons dans le graphène: couplage electron-phonon, écrantage et transport dans une configuration type transistor à effet de champ

soutenue le 22/09/2015

devant le jury composé de :

M.	Kristian Thygesen	Rapporteur
M.	Matthieu Verstraete	Rapporteur
M.	Bernard Plaçais	Examinateur
M.	Ludger Wirtz	Examinateur
M.	Jean-Noël Fuchs	Examinateur
M.	Matteo Calandra	Directeur de thèse
M.	Francesco Mauri	Co-Directeur de thèse

Contents

Notations

Variables and functions

$\mathbf{r} = (\mathbf{r}_p, z)$	position
$\mathbf{r}_p$	in-plane space variable
z	out-of-plane space variable
$\mathbf{R}$	lattice vectors (positions of crystal cells)
$\mathbf{G}$	reciprocal lattice vectors
$\mathbf{d}_a$	internal coordinate (within the cell) of atom a
$\mathbf{k}$	electronic wave vector (in-plane for graphene)
$\mathbf{q}$	phonon momentum (in-plane for graphene)
$n(\mathbf{r})$	electronic density
$\psi_{\mathbf{k},s}(\mathbf{r})$	wave function of state $\mathbf{k}$ in band s
$\varepsilon_{\mathbf{k},s}$	energy of state $\mathbf{k}$ in band s
$\omega_{\mathbf{q},\nu}$	phonon frequency (mode ν at $\mathbf{q}$)
$\mathbf{e}_{\mathbf{q},\nu}$	phonon eigenvector (mode ν at $\mathbf{q}$)
$\mathbf{u}$	atomic displacement
f	Fermi-Dirac distribution
$n_{\mathbf{q},\nu}$	Bose-Eistein distribution for phonon mode ν at $\mathbf{q}$
v_c	Coulomb interaction
χ	Susceptibility
ϵ	dielectric function
T	temperature

Parameters

b	lattice parameter (graphene)
b_0	interatomic distance (graphene)
S	unit cell area
Ω	unit cell volume
N	number of unit cells
μ_S	mass density per unit area (graphene)
v_F	Fermi velocity (graphene)
ε_F	Fermi level

Physical constants

e	elementary Coulomb charge (> 0)

$\hbar$	Planck constant
k_B	Boltzmann constant

Indices

i,j	run over Cartesian coordinates
s,s'	run over bands
a,a'	run over atoms
ν,μ	run over phonon modes
p	indicates in-plane quantity

Acronyms

3D	three-dimensional
2D	two-dimensional
EPC	Electron-Phonon Coupling
FET	Field Effect Transistor
QE	Quantum ESPRESSO
DFT	Density-Functional Theory
DFPT	Density-Functional Perturbation Theory
LDA	Local Density Approximation
KS	Kohn-Sham
XC	Exchange-Correlation
PBC	Periodic Boundary Conditions
TB	Tight Binding
RPA	Random Phase Approximation
DOS	Density Of States
BZ	Brillouin Zone

Introduction

Despite arguments against the stability of 2D materials at room temperature, Andre Geim and Kostantin Novoselov successfully produced graphene in 2004. The unique electronic properties of this monolayer of carbon atoms were first studied theoretically in 1947 by P.R. Wallace. During the following five decades, graphene raised the interest of several theoreticians as a condensed matter toy model for Dirac fermions physics. At the time, however, graphene was not believed to exist on its own. Rather than the discovery of a new material, it was Geim and Novoselov's experimental efforts to *isolate* and *characterize* graphene that earned them the 2010 Nobel prize in physics.

Dimensionality is well known to be a critical parameter in condensed matter. It often defines the characteristics and singularities of phase transitions, whether they are structural, electronic, magnetic or otherwise. Although theoreticians had been working in two-dimensional frameworks for a long time, the *isolation* of graphene meant that this dimensionality was accessible to experimentalists as well. Fundamental solid-state physics could finally benefit from the crucial interplay between theory and experiment in two dimensions.

Equally important as the actual 2D material is the ability to control and *characterize* its properties. A crucial aspect of Geim and Novoselov's characterization technique was the use of the electric field effect. The idea of using an electric field to modulate the electrical properties of materials was introduced by Julius Lilienfeld in 1925, but it took a few decades before John Atalla and Dawon Kahng fabricated the first working version of the modern field effect transistor in 1960. The field effect turned out to be a physical mechanism of the utmost importance, as the field effect transistor became the building block of the many electronic devices that we use everyday. The fundamental pertinence of the field effect relies on its capacity to induce significant changes in the electronic properties of the target material via a variation of the density of mobile charges. This is why field effect transistors, up to this day, are mostly made of semiconductors rather than metals or semimetals like graphite. In semiconductors, a relatively small electric field induces a sufficient density of mobile charges to switch between insulating and conducting regimes. In bulk metals or semimetals, the typical intensity of the electric field that we find in transistors turn out to induce a relatively small density of mobile charges compared to the already large intrinsic density. The electric field effect is then too small to be exploited. In his Nobel lecture, Geim states that one of the major motivations for initiating his research on thin graphitic films was the prospect of achieving significant electric field effects in materials other than semiconductors. To do this, it was necessary to further increase the *density* of charges induced in graphite. Rather than trying to increase the *number* of induced charges,

his ambition was to reduce the thickness of graphite and thus the volume in which the charges were induced. In a sense, eliminating one spatial dimension and using the field effect was a way to explore another dimension of the semimetallic graphite, its electronic structure.

For more technological motivations, the industry of semiconductor electronic devices has always been involved in the race towards thinner materials and downscaling in general. The isolation of graphene marked the attainment of the ultimate limit of that race, as well as the opening of a whole new range of 2D materials to explore. A remarkable aspect of Geim and Novoselov's Nobel prize is the short time delay that separates the actual research and the prize. A similarly short time separated the realization of the first transistor in 1947 by Bardeen, Brattain and Shockley, and the corresponding Nobel prize in 1956. The reason is that both works had a huge and immediate impact on research and technology. Considering the importance of transistors today, we can expect a bright future for graphene and 2D materials in general. In slightly over a decade, a formidable amount of research has been conducted on 2D materials. Their sensibility to external stimulations (electric or magnetic field, light, temperature, strain, etc...) calls for a great number of prospective applications in electronic devices, sensors, solar cells, batteries, thermoelectrics, and many more. For some new fields of applications such as spintronics, quantum computing and superconductivity, 2D materials might very well lead to some breakthroughs.

Electronic transport plays a role in many of those prospective applications. Developing good models and identifying all the different contributions that deteriorate transport is paramount to improve the performances of the devices. It is also a very common mean of characterization, extensively used in fundamental studies to observe the signature of diverse phenomena. Two essential concepts to consider when studying electronic transport are the electron-phonon interaction and screening. In some cases the electron-phonon interaction is a limiting factor. In the electronic devices discussed above, the scattering of electrons by phonons decreases the material's efficiency in transporting electrons. In other cases, like conventional superconductivity, the electron-phonon interaction induces the pairing of electrons, which is the driving mechanism. In any case, this interaction is omnipresent in condensed matter, and its understanding is necessary for both fundamental and applied physics. Screening is an important and complex aspect of the collective behavior of electrons in a material. It refers to the ability of mobile charge carriers to screen electric fields via a collective response driven by the long-range Coulomb interaction. As such, it modifies the response of electrons to perturbing fields and, in particular, the electron-phonon interaction. Screening is highly dependent on dimensionality, and requires a certain amount of careful modeling. A lot remains to be understood about the specificity of electronic transport, electron-phonon coupling and screening in 2D materials.

Ab initio simulations, as a complement to experiment, can help to understand the electronic, structural and transport properties of materials. Most often, being able to reproduce experimental results with simulations entails a good understanding of the underlying physical mechanisms. Carried out upstream, *ab initio* simulation is also a convenient tool to predict and explore 2D materials, pointing the way for experimental research and technology.

This PhD thesis was initiated by the observation that numerical simulations failed

to properly reproduce graphene's phonon-limited resistivity, a direct effect of electron-phonon interactions. Although theory gave a fairly good qualitative interpretation of the experimental resistivity, numerical studies fell short of experiments quantitatively. This pointed to some possible flaws or deficiencies in the models and *ab initio* simulations of electron-phonon interactions in graphene.

To achieve accurate simulations of electron-phonon interactions in this 2D material, existing *ab initio* methods based on plane-wave density-functional theory needed improvement. Those methods were initially implemented to simulate electrons and phonons in 3D-periodic materials. Although they have been successful on many occasions in that context, they are not adapted for the simulation of 2D materials. In particular, they fail to simulate screening and the electric field effect in 2D systems. Since both those mechanisms affect the electron-phonon interaction, it was important to improve their simulation. Furthermore, they are both subject to some debate and their importance extends much further than their influence on electron-phonon interactions. Indeed, as an inherent characteristic of the electrons, screening is involved in all electronic responses while the field effect is used in most experimental measurements of resistivity and many prospective applications. In order to simulate the influence of screening and the field effect on the interplay between electrons and phonons in 2D materials, we implemented rather extensive modifications of existing *ab initio* codes. Those new computational methods allowed us to establish quantitative models of electron-phonon interactions in graphene. We improved existing qualitative models and computed the parameters involved *ab initio*. The phonon-limited resistivity of graphene can then be found by including the electron-phonon interactions in a transport model. Usually, some approximations are made to solve the resulting equation analytically. To overcome those approximations, we implemented a more accurate numerical solution.

A direct objective of this work is to improve the understanding of electron-phonon interactions and their role in the electronic transport properties of graphene. However, beyond the study of graphene specifically, many of the issues approached in this thesis apply to other 2D materials. A less immediate but very important objective of this work is to provide several new computational methods that we hope will prove valuable for the simulation of 2D materials in general.

In the first chapter, we introduce and motivate the concepts treated in the thesis. In chapter 2, we present and improve analytical models for electrons, in-plane phonons and their interactions in graphene. In chapter 3, we evaluate the parameters involved in the electron-phonon coupling model using *ab initio* simulations. In chapter 4, we present the implementation of a computational method based on density-functional theory to compute the static screening function of 2D materials. We apply this method to graphene and compare it to analytical models. In chapter 5, we focus on the specificity of the field effect transistor setup, and study its effect on electron-phonon interactions. We modify a density-functional theory code to enable the simulation of 2D materials in such a setup. We detail the implementation and apply it to graphene. Finally, in chapter 6, we develop a numerical solution to Boltzmann transport equation to simulate the phonon-limited resistivity of graphene.

Chapter 1

Electrons and phonons in 2D materials

In this first chapter we introduce and motivate the concepts at the center of this thesis. In an effort to focus on the importance and general nature of the physical mechanisms, we will try to reduce the use of mathematical formalism to a minimum. The condensed matter concepts discussed here are well-known and well documented, see for example Refs. [1, 2, 3, 4]. We simply recall the most relevant characteristics of the phenomena in our context. Most importantly, the objective is to convey the importance of two-dimensional systems, the peculiarities of electrons and phonons in that context, and the challenges they present in terms of computational simulation. The purpose is to set the general framework of the thesis rather than to give an exhaustive or exact description. It is also an opportunity to specify some aspects that are usually implicit in the field.

First, we set the practical framework of this work, namely, two-dimensional (2D) materials. We present the typical setup in which they are found for the kind of applications we have in mind. Second, we set the theoretical framework used to study the corresponding quantum system. We introduce the tools necessary to describe electrons, phonons, as well as their interactions. In the process, we highlight the consequences of working in two dimensions. Finally, we identify the challenges encountered in the process of simulating 2D materials.

1.1 Two-dimensional materials

Since the experimental isolation of graphene [5, 6, 7], 2D materials have undergone unprecedented scrutiny due to their interesting properties both at the fundamental and applied levels. We first need to state what we mean by "2D material". An adequate definition in the context of this work would be "a material constructed by infinitely repeating a pattern of a few atoms in only two dimensions". This implies that two of the material's dimensions are much larger than the third one, which is the more general definition of 2D materials. With no periodicity in the third dimension, the thickness is limited to a few atomic layers while in the two other dimensions, the pattern is repeated infinitely. A more precise term for this system would be "2D-periodic crystal", and this

is what we will model. This model will be used to study the properties of more realistic 2D materials in which the periodicity is neither perfect (there can be some defects) nor infinite. In practice, the length and width of 2D materials are at the microscopic scale ($\sim$ µm). With a pattern at the atomic scale ($\sim$Å), the number of repetitions is then of the order of $\sim 10^4$ in each direction with periodicity. In the framework of our models and simulations, this number will be considered large enough to neglect edge effects. In other words, we assume that for the physical properties studied here, a 2D material of a few μm^2 is equivalent to an infinite 2D-periodic crystal. Typical examples of atomically thin monolayer systems are graphene and hexagonal boron nitride, made up of a honeycomb lattice of either carbon, or boron and nitrogen. Since the few atoms included in the pattern are not necessarily in the same plane, the above definition also includes compounds thicker than one atom. Examples of such compounds that are still considered as one layer are the monolayer transition-metal dichalcogenides. A few layers of any of those materials, or a combination thereof are called few-layer materials and are also included in our definition of 2D materials.

In practice, a 2D material can exist in various setups. The purest (yet not the simplest) form is probably when the 2D material is suspended. In that kind of setup, the edges of a sheet of material are attached to a support, while a significant part of the material is suspended in between those points of attach. A more common setup is to deposit the material on a certain supporting material, called substrate. The difference between those setups boils down to the nature of the surroundings of the 2D material in the third direction. Is it vacuum, an insulating dielectric material, a semiconductor? Does the environment interact with the 2D material? Is there some chemical reactions at the interface? Is there an external electric field? A great variety of situations are possible and the physical properties of the 2D material depend on them. In this work, we will focus on the very common field effect transistor (FET) setup [5, 8], as represented in Fig.1.1. In this setup, the 2D material is deposited on an insulating bulk substrate (silicon oxyde for example). On both extremities of the 2D material are contacts, a source and a drain, between which a current can be established. When the source and drain have different electric potential, an in-plane electric field is established between the two, which drives the electrons from one contact to the other. The efficiency of the 2D material in carrying the current from one contact to an other is referred to as its electronic transport properties and will be the main type of experimental measurement studied in the thesis (chapter 6).

On top of the 2D material is a dielectric material, a few tens of nanometers thick. This material is insulating, such that no charge can go through it. Finally, a metallic top gate or grid is deposited on top of the dielectric. The purpose of this gate is to induce additional charges in the 2D material. Following the same principle as a capacitor, applying a voltage difference between the 2D material and the gate results in the accumulation of opposite charges on both sides of the insulating dielectric. This process, called gate-induced doping, is represented in Fig. 1.2. This effect is particularly interesting in 2D materials. Indeed, due to their reduced dimensionality, the accumulated charges translate into large induced densities. Being able to change the density of free carriers implies the ability to tune the electronic properties of 2D materials. For example, in Fig. 1.3, a transition from a semimetallic to a metallic behavior is induced in monolayer graphene by varying the gate voltage [9]. This is of

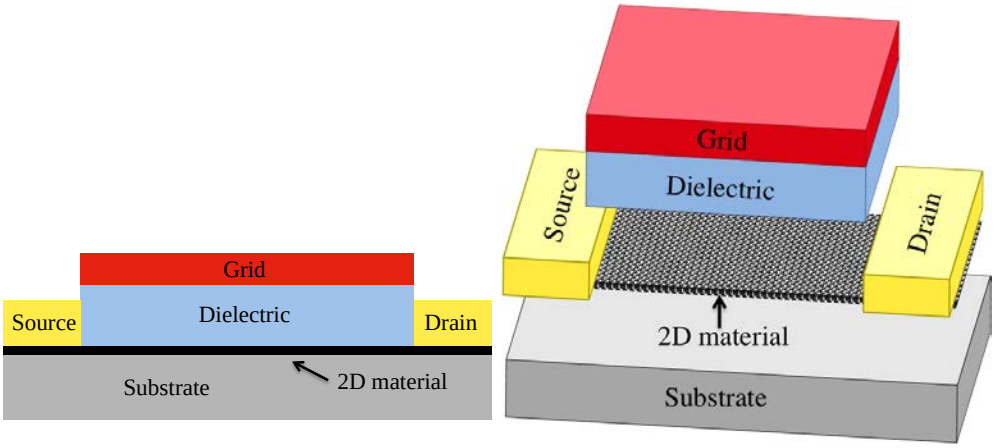

Figure 1.1: On the left is a schematic representation of a FET setup. On the right, the layers are separated to show the succession of piled materials.

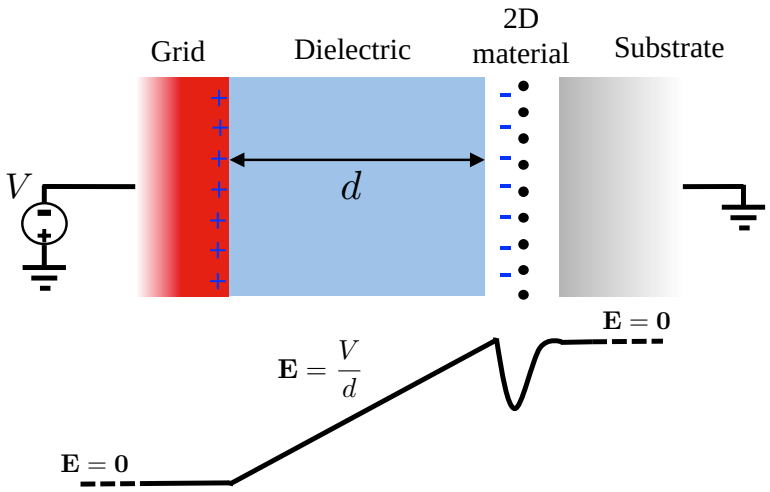

Figure 1.2: Within the FET setup, we focus on the above subsystem. Note that the system has been rotated with respect to the previous figure. We represent a monolayer 2D material, the black dots symbolizing the atoms. In this situation, electron doping is achieved. Additional electrons, represented by the blue "−" signs accumulate at the dielectric/2D material interface. Holes, represented by the "+" signs, accumulate on the gate/dielectric interface.

course essential to use graphene as a conductor of charges. Another beautiful example [10, 8] is the case of 2D transition-metal dichalchogenides, in which one can induce sufficiently high doping to obtain superconductivity. Fig. 1.2 is a rather simplistic representation of gate-induced doping. The form of the electric potential in the vicinity of the 2D material will be studied more extensively in this thesis. For now, let us recall some important general features of this setup. The accumulation of charges on either side of the dielectric implies the establishment of an electric field in between, corresponding to a linear variation of the potential. It is important to distinguish

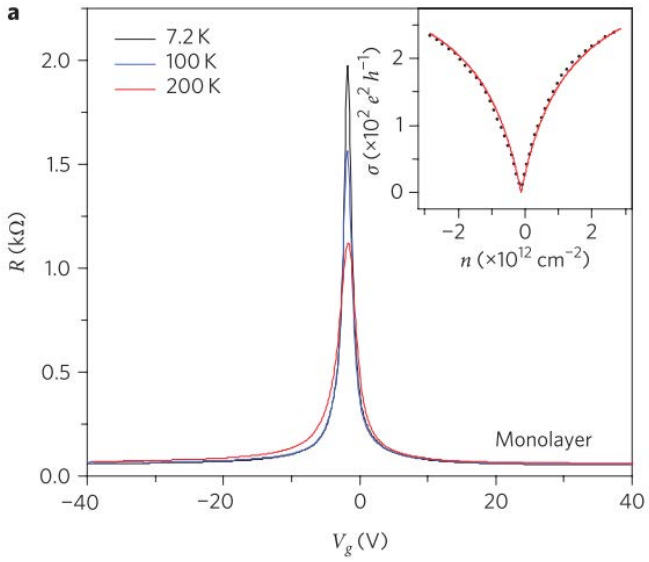

Figure 1.3: Taken from [9]. This figure shows the experimental resistivity of monolayer graphene deposited on a boron nitride substrate, as a function of the gate voltage. The inset shows the conductivity as a function of the carrier density. It is clear here that the gate voltage induces charge carriers in graphene, thus changing quite abruptly its tranport properties, going from a semimetallic to a metallic behavior.

this out-of-plane electric field from the in-plane one driving current between source and drain. The accumulation of charges also implies a global dipolar moment for the system. On either side of the system of Fig. 1.2 (on the right of the 2D material and on the left of the region of the gate where the charges accumulate), the electric field is zero. This means that the electric potential is a constant, but this constant is different on either side of the system. Indeed, the finite electric field in the dielectric induces a shift in the potential. This will be particularly important when trying to simulate this system with periodic boundary conditions. The system is quite asymmetric due to this potential shift. In the vicinity of the 2D material, we observe that the electric field is finite on one side while zero on the other.

We now proceed to the description of the electrons and phonons evolving in the 2D material.

1.2 Electrons and phonons in two dimensions

In this section we examine two central objects of condensed matter physics, electrons and phonons. Covering the very large span of physical properties in which they are involved would be a difficult task. Here, we will try to set up the minimal framework necessary to address important topics in this thesis, i.e. electron-phonon interactions, (gate-induced) doping and screening. We will concentrate on the particularities and challenges presented by those topics in a 2D framework.

It is useful to separate each atom of the material in two parts. The first consists

of the nucleus plus some core electrons that stay close to the nucleus and do not participate in bonding with neighbors. This subsystem is positively charged. The remaining electrons are valence electrons that participate in the bonding. They can travel in the material. In the following, the term "ion" will refer to the first subsystem (nucleus and core electrons), while the term "electron" will refer to the valence electrons unless specified otherwise. In solids, both ions and electrons can move, generating a gigantic number of degrees of freedom. Fortunately, in the Born-Oppenheimer (BO) approximation [11], we can decouple ionic and electronic degrees of freedom. The BO approximation roughly states that since the electrons are much lighter than the ions, they will react much faster than the ions can move. This means that the positions of the ions can be considered as parameters for the equations ruling the motion of electrons. We can then consider the movements of electrons and ions separately.

We first study an non-interacting electron gas moving in a charge compensating lattice of fixed ions. In this system, we can introduce the concepts of Bloch functions, band structure and charge doping. We then proceed to an interacting electron gas, introducing the concepts of electron-electron interactions and screening. Being aware of the key features of those concepts in 2D is the first step towards their correct treatment in the thesis. We then describe the motion of ions, using phonons. Phonons are quanta of vibrations of the ionic lattice. They have particularly interesting properties in 2D. Finally, we introduce the first order correction to the BO approximation, the electron-phonon interaction. We identify the important issues to consider for their modeling and simulation, which is the central topic of the thesis.

1.2.1 2D non-interacting electron gas in fixed ions

We consider a 2D electron gas moving in a background lattice of fixed ions. The lattice of ions is not included in the system, but its effect on the electrons can be captured by an effective periodic potential $\mathcal{U}$. This potential is a combination of the ion-ion interaction and the interaction between ions and electrons. It is a single-particle potential in the sense that its effect on a given electron does not depend on the other electrons. We start with the Bloch theory for non-interacting electrons moving in such a periodic single-particle potential. The Hamiltonian for the electrons is simply the sum of their kinetic energy and this potential:

$$\mathcal{H} = \mathcal{T}_{\text{el}} + \mathcal{U}$$

For the infinite and periodic system considered here, a plane-wave basis set is adequate to construct the wave functions. The Hamiltonian is solved by the Bloch wave functions:

$$\psi_{\mathbf{k},s}(\mathbf{r}_p,z) = \mathbf{w}_{\mathbf{k},s}(\mathbf{r}_p,z)e^{i\mathbf{k}\cdot\mathbf{r}_p}, \tag{1.2.1}$$

where $\mathbf{r}_p$ is a position vector in the plane defined by the 2D material and z is the space variable in the third dimension. The function $\mathbf{w}_{\mathbf{k},s}(\mathbf{r}_p,z)$ has the periodicity of the 2D crystal, and the factor $e^{i\mathbf{k}\cdot\mathbf{r}_p}$ represents a plane wave. The quantum numbers $\mathbf{k}, s$ represent the in-plane wave vector and band index, respectively.

The particularity of the Bloch wave functions in a 2D material is that they propagate only in the plane of the material. This is indicated by the in-plane nature of the

variables $\mathbf{k}$ and $\mathbf{r}_p$ in the plane-wave factor. The first quantum number, the momentum $\mathbf{k}$, gives the periodicity of the plane wave. The corresponding period is equal or larger than the unit cell of the crystal. The variations of the wave functions on the scale of the unit cell are given by $\mathbf{w}_{\mathbf{k},s}(\mathbf{r}_p,z)$. This function also gives the extension of the wave functions in the third dimension. The electrons are strongly attracted by the positively charged ions in the lattice and cannot go very far from them. This means that if the 2D material is situated around $z = 0$, $\mathbf{w}_{\mathbf{k},s}(\mathbf{r}_p,z)$ decays rapidly as a function of $|z|$.

The couple of indices $\mathbf{k}$,s defines an electronic quantum state. The electrons being fermions, the Pauli principle dictates that only two electrons of opposite spin can occupy one of those quantum states. We will not study spin-dependent phenomena and can consider a $\mathbf{k}$,s state as a single state with two degenerate electrons. To each $\mathbf{k}$,s state is associated an energy $\varepsilon_{\mathbf{k},s}$. Those allowed energies, as functions of the electron momenta, define the electronic band structure. Several energies might be allowed for a single momentum, thus the need for the quantum number indicating the band s.

In a neutral crystal and at zero temperature, the electrons occupy the lower-energy valence bands. For the purpose of this work, the energy of the highest occupied state at zero temperature will be called Fermi level and noted ε_F (the norm of the wave vectors for the corresponding states is the Fermi wave vector k_F). Higher in energy are the unoccupied conduction bands. As the temperature increases, some energy is available to promote some electrons to the conduction bands. The occupation of a state of energy $\varepsilon_{\mathbf{k},s}$ is then given by the Fermi-Dirac distribution:

$$f(\varepsilon) = \frac{1}{e^{\frac{\varepsilon-\varepsilon_F}{k_B T}} + 1} \tag{1.2.2}$$

where k_B is Boltzmann constant and T is the temperature. Using this function and the wave functions, one can calculate the electronic density:

$$n(\mathbf{r}_p,z) = 2\sum_{\mathbf{k},s} f(\varepsilon_{\mathbf{k},s})|\psi_{\mathbf{k},s}(\mathbf{r}_p,z)|^2. \tag{1.2.3}$$

where the factor 2 is for spin degeneracy. This quantity represents the probability of finding an electron at position $(\mathbf{r}_p,z)$.

By adding charges to the system, as can be done via the FET setup mentioned earlier, one can change the Fermi level [12]. This is called doping (or charging) the system. In the case of electron doping, the number of electrons is increased and the Fermi level is shifted higher in energy. In the case of hole doping, the number of electrons is decreased, thus creating vacancies or holes, and the Fermi level is shifted down. At zero temperature, the Fermi level defines a sharp boundary between occupied and unoccupied states. Temperature has the effect of smearing this boundary according to Eq. (1.2.2).

In 2D, an iso-energetic section of the band structure gives a line. When this section is done at the Fermi level, this line is called the Fermi surface (although it should be called the Fermi line). Doping the material changes the form of the Fermi surface. As mentioned earlier, large densities of charges can be added in 2D materials in the FET setup. This corresponds to a wide range of accessible Fermi levels, and thus the

opportunity to probe a large portion of the electronic structure. Gate-induced doping is crucial in numerous applications. Although the principle of gate-induced doping seems relatively simple, the details of its effects on the electrons of the 2D materials are not trivial. The presence of an electric field can change the form of the electronic density in the out-of-plane direction. When a few layers of material are present, the added charge will surely not be distributed homogeneously over the layers. In practice, doping the system is more complex than simply shifting the Fermi level. Understanding the side effects of gate-induced doping is a major challenge. Some of them will be treated in chap. 5.

The non-interacting gas in a lattice of fixed ions has provided us with a simple system in which to introduce basic tools. The validity of the Bloch theory extends to a system of electrons moving in any periodic single-particle potential.

1.2.2 2D electron gas: electron-electron interactions

Let us now turn on the electron-electron interactions. Those interactions are extremely complex, and the system is not exactly solvable anymore. However, we know that without any perturbation, the system stabilizes in its lowest-energy state, or ground state. The electrons then form the so-called Fermi sea. The details of what happens inside the Fermi sea are too complex. However, we can study its reaction to small perturbations. Thus, we start with the lowest-energy state of the system, and consider small excitations of the ground state. Within certain approximations (see Fermi liquid theory in Ref. [1]), the low-energy excitations of the Fermi sea can be described as quasiparticles that *behave like* single electrons weakly interacting with one another. Often, in condensed matter physics and in the following, the term "electron" actually refers to those quasiparticles. The Fermi liquid theory is fundamental because it justifies that we keep using all the previously introduced tools to study an interacting electron gas. We still need to treat the interactions between those electron quasiparticles, what we call electron-electron interactions. This is a very vast topic in condensed matter physics. For now, let us start with the contribution from the Hartree term, included throughout the thesis. The Hartree term accounts for the classical Coulomb repulsion that occurs between similarly charged particles. In our framework, it will be accounted for via the use of an additional term in the Hamiltonian for the electrons:

$$\mathcal{H} = \mathcal{T}_{\text{el}} + \mathcal{U} + V_{\text{H}}$$

where V_H is the Hartree potential, which is the electric potential generated by the electronic density. The sum $\mathcal{U}+V_H$ is still a periodic single particle potential, such that we don't go out of the Bloch framework. Reducing the electron-electron interactions to the Hartree potential amounts to a mean field approximation, since the sum of the contributions from each individual electron is averaged by the contribution from the electron density.

This "lowest-order" contribution is sufficient to introduce the concept of screening. Screening is the ability of the charges (electrons) to rearrange in order to counteract an external electric field. Any external perturbing potential that induces a varying electric field leads to a movement of the charges. The new configuration of charges will produce a new Hartree potential which tends to counteract the external perturbing potential. A

simple example is when a positive external charge is added to an electron gas. Electrons agglomerate around this added charge such that its influence is negated outside of certain region of space around it. This can be generalized to an arbitrary perturbing external potential. The effective potential felt by a test charge is the sum of the perturbing potential and the Hartree potential generated by the electrons (the induced potential). This effective potential is weaker than the original external potential, due to the global reaction of the electron gas. The electrons are said to screen the external potential.

Reduced dimensionality has substantial effects on screening [4]. This can be seen in the Fourier transform of the 2D/3D Coulomb interaction, which rules the interactions between charged particles, and thus the reaction of the electron gas:

$$v_c^{\mathrm{3D}}(|\mathbf{q}|) = \frac{4\pi e^2}{|\mathbf{q}|^2} \tag{1.2.4}$$

$$v_c^{\mathrm{2D}}(|\mathbf{q}|) = \frac{2\pi e^2}{|\mathbf{q}|} \tag{1.2.5}$$

where e is the elementary charge ($e > 0$). The different power-laws in $|\mathbf{q}|$ suggest completely different behaviors. We will see that for the transport applications we have in mind, the small momentum perturbations are most relevant. The divergent behavior of the Coulomb interaction at small $|\mathbf{q}|$ must then be carefully treated in the numerical calculations. The importance of dimensionality can also be sensed in the Lindhard function, Fig. 1.4, which gives the electron density response of the non-interacting gas to a static perturbative potential of wave vector $\mathbf{q}$. There we see that dimensionality yields different singularities near twice the Fermi wave vector. In view of the differing singularities of the Coulomb interaction at small momenta and the Lindhard function at twice the Fermi wave vector, we can expect drastically different screening behaviors from the electron gas depending on dimensionality.

In addition to those formal singularities, delicate issues arise on a more practical level. The screening properties of the 2D electron gas are subject to the influence of the environment of the 2D material. Indeed, the driving force of screening is the Coulomb interaction and the electric field generated by charged particles. Electrons in 2D materials are exposed to the influence of other charges from the environment in the out-of-plane direction. Modeling and simulating screening in 2D materials will be one of the major challenges of the following chapters.

Screening occurs as soon as there are mobile charges due to the classical Coulomb interaction between charged particles. However, electron-electron interactions beyond the Hartree term can of course play a role. Those interactions, of a more quantum nature, will be called electron correlations. Let us now quickly discuss their treatment. In general, they affect a wide variety of phenomena, basically everything that can be described as a reaction of the electrons to a certain perturbation. In strongly correlated systems, electron-electron interactions are very strong, and the formalism of the non-interacting gas (Bloch wave-functions, band structure, ...) may not make sense anymore. In weakly correlated systems, as studied in this thesis, the formalism of the non-interacting gas can be kept. Electron correlations then bring corrections to the band structure, finite lifetimes to the electrons, and they can renormalize the response of the electrons to a perturbation. Estimating those corrections is an important and

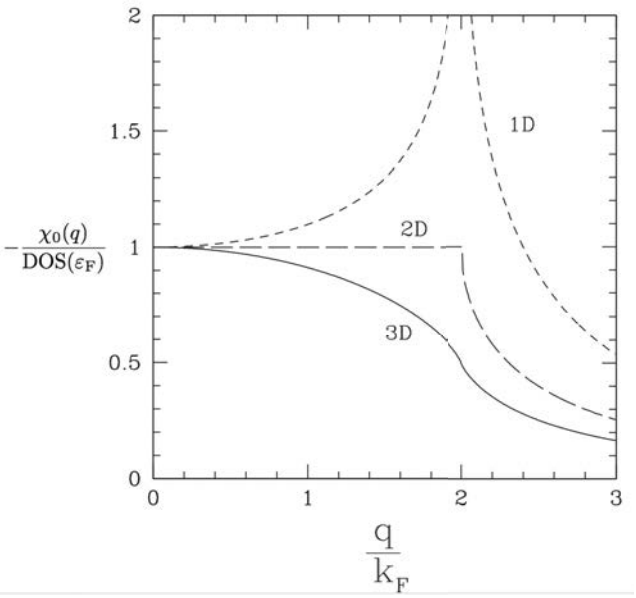

Figure 1.4: From [4]. This shows the Fourier transform of the Lindhard function in 1D, 2D and 3D, as a function of the norm of $\mathbf{q}$ in units of k_F. The Fermi wave vector k_F is the norm of the wave vector of a state on the Fermi surface (the band structure being isotropic here). The Lindhard function corresponds to the independant particle suceptibility of an electron gas χ_0 divided by its density of states at the Fermi level ($\mathrm{DOS}(\varepsilon_\mathrm{F})$ in this plot), derived in a non-interacting electron gas with a quadratic band structutre.

non-trivial task. In principle, one can use an additional potential, similar to the Hartree potential, to account for further electron-electron interactions. However, the exact form of this potential is not known, such that electron correlations are always treated within a certain approximation.

By discussing the 2D electron gas, we were able to introduce most of the peripheral topics treated in the thesis. Understanding the side effects of gate-induced doping, simulating the peculiarities of screening in 2D and estimating corrections for electron correlations are among the objectives of the next chapters. We now proceed to the description of the second central object of the thesis.

1.2.3 2D phonons

When thermal energy is available, the ions of the crystal vibrate around their equilibrium positions. Those vibrations are usually (in the scope of this work at least) well described by harmonic oscillators. They can be decomposed in a set of convenient quanta of vibrations called phonons. It does not concern an individual particle, but a collective movement of a very large (infinite) number of atoms. In the Born-Oppenheimer approximation used here, electrons adapt instantaneously to the changes in the positions of the ions. They simply act as the restoring force of the harmonic oscillators, always bringing the ions back to their equilibrium positions.

Phonon excitations are described by wave functions defining the displacements $\mathbf{u}_{\mathbf{q},\nu}(\mathbf{r}_a)$ of each atom a with respect to its equilibrium position $\mathbf{r}_a$. Those functions bear resemblance with the wave functions of the electrons. The function $\mathbf{u}_{\mathbf{q},\nu}$ is also a wave, and is similarly characterized by two quantum numbers $\mathbf{q}, \nu$. The momentum $\mathbf{q}$ gives the periodicity of the propagating wave of displacements and is an in-plane quantity in the case of a 2D material. The other index indicates a phonon branch, or mode. It specifies how the ions move. For example, for a small momentum, one may distinguish three kind of modes: (i) longitudinal modes in which the ions move in the same direction as the momentum; (ii) transverse modes in which the atoms move in the plane of the 2D material, in the direction perpendicular to the momentum; (iii) out-of-plane modes in which the ions move in the out-of-plane direction. If there are several atoms in a unit cell, the modes also distinguish whether those atoms move in phase (acoustic phonons) or out of phase (optical phonons), see Fig. 1.5. To a given phonon $\mathbf{u}_{\mathbf{q},\nu}$ is associated an energy $\hbar\omega_{\mathbf{q},\nu}$, where $\hbar$ is Planck's constant and ω is a frequency. Plotting those energies as functions of momenta gives the phonon dispersion, Fig. 1.5. Electrons and phonons are described in a quite similar way, using momentum, energy

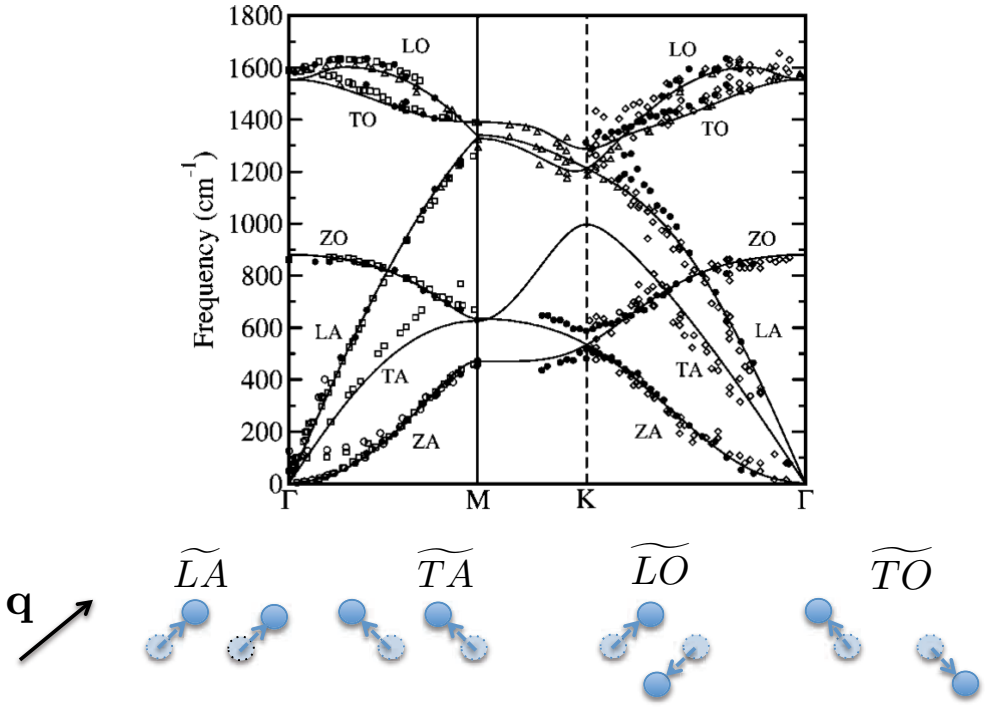

Figure 1.5: In a 2D materials with 2 atoms per unit cell, there are six phonon modes: longitudinal acoustic (LA), transverse acoustic (TA), out-of-plane acoustic (ZA), longitudinal optical (LO), transverse optical (TO), out-of-plane optical (ZO). (Top) Phonon dispersion of graphene, taken from Ref. [13]. The plain lines are *ab initio* dispersions, while the other symbols are experimental data. (Bottom) Schematic representation of the zero-momentum limit of the in-plane phonon modes (the use of tilde notation is to indicate that this is a simplified model, as will become clearer in the next chapter).

and bands or branches. A fundamental difference, however, is that phonons are bosons. This means that unlike fermions, there is no limit to the population of a given state. More precisely, the population of a given phonon state $\mathbf{q}, \nu$ of energy $\hbar\omega_{\mathbf{q},\nu}$ is given by the Bose-Einstein distribution:

$$n_{\mathbf{q},\nu}(\hbar\omega_{\mathbf{q},\nu}) = \frac{1}{e^{\frac{\hbar\omega_{\mathbf{q},\nu}}{k_B T}} - 1} \tag{1.2.6}$$

where the use of the indices $\mathbf{q}$,ν in $n_{\mathbf{q},\nu}$ distinguishes the Bose-Einstein distribution from the electronic density.

In 2D materials there is a clear distinction between in-plane and-out-plane phonon modes. The term in-plane phonons is used when the ions move only in the plane. We will see that having a good model to describe the in-plane motions of the ions is essential for modeling the transport properties of graphene. Out-of-plane phonons, and in particular flexural acoustic phonons represented in Fig. 1.6, are a peculiarity of 2D materials. In single-layer materials, they present a quadratic dispersion at small

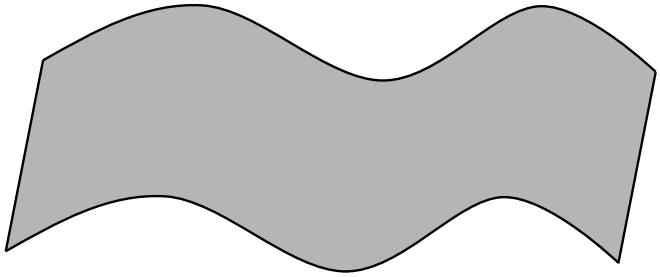

Figure 1.6: Flexural acoustic (ZA) phonon in a 2D material.

momenta $\hbar\omega_{\mathbf{q},\nu} \propto |\mathbf{q}|^2$, see Fig. 1.5. As a consequence, flexural phonons dominate low-energy, small-momentum structural properties of free-standing single-layer materials. At finite temperature, the quadratic dispersion makes the number of phonons divergent in the thermodynamic limit of an infinite system, prohibiting long-range structural order. This has generated surprise and debate concerning the existence of free-standing graphene. More in the scope of this thesis are the properties of out-of-plane phonons in the FET setup. The zero-momentum limit of the acoustic out-of-plane phonon is equivalent to a displacement of the whole 2D material in the out-of-plane direction. When the 2D material is enclosed between a substrate and a dielectric, the energy required to achieve such a displacement is finite. Contrary to a free standing material, the dispersion should then tend to a constant in the small-momentum limit. This is one of the side-effects of the FET setup that would be interesting to simulate.

Phonons are involved in many properties of the material. Their vibrational nature and the fact that their abundance is ruled by temperature makes them central for the description of the thermodynamical and mechanical properties of crystals. They are involved in many other physical properties via their coupling to the electrons.

1.2.4 Electron-phonon interactions

The ground state picture is that of electrons moving in a periodic potential generated by fixed ions. An electron in a Bloch state can move in the ionic potential without

disturbance. Phonons come as a perturbation of this picture. By displacing ions, charge imbalances are created with respect to the unperturbed ionic potential. This idea, for a single ion displacement, is represented in Fig. 1.7. A phonon can be seen as a creation of such charge imbalance for each ion, in a periodic manner. In terms of

Figure 1.7: From [1]. On the left, a Bloch electronic state propagates freely in the ionic potential. On the right, a displaced ion results in the creation of a charge imbalance and a scattering event from one Bloch state to another.

electronic structure, a phonon perturbation translates into the possibility for electrons to jump from one electronic state to another. This is called a scattering event, often represented as in Fig. 1.8. Such scattering events are characterized by the exchange of energy and momentum between phonons and electrons. Electron-phonon coupling (EPC) is a measure of how probable it is for a given electron to be scattered by a certain phonon.

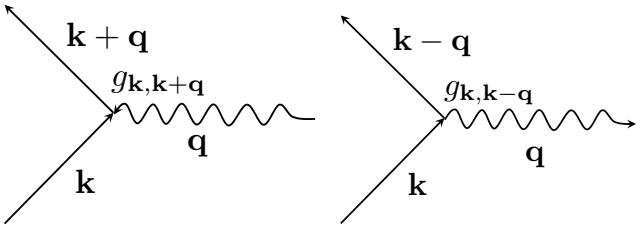

Figure 1.8: The electron-phonon vertex represents an echange of energy and momentum between an electron and a phonon. On the left, the electron-phonon matrix element $g_{\mathbf{k},\mathbf{k}+\mathbf{q}}$ is represented. An electron of momentum $\mathbf{k}$ and energy $\varepsilon_{\mathbf{k},s}$ is scattered to a state of momentum $\mathbf{k}+\mathbf{q}$ and energy $\varepsilon_{\mathbf{k},s}+\hbar\omega_{\mathbf{q},\nu}$ via the absorption of a phonon of momentum $\mathbf{q}$ and energy $\hbar\omega_{\mathbf{q},\nu}$. On the right, the electron-phonon matrix element $g_{\mathbf{k},\mathbf{k}-\mathbf{q}}$ is represented. An electron of momentum $\mathbf{k}$ and energy $\varepsilon_{\mathbf{k},s}$ is scattered to a state of momentum $\mathbf{k}-\mathbf{q}$ and energy $\varepsilon_{\mathbf{k},s}-\hbar\omega_{\mathbf{q},\nu}$ via the emission of a phonon of momentum $\mathbf{q}$ and energy $\hbar\omega_{\mathbf{q},\nu}$.

EPC is particularly relevant in the context of electron transport. If an in-plane electric field is applied to generate a net carrier current, the scattering events tend to counteract its effects. The phonons can then be seen as obstacles impeding the flow of carriers, and the material becomes resistive. We will study the corresponding physical quantity, the phonon-limited resistivity, in chapter 6. There are, of course, numerous other sources of scattering in practice. Defects are usually the major one. However, the intrinsic nature of phonon scattering makes it particularly interesting. Intrinsic sources of scattering set an ideal limit for electronic devices. Indeed, the fabrication processes can be improved to reduce the extrinsic sources of scattering such as defects. Scattering by phonons, however, will always be present. It is thus important to have a good understanding of it. An other common source of intrinsic scattering are electron-

electron interactions. However, when looking at the transport properties of a material as a function of temperature, EPC is the most relevant intrinsic scattering source. The typical behavior of resistivity as a function of temperature is shown in Fig. 1.9. The zero-temperature limit of the resistivity, called residual resistivity, is mainly due to the impurities and defects in the material. As temperature increases, more phonon states are populated, leading to more electron-phonon scattering events and an increasing resistivity.

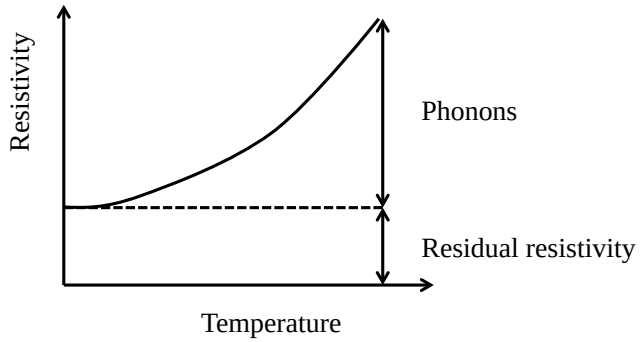

Figure 1.9: The typical behavior of a material's resisitivity is characterized by an increase with temperature as phonon states are populated.

EPC is important in other contexts than transport, such as spectroscopy. In photoemission spectroscopy, one probes the spectral function of an excited electron. Phonons interact with the excited electron, absorbing its extra energy. This translates into a finite lifetime for the excited electron and a broadening of its spectral function. Inversely, in neutron scattering or Raman spectroscopy, a phonon state is excited. Electron-phonon interactions then modify the signature of the phonon state. EPC is the origin of complex and fascinating phenomena such as Kohn anomalies [14], phonon softening and superconductivity [15]. Kohn anomalies and phonon softening relate to the effects of electrons on the phonon dispersions. They appear when the lattice vibrates at momenta and frequencies that happen to have a particular relevance for the electrons. Superconductivity, in conventional superconductors at least, occurs thanks to the pairing of electrons via phonons. Large EPC is one of the ingredients to obtain high-temperature superconductivity.

Reduced dimensionality has interesting implications on the interplay between electrons and phonons, via the previously introduced concepts of gate-induced doping, electron-electron interactions and screening. Large doping levels imply significant changes in the form of the Fermi surface along with the characteristics of the electrons involved in the electron-phonon interactions. Via temperature, the phonon momenta and energies can also be tuned. A fundamentally interesting aspect of 2D materials is thus the opportunity to explore a large span of momenta and energies for the electrons and phonons. The particular case of gate-induced doping in the FET setup has consequences for the coupling of electrons with out-of-plane phonons. Since this kind of modes involves atomic displacements in the out-of-plane direction, they are evidently influenced by the direct vicinity of the 2D material in this direction. The dispersion of those modes and their coupling to electrons can then be affected. In particular,

the out-of-plane symmetry of the system is important. A free-standing 2D material in vacuum presents certain symmetries with respect to the material's plane. In graphene, for example, the carbon-carbon π-bonds are anti-symmetric, as is the perturbation induced by an out-of-plane phonon. This forbids the coupling of electrons to a single out-of-plane phonon [16]. In the FET setup of Figs. 1.1 and 1.2, however, the anti-symmetry with respect to the plane is broken and scattering by a single out-of-plane phonon becomes possible.

EPC stems from the perturbation of the potential of the ions by phonons. As a perturbing potential, EPC can be screened. The previous remarks about the particularities of screening in 2D and in the FET setup thus apply to EPC if it is screened. Correctly simulating the screening of EPC in 2D materials is an important topic throughout the thesis. Electron-electron interactions, by bringing corrections to the energies of the electronic states, change the momentum-energy landscape in which the electron-phonon interactions occur. They can also bring corrections directly to the magnitude of the interaction. This will be discussed in chapter 3.

Accurate models and reliable simulations of electron-phonon interactions are essential to understand a wide variety of phenomena, including transport properties. This is the main objective of this thesis. We will need to understand the subtle way in which this interaction depends on the Fermi level, the electronic and phonon momenta, temperature, screening, the surrounding environment, etc... A good understanding can be achieved via computer simulations, but some aspects of the 2D system we described need to be dealt with carefully.

1.3 Simulation challenges

Our simulations are performed within the density-functional theory (DFT) framework, described in App. A and well documented in the literature, see for example Refs. [17, 18, 19, 20, 21]. We use the Quantum ESPRESSO (QE) distribution. In this section, we point out why the treatment of some of the previously introduced concepts will prove problematic in our simulations.

The first challenge is the treatment of electron-electron interactions in the calculation of EPC. DFT maps the problem of the interacting electron gas on a system of non-interacting electrons moving in an effective potential (see App. A for more details). In this framework, electron-electron interactions are accounted for by adding density-dependent potentials to the effective potential, like the Hartree potential mentioned earlier. The Hartree potential will always be included in our DFT calculations. Further quantum many-body aspects of electron-electron interactions will be approximately accounted for via the addition an exchange-correlation potential, determined within the local-density approximation [22] (LDA). In this approximation, the exchange-correlation potential is computed using analytical results derived for the 3D homogenous electron gas. The effects of this potential will be discussed further in the thesis, but it is reasonable to assume that its reliability for the non-homogenous 2D electron gases studied in the following is limited. For certain significant electron-phonon interactions, we will go beyond LDA and develop a method to compute EPC parameters within the GW approximation [23]. GW designates an approximation in

the calculation of the self-energy of interacting electrons. It provides corrections to the energies of the electronic eigenstates found by DFT. In graphene, the corresponding corrected band structure is in good agreement with experiment. The challenge is that those corrections cannot be included in the direct simulation of electron-phonon interactions. We developed a method to extract electron-phonon interactions from band structure calculations, which can be carried out within the GW approximation. This method is presented in Chapter 3.

The second challenge is related to the fact that our DFT calculations require periodic boundary conditions in the three dimensions (3D PBC). In practice, one defines a unit cell that is implicitly repeated infinitely in the three dimensions, resulting in a 3D-periodic system. To simulate a 2D material, we actually simulate a system that is a collection of copies of the 2D material arranged periodically in the out-of-plane direction. Those copies are called the periodic images. Their presence raises two important issues. The first one concerns the simulation of screening. As was pointed out earlier, the environment of the 2D material in the out-of-plane direction matters. We'll see that the presence of periodic images leads to some spurious screening. We can reduce this effect by increasing the distance between the periodic images, but the computational cost of the calculation increases linearly with this distance. The computational cost quickly becomes prohibitive when the 2D electron gas (in each periodic image) is perturbed at small wave vector. Indeed, the diverging behavior of the Coulomb interaction in the limit of small wave vectors implies long-range interactions between the periodic images. The small wave vector limit of screening is relevant for many applications, including phonon-limited transport. Thus, we need to find a way to simulate the correct screening properties of an isolated 2D material by getting rid of the periodic images. This issue is tackled in chapter 4.

We saw that gate-induced doping as in the FET setup relies on a certain asymmetry in terms of electric potential. We also determined that it is essential to be able to simulate this asymmetry to explore some interesting consequences of gate-induced doping on the electronic density and the phonons. 3D PBC present a challenge for the simulation of such an asymmetric system. Indeed, 3D PBC require equal values of the potential on both sides of the 2D system, since the right boundary of one periodic image is the left boundary of the next one. In the FET setup, Fig. 1.2, the out-of-plane electric field established in the dielectric induces a difference in the values of the potential on both sides. Consequently, the FET setup does not fulfill PBC in the third direction and simulating gate-induced doping is a challenge in our DFT framework. The current standard method to dope materials while fulfilling 3D PBC in DFT amounts to the use of a compensating uniform background of charges, the so-called jellium background. However, this "jellium-induced" doping is fundamentally different from gate-induced doping because the system remains symmetric with respect to the plane of the 2D material. To explore the effects of gate-induced doping and in particular the possibility of a linear coupling with out-of-plane phonons in graphene, it is essential to find a way around 3D PBC and simulate asymmetric setups like the FET. In chapter 5, we will devise a different approach concerning the treatment of PBC, effectively isolating the periodic images from each other and enabling the simulation of the FET setup.

The structure of the following chapters mirrors the successive tackling of those

challenges in the process of simulating electron-phonon interactions in graphene. Since the linear coupling with out-of-plane phonons is zero in graphene unless we are able to simulate the FET setup, we ignore out-of-plane phonons in the first place. We start with models for electrons, in-plane phonons and their interactions in chapter 2. Among the couplings between electrons and in-plane phonons, those that are *not screened* are readily calculable in the standard DFT framework. We go one step beyond in terms of electron-electron interactions and compute those EPC parameters within the GW approximation in chapter 3, tackling the first challenge. To obtain an estimation of the *screened* EPC parameters, we tackle the challenge presented by the presence of periodic images to study the screening properties of graphene in chapter 4. We then solve the issue of the periodic images more comprehensively to be able to simulate graphene in the FET setup and study the coupling with out-of-plane phonons in chapter 5. In chapter 6, we test our model of electron-phonon interactions by including it in a transport model, computing the phonon-limited resistivity of graphene and comparing our results to experimental data.

Chapter 2

Electron-phonon interactions model in graphene

The study of EPC involves the derivation of models for the interaction Hamiltonian as well as the phonon modes. The interaction Hamiltonian was derived within the tight-binding (TB) model (see Refs. [24, 25, 26, 14, 27, 28] and App. B) and in a symmetry-based approach [16]. In many works the simple set of strictly longitudinal and transverse phonon modes is used to find the EPC matrix elements. However, some qualitative [16] and quantitative [25, 26] models showed that more realistic phonon modes may be essential to obtain numerically accurate results for acoustic phonon scattering. In this chapter we improve the most general symmetry-based model of EPC [16] by introducing a DFT-based model for the phonon modes. Within this analytical model, we consider a single layer of graphene free standing in vacuum. In this context, out-of-plane phonon modes do not couple with electrons at the linear order [16]. They will thus be discarded for now. Their numerical study requires the implementation of the more complex FET setup. This is postponed to chapter 5. In this chapter, we focus on the coupling to in-plane phonon modes. After presenting the low-energy Hamiltonian for the electrons, we use density-functional perturbation theory (DFPT) calculations to obtain a realistic model for the relevant in-plane phonon modes. We then present the different terms that appear in the electron-phonon interaction Hamiltonian and derive the corresponding EPC matrix elements.

2.1 Electrons and phonons models

2.1.1 Dirac Hamiltonian for electrons

The crystal structure of graphene is represented in Fig. 2.1. Within DFT, this yields the band structure represented in Fig. 2.2. We consider low electron doping of graphene, i.e. the Fermi level energy shift from the Dirac point is $\varepsilon_F \lesssim 0.5$ eV (all energies throughout the thesis are measured with respect to the Dirac point). This corresponds to an additional surface charge density of less than 1.8×10^{13} cm^{-2}. In this regime, the electronic structure of doped graphene is well represented by two Dirac cones [29] at special points $\mathbf{K}$= (2/3,0)$2\pi/b$ and $\mathbf{K}' = (-2/3,0)2\pi/b$ in Cartesian

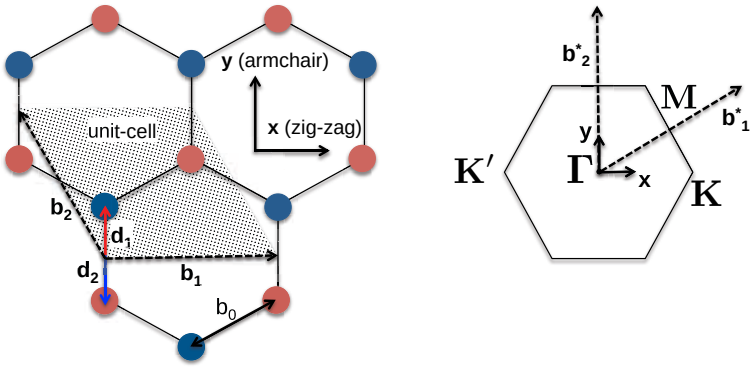

Figure 2.1: Definition of the real space unit cell (left) and the first Brillouin zone (right). $\mathbf{b_1} = (1,0)b$ and $\mathbf{b_2} = (-1/2,\sqrt{3}/2)b$ are the lattice vectors in Cartesian coordinates and $|\mathbf{b_1}| = |\mathbf{b_2}| = b = 2.46$ Å is the lattice parameter. $b_0 = b/\sqrt{3} = 1.42$ Å is the interatomic distance. The **x**-axis (**y**-axis) corresponds to the zig-zag (armchair) direction. $\mathbf{d_1} = (1/6,1/3)$ and $\mathbf{d_2} = (-1/6,-1/3)$ are the internal coordinates of the carbon atoms in the basis of the lattice vectors. In reciprocal space, $\mathbf{b_1^*} = (1,1/\sqrt{3})2\pi/b$ and $\mathbf{b_2^*} = (0,2/\sqrt{3})2\pi/b$ are the reciprocal lattice vectors in cartesian coordinates. In the Brillouin zone, the high symmetry points $\mathbf{\Gamma}$, $\mathbf{K}$, $\mathbf{K'}$ and $\mathbf{M}$ are represented.

coordinates, see Figs. 2.1 and 2.2. The x-axis is defined as the zig-zag direction of the graphene sheet, and $b = 2.46$ Å is the lattice parameter of graphene. We will extend the validity of the Dirac cones model to $\varepsilon_F \lesssim 1.0$ eV by assuming that the so-called trigonal warping of the bands has a negligible effect when the quantities of interest here are angularly averaged. In the absence of electron-phonon scattering the unperturbed Hamiltonian at momentum $\mathbf{k}$ expanded around the Dirac point $\mathbf{K}$ is

$$\mathcal{H}_{\mathbf{K}}(\mathbf{k}) = \hbar v_F \begin{pmatrix} 0 & k_x - ik_y \\ k_x + ik_y & 0 \end{pmatrix} \tag{2.1.1}$$

where v_F is the Fermi velocity and $\mathbf{k} = (k_x,k_y)$ is the electron-momentum measured with respect to the Dirac point $\mathbf{K}$, in a Cartesian basis. It can also be written as $\mathcal{H}_{\mathbf{K}}(\mathbf{k}) = \hbar v_F \mathbf{k}\cdot\sigma$, where $\sigma = (\sigma_x,\sigma_y)$ are the Pauli matrices. This Dirac Hamiltonian is written in the pseudospin [30] basis emerging from the two inequivalent sub-lattices of graphene. It satisfies the eigenvalues equation:

$$\mathcal{H}_{\mathbf{K}}(\mathbf{k})\psi_{\mathbf{k},s}(\mathbf{r}) = \varepsilon_{\mathbf{k},s}\psi_{\mathbf{k},s}(\mathbf{r}), \tag{2.1.2}$$

with $\varepsilon_{\mathbf{k},s} = s\ \hbar v_F|\mathbf{k}|$, and $s = \mp 1$ for the valence π and conduction π^* bands respectively. The Bloch functions are

$$\psi_{\mathbf{k},s}(\mathbf{r}) = \frac{1}{\sqrt{NS}} e^{i\mathbf{k}\cdot\mathbf{r}}|\mathbf{k},s\rangle, \tag{2.1.3}$$

where $S = \frac{\sqrt{3}b^2}{2}$ is the area of a unit cell, N is the number of unit cells in the sample and $|\mathbf{k},s\rangle$ is a pseudospinor eigenfunction, normalized to unity, corresponding to the

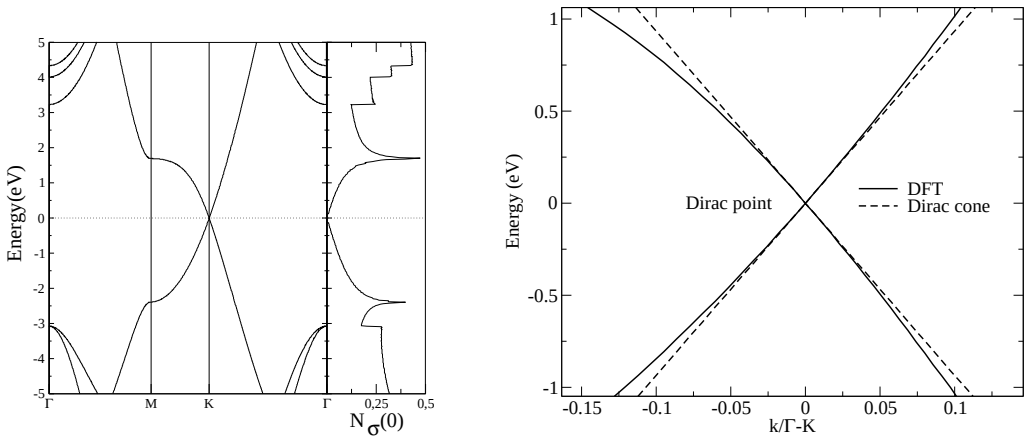

Figure 2.2: On the left is represented the band structure and density of states of graphene as obtained in DFT, along the high symmetry lines. On the right is a comparison of the DFT band structure with the Dirac cone model around the Dirac point.

in-plane state $\mathbf{k}$ of the band s. The eigenfunction $|\mathbf{k},s\rangle$ is defined in the pseudospin basis as:

$$|\mathbf{k},s\rangle = \frac{1}{\sqrt{2}} \begin{pmatrix} e^{-i\theta_{\mathbf{k}}/2} \\ s e^{i\theta_{\mathbf{k}}/2} \end{pmatrix}. \tag{2.1.4}$$

The angle $\theta_{\mathbf{k}}$ is the angle between $\mathbf{k}$ and the x-axis.

2.1.2 Phonons

We label $\mathbf{e}_{\mathbf{q},\nu}$ the eigenvector of the dynamical matrix corresponding to the phonon mode ν of momentum $\mathbf{q}$ and eigenvalue $\omega^2_{\mathbf{q},\nu}$ (those quantities are defined in App. A). This phonon eigenvector is normalized on the unit cell and $\omega_{\mathbf{q},\nu}$ is the frequency of the phonon mode. The components of the vector $\mathbf{e}_{\mathbf{q},\nu}$ are labeled $\mathbf{e}^{a,i}_{\mathbf{q},\nu}$ where $a = 1{,}2$ is an atomic index and $i = 1{,}2$ are the in-plane Cartesian coordinates (out-of-plane phonons are ignored here). For a scattering event to effectively occur, a phonon must scatter an electron from an occupied initial state to an available final state. Since the phonon energies are relatively small ($\lesssim 0.20$ eV) in comparison with the full range of the electronic band structure (≈ 5 eV), the electronic states involved in scattering processes stay relatively close to the Fermi surface. At the moderate doping levels considered, the Fermi level lies in the Dirac cones. Consequently, the relevant phonon momenta are those connecting electronic states in those cones. The relevant phonons are thus restricted to the regions around the $\mathbf{\Gamma}$ and $\mathbf{K}$ points of the phonon dispersion in Fig. 2.3. The small-momentum phonons near the $\mathbf{\Gamma}$ point scatter electrons within a single Dirac cone or valley. They are called intra-valley scattering modes. The phonons with momenta near the $\mathbf{K}$ point scatter electrons from one Dirac cone to an other and are called inter-valley scattering modes. We first focus on small-momentum

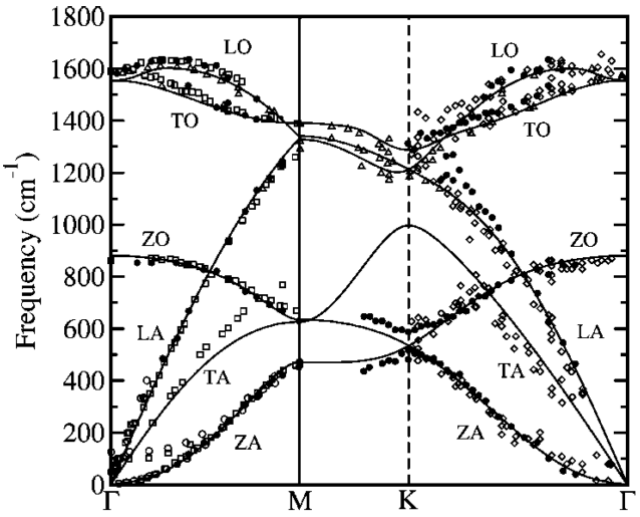

Figure 2.3: Phonon dispersion of graphene, taken from Ref. [13]. The plain lines are *ab initio* dispersions, while the other symbols are experimental data.

intra-valley phonons. Near the $\mathbf{\Gamma} = (0,0)$ point (i.e. $|\mathbf{q}| \to 0$), it is customary to use what will be called here the canonical representation of the four in-plane phonon modes to approximate the real ones. The construction of those canonical modes relies on the following rules: i) the eigenvector of a longitudinal (transverse) mode is parallel (perpendicular) to the phonon's momentum; ii) the phase differences between the two atoms of the unit cell is $e^{i\mathbf{q}\cdot(\mathbf{d_1}-\mathbf{d_2})}$ for acoustic modes and $-e^{i\mathbf{q}\cdot(\mathbf{d_1}-\mathbf{d_2})}$ for optical modes. This leads to the following eigenvectors:

$$\begin{aligned}
\mathbf{e}^a_{\mathbf{q},\widetilde{\mathrm{LA}}} &= \frac{1}{\sqrt{2}} e^{i\mathbf{q}\cdot(\mathbf{R}+\mathbf{d_a})} \frac{\mathbf{q}}{|\mathbf{q}|} \\
\mathbf{e}^a_{\mathbf{q},\widetilde{\mathrm{TA}}} &= \frac{1}{\sqrt{2}} e^{i\mathbf{q}\cdot(\mathbf{R}+\mathbf{d_a})} \frac{\mathbf{q}_\perp}{|\mathbf{q}_\perp|} \\
\mathbf{e}^a_{\mathbf{q},\widetilde{\mathrm{LO}}} &= \gamma_a \frac{1}{\sqrt{2}} e^{i\mathbf{q}\cdot(\mathbf{R}+\mathbf{d_a})} \frac{\mathbf{q}}{|\mathbf{q}|} \\
\mathbf{e}^a_{\mathbf{q},\widetilde{\mathrm{TO}}} &= \gamma_a \frac{1}{\sqrt{2}} e^{i\mathbf{q}\cdot(\mathbf{R}+\mathbf{d_a})} \frac{\mathbf{q}_\perp}{|\mathbf{q}_\perp|}
\end{aligned} \tag{2.1.5}$$

where $\mathbf{R}$ is the position of the unit cell, $\mathbf{d_a}$ $a = 1,2$ are defined in Fig. 2.1 and $\mathbf{q}_\perp$ is such that $\mathbf{q}_\perp \cdot \mathbf{q} = 0$. $\gamma_a = \pm 1$ for $a = 1,2$ respectively. The mode indices $\widetilde{\mathrm{LA}}$, $\widetilde{\mathrm{TA}}$ label the canonical longitudinal and transverse acoustic phonon modes, respectively. The canonical longitudinal and transverse optical phonon modes are labeled $\widetilde{\mathrm{LO}}$ and $\widetilde{\mathrm{TO}}$ respectively. In Fig. 2.4 is a schematic representation of those modes.

As noted in Ref. [16], the real phonon modes of graphene at finite momentum tend to the canonical modes in the long wavelength limit. However, at finite momentum, there is some mixing between the canonical acoustic and optical phonon modes in $o(|\mathbf{q}|)$. We find that the use of the canonical eigenvectors leads to a significant error in the following work. Therefore we seek an analytical model for the phonon modes that

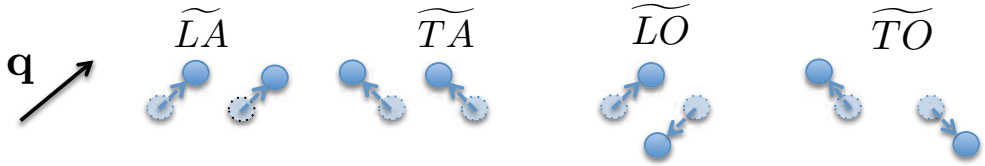

Figure 2.4: A schematic representation of the in-plane canonical phonon modes. This picture is valid in the limit $|\mathbf{q}| \to 0$ or in a perfectly square lattice. At finite $|\mathbf{q}|$, in graphene, the real phonon modes are a mixture of the above canonical modes.

includes acoustic-optical mixing. We diagonalize the dynamical matrix, calculated by DFPT (see App. A) on a small circle around the $\mathbf{\Gamma}$ point. This allows us to obtain the angular dependence in $\mathbf{q}$ at fixed $|\mathbf{q}|$. Comparing the DFT eigenvectors to the canonical ones, we obtain the following expressions:

$$\begin{aligned}
\mathbf{e}_{\mathbf{q},\mathrm{LA}} &= \sqrt{1-\delta^2|\mathbf{q}|^2}\ \mathbf{e}_{\mathbf{q},\widetilde{\mathrm{LA}}} - \delta\ |\mathbf{q}|\left(\sin(3\theta_{\mathbf{q}})\mathbf{e}_{\mathbf{q},\widetilde{\mathrm{LO}}} + \cos(3\theta_{\mathbf{q}})\mathbf{e}_{\mathbf{q},\widetilde{\mathrm{TO}}}\right)\\
\mathbf{e}_{\mathbf{q},\mathrm{TA}} &= \sqrt{1-\delta^2|\mathbf{q}|^2}\ \mathbf{e}_{\mathbf{q},\widetilde{\mathrm{TA}}} + \delta\ |\mathbf{q}|\left(\cos(3\theta_{\mathbf{q}})\mathbf{e}_{\mathbf{q},\widetilde{\mathrm{LO}}} - \sin(3\theta_{\mathbf{q}})\mathbf{e}_{\mathbf{q},\widetilde{\mathrm{TO}}}\right)\\
\mathbf{e}_{\mathbf{q},\mathrm{LO}} &= \sqrt{1-\delta^2|\mathbf{q}|^2}\ \mathbf{e}_{\mathbf{q},\widetilde{\mathrm{LO}}} - \delta\ |\mathbf{q}|\left(\sin(3\theta_{\mathbf{q}})\mathbf{e}_{\mathbf{q},\widetilde{\mathrm{LA}}} + \cos(3\theta_{\mathbf{q}})\mathbf{e}_{\mathbf{q},\widetilde{\mathrm{TA}}}\right)\\
\mathbf{e}_{\mathbf{q},\mathrm{TO}} &= \sqrt{1-\delta^2|\mathbf{q}|^2}\ \mathbf{e}_{\mathbf{q},\widetilde{\mathrm{TO}}} + \delta\ |\mathbf{q}|\left(\cos(3\theta_{\mathbf{q}})\mathbf{e}_{\mathbf{q},\widetilde{\mathrm{LA}}} - \sin(3\theta_{\mathbf{q}})\mathbf{e}_{\mathbf{q},\widetilde{\mathrm{TA}}}\right)
\end{aligned} \tag{2.1.6}$$

Where $\delta \approx 0.10$ Å is a small parameter, and $\theta_{\mathbf{q}}$ is the angle of $\mathbf{q}$ with respect to the x-axis. Our DFT results are consistent with the symmetry-based analysis of Ref. [16].

In addition to the intra-valley scattering modes at $\mathbf{\Gamma}$, we have to consider the optical A_1' inter-valley phonon mode, having momentum $\mathbf{K}+\mathbf{q}$, with $\mathbf{q}$ being small. The electron-phonon coupling for this mode will be parametrized as in Ref. [14].
At small $|\mathbf{q}|$, optical phonons frequencies can be considered constant ($\hbar\omega_{\mathrm{TO}} = \hbar\omega_{\mathrm{LO}} = 0.20$ eV, $\hbar\omega_{\mathrm{A}_1'} = 0.15$ eV). Acoustic phonon frequencies are of the form $\hbar\omega_{\mathbf{q},\nu} = v_\nu|\mathbf{q}|$, where v_ν is the sound velocity of ν mode (from our DFT calculations, $v_{\mathrm{TA}} = 13.6$ km/s and $v_{\mathrm{LA}} = 21.4$ km/s, independent of the direction).

2.2 Electron-phonon coupling matrix elements

In this section we develop the electron-phonon interactions model at small but finite momentum (i.e. $|\mathbf{q}| \to 0$). We use both the canonical and DFT-based eigenvectors of the phonon modes at $\mathbf{\Gamma}$ and compare the results. For the inter-valley scattering A_1' mode at $\mathbf{K}$, the model has already been developed [14] and is simply summarized in paragraph 2.2.3. We will focus on the case of the Hamiltonian expanded around the Dirac point $\mathbf{K}$. Similar results are obtained around $\mathbf{K}'$ by complex conjugation and the transformations $\mathbf{k} \to -\mathbf{k}$ and $\mathbf{q} \to -\mathbf{q}$.

The small $|\mathbf{q}|$ limit of the derivative of the Dirac Hamiltonian with respect to a general phonon displacement $\mathbf{e}_{\mathbf{q}}$ can be found from symmetry considerations. In the basis of Dirac pseudospinors, Eq. (2.1.4), it is written [16]:

$$\Delta\mathcal{H}_{\mathbf{q}} = \Delta\mathcal{H}_{\mathbf{q},\tilde{A}} + \Delta\mathcal{H}_{\mathbf{q},\tilde{O}} \tag{2.2.1}$$

where

$$\Delta\mathcal{H}_{\mathbf{q},\tilde{A}} = i|\mathbf{q}| \times \begin{pmatrix} 2\alpha(q)Q_{\widetilde{\mathrm{LA}}} & \tilde{\beta_A}e^{-2i\theta_q}(Q_{\widetilde{\mathrm{LA}}} - iQ_{\widetilde{\mathrm{TA}}}) \\ \tilde{\beta_A}e^{2i\theta_q}(Q_{\widetilde{\mathrm{LA}}} + iQ_{\widetilde{\mathrm{TA}}}) & 2\alpha(q)Q_{\widetilde{\mathrm{LA}}} \end{pmatrix} \tag{2.2.2}$$

accounts for the canonical in-plane acoustic modes and

$$\Delta\mathcal{H}_{\mathbf{q},\tilde{O}} = i \times \begin{pmatrix} 0 & \tilde{\beta_O}e^{i\theta_q}(Q_{\widetilde{\mathrm{LO}}} + iQ_{\widetilde{\mathrm{TO}}}) \\ -\tilde{\beta_O}e^{-i\theta_q}(Q_{\widetilde{\mathrm{LO}}} - iQ_{\widetilde{\mathrm{TO}}}) & 0 \end{pmatrix} \tag{2.2.3}$$

accounts for the canonical in-plane optical modes[1]. Parameters $\tilde{\beta_A}$ and $\tilde{\beta_O}$ are real constants and $\alpha(q)$ is a real function of the norm of the phonon momentum $q = |\mathbf{q}|$. In a tight-binding model, they are related to the derivatives of the hopping parameters with respect to bond length, see App. B. Here, we stay in the more general symmetry-based approach of Ref. [16]. The scalar quantities $Q_{\tilde{\nu}}$ are the components of $\mathbf{e_q}$ in the basis of the canonical eigenvectors, namely:

$$Q_{\tilde{\nu}} = \mathbf{e_q} \cdot \mathbf{e}_{\mathbf{q},\tilde{\nu}} \tag{2.2.4}$$

$\Delta\mathcal{H}_{\mathbf{q},\nu}$ is easily understood as a change of the electronic structure due to the phonon displacement, see Fig. 2.5. In more details:

- β-terms (normally labeled "gauge fields" [24]) in Eqs. (2.2.2), (2.2.3) are added to the off-diagonal terms of the Dirac Hamiltonian, Eq. (2.1.1). *They shift the Dirac point in the Brillouin zone without changing its energy.* As such, these terms do not alter the overall charge and are unaffected by electronic screening. In a TB model, these terms are related to a variation of the nearest neighbors hopping integral with respect to the in-plane lattice parameter. In a uni-axially strained graphene sheet, the β-terms correspond to the magnitude of the vector potential (the so-called "synthetic gauge field" [31, 32, 16]) that appear in the perturbed terms of the Dirac Hamiltonian. Note that in the presence of a non-uniform strain field, such a synthetic vector potential affects the band structure as an effective magnetic field [33].

- α-term (labeled "deformation potential") occurs only in the diagonal part of Eq. (2.2.2). *These terms shift the Dirac point in energy, without changing its position in the Brillouin zone.* As they imply a variation of the charge state, they are strongly affected by electronic screening. We use here the screened deformation potential $\alpha(q)$, in contrast with the original model of Ref. [16] where screening is ignored and a bare constant deformation potential α^{bare} is used. In a TB model this kind of term corresponds to a variation of the on-site energy. In mechanically strained graphene, it represents the magnitude of the scalar potential or "synthetic electric field" [31, 16] triggered by a change in the unit cell area.

The EPC matrix elements are defined as

$$g_{\mathbf{k}+\mathbf{q},s,\mathbf{k},s',\nu} = \sqrt{\frac{\hbar}{2M\omega_{\mathbf{q},\nu}}}\langle \mathbf{k}+\mathbf{q},s|\Delta\mathcal{H}_{\mathbf{q},\nu}|\mathbf{k},s'\rangle \tag{2.2.5}$$

[1]Sign differences with respect to Ref. [16] are due to switched definitions of $\mathbf{K}$ and $\mathbf{K}'$.

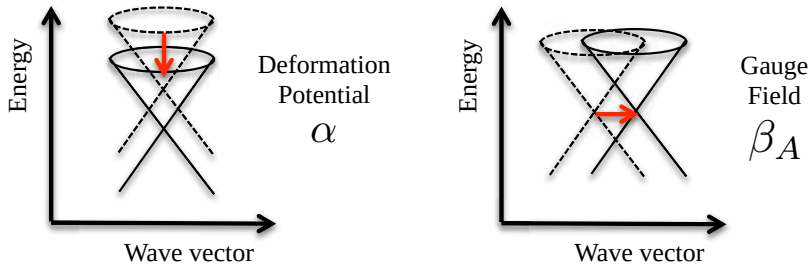

Figure 2.5: A schematic representation of the two different contributions to the coupling to in-plane acoustic phonons.

where M is the mass of a carbon atom, $|\mathbf{k},s'\rangle$ and $|\mathbf{k}+\mathbf{q},s\rangle$ are the initial and final electronic states of the scattering process. Since we are mostly interested in intraband scattering processes (with acoustic phonons), we will drop the s and set $s = s' = 1$. Setting $s = s' = -1$ would give the same final results due to electron-hole symmetry. When we consider interband scattering from optical phonons, we will specify the s-dependency. We further simplify the notation by setting:

$$\langle \mathbf{k}+\mathbf{q}, 1|\Delta\mathcal{H}_{\mathbf{q},\nu}|\mathbf{k}, 1\rangle = \Delta\mathcal{H}_{\mathbf{q},\nu}(\mathbf{k}) \tag{2.2.6}$$

We will now study the EPC models obtained using either canonical or DFT phonon modes at $\mathbf{\Gamma}$ with Eq. (2.2.1).

2.2.1 Coupling to canonical phonon modes at Γ

Using the canonical phonon modes, the small phonon-momentum limit ($|\mathbf{q}| \to 0$) of $\Delta\mathcal{H}_{\mathbf{q},\nu}(\mathbf{k})$ can be written as:

$$|\Delta\mathcal{H}_{\mathbf{q},\widetilde{\mathrm{TA}}}(\mathbf{k})| = \left|\tilde{\beta_A}|\mathbf{q}| \sin\left(2\theta_{\mathbf{q}} + \frac{\theta_{\mathbf{k}+\mathbf{q}} + \theta_{\mathbf{k}}}{2}\right)\right| \tag{2.2.7}$$

$$|\Delta\mathcal{H}_{\mathbf{q},\widetilde{\mathrm{LA}}}(\mathbf{k})| = \left|2\alpha(q)|\mathbf{q}| \cos\left(\frac{\theta_{\mathbf{k}+\mathbf{q}} - \theta_{\mathbf{k}}}{2}\right) + \tilde{\beta_A}|\mathbf{q}| \cos\left(2\theta_{\mathbf{q}} + \frac{\theta_{\mathbf{k}+\mathbf{q}} + \theta_{\mathbf{k}}}{2}\right)\right| \tag{2.2.8}$$

$$|\Delta\mathcal{H}_{\mathbf{q},\widetilde{\mathrm{LO}}}(\mathbf{k})| = \left|\tilde{\beta_O} \sin\left(\theta_{\mathbf{q}} - \frac{\theta_{\mathbf{k}+\mathbf{q}} + \theta_{\mathbf{k}}}{2}\right)\right| \tag{2.2.9}$$

$$|\Delta\mathcal{H}_{\mathbf{q},\widetilde{\mathrm{TO}}}(\mathbf{k})| = \left|\tilde{\beta_O} \cos\left(\theta_{\mathbf{q}} - \frac{\theta_{\mathbf{k}+\mathbf{q}} + \theta_{\mathbf{k}}}{2}\right)\right| \tag{2.2.10}$$

These expressions were obtained by symmetry considerations in Ref. [16]. Using the TB model of App. B, similar expressions can be obtained [27, 14, 24, 28]. Due to their high energy, $\widetilde{\mathrm{LO}}$ and $\widetilde{\mathrm{TO}}$ phonon modes can involve interband ($\pi - \pi^*$) scattering. However, setting $s = 1$ and $s' = -1$ simply exchanges the angular dependencies of $\widetilde{\mathrm{TO}}$ and $\widetilde{\mathrm{LO}}$. This has no impact in the following transport model since the contributions of those modes are always summed. We can thus keep the above expressions without loss of generality.

2.2.2 Coupling to DFT phonon modes at Γ

We now insert the DFT phonon modes, Eq. (2.1.6), into the canonical model of Eq. (2.2.1). In the expressions for the acoustic DFT eigenvectors (Eq. (2.1.6)), the angular dependency and $|\mathbf{q}|$ behavior of the $\widetilde{\mathrm{TO}}$ and $\widetilde{\mathrm{LO}}$ components are of the same form as in Eqs. (2.2.7) and (2.2.8), when considering a circular Fermi surface. It can be shown that the effect of using the DFT phonon eigenvectors in $\Delta\mathcal{H}_{\mathbf{q},\mathrm{TA}}(\mathbf{k})$ and $\Delta\mathcal{H}_{\mathbf{q},\mathrm{LA}}(\mathbf{k})$ is a simple redefinition of the magnitude $\tilde{\beta_A}$. Concerning the matrix elements derived from the DFT optical modes, the contribution of the canonical acoustic modes is in $o(|\mathbf{q}|^2)$ and can be neglected with respect to the dominant $o(1)$ term from the canonical optical modes. Optical EPC matrix elements are thus unaffected by the *ab initio* model for phonons. The small phonon-momentum limit ($|\mathbf{q}| \to 0$) of $\Delta\mathcal{H}_{\mathbf{q},\nu}(\mathbf{k})$ for the DFT modes can then be written:

$$|\Delta\mathcal{H}_{\mathbf{q},\mathrm{TA}}(\mathbf{k})| = \left|\beta_A|\mathbf{q}|\sin\left(2\theta_{\mathbf{q}} + \frac{\theta_{\mathbf{k+q}} + \theta_{\mathbf{k}}}{2}\right)\right| \tag{2.2.11}$$

$$|\Delta\mathcal{H}_{\mathbf{q},\mathrm{LA}}(\mathbf{k})| = \left|2\alpha(q)|\mathbf{q}|\cos\left(\frac{\theta_{\mathbf{k+q}} - \theta_{\mathbf{k}}}{2}\right) + \beta_A|\mathbf{q}|\cos\left(2\theta_{\mathbf{q}} + \frac{\theta_{\mathbf{k+q}} + \theta_{\mathbf{k}}}{2}\right)\right| \tag{2.2.12}$$

$$|\Delta\mathcal{H}_{\mathbf{q},\mathrm{LO}}(\mathbf{k})| = \left|\beta_O\sin\left(\frac{\theta_{\mathbf{k+q}} + \theta_{\mathbf{k}}}{2} - \theta_{\mathbf{q}}\right)\right| \tag{2.2.13}$$

$$|\Delta\mathcal{H}_{\mathbf{q},\mathrm{TO}}(\mathbf{k})| = \left|\beta_O\cos\left(\frac{\theta_{\mathbf{k+q}} + \theta_{\mathbf{k}}}{2} - \theta_{\mathbf{q}}\right)\right| \tag{2.2.14}$$

Where $\beta_A = \sqrt{1-\delta^2|\mathbf{q}|^2}\tilde{\beta_A} - \delta\tilde{\beta_O} \approx \tilde{\beta_A} - \delta\tilde{\beta_O}$ and $\beta_O \approx \tilde{\beta_O}$ are effective parameters, and $\alpha(q)$ is unchanged because there are no diagonal terms in Eq. (2.2.3).

2.2.3 Coupling to inter-valley A_1' mode at K

The inter-valley A_1' mode at $\mathbf{K}$ scatters an electron from state $\mathbf{k}$ around $\mathbf{K}$ to state $\mathbf{k}+\mathbf{q}$ around $\mathbf{K}'$, where $\mathbf{q}$ is still small. Using a TB model, it is found to be [14]:

$$|\Delta\mathcal{H}_{\mathbf{K+q},\mathrm{A}_1'}(\mathbf{k})| = \left|\sqrt{2}\beta_K\sin\left(\frac{\theta_{\mathbf{k+q}} - \theta_{\mathbf{k}}}{2}\right)\right| \tag{2.2.15}$$

where β_K is a real constant. This high energy mode will involve interband scattering. In the case $s = -s'$, the above expression becomes:

$$|\langle\mathbf{k}+\mathbf{q}|\Delta\mathcal{H}^{s=-s'}_{\mathbf{K+q},\mathrm{A}_1'}|\mathbf{k}\rangle| = \left|\sqrt{2}\beta_K\cos\left(\frac{\theta_{\mathbf{k+q}} - \theta_{\mathbf{k}}}{2}\right)\right| \tag{2.2.16}$$

Summary

- Derivation of a reliable EPC model.
- Acoustic EPC is decomposed into a gauge field and a deformation potential.
- The gauge field shifts the position of Dirac point. It is not screened.
- The deformation potential shifts the Dirac cone in energy. It is screened.
- Using DFT acoustic phonons leads to a renormalization of the gauge field.

Chapter 3

Ab initio calculations of electron-phonon coupling in graphene

For *optical* phonons, EPC parameters have been estimated using *ab initio* calculations at the DFT and GW levels [14, 34, 35, 27]. We will simply review the results of those calculations. The main interest of this chapter is the study and calculation of EPC for *acoustic* phonons. The coupling to acoustic phonons was studied at the DFT level in Refs. [36, 37, 28]. However, the DFT calculations were compared with different analytical models. The screening of the deformation potential was ignored in Refs. [36, 37], and a tight-binding model for EPC was used in Ref. [28]. Overall, some important details remained to be clarified concerning the consistency between the analytical symmetry-based model of EPC and the simulations. Furthermore, although the effect of electron-electron interactions was discussed, direct calculation of EPC parameters within the GW approximation remained to be achieved.

DFPT calculations can be performed to calculate the EPC matrix elements at any chosen electron and phonon momenta. This flexibility makes DFPT a convenient method to check the validity of the analytical expressions derived in the previous chapter. This will be the first objective of this chapter. We then need accurate numerical values for EPC parameters, including the acoustic gauge field and deformation potential. At that point, we are faced with the two aforementioned challenges of the DFPT method. The first is the approximative treatment of electron-electron interactions and the second is the presence of periodic images. To tackle the first challenge, we would like to estimate the effects of electron-electron interactions on the EPC parameters within the GW approximation. This was done for the coupling to optical phonons at the Γ point using frozen phonons [34]. We propose a similar method to calculate the coupling to acoustic phonons within the GW approximation. We interpret the zero-momentum limit of in-plane acoustic phonons as a strain of the crystal unit cell and link electron-phonon coupling parameters to the strain-induced fields. This allows for the extraction of the gauge field parameter from band structure calculations in strained graphene, which can be carried out within the GW approximation. The "static strain" method also gives access to the bare deformation potential. This will be useful to tackle the second challenge. Indeed, the presence of periodic images leads to some spurious screening of the deformation potential in standard DFPT calcula-

tions. However, with a value for the bare deformation potential, along with the static screening function of graphene calculated in chapter 4, we will be able to estimate the screened deformation potential.

Technical details of ab initio calculations

In this chapter, we perform density-functional theory (DFT) calculations within the local density approximation [22] (LDA) using the Quantum ESPRESSO (QE) distribution [38]. We use norm-conserving pseudo-potentials with 2s and 2p states in valence and cutoff radii of 0.78 Å. We use a 0.01 Ry Methfessel-Paxton smearing function for the electronic integrations and a 65 Ry kinetic energy cutoff. The electron momentum grid depends on the type of calculations performed. Accurate band structures can be obtained at a relatively low computational cost with a $16 \times 16 \times 1$ electron momentum grid. In the same framework, we used density functional perturbation theory (DFPT) in the linear response [20] to perform phonon and electron-phonon coupling calculations. In this case, however, a $96 \times 96 \times 1$ electron momentum grid was needed to reach convergence. The distance between graphene and its periodic images is ≈ 20 Å.

The GW part of the calculations were done with BerkeleyGW package [39]. Electronic wave-functions in a $72 \times 72 \times 1$ k-point grid are expanded in a plane-waves basis with a kinetic energy cutoff of 65 Ry. Graphene layers between adjacent supercells are separated by 8.0 Å and the Coulomb interaction is truncated to prevent spurious inter-supercell interactions [40]. The inverse dielectric matrix at zero frequency is calculated with a kinetic energy cutoff of 12 Ry and we take into account dynamical screening effects in the self energy through the generalized plasmon pole model [41].

3.1 EPC parameters at finite phonon momentum from DFPT

In this section we perform direct *ab initio* calculations of acoustic EPC matrix elements by using DFPT [20] in the linear response. The parameters β_O, β_K for optical phonons have already been evaluated using this method [14, 27] and compared to experimental Raman measurements. Their numerical values are reported in Table 3.1. We will mainly focus here on the acoustic phonon EPC parameters. DFPT calculations of EPC can be performed at chosen $\mathbf{k}$ and $\mathbf{q}$ vectors. This enables the verification of the angular and $|\mathbf{q}|$ dependencies of the matrix elements. EPC matrix elements can also be calculated for a chosen set of phonon modes. This involves minor modifications of the QE code to print out the EPC matrix in the basis of atomic displacements along the Cartesian directions, and the development of a small post-processing program to project the matrix on a chosen set of phonon modes. This allows for the calculation of both the canonical ($\tilde{\beta_A}$) and effective (β_A) gauge field parameters to verify the consistency of our model.

By choosing the phonon momentum $\mathbf{q}$ along the high symmetry directions $\mathbf{\Gamma} \to \mathbf{K}$ and $\mathbf{\Gamma} \to \mathbf{M}$, we have $\theta_{\mathbf{q}} = 0$ and $\pi/6$, respectively. If initial and scattered states are taken on a circular iso-energetic line, i.e. if $|\mathbf{k}| = |\mathbf{k} + \mathbf{q}|$, then $\frac{\theta_{\mathbf{k}+\mathbf{q}} + \theta_{\mathbf{k}}}{2} = \theta_{\mathbf{q}} \pm \frac{\pi}{2}$. From

Eqs. (2.2.11) and (2.2.12) we obtain:

$$|\Delta\mathcal{H}^{(\mathbf{\Gamma}\to\mathbf{K})}_{\mathbf{q},\mathrm{TA}}(\mathbf{k})| = |\mathbf{q}|\beta_A \tag{3.1.1}$$

$$|\Delta\mathcal{H}^{(\mathbf{\Gamma}\to\mathbf{K})}_{\mathbf{q},\mathrm{LA}}(\mathbf{k})| = |\mathbf{q}|\left|2\alpha(q)\cos\left(\frac{\theta_{\mathbf{k}+\mathbf{q}}-\theta_{\mathbf{k}}}{2}\right)\right| \tag{3.1.2}$$

$$|\Delta\mathcal{H}^{(\mathbf{\Gamma}\to\mathbf{M})}_{\mathbf{q},\mathrm{TA}}(\mathbf{k})| = 0 \tag{3.1.3}$$

$$|\Delta\mathcal{H}^{(\mathbf{\Gamma}\to\mathbf{M})}_{\mathbf{q},\mathrm{LA}}(\mathbf{k})| = |\mathbf{q}|\left|\pm\beta_A + 2\alpha(q)\cos\left(\frac{\theta_{\mathbf{k}+\mathbf{q}}-\theta_{\mathbf{k}}}{2}\right)\right| \tag{3.1.4}$$

We then consider an iso-energetic line at $\varepsilon = \hbar v_F|\mathbf{q}|/2$ and select the electron-momentum $\mathbf{k}$ point such that $\theta_{\mathbf{k}+\mathbf{q}} - \theta_{\mathbf{k}} = \pi$. In this way the cosines in Eqs. (3.1.2) and (3.1.4) are null and only the contribution of the β_A coefficient remains. Although we used the notations of the effective model here, the same strategy can be applied to the canonical model. The EPC matrix element is then calculated in either the canonical or DFT eigenvectors basis to obtain $\tilde{\beta_A}$ or β_A, respectively. In Fig. 3.1, we plot the resulting $\tilde{\beta_A}$ and β_A for different doping conditions (jellium-induced doping) and for $\mathbf{q}$ along $\mathbf{\Gamma}\to\mathbf{K}$ and $\mathbf{\Gamma}\to\mathbf{M}$. The fact that we obtain constants for this particular angular setup confirms the angular dependencies of Eqs. (2.2.11) and (2.2.12). Moreover, this is true whether the canonical or DFT phonon modes are used. This confirms that the effects of mode mixing is a simple (yet significant) renormalization of the gauge field parameter. As expected, the gauge field parameters $\tilde{\beta_A}$ and β_A are essentially doping independent and screening has no effect on them. A direct consequence is that scattering by gauge field is independent of the doping, the dielectric background and the general environment of the 2D material, since all those dependencies come via screening. The numerical results are reported in the first column of Table 3.1.

Knowing the value of $\tilde{\beta_A}$ and β_A, we adopt a similar strategy to obtain the *screened* $\alpha(q)$ coefficient by setting $\theta_{\mathbf{k}+\mathbf{q}} - \theta_{\mathbf{k}} = 2\pi/3$. It is important to underline that those DFPT calculations do not provide access to the bare deformation potential parameter α^{bare} due to electronic screening. In linear response at small finite (i.e. non-zero) phonon momentum $\mathbf{q}$, the phonon displacement induces a small but finite $\mathbf{q}$-modulated electric field. The electrons screen the finite electric field and consequently the magnitude of EPC. Thus, a finite induced electric field is always present in the linear response calculation at any non-zero phonon momentum and the screened parameter $\alpha(q)$ is obtained. We find that the $\alpha(q)$ coefficient is very small ($\ll 1$ eV). It is then completely negligible with respect to the other parameters. However, note that the present DFPT calculations are performed in a multilayered system where the graphene planes are separated by 20 Å. For the phonon momenta considered in the paper, the spurious screening from the periodic images is not negligible at all. Indeed, a phonon of wave vector $\mathbf{q}$ induces a charge fluctuation with a periodicity equal to $2\pi/|\mathbf{q}|$. The electric field induced by such a charge fluctuation decays exponentially, along the out-of-plane direction, on a typical length scale of $1/|\mathbf{q}|$. Therefore, for the interlayer distance of 20 Å used in our calculations, the electric field induced by the periodic images is negligible only for $|\mathbf{q}|$ much larger than $1/20$ Å$^{-1} = 0.05$ Å^{-1}. Such requirement is not satisfied by our DFPT calculations where $|\mathbf{q}|$ is in the range $0.013 - 0.077$ Å^{-1}.

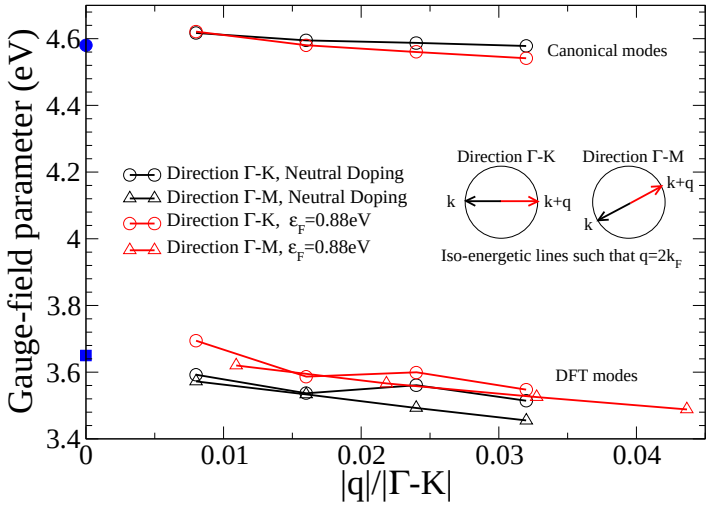

Figure 3.1: *Ab initio* calculations of $\frac{|\Delta\mathcal{H}_{\mathbf{q},\mathrm{LA/TA}}(\mathbf{k})|}{|\mathbf{q}|}$ in high symmetry $(\mathbf{\Gamma}\rightarrow\mathbf{M})/(\mathbf{\Gamma}\rightarrow\mathbf{K})$ directions respectively lead to gauge field EPC parameters, which depend neither on direction nor doping. $\tilde{\beta}_A(\beta_A)$ is obtained when the canonical (DFT) phonon modes are used. The blue square and dot at $|\mathbf{q}|=0$ represent the values of β_A and $\tilde{\beta}_A$ found in strained graphene calculations, respectively.

3.2 EPC in the tight-binding model

In this section we compare the results of DFPT with other results obtained within the tight binding (TB) model. In particular, we compare with the TB model of EPC used in the collaborative work of Ref. [28].

The TB model provides a computationally cheap way to calculate EPC to a first approximation. In the two-nearest-neighbors TB model of EPC, App. B, the gauge field parameters are all proportional to the derivative η_1 of the first-neighbor hopping integral with respect to bond length. We also have a link between the bare deformation potential α^{bare} and the derivative η_2 of the second-neighbor hopping integral. Such relationships are obviously very specific to the TB model and are not enforced in the symmetry-based model used here. The hopping to the first neighbors is linked to the Fermi velocity, while hopping to the second neighbors is linked to the work function. By performing DFT calculations of the band structure of graphene for varying bond lengths, one can calculate η_1 and η_2. Those DFT calculations of η_1 and η_2 result in the numerical values of EPC parameters reported in Table 3.1, column "TB-DFT". It is important to underline that within this TB model, the canonical phonon modes are used to calculate the perturbation to the TB Hamiltonian. Thus, we obtain the canonical EPC parameters $\widetilde{\beta_A}$, $\widetilde{\beta_O}$. There is no further modeling of the phonon modes, and therefore, no values for the effective parameters β_A and β_O. This is not really relevant for the optical phonons, because we have seen that the phonon model has

Table 3.1: Electron-Phonon Coupling parameters, calculated by different methods: (i) DFPT EPC: direct DFPT LDA calculation of EPC, Sec. 3.1. This method does not give access to unscreened α^{bare}. (ii) $|\mathbf{q}| = 0$: from zero-momentum model, see Sec. 3.3. Acoustic parameters are obtained by calculating the magnitude of strained-induced scalar and vector potentials. Optical parameters are obtained with the frozen phonon method from Ref. [34]. (iii)TB-DFT: results obtained in Ref. [28] using a TB model (App. B) and DFT to calculate the derivative of the hopping parameter with respect to bond length (see Sec. 3.2). (iv) GW calculations of EPC parameters. For phonons at $\mathbf{\Gamma}$, the renormalization is 20%, as the Fermi velocity. For the A_1' mode, results are taken from Ref. [35]. (v) Exp: obtained by fitting our numerical solution of Boltzmann transport equation to experiment. $\tilde{\beta_A}$ and α^{bare} are not used in the simulations. The values of β_K in the last line are doping dependent, see chapter 6, Sec. 6.3 for plots (Fig. 6.3) and discussion.

	DFPT EPC	$\|\mathbf{q}\| = 0$	TB-DFT [28]	GW	Exp
$\tilde{\beta_A}$ (eV)	4.60	4.58	3.58	5.52	–
β_A (eV)	3.60	3.64	–	4.32	4.97
α^{bare}(eV)	–	2.96	3.25	–	–
$\beta_O = \tilde{\beta_O}$ (eV/Å)	9.5	9.5	10.08	11.39	11.39
β_K (eV/Å)	9.5	9.5	10.08	$12.5 \sim 14$	$17 \sim 40$

a small effect on those. It has however, a sizable effect on the acoustic gauge field. By chance, the DFT value of η_1 leads to a canonical EPC $\widetilde{\beta_A}$ that happens to be close to the value of the effective EPC β_A found by DFPT. Thus, there is a seemingly very good *numerical* agreement between the simple TB model and the results of DFPT calculations. However, we would like to point out that this agreement is fortuitous, and in view of the analysis made here, it should rather be interpreted as a manifestation of the limits of the TB model. Indeed, when the distinction between canonical and DFT phonon modes is made, the numerical values are no longer consistent. Also, note that in a nearest neighbor TB model $\beta_K = \beta_O$. This is verified [14] within a 1% error in the frameworks of the first two columns. At the GW level however, this equality does not hold.

An other way to evaluate EPC matrix elements for acoustic phonons can be found in Refs. [25, 26]. The Hamiltonian for electron-phonon is similarly derived from a TB model. The important difference is the use of a microscopic "valence-force-field" model to derive the dynamical matrix and the resulting phonon modes. This model involves two parameters describing the forces resulting from changes in bond lengths and angles in the lattice. Those parameters are fitted on graphene's phonon dispersion derived from models using the force-constants measured in graphite. The resulting phonon modes are then inserted in the TB electron-phonon interaction Hamiltonian. Results qualitatively similar to our work are obtained. In particular, a reduction factor originating from the mixing of the acoustic and optical canonical modes appears in the coupling to acoustic modes. The parameter obtained in our DFPT calculations using

the canonical phonon modes ($\widetilde{\beta_A}$) falls in the interval estimated in Refs. [25, 26]. However, the aforementioned reduction factor, equivalent to the ratio $\beta_A/\widetilde{\beta_A}$, is found to be ≈ 0.5 in Refs. [25, 26] while we find $\beta_A/\widetilde{\beta_A} \approx 0.78$.

Finally, note that the TB model enables to form a link between EPC and the variation of the band structure with respect to structural changes. However, this link is less reliable and captures less physical meaning that the one we present in the next section.

3.3 EPC at zero momentum from static strain method

In order to calculate the electron-phonon matrix elements in the GW approximation, we calculate the GW band structure for suitably chosen deformation patterns. If the displacement pattern is chosen to reproduce the zero-momentum limit of a given phonon, the matrix elements of the resulting perturbation Hamiltonian can be linked to the EPC parameters. Following this approach, the frozen phonons method [34] was used to calculate the electron-electron renormalization of the coupling to *optical* modes (LO, TO, A_1') within GW. In order to perform GW calculations and to check the consistency of the small momentum EPC model, we also seek an interpretation of the *acoustic* EPC parameters at momentum exactly zero. This is achieved by linking acoustic EPC parameters to the perturbation potentials induced by a mechanical strain. This link is then verified numerically at the DFT level. Finally, we present the results of GW calculations for acoustic EPC parameters using this method, and summarize the already existing results on the optical EPC parameters.

3.3.1 Acoustic EPC and strain-induced potentials

For acoustic phonons at Γ, a static phonon displacement in the zero momentum limit is equivalent to a strain deformation. We consider the long wavelength limit of an acoustic phonon and the corresponding perturbation occurring on a portion of the graphene sheet of scale $d << \frac{2\pi}{q}$. Provided there is no long-range (Coulomb) interaction between such zones distant to each other, the phonon perturbation can be seen locally as a simple mechanical strain of the sheet. Author of Ref. [16] derived the $|\mathbf{q}| \to 0$ limit of the electron-phonon interaction (Eqs. (2.2.7) and (2.2.8)) for the canonical acoustic modes presented in Sec. 2.2 (Eq. (2.1.5)). Since screening was ignored in this EPC model, the magnitude of the *bare* deformation potential α^{bare} was used. Without screening, there is no long-range interaction and strain can be considered to be the exactly $|\mathbf{q}| = 0$ equivalent of the $|\mathbf{q}| \to 0$ limit of an acoustic phonon. We will discuss the consequences of screening on the interpretation of the deformation potential in the zero-momentum limit in paragraph 3.3.2. We first review the model of strain introduced in Ref. [16]. This model will be called canonical. The strained unit cell is defined with the lattice vectors $\mathbf{b_1'}, \mathbf{b_2'}$ such that:

$$\mathbf{b_i'} = (\mathcal{I} + \mathcal{U})\ \mathbf{b_i} \tag{3.3.1}$$

$$\mathcal{U} = \begin{pmatrix} u_{xx} & u_{xy} \\ u_{yx} & u_{yy} \end{pmatrix} \tag{3.3.2}$$

where $\mathcal{I}$ and $\mathcal{U}$ are the identity matrix and strain tensor, respectively. In this first canonical model, the vectors defining the positions of the carbon atoms in real space are given by the same transformation as the lattice vectors. Namely, the internal coordinates of atoms are unchanged in the basis of the lattice vectors $\{\mathbf{b}'_1,\mathbf{b}'_2\}$, see Fig. 3.2. Evidently, strain also changes the reciprocal lattice vectors according to the transformation $\mathbf{b}^{*\prime}_{\mathbf{i}} = (\mathcal{I}+\mathcal{U})^{-1}\mathbf{b}^{*}_{\mathbf{i}}$. It is then natural to develop the Hamiltonian around the special point $\mathbf{K} = (2/3,-1/3)$, as defined in the basis of those new reciprocal lattice vectors. While the coordinates of $\mathbf{K}$ in the basis of the reciprocal lattice vectors are unchanged, it is useful for DFT calculations to note that the Cartesian coordinates of this special point changed compared to the unstrained case. This change is only due to the geometrical redefinition of the lattice vectors. The canonical perturbed Hamiltonian $\widetilde{\mathcal{H}}^{\mathcal{U}}_{\mathbf{K}}$, expanded around point $\mathbf{K}$ of strained graphene is then written in terms of a vector potential $\tilde{\mathbf{A}} = (\tilde{A}_x,\tilde{A}_y)$ and a scalar potential ϕ [16]:

$$\widetilde{\mathcal{H}}^{\mathcal{U}}_{\mathbf{K}}(\mathbf{k}) = \phi\,\mathcal{I} + (\hbar v_F\mathbf{k} + \tilde{\mathbf{A}})\cdot\sigma \tag{3.3.3}$$

where

$$\tilde{A}_x = \sqrt{2}\tilde{\beta}_A(u_{xx} - u_{yy}) \tag{3.3.4}$$

$$\tilde{A}_y = -\sqrt{2}\tilde{\beta}_A(u_{xy} + u_{yx}) \tag{3.3.5}$$

$$\phi = \sqrt{2}\alpha^{\text{bare}}(u_{xx} + u_{yy}) \tag{3.3.6}$$

ϕ acts as a global energy shift while $\tilde{\mathbf{A}}$ yields a redefinition of the Dirac point's position. In strained graphene and in the presence of gauge fields, it is then important to distinguish special point $\mathbf{K}$ from the Dirac point labeled $\bar{\mathbf{K}}$ here. The former is defined geometrically while the latter is defined as where the π and π^* bands intersect. The Dirac point is now $\bar{\mathbf{K}} = \mathbf{K} - \frac{\tilde{\mathbf{A}}}{\hbar v_F}$, as can be seen in Eq. (3.3.3). Similar expressions are obtained around the other Dirac cone $\mathbf{K}'$, by complex conjugation and the transformations $\mathbf{k}\to-\mathbf{k}$ and $\tilde{\mathbf{A}}\to-\tilde{\mathbf{A}}$.

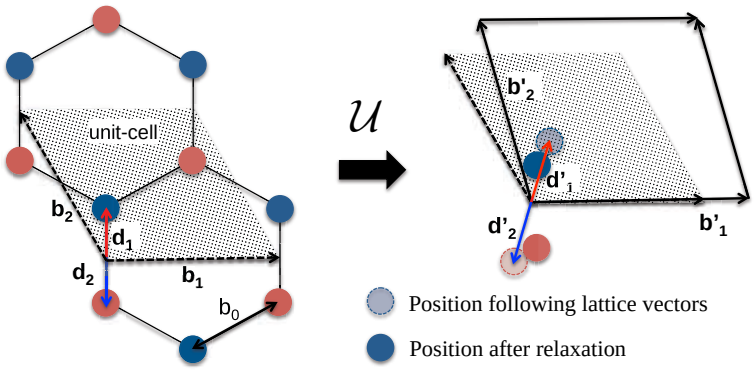

Figure 3.2: Schematic of a strain in the unit cell. The lattice vectors are transformed as described by the strain tensor $\mathcal{U}$. Within the canonical model of strain, the strained internal coordinates $\mathbf{d}'_1$ and $\mathbf{d}'_2$ are given by the same tranformation. Within the effective model, we allow the relaxation of internal coordinates.

In chapter 2, an addition to the canonical model of EPC Eqs. (2.2.7) and (2.2.8) was the use of the DFT phonon modes of Eq. (2.1.6). In order to obtain the strain

pattern equivalent to the $|\mathbf{q}| = 0$ limit of those modes, we allow the relaxation of internal coordinates after imposing a given strain to the crystal axes. This structural optimization of the internal coordinates is crucial as after the strain deformation, there are non-zero forces on the atoms. To give some numerical example, consider the positions of the two carbon atoms as defined in Fig. 2.1. If we apply to the unit cell a 1% uni-axial strain in the **y**-direction,

$$\mathcal{U} = \begin{pmatrix} 0 & 0 \\ 0 & 0.01 \end{pmatrix} \tag{3.3.7}$$

and allow the relaxation of internal coordinates, we obtain the new atomic positions $\mathbf{d'_1} = -\mathbf{d'_2} \approx 0.9987 \times (1/6, 1/3)$ in the $\{\mathbf{b'_1}, \mathbf{b'_2}\}$ basis. As was the case for phonon modes at small momenta, this relaxation has substantial numerical consequences. We assume that the process of relaxing internal coordinates leads to a strain model with gauge field parameter β_A (as in Eqs. (2.2.11) and (2.2.12)) instead of $\tilde{\beta}_A$ (as in Eqs. (2.2.7) and (2.2.8)). This is analogous to the effects of using the DFT phonon modes of Eq. (2.1.6) in DFPT. We will thus use the following effective strain model:

$$\mathcal{H}^{\mathcal{U}}_{\mathbf{K}}(\mathbf{k}) = \phi\, \mathcal{I} + (\hbar v_F \mathbf{k} + \mathbf{A}) \cdot \sigma \tag{3.3.8}$$

$$A_x = \sqrt{2}\beta_A(u_{xx} - u_{yy}) \tag{3.3.9}$$

$$A_y = -\sqrt{2}\beta_A(u_{xy} + u_{yx}) \tag{3.3.10}$$

$$\phi = \sqrt{2}\alpha^{\text{bare}}(u_{xx} + u_{yy}) \tag{3.3.11}$$

3.3.2 Calculation of strain-induced potentials at the DFT level

In this section we calculate the changes in the electronic structure of graphene [42] under strain within DFT. The magnitudes of the scalar and vector potentials are then extracted from the displacement in the Brillouin zone and the energy shift of the Dirac cone. Within DFT, doping has a negligible effect on this process. By comparing the results to the previous DFPT results, we validate the zero-momentum strain model.

Calculation and interpretation of the strain-induced bare deformation potential

If there are no long-range interactions and screening is ignored in the EPC model, then the deformation potential part of the EPC is bare and its $|\mathbf{q}| = 0$ limit is directly related to the global energy shift ϕ. Since long-range Coulomb interactions and screening are present in our EPC model, however, an additional complication appears. In finite differences calculations (DFT calculations on strained graphene), differently to what happens in DFPT, the diagonal perturbation ϕ shifts the Dirac Point in energy just by adding a constant potential with no modulation in $\mathbf{q}$. As a result, the scalar potential ϕ obtained with finite differences is bare and does not correspond to the $|\mathbf{q}| \to 0$ limit of the screened deformation potential used in our EPC model. However, we can obtain the screened $\alpha(q)$ by assuming:

$$\alpha(q) = \frac{\alpha^{\text{bare}}}{\epsilon_{2D}(q)} \tag{3.3.12}$$

where $\epsilon_{2D}(q)$ is the static dielectric function of graphene. Provided the value of α^{bare} and a reliable static dielectric function for a single layer of graphene $\epsilon_{2D}(\mathbf{q})$, we could thus evaluate $\alpha(q)$ in single-layer graphene. The static dielectric function of single layer graphene will be the focus of chapter 4.

The parameter α^{bare} is obtained by a global variation of lattice parameter b and is related to the scalar potential ϕ:

$$\mathcal{U} = \begin{pmatrix} \frac{\delta b}{b} & 0 \\ 0 & \frac{\delta b}{b} \end{pmatrix} \tag{3.3.13}$$

$$A_x = A_y = 0 \tag{3.3.14}$$

$$\phi = 2\sqrt{2}\alpha^{\text{bare}}\frac{\delta b}{b} \tag{3.3.15}$$

The structure obtained with such biaxial uniform strain is already relaxed. The relaxation process is thus irrelevant for α^{bare}, as was the use of canonical or DFT phonon modes for $\alpha(q)$. We obtain the value reported in the second column of Table 3.1.

Calculation of strain-induced gauge fields

The parameter β_A is obtained by applying a strain in the armchair ($\mathbf{y}$) direction:

$$\mathcal{U} = \begin{pmatrix} 0 & 0 \\ 0 & u_{yy} \end{pmatrix} \tag{3.3.16}$$

$$A_x = -\sqrt{2}\beta_A u_{yy} \tag{3.3.17}$$

$$A_y = 0 \tag{3.3.18}$$

$$\phi = \sqrt{2}\alpha^{\text{bare}} u_{yy} \tag{3.3.19}$$

Such uni-axial strain induces a shift in the position of the Dirac point in the $\mathbf{x}$-direction or, equivalently, the opening of a gap ΔE_g at special point $\mathbf{K}$. At this point, the value of the Hamiltonian expanded around $\mathbf{K}$ is:

$$\mathcal{H}^{\mathcal{U}}_{\mathbf{K}}(\mathbf{0}) = \begin{pmatrix} 0 & -\sqrt{2}\beta_A u_{yy} \\ -\sqrt{2}\beta_A u_{yy} & 0 \end{pmatrix} \tag{3.3.20}$$

The gap is thus:

$$\Delta E_g(\mathbf{0}) = 2\sqrt{2}\beta_A u_{yy} \tag{3.3.21}$$

After imposing a strain on the lattice vectors, the internal coordinates of atoms are relaxed within DFT, and the band energies are calculated at special point $\mathbf{K}$. We repeat the process for two values of strain $u_{yy} = -0.01, 0.01$. The resulting β_A is reported in the second column of Table 3.1. We repeat the whole process without relaxing the internal coordinates of the atoms and find the value of $\tilde{\beta_A}$ reported in Table 3.1.

Direct DFPT calculations and this static strain method at the DFT level are two different techniques to calculate the same gauge field. Comparing their results is useful to check the validity of the models and gain more depth in our understanding of

electron-phonon interactions. The unscreened gauge field parameters $\tilde{\beta_A}$ and β_A are in good agreement with the results of the previous section (see Table 3.1 and Fig. 3.1), confirming the validity of the $|\mathbf{q}| \to 0$ and $|\mathbf{q}| = 0$ models (canonical and effective) in our simulation framework. The significant difference between the values of canonical and effective parameters emphasizes the necessity of DFT phonons and relaxation. The static strain method we propose here for acoustic parameters is especially well-suited for the computationally expensive GW calculations since the energy bands are needed only for one **k**-point.

3.3.3 EPC parameters at the GW level

Here we discuss how the relevant quantities are renormalized by electron-electron interactions within GW [23]. The Fermi velocity is renormalized by approximately 20%, depending slightly on doping [35]. The renormalization is strongest for neutral (or very low-doped[1]) graphene ($\approx +21\%$) and slightly decreases with increasing doping ($\approx +17\%$ at $\varepsilon_F = 1$eV). It can be argued theoretically [34, 43] that the renormalization of the coupling with phonon modes at $\mathbf{\Gamma}$ scales with that of the Fermi velocity because those intra-valley scattering modes involve only a gauge transformation (change in the position of the Dirac cone). This can be illustrated here by noticing that we have for acoustic phonons:

$$|\bar{\mathbf{K}} - \mathbf{K}| = \left| \frac{\mathbf{A}}{\hbar v_F} \right| \propto \frac{\beta_A}{\hbar v_F} \tag{3.3.22}$$

where the quantity $|\bar{\mathbf{K}} - \mathbf{K}|$ and thus the ratio $\frac{\beta_A}{\hbar v_F}$ are unaffected by electron-electron interactions between low energy Dirac electrons. Indeed, since such interactions are centro-symmetric, their inclusion cannot displace the position of the Dirac cone, both in presence and absence of a strain distortion. In simpler terms, as far as the electrons (and only the electrons) are concerned, there is no preferential direction, since they "live" in a cone. Thus their interactions are also direction-independent and cannot induce a displacement of the cone in a particular direction. Using the frozen phonon method, it was verified [35] that the renormalization of optical modes at $\mathbf{\Gamma}$ is relatively weak and is equal to the renormalization of the Fermi velocity. In order to verify that this is the case for acoustic modes as well, we repeat the process of the previous paragraph within GW. The band energies are calculated at one additional **k**-point to access the Fermi velocity. We use two different doping levels ($\varepsilon_F = 0.5$ eV and 0.75 eV) to study the doping dependency of the renormalization. The doping levels are rather high to ensure that the Fermi surface is satisfactorily sampled by our grid. The results are presented in Table 3.2.

Our calculations[2] confirm the $\approx 20\%$ renormalization of v_F at low doping. More importantly, they confirm that the electron-electron interactions renormalize β_A as the

[1] Strictly speaking, for graphene very close to charge neutrality, there is a logarithmic singularity in the group velocity near the Dirac point. We do not consider this effect here. By neutral graphene, we mean doping levels very low compared to those mentionned in the text, but high enough that the logarithmic singularity can be neglected

[2] I am particularly thankful to Cheol-Hwan Park for performing the GW calcualtions.

Table 3.2: Renormalization of Fermi velocity and acoustic gauge field parameter by electron-electron interactions within GW, presented for two different values of doping and for uniaxial strain $u_{yy} = -0.01, +0.01$ as explained in Sec. 3.3.2.

Strain u_{yy}	-0.01		$+0.01$	
Fermi energy ε_F	0.50 eV	0.75 eV	0.50 eV	0.75 eV
v_F^{GW}/v_F^{DFT}	1.203	1.166	1.204	1.164
$\beta_A^{GW}/\beta_A^{DFT}$	1.215	1.172	1.202	1.165

Fermi velocity:

$$\frac{v_F^{GW}}{v_F^{DFT}} \approx \frac{\beta_A^{GW}}{\beta_A^{DFT}}$$

In contrast, the interaction of electrons with the inter-valley A_1' mode is not just a gauge transformation of the electronic Hamiltonian. The renormalization of this mode is much stronger overall, and its doping dependency is more pronounced. According to Ref. [35], β_K is renormalized by $\approx +46\%$ close to neutrality, and $\approx 20\%$ at $\varepsilon_F = 1$eV.

Summary

- Validation of EPC model for in-plane phonons within the DFT framework.
- Spurious screening of the deformation potential in standard DFPT.
- Development of the static strain approach to calculate acoustic EPC in GW.
- It is essential to relax internal coordinates to obtain *effective* acoustic EPC.
- Static strain method gives an estimation for the *bare* deformation potential.
- Acoustic gauge field is renormalized as Fermi velocity within GW.
- Numerical GW values for EPC parameters β_A, β_O, β_K.

Chapter 4

Static screening in 2D materials within DFPT: application to graphene

We saw in the previous chapter that the presence of periodic images led to some spurious screening of the deformation potential. This invalidates the direct DFPT calculation of the screened deformation potential. Nevertheless, we obtained the bare deformation potential from the static strain method. One way to estimate the screened deformation potential would be to apply the static screening function of isolated graphene to the bare deformation potential. We would like to calculate this quantity with our DFT framework. Having a reliable expression for the static screening of graphene is crucial for many uses beyond the particular case of the deformation potential. Staying in the context of electronic transport in graphene, screening is important for electron scattering by charged impurities [44, 45, 46, 47], electron-phonon coupling [31, 48, 49], or electron-electron interactions [50].

Dimensionality is well known to be essential in determining the physical properties of materials. Correctly describing the physics of 2D materials requires careful modeling and definition of the relevant physical quantities. This is particularly true in our DFT framework, due to the presence of periodic images. For some physical properties, the interactions between the periodic images are sufficiently suppressed by imposing large distances between them [51]. However, if the electronic density is perturbed at small wave vector, long-range Coulomb interactions between electrons from different periodic images persist even for very large distances, leading to some spurious screening. Despite this drawback, *ab initio* calculations have the advantage of describing a complete band structure and accounting for local fields. Local fields designate electronic density perturbations at wavelengths smaller than the unit cell dimensions [52, 53, 54]. Accounting for local fields usually requires heavier analytical and computational work [55, 56, 57]. They have been estimated in various semiconductors using first-principles calculations [58, 59, 60, 61, 62] and often renormalize the screening by a few tens of percent.

The static dielectric function of graphene has been derived analytically within a 2D Dirac cone model [63, 64, 65, 66, 67, 68, 69] in the random phase approximation (RPA). In those derivations, the role of higher energy electronic states, the deviation from conical bands and the so-called local fields were neglected. Later, quasiparticle self-

consistent GW calculations [70] of the screening of point charges in neutral graphene seemed to indicate a significant contribution from the local fields. The general behavior of the static dielectric function was found to be quite different from the analytical RPA derivation. However, Coulomb interactions between periodic images were not disabled. There have been some propositions [71, 72], within density-functional theory, to correct the contributions from the periodic images. More simply, complete suppression of those spurious interactions can be achieved by cutting off the Coulomb interactions between periodic images [73, 74, 40]. In a recent study of the energy loss function of neutral isolated graphene [75], the use of a truncated Coulomb interaction (Coulomb cutoff) was implemented in the framework of time-dependent density-functional theory. It was found that the dynamical screening properties of graphene were strongly affected by the spurious interactions between periodic images.

In this chapter, we focus on the long-wavelength and static screening properties of both neutral and doped graphene. We use DFPT as it includes the complete band structure of graphene and the effects of local fields [76, 20] and exchange correlation in the local density approximation (LDA). We implement the Coulomb cutoff technique and carefully address the issue of extracting two dimensional dielectric properties from simulated three-dimensional potentials. We then compare our DFPT calculations with the analytical derivations for the two dimensional massless Dirac fermions within RPA.

In Sec. 4.1, we set the general background of this chapter by defining the static dielectric function in different dimensionality frameworks. In Sec. 4.2, we present different methods to calculate the static dielectric function of graphene. This includes analytical derivations previously developed [63, 64, 65, 66, 67, 68, 69] and a self-consistent solution implemented in the phonon package of the Quantum ESPRESSO (QE) distribution. In Sec. 4.3 those methods are applied to both doped and neutral graphene and the results are compared.

4.1 Static dielectric function

In this section we introduce the quantities of interest in the formulation of the static dielectric response. We use the DFT framework within LDA and atomic units to be consistent with the following *ab initio* study. Both the unperturbed system and its response to a perturbative potential are described within this framework. We start with a quick description of the unperturbed system. Since we are interested only in the static limit here, we consider a time-independent Kohn-Sham (KS) potential [77] $V_{\mathrm{KS}}(\mathbf{r})$, where $\mathbf{r} = (x,y,z)$ is a space variable. This potential is the sum of three potentials:

$$V_{\mathrm{KS}}(\mathbf{r}) = V_{\mathrm{ext}}(\mathbf{r}) + V_{\mathrm{H}}(\mathbf{r}) + V_{\mathrm{XC}}(\mathbf{r}). \tag{4.1.1}$$

In the unperturbed system, the external potential V_{ext} is simply the potential generated by the ions of the lattice. The remaining potentials are functionals of the electronic density. The Hartree potential V_{H} reads:

$$V_{\mathrm{H}}(\mathbf{r}) = e^2 \int d\mathbf{r}' \frac{n(\mathbf{r}')}{|\mathbf{r} - \mathbf{r}'|}, \tag{4.1.2}$$

and V_{XC} is the exchange-correlation potential. Since the KS potential determines the solution for the density which in turn generates part of the KS potential, this approach leads to a self-consistent problem. When solved for the system at equilibrium with no perturbation, the ground-state density $n(\mathbf{r})$ is found.

We now proceed to the description of this system within perturbation theory. An external perturbing potential δV_{ext} is applied. This triggers a perturbation of the electronic density such that the total density is $n + \delta n$, where δn is the first-order response to the perturbing potential. Likewise, all the previously introduced potentials can be separated into an equilibrium and a perturbed part. The screened perturbation δV_{KS} felt by an individual electron is the sum of the bare external perturbation δV_{ext} and the screening potential $\delta V_{\mathrm{H}} + \delta V_{\mathrm{XC}}$ induced by the density response δn:

$$\delta V_{\mathrm{KS}}(\mathbf{r}) = \delta V_{\mathrm{ext}}(\mathbf{r}) + \delta V_{\mathrm{H}}(\mathbf{r}) + \delta V_{\mathrm{XC}}(\mathbf{r}). \tag{4.1.3}$$

This leads to another self-consistent system [61] solved by the density response δn. From this response we can extract the quantities characterizing the screening properties of a material. The induced electron density δn can be seen as independent electrons responding to the effective perturbative potential δV_{KS}:

$$\delta n(\mathbf{r}) = \int d\mathbf{r}' \chi^0(\mathbf{r},\mathbf{r}') \delta V_{\mathrm{KS}}(\mathbf{r}'), \tag{4.1.4}$$

thus defining the independent particle static susceptibility χ^0. It can also be seen as interacting electrons responding to the bare external perturbative potential:

$$\delta n(\mathbf{r}) = \int d\mathbf{r}' \chi(\mathbf{r},\mathbf{r}') \delta V_{\mathrm{ext}}(\mathbf{r}'), \tag{4.1.5}$$

thus defining the interacting particle susceptibility χ.

We can now proceed to further description of the screening properties of the material. The static dielectric function is first defined in three- and two-dimensional frameworks in order to highlight and clarify their differences. We then treat the intermediary cases of a 2D-periodic system of finite thickness and a periodically repeated 2D system, particularly relevant for *ab initio* calculations. For those cases, we will determine the conditions in which it is suitable to define a 2D static dielectric function.

4.1.1 Three-dimensional materials

In a periodic system, it is more convenient to work with the Fourier transform of Eq. (4.1.4). We consider a periodic external potential $\delta V_{\mathrm{ext}}(\mathbf{r}) = \delta V_{\mathrm{ext}}(\mathbf{q}) e^{i\mathbf{q}\cdot\mathbf{r}}$ of wave vector $\mathbf{q}$. In this chapter, $\mathbf{q}$ is not a phonon wave vector in the plane of a 2D material, it is a generic wave vector. We have in linear response theory:

$$\delta n(\mathbf{q} + \mathbf{G}) = \sum_{\mathbf{G}'} \chi^0(\mathbf{q}, \mathbf{G}, \mathbf{G}') \delta V_{\mathrm{KS}}(\mathbf{q} + \mathbf{G}'). \tag{4.1.6}$$

Here, reciprocal lattice wave vectors $\mathbf{G}$,$\mathbf{G}'$ were introduced. Even though $\delta V_{\mathrm{ext}}(\mathbf{r})$ only has a $\mathbf{q}$ component, the electronic density response can include larger wave vectors $\mathbf{q} + \mathbf{G}$. Consequently, the induced and total potentials can also have $\mathbf{q} + \mathbf{G}$

components. Those small wavelength components (smaller than the lattice periodicity) in the response of the electrons are called local fields [70]. In a three-dimensional framework, the Fourier components of the induced Hartree potential are:

$$\delta V_{\mathrm{H}}(\mathbf{q}+\mathbf{G}) = \frac{v_c^{3D}(\mathbf{q}+\mathbf{G})}{\kappa_0}\delta n(\mathbf{q}+\mathbf{G}) \tag{4.1.7}$$

$$v_c^{3D}(\mathbf{q}+\mathbf{G}) = \frac{4\pi e^2}{|\mathbf{q}+\mathbf{G}|^2}, \tag{4.1.8}$$

where $v_c^{3D}(\mathbf{q}+\mathbf{G})$ is the $\mathbf{q}+\mathbf{G}$ component of the Fourier transform of the 3D Coulomb interaction. The static dielectric constant κ_0 renormalizes the Coulomb interaction depending on the dielectric environment. We will focus on an isolated graphene layer, so that $\kappa_0 = 1$. This constant can also be used in a simple Dirac cone model to include the effects of other bands [63, 64, 65, 66, 67, 68, 69], though no definite value has been proposed. This will be discussed in Sec. 4.3. Until then, we set $\kappa_0 = 1$. The Fourier components of the XC potential are written $\delta V_{\mathrm{XC}}(\mathbf{q}+\mathbf{G})$. From Eqs. (4.1.3), (4.1.6) and (4.1.7), we can write:

$$\begin{aligned}\delta V_{\mathrm{KS}}(\mathbf{q}+\mathbf{G}) =& \delta V_{\mathrm{ext}}(\mathbf{q})\ \delta_{\mathbf{G},\mathbf{0}} + \delta V_{\mathrm{XC}}(\mathbf{q}+\mathbf{G}) \\ &+ v_c^{3D}(\mathbf{q}+\mathbf{G})\sum_{\mathbf{G}'}\chi^0(\mathbf{q},\mathbf{G},\mathbf{G}')\delta V_{\mathrm{KS}}(\mathbf{q}+\mathbf{G}'),\end{aligned} \tag{4.1.9}$$

where $\delta_{\mathbf{G},\mathbf{0}}$ represents Kronecker's delta.

The inverse screening function is defined as the ratio of the $\mathbf{G}=\mathbf{0}$ component of the KS potential (the coarse-grained effective potential) over the external potential:

$$\epsilon_{3D}^{-1}(\mathbf{q}) = \frac{\delta V_{\mathrm{KS}}(\mathbf{q})}{\delta V_{\mathrm{ext}}(\mathbf{q})}. \tag{4.1.10}$$

4.1.2 2D materials

We now wish to work with 2D electronic densities $\delta\tilde{n}(\mathbf{r}_p)$, defined in the $\{x,y\}$ plane as follows:

$$\delta\tilde{n}(\mathbf{r}_p) \equiv \int_{-\infty}^{+\infty}\delta n(\mathbf{r}_p, z)dz, \tag{4.1.11}$$

where $\mathbf{r}_p$ is the in-plane component of $\mathbf{r}$, and z is the out-of-plane component.

We first consider the system usually studied in analytical derivations, which will be called the strictly 2D framework. By strictly 2D, we mean that the electronic density can be written as follows:

$$\delta n(\mathbf{r}_p, z) = \delta\tilde{n}(\mathbf{r}_p)\delta(z), \tag{4.1.12}$$

where $\delta(z)$ is the Dirac delta distribution. There is no periodicity in the out-of-plane direction. Considering an external potential $\delta V_{\mathrm{ext}}(\mathbf{q}_p)$ with an in-plane wave vector $\mathbf{q}_p$, we can define the Fourier transform of the 2D electronic density $\delta\tilde{n}(\mathbf{q}_p+\mathbf{G}_p)$ where $\mathbf{G}_p$ is a 2D reciprocal lattice vector. The Hartree potential $\delta V_{\mathrm{H}}(\mathbf{r}_p, z)$ generated by this infinitely thin electronic distribution is three-dimensional. We thus separate in-plane

and out-of-plane space variables to stress the fact that the induced Hartree potential does extend in the out-of-plane (z) direction, in contrast with the density. Using Eq. (4.1.7) and performing an inverse Fourier transform in the out-of-plane direction only, we find:

$$\delta V_{\mathrm{H}}(\mathbf{q}_p + \mathbf{G}_p, z) = \frac{2\pi e^2}{|\mathbf{q}_p + \mathbf{G}_p|}\delta\tilde{n}(\mathbf{q}_p + \mathbf{G}_p)e^{-|\mathbf{q}_p+\mathbf{G}_p|z}. \tag{4.1.13}$$

For our purpose, only the value of the Hartree potential where the electrons lie $\delta V_{\mathrm{H}}(\mathbf{q}_p + \mathbf{G}_p, z = 0)$ is of interest. Similarly, the KS potential also extends in the out-of-plane direction, but we consider only the $z = 0$ value. We can work in a 2D reciprocal space with $\delta\tilde{n}(\mathbf{q}_p + \mathbf{G}_p)$ and the following potentials:

$$\begin{aligned}
\delta\tilde{V}_{\mathrm{H}}(\mathbf{q}_p + \mathbf{G}_p) &\equiv \delta V_{\mathrm{H}}(\mathbf{q}_p + \mathbf{G}_p, z = 0) \\
\delta\tilde{V}_{\mathrm{KS}}(\mathbf{q}_p + \mathbf{G}_p) &\equiv \delta V_{\mathrm{KS}}(\mathbf{q}_p + \mathbf{G}_p, z = 0) \\
\delta\tilde{V}_{\mathrm{XC}}(\mathbf{q}_p + \mathbf{G}_p) &\equiv \delta V_{\mathrm{XC}}(\mathbf{q}_p + \mathbf{G}_p, z = 0) \\
\delta\tilde{V}_{\mathrm{ext}}(\mathbf{q}_p) &\equiv \delta V_{\mathrm{ext}}(\mathbf{q}_p, z = 0).
\end{aligned} \tag{4.1.14}$$

Note that since $\mathbf{q}_p$ is in-plane, $\delta\tilde{V}_{\mathrm{ext}}(\mathbf{q}_p) = \delta V_{\mathrm{ext}}(\mathbf{q}_p, z)$. It is then common practice to use the 2D version of Eq. (4.1.7), with the 2D Coulomb interaction $v_c^{2D}(\mathbf{q}_p + \mathbf{G}_p)$ (and $\kappa_0 = 1$):

$$\delta\tilde{V}_{\mathrm{H}}(\mathbf{q}_p + \mathbf{G}_p) = v_c^{2D}(\mathbf{q}_p + \mathbf{G}_p)\delta\tilde{n}(\mathbf{q}_p + \mathbf{G}_p) \tag{4.1.15}$$

$$v_c^{2D}(\mathbf{q}_p + \mathbf{G}_p) = \frac{2\pi e^2}{|\mathbf{q}_p + \mathbf{G}_p|}. \tag{4.1.16}$$

We also define a 2D independent particle susceptibility as follows:

$$\delta\tilde{n}(\mathbf{q}_p + \mathbf{G}_p) = \sum_{\mathbf{G'}_p} \tilde{\chi}^0(\mathbf{q}, \mathbf{G}_p, \mathbf{G}'_p)\delta\tilde{V}_{\mathrm{KS}}(\mathbf{q}_p + \mathbf{G}'_p). \tag{4.1.17}$$

Working with the 2D quantities defined above, Eq. (4.1.9) becomes:

$$\begin{aligned}
\delta\tilde{V}_{\mathrm{KS}}(\mathbf{q}_p + \mathbf{G}_p) =& \delta\tilde{V}_{\mathrm{ext}}(\mathbf{q}_p)\ \delta_{\mathbf{G}_p,\mathbf{0}} + \delta\tilde{V}_{\mathrm{XC}}(\mathbf{q}_p + \mathbf{G}_p) \\
&+ v_c^{2D}(\mathbf{q}_p + \mathbf{G}_p) \sum_{\mathbf{G}'_p} \tilde{\chi}^0(\mathbf{q}_p, \mathbf{G}_p, \mathbf{G}'_p)\delta\tilde{V}_{\mathrm{KS}}(\mathbf{q}_p + \mathbf{G}'_p),
\end{aligned} \tag{4.1.18}$$

and the definition of the inverse screening function is modified as follows:

$$\epsilon_{2D}^{-1}(\mathbf{q}_p) = \frac{\delta\tilde{V}_{\mathrm{KS}}(\mathbf{q}_p)}{\delta\tilde{V}_{\mathrm{ext}}(\mathbf{q}_p)}. \tag{4.1.19}$$

We wish to use this definition in an *ab initio* framework. This raises some issues that we address now.

4.1.3 2D-periodic materials with finite thickness

In *ab initio* calculations, the electronic density extends also in the out-of-plane direction. In this section we consider the consequences of a finite out-of-plane thickness of

the electronic density. We consider now an isolated layer with an electron density of thickness $2t$. The results of the purely 2D system should be recovered if the wavelength of the perturbation is very large compared to t. We illustrate this idea by considering an electronic density such that:

$$\int_{-\infty}^{+\infty} \delta n(\mathbf{r}_p, z)dz = \delta\tilde{n}(\mathbf{r}_p) \quad , \quad \delta n(\mathbf{r}_p, z) = 0 \ \text{ if } |z| > t \ . \tag{4.1.20}$$

Using Eq. (4.1.7), the $z = 0$ value of the Hartree potential is then found to be:

$$\delta\tilde{V}_{\mathrm{H}}(\mathbf{q}_p + \mathbf{G}_p) = v_c^{2D}(\mathbf{q}_p + \mathbf{G}_p) \times \int_{-t}^{+t} e^{-|\mathbf{q}_p+\mathbf{G}_p||z|}\delta n(\mathbf{q}_p + \mathbf{G}_p, z)dz. \tag{4.1.21}$$

From this equation one can easily deduce that the condition $|\mathbf{q}_p+\mathbf{G}_p|t \ll 1$ is necessary to obtain results equivalent to the strictly 2D system. Since the largest value of $|\mathbf{G}_p|^{-1}$ is only a fraction of the lattice parameter, the above condition can only be fulfilled for $\mathbf{G}_p = \mathbf{0}$. The $\mathbf{q}_p + \mathbf{G}_p$ components of the induced perturbation have wavelengths comparable to or much smaller than t and the thickness of the electronic density cannot be ignored. However, as long as $|\mathbf{q}_p|t \ll 1$, the coarse-grained induced potential can be written:

$$\delta\tilde{V}_{\mathrm{H}}(\mathbf{q}_p) \approx v_c^{2D}(\mathbf{q}_p)\delta\tilde{n}(\mathbf{q}_p). \tag{4.1.22}$$

Working with reasonably small perturbation wave vectors, the $z = 0$ value of the coarse-grained induced potential is equivalent to that of the purely 2D system. It is then reasonable to use Eq. (4.1.18) at $\mathbf{G}_p = \mathbf{0}$ and it makes sense to define the dielectric function as in Eq. (4.1.19).

4.1.4 2D materials periodically repeated in the third dimension

In *ab initio* calculations, in addition to the non-zero thickness of the simulated electronic density, another issue arises. Current DFT packages such as QE rely on the use of 3D plane waves, requiring the presence of periodic images of the 2D system in the out-of-plane direction, separated by a distance c (interlayer distance). For many quantities, imposing a large distance between periodic images is sufficient to obtain relevant results for the 2D system. However, simulating the electronic screening of 2D systems correctly is computationally challenging due to the long-range character of the Coulomb interaction. As illustrated in Eq. (4.1.13), the Hartree potential induced by a 2D electronic density perturbed at wave vector $\mathbf{q}_p$ goes to zero in the out-of-plane direction on a length scale $1/|\mathbf{q}_p|$. For the layers (or periodic images) to be effectively isolated, they would have to be separated by a distance much greater than $1/|\mathbf{q}_p|$. The computational cost of calculations increasing linearly with interlayer distance, fulfilling this condition is extremely challenging for the wave vectors considered in the following. It is thus preferable to use an alternative method.

In order to isolate the layers from one another, the long-range Coulomb interaction is cut off between layers, as previously proposed in such context [74, 40, 75]. We use the following definition of the Coulomb interaction in real space:

$$\bar{v}_c(\mathbf{r}_p, z) = \frac{e^2\theta(l_z - |z|)}{\sqrt{|\mathbf{r}_p|^2 + z^2}}, \tag{4.1.23}$$

where $\theta(z) = 1$ if $z \geq 0$ and $\theta(z) = 0$ if $z < 0$. The cutoff distance l_z should be small enough that electrons from different layers do not see each other, but large enough that electrons within the same layer do. In other words, if t is representative of the thickness of the electronic density, we need the following inequalities to be true:

$$t < l_z < c - t. \tag{4.1.24}$$

The interlayer distance can be chosen such that $c \gg t$ within reasonable computational cost. Then we choose to cut off the Coulomb potential midway between the layers, $l_z = \frac{c}{2}$. The Coulomb interaction is generally used in reciprocal space. Setting $l_z = \frac{c}{2}$ and considering an external perturbative potential with in-plane wave vector $\delta V_{\text{ext}}(\mathbf{q}_p)$, the Fourier transform of the above Coulomb interaction is written as follows [74, 40]:

$$\bar{v}_c(\mathbf{q}_p + \mathbf{G}_p, G_z) = \frac{4\pi e^2}{|\mathbf{q}_p + \mathbf{G}_p|^2 + G_z^2} \times \left[1 - e^{-|\mathbf{q}_p + \mathbf{G}_p| l_z} \cos(G_z l_z)\right], \tag{4.1.25}$$

where G_z is the out-of-plane component of the reciprocal lattice vector $\mathbf{G}$. In an *ab initio* framework, the 3D Coulomb interaction v_c^{3D} should thus be replaced by the cutoff Coulomb interaction $\bar{v}_c$:

$$\delta V_{\text{H}}(\mathbf{q}_p + \mathbf{G}_p, G_z) = \bar{v}_c(\mathbf{q}_p + \mathbf{G}_p, G_z) \delta n(\mathbf{q}_p + \mathbf{G}_p, G_z). \tag{4.1.26}$$

Within the DFT LDA framework, the exchange-correlation potential is short-range, such that we can neglect interlayer interactions originating from that term. When the Coulomb interaction is cut off and within the region $z \in [-l_z; +l_z]$, everything happens as if the system was isolated, and it can be treated as the 2D-periodic system with finite thickness of the previous paragraph. For the layer at $z = 0$, and as long as $|\mathbf{q}_p| t \ll 1$, we can thus work with the $z = 0$ values of the potentials and use the definition of Eq. (4.1.19) for the dielectric function.

4.2 Static screening properties of graphene

In this section we present several methods to calculate the inverse static dielectric function of graphene. First, the derivation of an analytical expression and a semi-numerical solution are presented, following Refs. [63, 64, 65, 66, 67, 68, 69]. Graphene is treated as a strictly 2D material, its electronic structure is represented by the Dirac cone model, the random phase approximation (RPA) is used and local fields are neglected. Then, we present an *ab initio* method based on the phonon package of QE. This second method allows one to relax the approximations involved in the analytical derivations.

4.2.1 Analytical and semi-numerical solutions

When the out-of-plane thickness of the electronic density can be neglected with respect to the wavelength of the external potential, we can work in a strictly 2D framework and Eqs. (4.1.18) and (4.1.19) can be used. In this section, two other approximations

are used to simplify Eq. (4.1.18). Namely, we set $\delta\tilde{V}_{\mathrm{XC}}(\mathbf{q}_p + \mathbf{G}_p) = 0$ (RPA) and we neglect the local fields, that is, all $\mathbf{G}_p \neq 0$ components. Eq. (4.1.19) then reads:

$$\epsilon_{2D}^{-1}(\mathbf{q}_p) = \frac{1}{1 - \frac{2\pi e^2}{|\mathbf{q}_p|}\tilde{\chi}^0(\mathbf{q}_p)}, \tag{4.2.1}$$

where it is understood that $\tilde{\chi}^0(\mathbf{q}_p) = \tilde{\chi}^0(\mathbf{q}_p, \mathbf{0}, \mathbf{0})$. In a model including only $\pi - \pi^*$ bands, the independent particle susceptibility is written as follows [63, 64, 65, 66, 67, 68, 69]:

$$\tilde{\chi}^0(\mathbf{q}_p) = \frac{1}{\pi^2}\int_{\mathbf{K}} d^2\mathbf{k} \sum_{s,s'} |\langle \mathbf{k},s|\mathbf{k}+\mathbf{q}_p,s'\rangle|^2 \frac{f(\varepsilon_{\mathbf{k},s}) - f(\varepsilon_{\mathbf{k}+\mathbf{q}_p,s'})}{\varepsilon_{\mathbf{k},s} - \varepsilon_{\mathbf{k}+\mathbf{q}_p,s'}}. \tag{4.2.2}$$

The integral is carried out over electronic wave vectors $\mathbf{k}$ in one valley around Dirac point $\mathbf{K}$, with a factor two for valley degeneracy. The indexes s and s' designate the π or π^* bands. The occupation of the state of momentum $\mathbf{k}$ in band s is $f(\varepsilon_{\mathbf{k},s})$ and $\varepsilon_{\mathbf{k},s}$ is the corresponding energy. Within the Dirac cone model, a linear dispersion is assumed $\varepsilon_{\mathbf{k},s} = s\ \hbar v_F|\mathbf{k}|$, with $s = -1$ ($s = +1$) for the π (π^*) band, and v_F is the Fermi velocity. The wave functions overlap is then written $|\langle \mathbf{k},s|\mathbf{k}+\mathbf{q},s'\rangle|^2 = (1 + ss'\cos(\theta_{\mathbf{k}} - \theta_{\mathbf{k}+\mathbf{q}_p}))/2$, where $\theta_{\mathbf{k}}$ ($\theta_{\mathbf{k}+\mathbf{q}_p}$) is the angle between $\mathbf{k}$ ($\mathbf{k}+\mathbf{q}_p$) and an arbitrary reference axis. The Dirac cone band structure is isotropic and $\tilde{\chi}^0$ depends only on the norm of the perturbation wave vector $|\mathbf{q}_p|$. The numerical implementation of this integral in the Dirac cone model will be referred to as the "semi-numerical solution". It has the advantage of accounting for temperature effects. In the zero temperature limit and following the tedious but straightforward calculus of App. C, the following analytical forms can be found. In the case $|\mathbf{q}_p| \leq 2k_F$:

$$\epsilon_{2D}(|\mathbf{q}_p|) = 1 + \frac{2e^2}{\hbar v_F}\frac{2k_F}{|\mathbf{q}_p|}, \tag{4.2.3}$$

where $k_F = \frac{|\varepsilon_F|}{\hbar v_F}$ is the Fermi wave vector, if ε_F is the Fermi energy taken from the Dirac point. Note that in the limit of small wave vectors, ϵ_{2D} diverges, indicating complete screening of long-wavelength perturbations. In the case $|\mathbf{q}_p| > 2k_F$:

$$\epsilon_{2D}(|\mathbf{q}_p|) = 1 + \frac{2e^2}{\hbar v_F}\frac{2k_F}{|\mathbf{q}_p|} \times \left[\frac{\pi|\mathbf{q}_p|}{8k_F} + 1 - \frac{1}{2}\sqrt{1 - \frac{4k_F^2}{|\mathbf{q}_p|^2}} - \frac{|\mathbf{q}_p|}{4k_F}\sin^{-1}\left(\frac{2k_F}{|\mathbf{q}_p|}\right)\right]. \tag{4.2.4}$$

For large wave vectors ($|\mathbf{q}_p| \gg k_F$), we find that $\epsilon_{2D} \approx 5$. Those expressions are relevant for doped graphene. For neutral graphene, we are in the case $|\mathbf{q}_p| > 2k_F$, but since $k_F \to 0$, Eq. (4.2.4) simplifies to:

$$\epsilon_{2D}(|\mathbf{q}_p|) = 1 + \frac{\pi e^2}{2\hbar v_F} \approx 5. \tag{4.2.5}$$

Here, we naturally recover the $|\mathbf{q}_p| \gg k_F$ limit of the doped case. The following *ab initio* study aims at investigating the validity of those expressions.

4.2.2 DFPT LDA solution

Several approximations (Dirac cone model, neglecting local fields, RPA, etc.) were used in order to derive the previous analytical expressions. Their validity is not obvious in graphene. *Ab initio* methods such as DFPT offer the opportunity to relax those approximations [61]. In this section we detail how we obtain the 2D static dielectric function as defined in Eq. (4.1.19) from DFPT. The equilibrium system is calculated using the usual plane-wave DFT package. At that point, interlayer interactions can be neglected in graphene. At the DFPT level, the issues of the periodic images and finite thickness in the out-of-plane direction are treated as previously discussed. The remaining issues are to apply the adequate perturbation and extract relevant 2D quantities. To study the screening properties, we develop the response of the electronic density to an external potential within QE. The code originally calculates the induced electronic density in response to a phonon perturbation [20]. Here, we replace the phonon perturbation by the perturbation $\delta V_{\text{ext}}(\mathbf{q}_p)$. This perturbation is constant in the out-of-plane direction and modulated by a single wave vector $\mathbf{q}_p$ in the plane. As shown previously, the relevant quantity is the $z = 0$ value of the KS potential, coarse-grained in the plane $\delta\tilde{V}_{\text{KS}}(\mathbf{q}_p)$. Note that the $G_z \neq 0$ components are needed to perform a Fourier transform and then take the $z = 0$ value. The number of G_z elements is limited only by the kinetic energy cutoff. We then use the definition of Eq. (4.1.19).

Technical details of DFPT calculations

Our DFT/DFPT calculations were performed using the Quantum ESPRESSO (QE) distribution [38]. The electronic structure is obtained by DFT calculations within the local density approximation [22] (LDA). Since the electronic structure is calculated without cutoff, it can contain some spurious interlayer states above the Dirac point. In the calculations, it is thus safer to dope graphene with holes to avoid those states. We will assume electron-hole symmetry and consider the following results valid for both electron and hole doping. The doping is jellium-induced. We use norm-conserving pseudo-potentials with 2s and 2p states in valence and cutoff radii of 0.78 Å. We use a 0.01 Ry Methfessel-Paxton smearing function for the electronic integrations, a 65 Ry kinetic energy cutoff, and a $96 \times 96 \times 1$ electron momentum grid. The lattice parameter is $b = 2.46$ Å and the distance between graphene and its periodic images is $c = 4.0 \times b \approx 9.8$ Å. The Coulomb interaction is cutoff when calculating the response of the system to an external perturbative potential. The results presented here were obtained for a perturbation wave vector in the direction $\mathbf{\Gamma} \rightarrow \mathbf{K}$ of the Brillouin zone. Identical calculations were performed in different directions. The variations of the results were small enough to assume that the screening properties of graphene are isotropic. Occasionally, variations from this setup were required and will be specified.

Validity of the 2D framework

Now we quickly discuss the validity of the 2D treatment with respect to the thickness of the electronic density. Fig. 4.1 shows the out-of-plane variations of the coarse-grained induced potential $\delta V_{\text{H}}(\mathbf{q}_p,z)$ and the equilibrium electronic density $n_0(\mathbf{G}_p = \mathbf{0},z)$ of a single isolated graphene layer in our *ab initio* framework. We use three values of

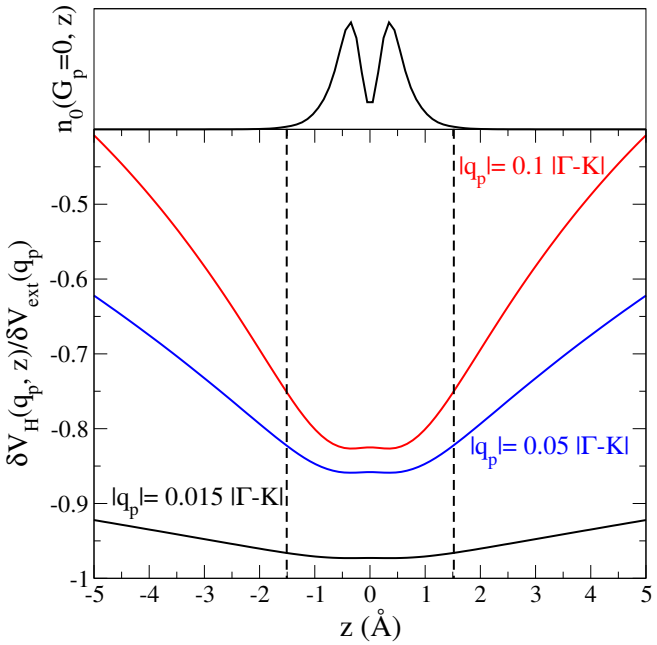

Figure 4.1: The induced potential $\delta V_{\mathrm{H}}(\mathbf{q}_p, z)$ in the out-of-plane direction at different values of $|\mathbf{q}_p|$, expressed in units of the distance between the $\mathbf{\Gamma}$ and $\mathbf{K}$ points of the Brillouin zone. Calculations were performed for a Fermi level of $\varepsilon_F = 0.25$ eV, taken from the Dirac point. Details of the numerical calculations can be found in Sec. 4.2.2. The typical profile of $n_0(\mathbf{G}_p = \mathbf{0}, z)$ is represented. The equilibrium density was chosen here to have a common reference for all perturbations.

$|\mathbf{q}_p|$ covering the range of values used in the following section. In that range, Fig. 4.1 shows negligible variations of the induced potential over the extent of the electron distribution. The two-dimensional description of the screening properties is thus valid. This range of wave vectors covers a large span of situations where static screening plays a role. For example, in the case of electronic transport we are typically interested in values of $|\mathbf{q}_p|$ on the scale of the Fermi wave vector for relatively small doping levels. Thickness effects are negligible in this situation.

4.3 Results in graphene

In this section we present the results of the full DFPT LDA method (Sec. 4.2.2, labeled "LDA") and compare them to the analytical solution (Eqs. (4.2.3)-(4.2.5), labeled "Analytical") for the static dielectric function of doped and neutral graphene. We identify the contributions of temperature, bands, local fields, and exchange correlation by using different methods. When the analytical derivation presented in Sec. 4.2.1 is used, the Fermi velocity is the only parameter needed to define the Dirac cone band structure. For consistency with the *ab initio* methods, we use the Fermi velocity obtained in the linear part of the DFT band structure, such that $\hbar v_F = 5.49$ eV·Å. It is well known that electron-electron interactions increase this value by approximately

20% (depending on doping) within the GW approximation [35]. The renormalized value is in good agreement with experiments. This renormalization is ignored here, but should be accounted for when comparing with experiment. Three intermediary methods were used to investigate the differences between the analytical solution and the self-consistent DFPT LDA solution. The first is the semi-numerical method introduced in Sec. 4.2.1. The independent particle susceptibility $\tilde{\chi}^0(\mathbf{q}_p)$ is obtained by numerical integration of Eq. (4.2.2), and inserted into Eq. (4.2.1). This solution relies on the same approximations as the analytical solution but it can be carried out at a chosen temperature (or energy smearing) as long as the integration grid is adequately fine. The second is labeled "RPA" and consists in setting the exchange-correlation potential to zero within the DFPT method. The third is labeled "RPA no LF" and consists in evaluating the DFPT independent particle susceptibility and inserting it in Eq. (4.2.1). This implies using RPA and neglecting local fields, as well as a strictly 2D treatment, since Eq. (4.2.1) was derived in a strictly 2D framework. This method boils down to the evaluation of Eq. (4.2.1) within a more complete *ab initio* model for the band structure. Table 4.1 summarizes the labels and main characteristics of the various methods used in the following plots.

Table 4.1: Summary of the various methods used in the plots of Sec. 4.3. For each method, we report: (i) the treatment of electron-electron correlation, LDA referring to the use of the XC potential within LDA, "= 0" meaning that the XC potential is set to zero ; (ii) whether local fields are included (YES) or neglected (NO) ; and (iii) which band structure model was used, the full *ab initio* band structure or the simpler Dirac cone model for $\pi - \pi^*$ bands.

Label	Exchange-Correlation	Local Fields	Bands
LDA	LDA	YES	*ab initio*
RPA	= 0	YES	*ab initio*
RPA no LF	= 0	NO	*ab initio*
Analytical	= 0	NO	Dirac cones

4.3.1 Importance of cutting off the Coulomb interactions

We begin by presenting the DFPT LDA results and pointing out the importance of the 2D Coulomb cutoff in Fig. 4.2. We plot the inverse dielectric function obtained with the LDA method with and without cutoff. In the latter case, we follow the process of Sec. 4.2.2 but the original 3D Coulomb interaction v_c^{3D} is used. Two different interlayer distances are displayed, namely $c \approx 9.8$ Å and $c \approx 40$ Å . It is clear that interlayer interactions play a major role in the screening without cutoff, as a strong dependency on the interlayer distance is shown. For $c \approx 9.8$ Å, the effect of the cutoff is drastic. When the interlayer distance is increased, the results without cutoff slowly approach the results with cutoff. This is also the case in the limit of large wave vectors. In general, the results with and without cutoff are similar when the scale on which the induced Hartree potential decreases $1/|\mathbf{q}_p|$ is negligible compared to the interlayer

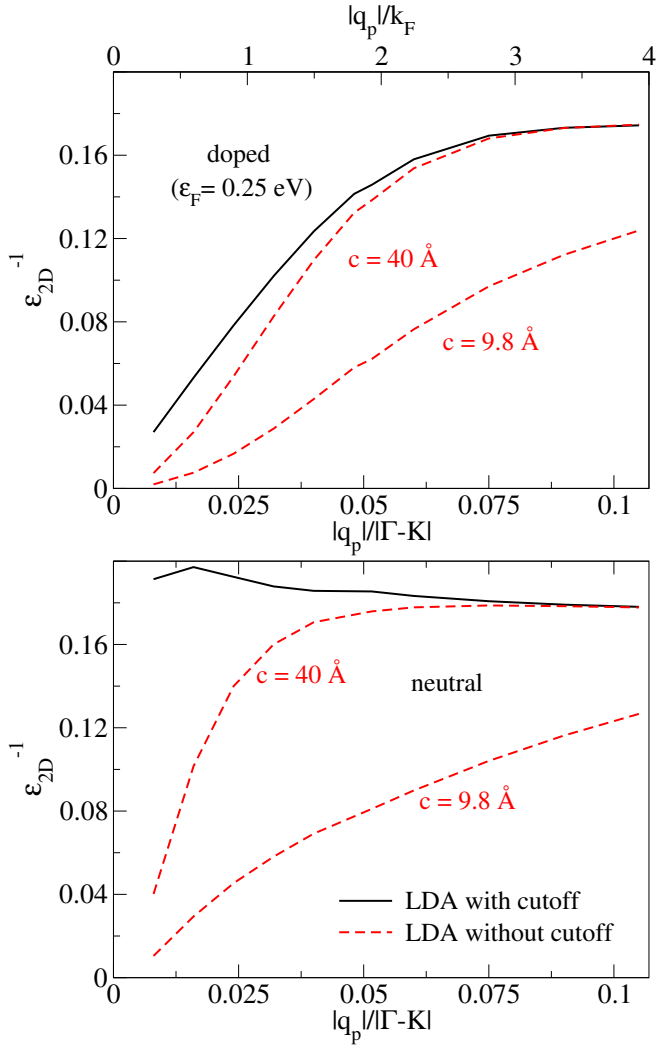

Figure 4.2: DFPT LDA results are plotted with and without cutoff of the Coulomb interactions. The inverse dielectric function, as defined in Eq. (4.1.19), is plotted as a function of the adimensional variable $|\mathbf{q}_p|/|\mathbf{\Gamma}-\mathbf{K}|$, where $|\mathbf{\Gamma}-\mathbf{K}| \approx 1.7$ Å^{-1} is the distance between the $\mathbf{\Gamma}$ and $\mathbf{K}$ points of the Brillouin zone. The calculations were performed for neutral graphene (lower panel) and doped graphene (upper panel) with $\varepsilon_F = 0.25$ eV, measured with respect to the Dirac point. In the upper panel, we also represent the scale $|\mathbf{q}_p|/k_F$ where $k_F \approx 0.27|\mathbf{\Gamma}-\mathbf{K}|$ refers to the Fermi wave vector in the doped case. Two interlayer distances were used $c \approx 40$ Å and $c \approx 9.8$ Å to convey the dependency of the results (without cutoff) on that parameter. When the Coulomb interaction is cutoff, the results are independent of the interlayer distance c. Finally, note that for the neutral case at small wave vectors and with cutoff, the results are quite sensitive to energy smearing/grid effects. In this situation, we used a $140 \times 140 \times 1$ grid and 0.005 Ry energy smearing to be as close as room temperature as manageable.

distance c. However, even using large interlayer distances, the effect of cutting off the Coulomb interactions remains significant. To obtain accurate *ab initio* results for an isolated layer, it is thus essential to cut off the Coulomb interactions. To give a clearer picture of the effects of the Coulomb cutoff, we plot the Hartree potential with and without cutoff for two different interlayer distances c in Fig. 4.3. With cutoff, the Hartree potentials corresponding to the two interlayer distances coincide exactly with each other within the region $[-l_z; +l_z]$, l_z being half the smaller interlayer distance here. This confirms that within this region, everything happens as if the layers were isolated. Without cutoff, in contrast, the Hartree potentials are significantly different, stressing the fundamental difference in the response of systems with different interlayer distances.

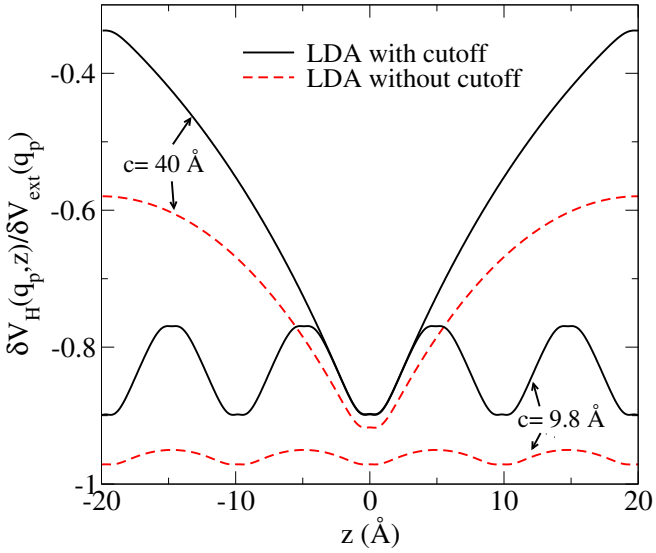

Figure 4.3: The Hartree potentials are plotted in the out-of-plane direction with and without cutoff and for two different interlayer distances $c \approx 40$ Å and $c \approx 9.8$ Å . The calculations were performed for doped graphene with $\varepsilon_F = 0.25$ eV, at $|\mathbf{q}_p| \approx 0.32\ |\mathbf{\Gamma} - \mathbf{K}| \approx 1.2\ k_F$.

4.3.2 Comparison of analytical and LDA methods: band structure effects

In Fig. 4.4, we compare the LDA results (with cutoff) to the analytical solution of Eqs. (4.2.3)-(4.2.5). The results of the two methods are rather close overall. In doped graphene, the LDA results are in very good agreement ($\approx 3\%$) with the analytical method for $|\mathbf{q}_p| \leq 2k_F$. A more pronounced discrepancy ($\approx 10\%$) is observed for $|\mathbf{q}_p| > 2k_F$. In the neutral case, a similar $\approx 10\%$ discrepancy occurs for most values of $|\mathbf{q}_p|$, but agreement seems to be reached in the small $|\mathbf{q}_p|$ limit. For neutral graphene at small wave vectors, smearing plays a significant role. Though not plotted here, the semi-numerical method is equivalent to the analytical solution when performed with an energy smearing corresponding to room temperature. Using the same energy smearing and grid as in DFPT to perform the numerical integration of Eq. (4.2.2) showed that smearing effects are negligible except in the small wave vector limit of the

neutral case. For DFPT LDA calculations in this regime, we lowered the smearing to 0.005 Ry and changed the grid accordingly to $140 \times 140 \times 1$ in Figs. 4.2 and 4.4. For this smearing, agreement between LDA and analytical results is reached around $|\mathbf{q}_p| \approx 0.025|\mathbf{\Gamma} - \mathbf{K}|$. Although quite low in terms of what is computationally manageable in DFT, this energy smearing is still large compared to the value corresponding to room temperature. At room temperature, we expect that DFPT LDA calculations would show the agreement to be reached for smaller $|\mathbf{q}_p|$. In the zero temperature limit, it should be reached for $|\mathbf{q}_p| \to 0$. Thus, for graphene in general, we can consider that LDA and analytical results significantly differ only for $|\mathbf{q}_p| > 2k_F$, which corresponds to $|\mathbf{q}_p| > 0$ in the neutral case.

To investigate the origin the $\approx 10\%$ discrepancy above $2k_F$, we use the aforementioned "RPA no LF" method. In Fig. 4.4, this method gives a smaller inverse dielectric constant than both the LDA ($\approx 8\%$) and analytical ($\approx 16\%$) methods above $2k_F$. Comparing the "RPA no LF" and LDA methods indicates that the combined effect of RPA, neglecting local fields, and a strictly 2D framework is a $\approx 8\%$ decrease of the results. As mentioned before, the band structure model is the only difference between the "RPA no LF" and analytical methods. This suggests that the effects of using the Dirac cone approximation are more sizable ($\approx 16\%$) but somewhat compensate the other approximations. Overall, we end up with the $\approx 10\%$ discrepancy above $2k_F$ between LDA and analytical method. When setting the exchange-correlation potential to zero in DFPT, see "RPA" in Fig.4.4, the results are only slightly changed. This means that neglecting the local fields in the plane (what is meant by neglecting local fields in the derivation of Eq. (4.2.1)) and out-of-plane (equivalent to making the strictly 2D approximation) has more important effects than exchange-correlation. Although the use of an LDA exchange-correlation potential has negligible consequences for the results presented here, we would like to point out that such potentials are derived in the framework of a three-dimensional electron gas. Consequently, their relevance in a 2D framework is limited and the RPA method might be more reliable than the LDA one.

A better interpretation of the effects of band structure can be achieved by comparison of the independent particle susceptibility $\tilde{\chi}^0$ from the "RPA no LF" and analytical methods in Fig. 4.5. In the $|\mathbf{q}_p| \leq 2k_F$ regime, the screening is dominated by the zeroth-order of $\tilde{\chi}^0$, proportional to the density of states. The linear part of the DFT band structure of graphene is well represented by the Dirac cone model. As long as the Fermi level is reasonably small (but finite), the densities of states obtained in DFT and analytically are very close. We then find a very good agreement with the analytical derivation in this regime. In the upper panel of Fig. 4.5, it is clear that a higher-order (in $|\mathbf{q}_p|$) term in $\tilde{\chi}^0$ from DFPT is responsible for the gradual disagreement with the analytical solution as $|\mathbf{q}_p|$ increases. In the neutral case, the zeroth order of $\tilde{\chi}^0$ vanishes with the density of state, and $\tilde{\chi}^0$ is always dominated by contributions of higher-order terms. For the $|\mathbf{q}_p| > 2k_F$ regime in general, the first-order in $|\mathbf{q}_p|$ seems to dominate. The susceptibility $\tilde{\chi}^0$ is then ruled by interband processes, some of them going beyond the range of validity of the Dirac cone model.

Overall, we find a rather good agreement with the analytical derivation of Refs. [63, 64, 65, 66, 67, 68, 69]. This is in strong contrast with the conclusions of a previous *ab initio* study [70] of the screening of point charges in neutral graphene. Our work

differs mainly on the use of a Coulomb cutoff, and the treatment of *ab initio* results to extract the 2D screening properties of a system that is effectively 3D. Finally, we can comment on the use of the constant κ_0 in Eq. (4.1.7) to include the effects of other bands. Such a constant is not appropriate since it would affect all the orders in $\tilde{\chi}^0$, including the zeroth order that is correct. To have an analytic expression quantitatively closer to the DFPT LDA results, one should only renormalize the contribution from the interband processes.

4.3.3 Estimation of the screened deformation potential

Using the bare deformation potential and the analytical 2D static dielectric function of Eqs. (4.2.3)-(4.2.5), we can estimate $\alpha(|\mathbf{q}_p|)$ in single-layer graphene. This gives the results of Fig. 4.4, multiplied by a factor three. We find that $\alpha(|\mathbf{q}_p|) \leq \alpha(|\mathbf{q}_p| = 2k_F) \approx 0.5$ eV. Note that underlying this present estimation is the assumption that the deformation potential can be approximated as a simple perturbing potential with a single Fourier component at $\mathbf{q}_p$. In truth, the phonon perturbation associated to the deformation potential has Fourier components at $\mathbf{q}_p + \mathbf{G}$. The simple $\mathbf{q}_p$-modulated external potential considered in this chapter does induce a response of the electronic density with components $\mathbf{q}_p + \mathbf{G}$, the so-called local fields contributions. Those local fields were shown to have relatively small effects on the static dielectric function. However, in case of a phonon, the source of the perturbation includes local fields. This more direct excitation of the small wavelength components of the electronic density could lead to more significant local fields. In this estimation, we also neglect some possible variations of the bare perturbation as a function of $\mathbf{q}_p$, and take the $\mathbf{q}_p = \mathbf{0}$ value found using the static strain method. Note finally that the DFPT values of $\alpha(|\mathbf{q}_p|)$ from Chapter 3, with some spurious screening by the periodic images, were much smaller than this estimation.

Summary

- Definition of screening function depends on dimensionality.
- Careful treatment is necessary to extract 2D quantities.
- New method to calculate screening properties of 2D materials within DFPT.
- Implementation of 2D Coulomb cutoff is essential.
- Good agreement with strictly 2D, Dirac cones, RPA, no local fields model.
- $\sim 10\%$ discrepancy above $2k_F$ due to Dirac cone model.

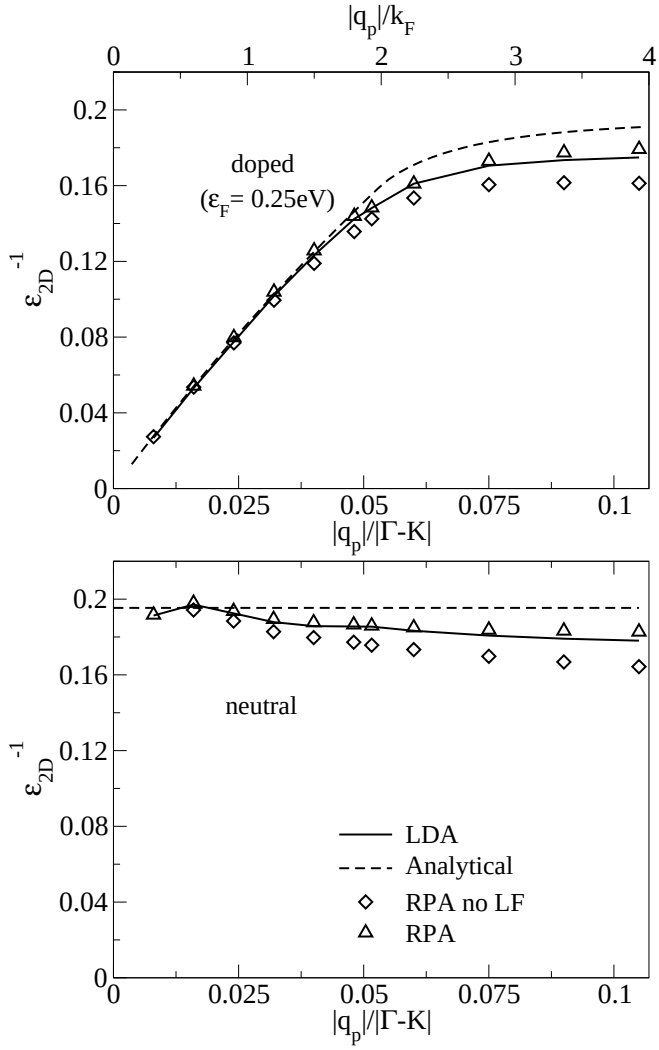

Figure 4.4: Comparison of the static dielectric function of graphene obtained within the LDA and analytical methods. We use the same axes as in Fig. 4.2. We also plot the results of the "RPA" and "RPA no LF" methods. For this last method applied to neutral graphene, the point with the smallest $|\mathbf{q}_p|$ was not converged and is not represented.

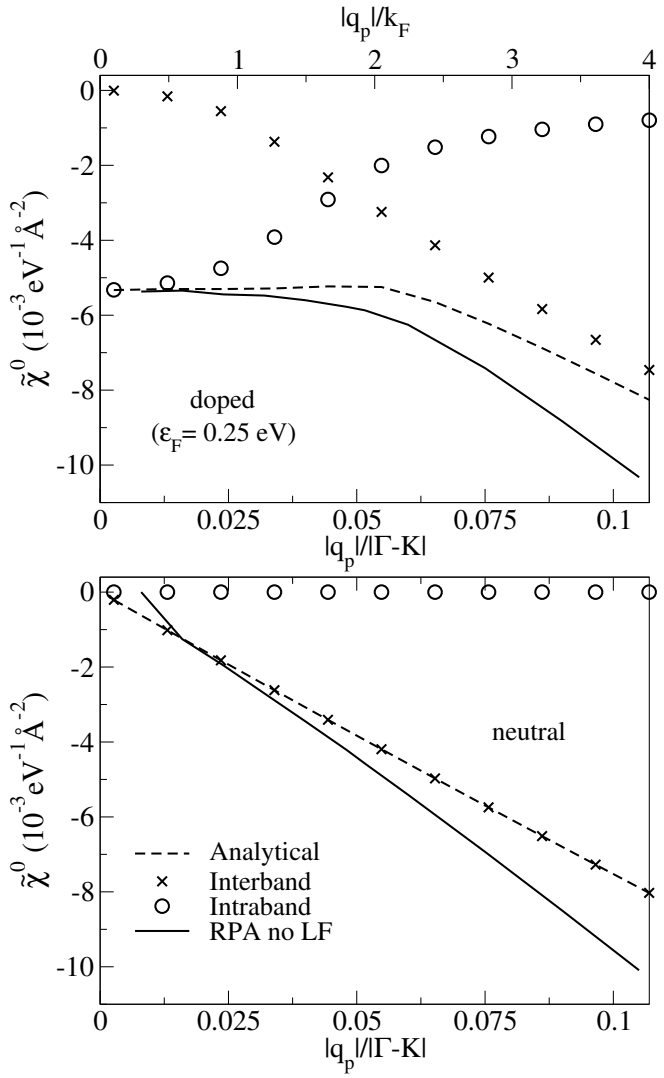

Figure 4.5: Comparison of the independent electron susceptibility of graphene obtained within the "RPA no LF" and analytical methods. We use the same axes as in Fig. 4.2. The contribution of intraband and interband processes to $\tilde{\chi}^0$ are represented by circles and crosses, respectively. To calculate those contributions, we used the semi-numerical solution with a small energy smearing (0.001 Ry). The analytical and semi-numerical methods are equivalent in that case.

Chapter 5

DFT and DFPT for 2D materials doped in the FET setup

DFT based on plane-wave basis sets, Kohn-Sham equations and pseudopotentials (simply called DFT in this thesis), has proven to be a valuable tool to understand and predict electronic and structural properties of materials. DFT studies can help in the process of understanding and controlling experimentally observed phenomena. Inversely, an exciting prospect is the use of DFT to identify potentially interesting new 2D compounds, thus encouraging their experimental study. The wide range of potential applications and fascinating phenomena offered by 2D materials would benefit from accurate DFT simulation.

As discussed before, a particularly interesting aspect of 2D materials is the possibility to induce large gate-induced doping in a FET setup. However, current implementations of plane-wave DFT with three-dimensional periodic boundary conditions (3D PBC) are not adequate to the simulation of 2D materials doped in the FET setup. While doping the material is possible via the use of a compensating jellium background, to simulate gate-induced doping remains a difficult task. The fundamental issue is that its asymmetric configuration in terms of electric field breaks 3D PBC. Some methods have been proposed to palliate this issue at the DFT level. A dipole correction [78, 79, 80] can be used to recover 3D PBC in systems with an out-of-plane dipole moment. This method has been used to simulate chloronitrides [12] and transition-metal dichalcogenides [81] in the FET setup. Another way to deal with those issues is to separate the solving of the Poisson equation and that of the Kohn-Sham (KS) equations. In the effective screening medium (ESM) technique [82], the Poisson equation is solved without 3D PBC, resulting in the correct potentials. The potentials are then modified where the electron density is negligibly small to allow their use in the KS equations with 3D PBC. This method has recently been used to simulate a graphene-based vertical field-effect tunneling transistor [83] at the DFT level.

Here, we use the Coulomb cutoff technique [73, 40, 74], effectively isolating each periodic images from one another. This is implemented at the DFT level for the calculation of the ground-state electronic density, total energy and forces. In addition to be more adapted to the specific case of the FET setup, the 2D Coulomb cutoff technique can be considered simpler and more flexible than the previous dipole correction and

ESM techniques for the simulation of 2D materials in DFT. We also implement the 2D Coulomb cutoff at the DFPT level to compute the linear response of the system to a perturbation. An important addition with respect to the previous methods is then the possibility to compute phonon dispersions and EPC in 2D, and in particular for 2D materials doped in the FET setup. This offers the possibility of simulating phonon features and electron-phonon interactions that are specific to the FET setup. The ability to simulate an isolated 2D system in DFPT is also important in view of the conclusions drawn in the previous chapter [84], where we have shown that interactions between periodic images are important for 2D materials perturbed at small wave vectors. In the previous chapter, it was sufficient to cut the perturbation part of the Hartree potential off, since we were only interested in the electronic response. Since we were not in the FET setup, the periodic images were not a problem for the ground-state density, energy and bands. Also, we did not consider any phonon perturbation. Here, however, we wish to compute the KS potential, total energy, forces, phonon dispersions and EPC of a 2D material doped in the FET setup. Although the concept of the 2D Coulomb cutoff stays the same, the modifications implemented here are much more extensive.

The chapter is structured as follows. We begin with a description of our model for 2D materials doped in the FET setup in Sec. 5.1. We restrict ourselves to a description in terms of potentials. In Sec. 5.2, we highlight the issues raised by the presence of periodic images to simulate the KS potential of 2D materials in the FET setup, and show how the 2D Coulomb cutoff technique can solve those issues. In Sec. 5.3, we detail the implementation of the 2D Coulomb cutoff for the KS potential, total energy, forces, phonons and EPC in the Quantum ESPRESSO (QE) code. Finally, we use our implementation of the 2D Coulomb cutoff to study some previously inaccessible properties of graphene in the FET setup. Namely, we observe the emergence of a finite phonon frequency for the ZA phonons at $\mathbf{\Gamma}$, simulate the screened deformation potential for graphene without the periodic images, and demonstrate a finite coupling of the electrons with the out-of-plane phonons.

5.1 Description of a 2D material doped in the FET setup

In this section we present our model for a 2D material doped in the FET setup, focusing on the potential of such a system. Other quantities (e.g. the total energy) will be treated when we detail the implementation.

The central object is the 2D material in itself. We consider a system which has periodicity in the $\{x, y\}$ plane, defined as the infinite periodic repetition in the plane of a unit cell. The positions of the cells are $\mathbf{R}_p = m_1\mathbf{b}_1 + m_2\mathbf{b}_2$, where m_1 and m_2 are two integers. The primitive lattice vectors $\mathbf{b}_1$,$\mathbf{b}_2$ have coordinates in the $\{x, y\}$ plane. The z-component of $\mathbf{R}_p$ is a constant. The position of atom a within the unit cell is labeled $\mathbf{d}_a$. The atomic internal coordinates $\mathbf{d}_a$ can have different z-components such that all atoms are not necessarily on the same plane, e.g. in the case of multilayered 2D materials. In reciprocal space, the crystal is described by reciprocal vectors $\mathbf{G}_p$, generated by two in-plane primitive reciprocal lattice vectors $\mathbf{b}_1^*$ and $\mathbf{b}_2^*$.

Within our DFT framework, the ground state properties of the system are deter-

mined by the ground-state electronic density $n(\mathbf{r}_p, z)$, where we separate in-plane ($\mathbf{r}_p$) and out-of-plane (z) space variables, as they clearly have different roles in a 2D system:

$$n(\mathbf{r}_p, z) = 2\sum_{\mathbf{k},s} f(\varepsilon_{\mathbf{k},s})|\psi_{\mathbf{k},s}(\mathbf{r}_p,z)|^2 \tag{5.1.1}$$

$$\psi_{\mathbf{k},s}(\mathbf{r}_p, z) = \mathbf{w}_{\mathbf{k},s}(\mathbf{r}_p, z)e^{i\mathbf{k}\cdot\mathbf{r}_p}. \tag{5.1.2}$$

The in-plane wave vector $\mathbf{k}$ and the band index s define an electronic state. The Bloch wave functions $\psi_{\mathbf{k},s}$ are the solutions of the Kohn-Sham (KS) equations. The KS potential of the 2D system is the sum of the external potential $V^{\text{2D}}_{\text{ext}}$ (which, for now, consists of the potential generated by the ions $V^{\text{2D}}_{\text{ion}}$), the Hartree potential V^{2D}_{H}, and the exchange-correlation potential $V^{\text{2D}}_{\text{XC}}(\mathbf{r}_p, z)$:

$$V^{\text{2D}}_{\text{KS}}(\mathbf{r}_p, z) = V^{\text{2D}}_{\text{ext}}(\mathbf{r}_p, z) + V^{\text{2D}}_{\text{H}}(\mathbf{r}_p, z) + V^{\text{2D}}_{\text{XC}}(\mathbf{r}_p, z). \tag{5.1.3}$$

The above quantities possess the 2D-periodicity of the crystal. That is, for any $f \equiv n, V^{\text{2D}}_{\text{KS}}, V^{\text{2D}}_{\text{ext}}, V^{\text{2D}}_{\text{H}}$ or $V^{\text{2D}}_{\text{XC}}$, we can write:

$$f(\mathbf{r}_p + \mathbf{R}_p, z) = f(\mathbf{r}_p, z)\ . \tag{5.1.4}$$

We can define the 2D Fourier transform of those quantities as:

$$f(\mathbf{G}_p, z) = \frac{1}{S}\int_S f(\mathbf{r}_p, z)e^{-i\mathbf{G}_p\cdot\mathbf{r}_p}d\mathbf{r}_p, \tag{5.1.5}$$

where the integral is over the area of the unit cell S. We will write in-plane averages as $f(\mathbf{G}_p = 0, z) = \langle f\rangle_p(z)$. Those quantities also extend in the out-of-plane direction. A relevant scale for the out-of-plane extension of the 2D material would be the electronic density's thickness t, defined such that:

$$\int_{-t/2}^{t/2}\langle n\rangle_p(z)\ dz \approx n_0\ , \tag{5.1.6}$$

where $n_0 \times S$ is the number of valence electrons per unit cell in the system, equal to the sum of the ionic charges $\sum_a Z_a$ in the neutral case. The total energy, forces, phonons and electron-phonon interactions of a neutral 2D material can be computed using the formalism of App. A.

We now consider what we must do to simulate this 2D material doped in conditions emulating the FET setup. In the out-of-plane direction, it is essential that we simulate the correct 2D potentials in a region at least as large as the thickness t. We do not need to simulate the ions and electrons in the dielectric, substrate or gate. We simply need to simulate the effects of those on the 2D material. The first effect is doping. We consider an electron density such that:

$$\int_{-t/2}^{+t/2}\langle n\rangle_p(z)\ dz = n_0 = \sum_a \frac{Z_a}{S} + n_{\text{dop}}\ , \tag{5.1.7}$$

where Z_a is the number of pseudo charges of atom a, and $n_{\text{dop}} \times S$ is the number of electrons added per unit cell. We focus now on the general electrostatic properties

of the FET setup. If we look at the planar-averaged potential generated by the 2D material at distances $|z| > t/2$, we can approximate the sum of the charge distributions of the ions and electrons $\varrho_{\text{ion}} + \varrho_{\text{elec}}$ as a simple charged plane of surface charge density $-en_{\text{dop}}$. The associated electrostatic potential is defined up to a constant electric field (that is a linear potential $\propto z$) that we choose to be zero:

$$\langle \varrho_{\text{ion}} + \varrho_{\text{elec}} \rangle_p(z) \approx -en_{\text{dop}}\delta(z) \tag{5.1.8}$$

$$\langle V_{\text{ion}}^{\text{2D}} + V_{\text{H}}^{\text{2D}} \rangle_p(z) \approx -2\pi e^2 n_{\text{dop}}|z|. \tag{5.1.9}$$

Considered alone, this potential is quite different from the one present in the FET setup. In particular, it is still symmetric with respect to the plane of the material. We have established that a key feature of the FET setup is its asymmetry. In the FET setup, the doping comes from the presence of accumulated counter-charges in the gate. We add a charged plane of opposite surface charge density $+en_{\text{dop}}$ at $z_{\text{g}} < -t/2$, playing the role of the gate:

$$\varrho_{\text{gate}}(z) = +en_{\text{dop}}\delta(z - z_{\text{g}}) \tag{5.1.10}$$

$$V_{\text{gate}}^{\text{2D}}(z) = +2\pi e^2 n_{\text{dop}}|z - z_{\text{g}}|. \tag{5.1.11}$$

We now have a globally neutral system:

$$\int \langle \varrho_{\text{ion}} + \varrho_{\text{elec}} \rangle_p(z) + \varrho_{\text{gate}}(z)\ dz = 0. \tag{5.1.12}$$

The potential of the gate is included in the external potential:

$$\langle V_{\text{ext}}^{\text{2D}} \rangle_p(z) = V_{\text{gate}}^{\text{2D}}(z) + \langle V_{\text{ion}}^{\text{2D}} \rangle_p(z), \tag{5.1.13}$$

and the planar-averaged KS potential $V_{\text{KS}}^{\text{2D}}$ reads:

$$\langle V_{\text{KS}}^{\text{2D}} \rangle_p(z) = 2\pi e^2 n_{\text{dop}} \begin{cases} z_{\text{g}} & \text{if } z < z_{\text{g}} \\ 2z - z_{\text{g}} & \text{if } z_{\text{g}} < z < -t/2 \\ -z_{\text{g}} & \text{if } t/2 < z \end{cases} \tag{5.1.14}$$

In the case of hole doping ($n_{\text{dop}} < 0$), the effective KS potential $\langle V_{\text{KS}}^{\text{2D}} \rangle_p(z)$ is then as shown in Fig. 5.1. The derivative of the KS potential gives the electric field experienced by an electron:

$$\frac{d\langle V_{\text{KS}}^{\text{2D}} \rangle_p(z)}{dz} = \begin{cases} 0 & \text{if } z < z_{\text{g}} \\ 4\pi e^2 n_{\text{dop}} & \text{if } z_{\text{g}} < z < -t/2 \\ 0 & \text{if } t/2 < z \end{cases} \tag{5.1.15}$$

The system has acquired an out-of-plane dipolar moment which induces a shift in the KS potential:

$$\langle V_{\text{KS}}^{\text{2D}} \rangle_p(+\infty) - \langle V_{\text{KS}}^{\text{2D}} \rangle_p(-\infty) = 4\pi e^2 n_{\text{dop}}|z_{\text{g}}|. \tag{5.1.16}$$

The last component we have to consider to have a working minimal model for the FET setup is the dielectric. Its necessity appears in the case of electron-doping. In

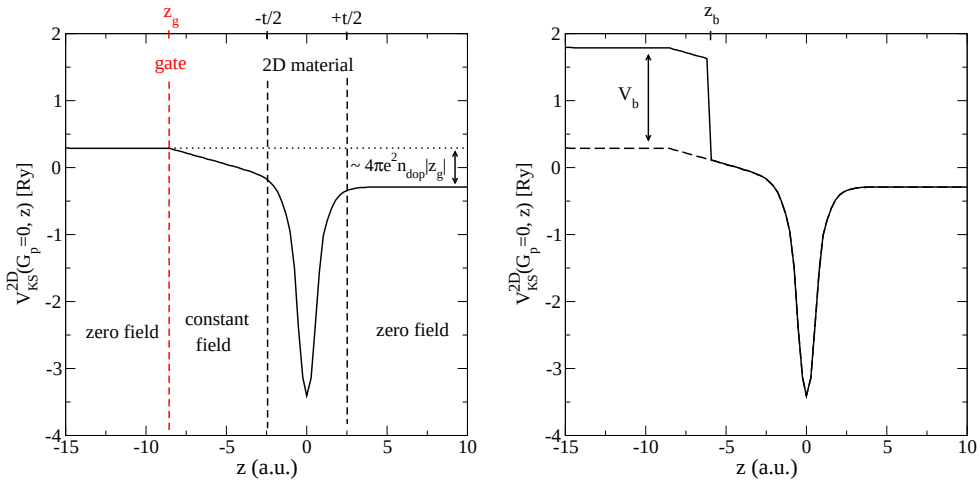

Figure 5.1: On the left, out-of-plane behavior of the KS potential of a hole-doped single-layer 2D material (graphene) with a charged plane to simulate the gate. On the right, we add a potential barrier to simulate the dielectric material.

that situation, the polarity of the system pictured in Fig. 5.1 is reversed. This means that the gate lies at a lower potential than the 2D material. In our simulations, there would then be some leaking of electrons towards the gate. This is not physical [1]. In a FET setup, this is prevented by the presence of the insulating dielectric material. The dielectric also has a more mechanical purpose. Indeed, there is an attractive force between the gate and the material, which is simply the electrostatic attraction between two oppositely charged plates:

$$\mathbf{F}_{\text{gate}-\text{material}} = S \times 2\pi e^2 n_{\text{dop}}^2 \ \text{sign}(z_{\text{g}}). \tag{5.1.17}$$

In this context, the dielectric provides a counteracting repulsive force. To simulate the insulating and repulsive roles of the dielectric we can add a potential barrier in between the material and the gate:

$$V_{\text{barrier}}^{\text{2D}}(z) = \begin{cases} V_{\text{b}} & \text{if } z < z_{\text{b}} \\ 0 & \text{otherwise} \end{cases} \tag{5.1.18}$$

where $z_{\text{g}} < z_{\text{b}} < 0$. This potential can be included in the external potential $V_{\text{ext}}^{\text{2D}}$. Adding such a barrier results in the potentials shown on the right side of Fig. 5.1. This barrier potential essentially forbids (or makes highly unlikely) the presence of electrons for $z < z_{\text{b}}$, thus preventing electrons from leaking towards the gate. Since the electrons cannot go past the barrier, and since the ions are strongly attracted by the electrons, the barrier repulses the 2D material as a whole. As will be detailed later, the position of the barrier is determined by relaxation of the forces in the system.

[1] We could think about cold emission (an electron being emitted from a metal plate towards an other under a strong electric field), but in that case we would have to account for the work function of the gate.

In the following section, we explain how we deal with the periodic images to obtain the KS potential we just described in a plane-wave DFT code. Then, we will detail the modifications implemented to compute the total energy, forces, phonons and electron-phonon interactions for a 2D material doped in the FET setup.

5.2 Treatment of the periodic images

Ab initio calculations based on plane-wave basis sets require periodic boundary conditions along the three dimensions (3D PBC). In this framework, periodic images of the 2D system are present in the out-of-plane direction. Our goal is for each periodic image to be strictly equivalent to the 2D system presented in the previous section, at least within a certain "physical region" around the 2D material (for example, within the boundaries of Fig. 5.1). In this section, we detail the issues that arise from the use of 3D PBC for the simulation of doped systems, systems with out-of-plane dipolar moment, and systems perturbed at long wavelengths. We then show how the Coulomb cutoff technique can solve those issues.

5.2.1 Inadequacy of 3D PBC

The 3D-periodic system obtained by adding translated copies of the 2D system generates potentials that are different from the ones described in the previous section. This comes from interactions between periodic images, due to the combination of their potentials while satisfying PBC. The sum of the KS potential from each periodic image can be written:

$$V_{\mathrm{KS}}(\mathbf{r}_p, z) = \sum_i V_{\mathrm{KS}}^{\mathrm{2D}}(\mathbf{r}_p, z - ic), \tag{5.2.1}$$

where i is an integer, and c is the distance between the periodic images (interlayer distance). $V_{\mathrm{KS}}^{\mathrm{2D}}$ is the potential of the 2D system, while V_{KS} is the one simulated in DFT with 3D PBC. In addition to the 2D PBC of Eq. (5.1.4) that $V_{\mathrm{KS}}^{\mathrm{2D}}$ already fulfills, V_{KS} has to fulfill the PBC in the third direction:

$$V_{\mathrm{KS}}(\mathbf{r}_p, z + ic) = V_{\mathrm{KS}}(\mathbf{r}_p, z) \quad , \ \forall\ i. \tag{5.2.2}$$

We first consider a doped 2D material. Away from the direct vicinity of the ions, this system behaves like a monopole, with $\lim_{|z|\to\infty} \langle V_{\mathrm{KS}}^{\mathrm{2D}} \rangle_p(z) = \infty$, and V_{KS} is obviously ill-defined. As mentioned before the standard method in current plane-wave DFT packages amounts to the use of a jellium background. Each slab is then globally neutral, containing the doped material and a uniform distribution of compensating charges. In between the periodic images, the resulting potential is quadratic in z, with extrema at mid-distance between layers, see Fig. 5.2. This potential does fulfill the PBC and doesn't diverge. However, it is quite different from the linear potential of Eq. (5.1.9).

Now we consider a 2D system with a global dipolar moment in the out-of-plane direction and a $V_{\mathrm{KS}}^{\mathrm{2D}}$ potential like in Fig. 5.1. Here, each periodic image is globally neutral. However, the potential $\langle V_{\mathrm{KS}} \rangle_p(z)$ would experience a shift with each periodic

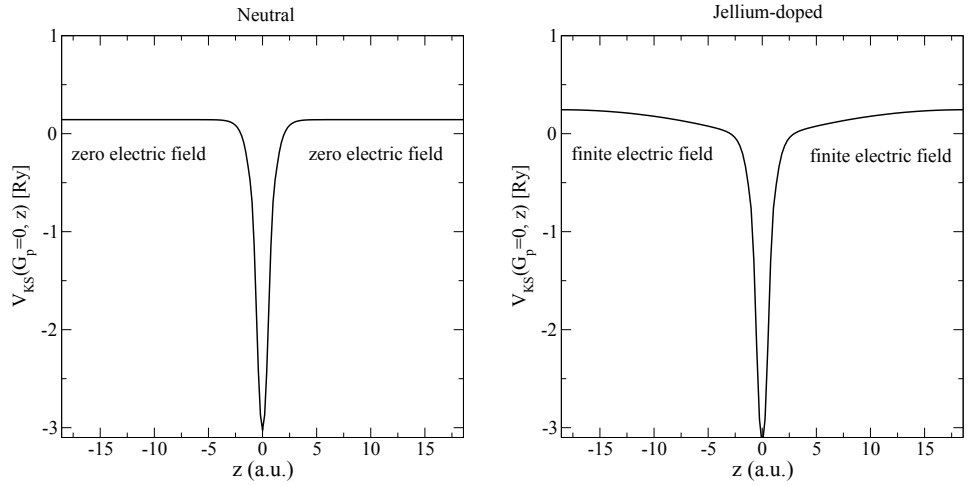

Figure 5.2: Planar-averaged KS potential in the out-of-plane direction as simulated in DFT with 3D PBC for neutral (left) and doped (right) graphene. In the case of doped graphene, the quadratic behavior of the KS potential indicates the presence of a jellium background.

images, eventually diverging. Imposing PBC forbids this kind of situation. Instead, it leads to a combination of additional electric field and re-organization of the charge so that the total average electric field in one slab is zero [79, 78, 80], see Fig. 5.3. Here again, we loose the equivalence with $V_{\mathrm{KS}}^{\mathrm{2D}}$.

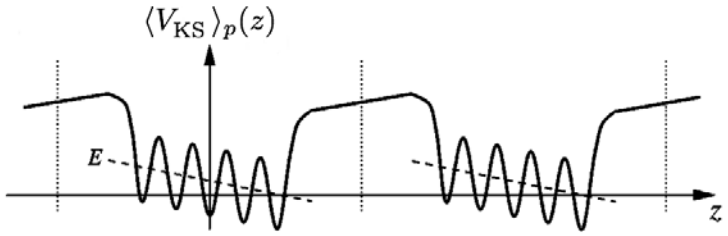

Figure 5.3: From Ref. [80]. Schematic representation of the effects of 3D PBC on the planar-averaged KS potential $\langle V_{\mathrm{KS}} \rangle_p(z)$ of a polar system. The finite slope of the potential in between the periodic images indicates the presence of an external electric field. The slope of the average potential within the material (dashed line) indicates an internal electric field.

Finally, 3D PBC are also problematic when the system is perturbed at small wave vector. As seen in chapter 4, the Hartree potential generated by an electronic density perturbed at an in-plane wave vector $\mathbf{q}$ decreases on a scale $\mathbf{q}^{-1}$ in the out-of-plane direction. At small wave vector, the extent of the potential induced by the electron density is thus very large. When it is of the order of the distance between periodic images, there is some spurious screening. This issue holds in the case of a phonon perturbation.

5.2.2 Isolate the layers with 2D Coulomb cutoff

To reduce interlayer interactions, a naive solution is to increase the distance between the periodic images. Eventually, interlayer interactions are bound to fade away. However, the cost of the calculations increasing linearly with the distance, this method can be very expensive, especially in the particular cases presented before. One solution for the FET setup and for systems with an out-of-plane dipolar moment in general is to add a dipole correction to catch up the potential shift [78, 79, 80, 12]. However, the dipole correction has to be recalculated self-consistently at each iteration.

Here, we tackle 3D PBC issues by using the Coulomb cutoff technique, successfully used in the previous chapter for screening. The general idea is to cut all the potentials off between the periodic images. In effect, all physical links between periodic images are severed because the potential generated by one periodic image does not reach the others. Each slab is effectively isolated. There is no *physical* 3D-periodic system anymore. There is a 2D-periodic system, copied and repeated in the third dimension in order to build something that *mathematically* fulfills 3D PBC.

Each long-range potential ($V \equiv V_{\text{ion}}$,V_{H},V_{gate}) in the original 3D code is generated by a certain distribution of charges via the Coulomb interaction $v_c(\mathbf{r}) = \frac{e^2}{|\mathbf{r}|}$. To build the corresponding cutoff potentials in the code ($\bar{V} \equiv \bar{V}_{\text{ion}}$,$\bar{V}_{\text{H}}$,$\bar{V}_{\text{gate}}$), we use the following cutoff Coulomb interaction:

$$\bar{v}_c(\mathbf{r}) = \frac{e^2\theta(l_z - |z|)}{|\mathbf{r}|}, \tag{5.2.3}$$

where $\mathbf{r} \equiv (\mathbf{r}_p, z)$ is a generic 3-dimensional space variable . An arbitrary charge density ϱ then generates the following potential:

$$\bar{V}(\mathbf{r}) = \int \frac{e\varrho(\mathbf{r}')}{|\mathbf{r} - \mathbf{r}'|}\theta(l_z - |z|)d\mathbf{r}'. \tag{5.2.4}$$

Roughly speaking, considering a single charged plane, we generate its potential only within a certain slab of thickness $2l_z$ centered on the charge distribution. Within this slab, we have that $\bar{V}(\mathbf{r}) = V^{\text{2D}}(\mathbf{r})$. Outside of this slab, the potential is zero. Each periodic image of each charge distribution (ϱ_{ion},ϱ_{elec},ϱ_{gate}) generates its own potential within its own slab. To fulfill 3D PBC, the simpler way is to cut off midway between the periodic images:

$$l_z = \frac{c}{2}. \tag{5.2.5}$$

Since the potentials $V^{\text{2D}}_{\text{ion}}$, V^{2D}_{H}, and $V^{\text{2D}}_{\text{gate}}$ are symmetric with respect to the plane of the associated subsystem (ions, electrons, gate), they have the same value on both sides of the corresponding slab. $\bar{V}_{\text{ion}}$, $\bar{V}_{\text{H}}$, and $\bar{V}_{\text{gate}}$ are each continuous and periodic, and so is their sum $\bar{V}_{\text{KS}}$. However, since the slabs of each subsystem do not coincide, the KS potential is only physical within the overlap of the subsystems' slabs. This overlap region defines a "physical region", as illustrated in Fig. 5.4 , where all the potentials make sense. Outside of this region, there are some spurious unphysical variations of the KS potential. Those spurious variations are a necessary consequence of fulfilling 3D PBC. Let us consider the example Fig. 5.4 in more details. The simplest subsystem

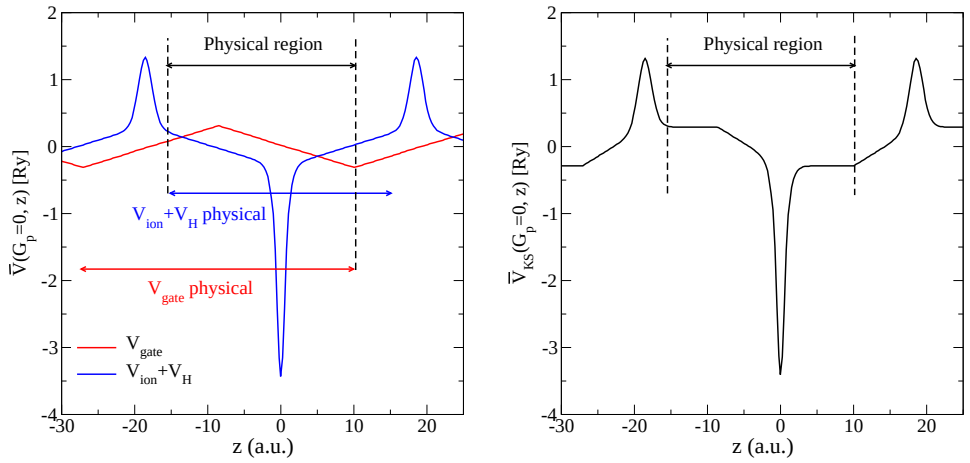

Figure 5.4: Determination of the physical region. On the left, we show the gate potential and the material's potential $\langle \bar{V}_{\text{ion}} + \bar{V}_{\text{H}} \rangle_p(z)$, and indicate where they make sense physically. The physical region is the overlap between those regions. On the right, we show that the KS potential $\langle \bar{V}_{\text{KS}} \rangle_p(z)$ (the sum of the potentials on the left) makes sense within the physical region. In both plots, $c \approx 37$ a.u. and $z_{\text{g}} \approx -8.5$ a.u.

is the gate because ϱ_{gate} is infinitely thin in the out-of-plane direction. Within the slab $z \in [z_{\text{g}} - \frac{c}{2}; z_{\text{g}} + \frac{c}{2}]$, we see the potential generated by the gate at z_{g}.

$$\bar{V}_{\text{gate}}(\mathbf{r}_p, z) = \sum_i V^{2D}_{\text{gate}}(\mathbf{r}_p, z - ic)\theta(\frac{c}{2} - |z - ic|) \tag{5.2.6}$$

$$= V^{2D}_{\text{gate}}(\mathbf{r}_p, z) \text{ if } z \in [z_{\text{g}} - \frac{c}{2}; z_{\text{g}} + \frac{c}{2}]. \tag{5.2.7}$$

For z outside of this interval, we see the potential generated by the neighboring periodic images of the gate, which has no physical sense with respect to the 2D system represented in Fig. 5.4. For the electrons, the charge distribution ϱ_{elec} is spread in the out-of-plane direction. Each infinitesimal slice of electronic density with surface charge density $\varrho_{\text{elec}}(z)dz$ generates its contribution to the Hartree potential only within a certain slab. The Hartree potential is physical only within the overlap of all those slabs. If the electrons are centered around a position z_{e}, that would be $z \in [z_{\text{e}} - \frac{c}{2} + \frac{t}{2}; z_{\text{e}} + \frac{c}{2} - \frac{t}{2}]$. The ions are in a similar situation, but the charge distribution is much less spread. The difference in the spreading of ϱ_{elec} and ϱ_{ion} leads to the "bumps" we can observe for $\bar{V}_{\text{ion}} + \bar{V}_{\text{H}}$, at $z \approx \pm 18.5$ a.u. in Fig. 5.4. Thus, the unphysical variations of the KS potential outside the physical region are due to the addition of potentials generated by incomplete subsystems or different periodic images.

Nevertheless, everything happens as in the previous section within the physical region associated to the KS potential. To simulate the system, we just need to make sure that the 2D material lies in this physical region. We will need 3D Fourier transforms

$\bar{V}(\mathbf{G}_p, G_z)$, easily related to the 2D Fourier transform of $V^{2D}(\mathbf{G}_p, z)$ as follows:

$$\bar{V}(\mathbf{G}_p, G_z) = \frac{1}{Nc}\int_{-\infty}^{\infty} dz\ \bar{V}(\mathbf{G}_p, z)e^{-iG_z z} \tag{5.2.8}$$

$$= \frac{1}{c}\int_{-c/2}^{c/2} dz\ V^{\mathrm{2D}}(\mathbf{G}_p, z)e^{-iG_z z}. \tag{5.2.9}$$

5.3 Implementation

In this section we detail the implementation of the Coulomb cutoff for the potentials, and show how it affects the energies, forces, phonons and EPC in the code. Most of the potentials, or at least their long-range part, are calculated in reciprocal space. We thus need the cutoff Coulomb interaction in reciprocal space, as defined in Ref. [74]:

$$\begin{aligned} \bar{v}_c(\mathbf{G}_p, G_z \neq 0) &= \frac{4\pi e^2}{|\mathbf{G}_p|^2 + G_z^2} \times \left[1 - e^{-|\mathbf{G}_p| l_z} \cos(G_z l_z)\right], \\ \bar{v}_c(\mathbf{G} = 0) &= 0. \end{aligned} \tag{5.3.1}$$

The choice of the $\mathbf{G} = 0$ value is just a convention since every potential is defined up to a constant. Here, we choose the same convention as in the original 3D code, such that the average of a potential over the unit cell is zero. A more detailed justification about this choice, especially its implications in terms of energy, can be found in App. D. Our modifications concern mostly the potentials. On some occasions, we will first need to describe the implementation of the original 3D code in order to identify what needs to be modified. We use different notations to distinguish the potentials that stay as implemented in the original 3D code (noted V) and those that were modified with the implementation of the 2D Coulomb cutoff (noted $\bar{V}$). For other quantities (energy, forces, phonons and EPC), such distinction in the notation is not necessary. Indeed, their definition essentially does not change. It is the potential that is used to compute them that changes.

5.3.1 KS Potential

The KS potential is the sum of the external potential, the Hartree potential, and the exchange-correlation potential:

$$\bar{V}_{\mathrm{KS}}(\mathbf{r}_p, z) = \bar{V}_{\mathrm{ext}}(\mathbf{r}_p, z) + \bar{V}_{\mathrm{H}}(\mathbf{r}_p, z) + V_{\mathrm{XC}}(\mathbf{r}_p, z). \tag{5.3.2}$$

The exchange-correlation potential, at least within the LDA approximation used in this thesis, is short-range and does not need to be cut off[2]. The external potential is the sum of the ionic, gate and barrier potentials:

$$\bar{V}_{\mathrm{ext}}(\mathbf{r}) = \bar{V}_{\mathrm{ion}}(\mathbf{r}) + \bar{V}_{\mathrm{gate}}(z) + \bar{V}_{\mathrm{barrier}}(z). \tag{5.3.3}$$

[2]As mentioned in the previous chapter, the relevance of current LDA functionals for 2D materials is limited, since they are derived in the framework of a 3D electron gas. In any case, the treatment of exchange-correlation functionals is out of scope for this work.

The ionic potential is separated in local and non-local parts $\bar{V}_{\text{ion}} = \bar{V}_{\text{ion}}^{\text{loc}} + V_{\text{ion}}^{\text{non-loc}}$. The non-local part is short-range. It does not need to be cut off and is ignored here. We need to compute the Fourier transform of the cutoff local potential $\bar{V}_{\text{ion}}^{\text{loc}}(\mathbf{G})$. It is computed from the the pseudopotentials, which are separated in short-range and long-range parts. We first describe this separation as it is done in the original code, identify what we must modify, then present the implementation of the cutoff.

In the original 3D code, the local part of the pseudopotential is a radial function in real space $v_a(|\mathbf{r}|)$ associated to each type of atom. It is separated in short-range (SR) and long-range (LR) parts:

$$v_a(|\mathbf{r}|) = v_a^{\text{SR}}(|\mathbf{r}|) + v_a^{\text{LR}}(|\mathbf{r}|) \tag{5.3.4}$$

$$v_a^{\text{SR}}(|\mathbf{r}|) = v_a(|\mathbf{r}|) + \frac{Z_a e^2 \text{erf}(|\mathbf{r}|)}{|\mathbf{r}|} \tag{5.3.5}$$

$$v_a^{\text{LR}}(|\mathbf{r}|) = -\frac{Z_a e^2 \text{erf}(|\mathbf{r}|)}{|\mathbf{r}|}, \tag{5.3.6}$$

where $\text{erf}(|\mathbf{r}|)$ is the error function and $v_a^{\text{SR}}(\mathbf{r})$ is indeed short-range because the pseudopotential always behaves as $-\frac{Z_a e^2 \text{erf}(|\mathbf{r}|)}{|\mathbf{r}|}$ for $|\mathbf{r}|$ large enough. In particular, we have that $v_a^{\text{SR}}(\mathbf{r}) = 0$ for $|\mathbf{r}| \geq r_{\text{SR}}$. The Fourier transform of the SR part is calculated via numerical integration, while the LR part is analytic. The SR part, specific to each atom, is Fourier transformed on a finite sphere:

$$v_a^{\text{SR}}(\mathbf{G}) = \frac{1}{\Omega} \int_0^{|\mathbf{r}|=r_{\text{SR}}} v_a^{\text{SR}}(\mathbf{r}) e^{-i\mathbf{G}\cdot\mathbf{r}} \, d\mathbf{r}, \tag{5.3.7}$$

where $\Omega = S \times c$ is the volume of the unit cell. The potential v_a^{SR} does not need to be cut off as long as $r_{\text{SR}} < l_z$, which is easily satisfied. The Fourier transform of the LR part $v_a^{\text{LR}}(\mathbf{G})$ is easily found analytically, since $v_a^{\text{LR}}(|\mathbf{r}|)$ is the potential generated by a gaussian distribution of charges. This SR/LR separation is implemented in the original 3D code to restrict the numerical Fourier transform to a finite region of space. The original code also relies heavily on the rotational invariance of the radial pseudopotentials to define the arrays containing their Fourier transforms.

In our implementation, we replace the analytic LR part of the pseudopotential by its cutoff version:

$$\bar{v}_a^{\text{LR}}(\mathbf{G}) = -\frac{Z_a}{\Omega} \bar{v}_c(\mathbf{G}) e^{-|\mathbf{G}|^2/4}. \tag{5.3.8}$$

The SR/LR separation turns out to be very convenient to implement the Coulomb cutoff. However, since the Coulomb cutoff breaks the rotational invariance, it cannot be implemented as a simple modification of the existing array. A separate array for the cutoff LR part is calculated in a separate routine. It is then added to the SR part when constructing the local part of the ionic potential:

$$\bar{V}_{\text{ion}}^{\text{loc}}(\mathbf{G}) = \sum_a e^{-i\mathbf{G}\cdot\mathbf{d}_a} \left(v_a^{\text{SR}}(\mathbf{G}) + \bar{v}_a^{\text{LR}}(\mathbf{G}) \right). \tag{5.3.9}$$

The Hartree potential is relatively easy to cut off. It is computed in reciprocal space from the electronic density:

$$\bar{V}_{\mathrm{H}}(\mathbf{G}) = \bar{v}_c(\mathbf{G})n(\mathbf{G}). \tag{5.3.10}$$

The gate potential must be added for a doped system. In practice, the potential of the gate is added in real space to the external potential. We define directly in real-space the saw-tooth potential generated by ϱ_{gate}, Eq. (5.1.10) via the cutoff Coulomb interaction Eq. (5.3.1). Within the interval $z \in [z_{\mathrm{g}} - \frac{c}{2}, z_{\mathrm{g}} + \frac{c}{2}]$, it is defined as:

$$\bar{V}_{\mathrm{gate}}(z) = 2\pi e^2 n_{\mathrm{dop}} \left(|z - z_{\mathrm{g}}| - \frac{l_z}{2} \right), \tag{5.3.11}$$

where the constant term is due to the definition of $\bar{v}_c(\mathbf{G} = 0)$. It sets the out-of-plane average of the potential to zero.

The barrier potential is necessary to relax the forces in the system and to prevent electrons from leaking to the gate. It is also used to prevent electrons from going outside the physical region. Indeed, the variations of the potential outside the physical region can lead to the presence of potential wells. Placing a barrier potential outside the physical region ensures that no unphysical leaking occurs. The barrier is added in real space along with the gate. In practice, this barrier consists in the addition of a constant to the external potential within a certain region in the out-of-plane direction. For $z \in [-\frac{c}{2}, +\frac{c}{2}]$, it is defined as:

$$\bar{V}_{\mathrm{barrier}}(z) = \begin{cases} V_{\mathrm{b}} & \text{if } z < z_{\mathrm{b1}} \text{ or } z_{\mathrm{b2}} < z \\ 0 & \text{otherwise} \end{cases} \tag{5.3.12}$$

The borders of the barrier at z_{b1} and z_{b2} are smoothed via a linear transition from V_{b} to 0 on a small distance. The implementation of the gate and the barrier was adapted from a previous modification of the code, discussed in Ref. [12].

Verifications: To check the consistency of our modifications on the potentials, we can first simulate the potentials of a neutral and non-polar 2D system, without gate or barrier. The corresponding ionic, Hartree and KS potentials are plotted with and without the 2D Coulomb cutoff in Fig. 5.5. With 3D PBC, setting the $\mathbf{G} = 0$ value of the ionic or Hartree potential to zero is equivalent to the inclusion of a compensating jellium background (see App. D). The potentials we observe then correspond to either ions or electrons bathed in the associated jellium. This leads to a quadratic behavior in z between the periodic images. When the 2D Coulomb cutoff is applied, we recover the linear behavior in z. Setting the $\mathbf{G} = 0$ value of the ionic or Hartree potential to zero leads to a simple shift. For such a neutral and non-polar system, the KS potentials with and without cutoff coincide up to a constant within the physical region. This constant comes from the fact that both KS potential average to zero but the cutoff KS potential has "bumps" outside the physical region while the other does not.

Let us now simulate the KS potential of a hole-doped 2D material as shown in Fig. 5.6. Using the original code with 3D PBC, we obtain the potential of the material bathed in a jellium compensating for the added charge (or missing electrons). In that case, the KS potential is quadratic, with a varying slope and thus a varying electric

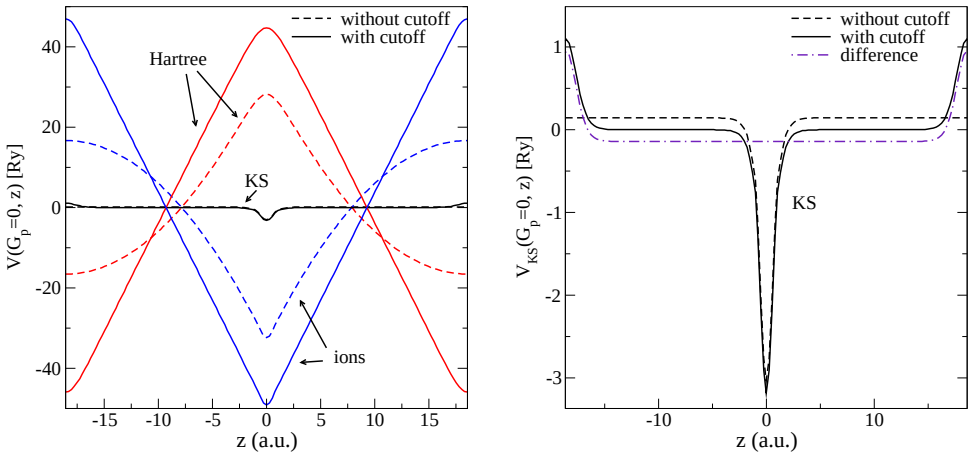

Figure 5.5: On the left, we show the planar-averaged ionic, Hartree and KS potential obtained with and without the 2D Coulomb cutoff. On the right, we zoom in on the KS potential. Within the physical region, the KS potentials with and without cutoff coincide up to a constant, as is desmonstrated by the difference $\langle \bar{V}_{\mathrm{KS}} - V_{\mathrm{KS}} \rangle_p(z)$ (dash-dot indigo line).

field. The electric field is symmetric with respect to the plane of the 2D material. It vanishes midway between the periodic images, on the left and right borders of Fig. 5.6. If we use the 2D Coulomb cutoff without adding a gate, we obtain the potential that would be generated by the doped 2D material in vacuum, as in Eq. (5.1.9), within the physical region. If we add a compensating charged plane to simulate the gate, we obtain the configuration of the FET setup, with a finite electric field on the left of the 2D material, and zero electric field on the right.

Finally, we simulate the KS potential of an electron-doped system to show the necessity of the barrier potential in Fig. 5.7. Without the barriers, some potential wells appear on both sides of the 2D material. On the left, this is due to the presence of the positively charged gate. On the right, this is due to the unphysical variations of the KS potential outside the physical region. Electrons leak towards those potential wells, which can be inferred here from the slopes of the KS potential in the vicinity of the 2D material. Compared to what we should obtain in the FET setup, the slope of the KS potential on the left of the 2D material is too small while the slope on the right is not zero. This is due to the Hartree potential contribution from the electrons that leaked in the potential wells. This is not what we want to simulate. The addition of a potential barrier prevents the electrons from leaking towards the barrier or outside the physical region, and we find the right slopes (or electric field) in the vicinity of the material.

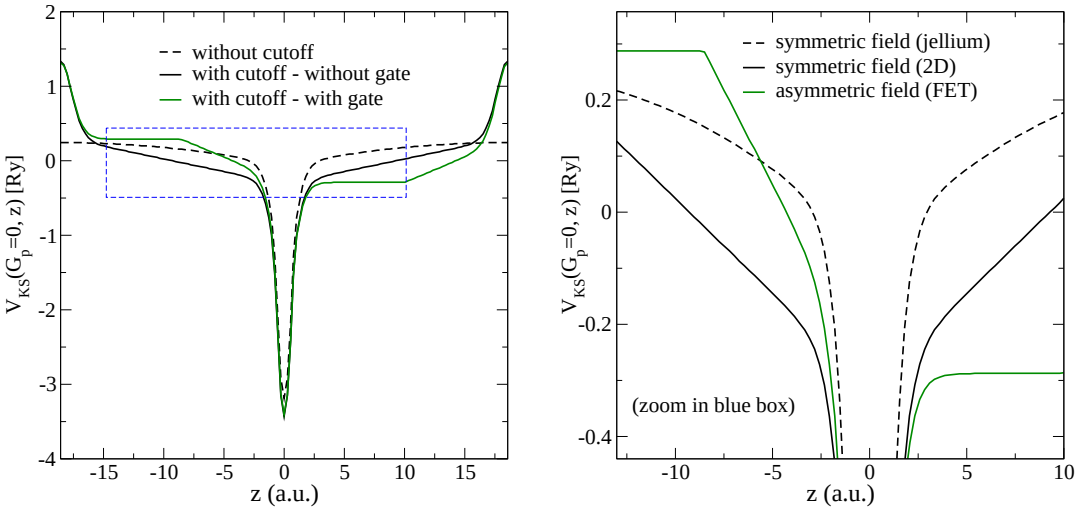

Figure 5.6: The planar-averaged KS potential of hole-doped graphene is simulated in various situations. The label "without cutoff" means that the standard 3D code was used. The label "with cutoff" means that the 2D Coulomb cutoff was implemented. In that case, we plotted the result with and without a gate. The right panel is a zoom in the region delimited by the blue box in the left panel. We show the different configurations in terms of electric field.

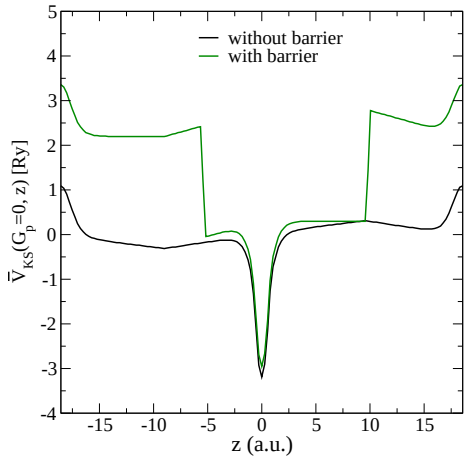

Figure 5.7: Planar-averaged KS potential in the case of electron doping. The gate is always included. We plot the potential without barrier to show how there is some unphysical leakage. With the barrier, we effectively prevent electrons from reaching any of the unphysical potential wells.

5.3.2 Total Energy

The total energy per unit cell associated with the system is:

$$E_{\text{tot}} = E_{\text{kin}} + E_{\text{ext}} + E_{\text{H}} + E_{\text{XC}} + E_{\text{i-i}} + E_{\text{g-i}} + E_{\text{g-g}}. \tag{5.3.13}$$

It is the sum of the kinetic energy of the electrons, the energy of the electrons in the external potential, the Hartree energy, the exchange-correlation energy, the ion-ion interaction energy, the energy of the ions in the potential of the gate, and finally, the self-interaction energy of the gate. The terms E_{kin} and E_{XC} are short-range. They are computed as in the standard 3D code and will be ignored here. The computation of the remaining terms is detailed in the following. A general definition of E_{ext}, E_{H} and $E_{\text{i-i}}$ can be found in App. A. Those definitions stay valid provided one uses the cutoff potentials $\bar{V}_{\text{ext}}$, $\bar{V}_{\text{H}}$ and $\bar{\Phi}$. Unlike the potentials, the total energy is not defined up to a constant. The choice of the $\bar{v}_c(\mathbf{G} = 0)$ can affect the value of the energy contributions, but it should not affect the total energy. This is checked in App. D.

The external energy E_{ext} is calculated via the sum of the eigenvalues of the KS system. It includes the energy of the electrons in the potential of: i) the ions $E_{\text{ext}}^{\text{ion}}$, ii) the gate $E_{\text{ext}}^{\text{gate}}$ and iii) the barrier $E_{\text{ext}}^{\text{barrier}}$. We use sufficiently sharp and high barrier potentials to write that $E_{\text{ext}}^{\text{barrier}} \approx 0$ because there are (almost) no electrons where there is a potential barrier. The other contributions $E_{\text{ext}}^{\text{ion}}$ and $E_{\text{ext}}^{\text{gate}}$ are non-zero, but we have no further modifications to make as soon as $\bar{V}_{\text{ext}}$ is defined.

The Hartree energy is easily written in reciprocal space as:

$$E_{\text{H}} = \frac{\Omega}{2} \sum_{\mathbf{G}} n^*(\mathbf{G}) \bar{V}_{\text{H}}(\mathbf{G}), \tag{5.3.14}$$

and is computed in practice by replacing $\bar{V}_{\text{H}}(\mathbf{G})$ by its expression (Eq. (5.3.10)):

$$E_{\text{H}} = \frac{\Omega}{2} \sum_{\mathbf{G}} |n(\mathbf{G})|^2 \bar{v}_c(\mathbf{G}). \tag{5.3.15}$$

The ion-ion interaction energy $E_{\text{i-i}}$ is computed using the ion-ion interaction potential $\bar{\Phi}$. The computation is based on the Ewald summation technique [85], which involves a separation into SR and LR parts $E_{\text{i-i}} = E_{\text{i-i}}^{\text{SR}} + E_{\text{i-i}}^{\text{LR}}$. Much like for the ionic potential, we do not need to modify the SR part. Here again, we start by presenting what is done in the original code, identify what we must modify, then present the implementation of the cutoff.

In the original 3D code, the ion-ion interaction potential Φ is separated in SR and LR part as follows:

$$\Phi(\mathbf{r}) = \Phi^{\text{SR}}(\mathbf{r}) + \Phi^{\text{LR}}(\mathbf{r}) - \Phi^{\text{self}} \tag{5.3.16}$$

$$\begin{aligned} &= {\sum_{\mathbf{R}'}}' \sum_{a'} \frac{e^2 Z_{a'}}{|\mathbf{r} - \mathbf{R}' - \mathbf{d}_{a'}|} \text{erfc}(\sqrt{\eta}|\mathbf{r} - \mathbf{R}' - \mathbf{d}_{\text{a}'}|) \\ &\quad + \sum_{\mathbf{R}'} \sum_{a'} \frac{e^2 Z_{a'}}{|\mathbf{r} - \mathbf{R}' - \mathbf{d}_{a'}|} \text{erf}(\sqrt{\eta}|\mathbf{r} - \mathbf{R}' - \mathbf{d}_{\text{a}'}|) - \Phi^{\text{self}}, \end{aligned} \tag{5.3.17}$$

where the prime in the first sum excludes the case $\{\mathbf{R}' = \mathbf{R}, a' = a\}$ if $\mathbf{r} = \mathbf{R} + \mathbf{d}_a$ and Φ^{self} subtracts that term from the second sum. The constant η tunes the SR/LR separation. The SR part of the ion-ion interaction potential Φ^{SR} is dealt with in real space and does not need to be modified as long as $\text{erf}(\sqrt{\eta} l_z) \approx 1$ (easily satisfied). Φ^{self} is simply the value of $\Phi^{\text{LR}}(\mathbf{r})$ for $\mathbf{r} - \mathbf{R}' - \mathbf{d}_{a'} = \mathbf{0}$. As such Φ^{self} is also short-range. We include the corresponding energy contributions in $E_{\text{i-i}}^{\text{SR}}$. Those contributions do not need to be cut off. The contribution of the LR potential Φ^{LR} to the energy is computed in reciprocal space and needs to be be modified.

In our implementation, we replace the Fourier transform of the LR part of the ion-ion interaction potential by its cutoff version:

$$\bar{\Phi}^{\text{LR}}(\mathbf{G}) = \frac{1}{\Omega} \sum_a Z_a e^{i\mathbf{G}\cdot\mathbf{d}_a} \bar{v}_c(\mathbf{G}) e^{-|\mathbf{G}|^2/4\eta}. \tag{5.3.18}$$

The LR contribution to the ion-ion interaction energy is then computed in reciprocal space as follows:

$$E_{\text{i-i}}^{\text{LR}} = \frac{\Omega}{2} \sum_{\mathbf{G}} n_{\text{ion}}^*(\mathbf{G}) \bar{\Phi}^{\text{LR}}(\mathbf{G}) = \frac{1}{2\Omega} \sum_{\mathbf{G}} \left| \sum_a Z_a e^{i\mathbf{G}\cdot\mathbf{d}_a} \right|^2 \bar{v}_c(\mathbf{G}) e^{-|\mathbf{G}|^2/4\eta}, \tag{5.3.19}$$

where $n_{\text{ion}}(\mathbf{G}) = \frac{1}{\Omega} \sum_a Z_a e^{i\mathbf{G}\cdot\mathbf{d}_a}$ is the Fourier transform of the distribution of ions ($\varrho_{\text{ion}} = e n_{\text{ion}}$).

The other energies to account for are the energy of the ions in the potential of the gate $E_{\text{g-i}}$, and the self interaction of the gate $E_{\text{g-g}}$.

$$E_{\text{g-i}} = \int_\Omega d\mathbf{r}\ n_{\text{ion}}(\mathbf{r})(-\bar{V}_{\text{gate}}(\mathbf{r})) = \sum_a Z_a 2\pi e^2 n_{\text{dop}} \left(-|d_{a,z} - z_{\text{g}}| + \frac{l_z}{2} \right) \tag{5.3.20}$$

$$E_{\text{g-g}} = \frac{1}{2} \int_\Omega d\mathbf{r}\ n_{\text{dop}} \delta(z - z_{\text{g}})(-\bar{V}_{\text{gate}}(z)) = n_{dop}^2 \pi e^2 l_z, \tag{5.3.21}$$

where $d_{a,z}$ is the z-component of $\mathbf{d}_a$. Note that those contributions to the energy have a manifest dependency on the cutoff distance l_z. The total energy, of course, should not depend on l_z. As detailed in App. D, the l_z-dependent terms in the expression above will cancel with corresponding terms in E_{ext} and E_{H}.

Verifications. In the absence of doping, gate and barrier, the total energy is:

$$E_{\text{tot}}^{\text{neutral}} = E_{\text{kin}} + E_{\text{ext}}^{\text{ion}} + E_{\text{H}} + E_{\text{XC}} + E_{\text{i-i}}. \tag{5.3.22}$$

We can thus check the consistency of the implementation of $E_{\text{ext}}^{\text{ion}}$, E_{H} and $E_{\text{i-i}}$ in a neutral system. We first compute the total energy of the neutral, non-polar system of Fig. 5.5 with and without cutoff. We should obtain the same result as there is no issue with the periodic images in that case. We checked that the difference is below numerical precision. We can then use a neutral system with an out-of-plane dipolar moment such that interlayer interactions do play a role without the 2D Coulomb cutoff. We use graphene with hydrogen atoms on top of half of the carbon atoms, see Fig. 5.8. The effect of the Coulomb cutoff is clear on both the KS potential and total energy. The KS potential of the system without cutoff illustrates the comments of Sec. 5.2. Namely, imposing 3D PBC leads to the compensation of the out-of-plane

dipolar moment by an external electric field, visible here via the finite slope of the KS potential away from the material. When we use the 2D Coulomb cutoff, we observe the right behavior, with a potential shift and no external electric field. The energy of the system simulated without cutoff tends to the one with cutoff at large interlayer distances. With the cutoff, the energy is independent of interlayer distance. There is a lower limit to the interlayer distance, which is when the boundaries of the physical region are too close to the material. Still, the minimal distance we can use in our implementation of the code is negligible with respect to what we would have to use without cutoff. A way to get the right total energy in this kind of polar material is to simulate the mirror image of the system within the unit cell. In that case, we obtained the same energy as with the use of the 2D Coulomb cutoff. The advantage of the Coulomb cutoff, in that case, is a drastic reduction of the computational cost.

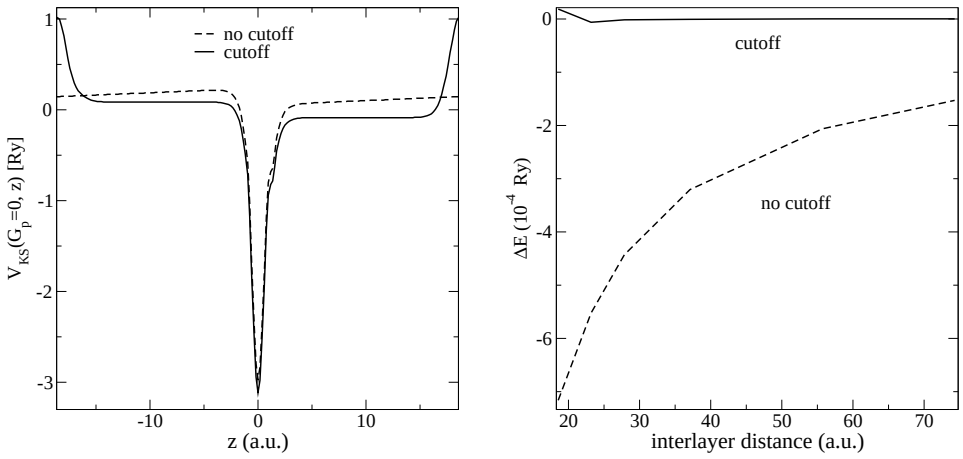

Figure 5.8: DFT simulation of graphene with hydrogen atoms on top ($z > 0$) of half the carbon atoms. On the left is the planar-averaged KS potential, with and without using the 2D Coulomb cutoff. On the right is the total energy per unit cell as a function of the interlayer distance, with and without using the 2D Coulomb cutoff. The zero for the energies corresponds to the total energy per unit cell obtained with cutoff.

5.3.3 Forces

The forces on the ions are found by computing the derivative of the total energy with respect to a displacement $\mathbf{u}_{a,i}$ of atom a in direction i. Only the terms related to an interaction in which the ions are involved remain. The force acting on ion a in direction i is written:

$$\mathbf{F}_{a,i} = -\frac{\partial E_{\text{tot}}}{\partial \mathbf{u}_{a,i}} = -\int_{\Omega} n(\mathbf{r}) \frac{\partial \bar{V}_{\text{ion}}}{\partial \mathbf{u}_{a,i}} d\mathbf{r} - \frac{\partial E_{\text{i-i}}}{\partial \mathbf{u}_{a,i}} + \mathbf{F}_{a,i}^{\text{g-i}} + \mathbf{F}_{a,i}^{\text{b-i}}, \tag{5.3.23}$$

where the first term is the force on the ion from the electrons, the second is from the other ions, the third is from the gate and the last from the barrier. The notation $\frac{\partial}{\partial \mathbf{u}_{a,i}}$

implies taking the derivative at zero displacement $\mathbf{u}_{a,i} = 0$. All the quantities involved are known once the self-consistent calculation is completed. We will only detail the terms for which we need to apply the 2D Coulomb cutoff. The first term is calculated by computing the derivative of the ionic potential, separated in local and non-local parts. The derivative of the local part is found by using the Fourier transform of the pseudopotentials:

$$\frac{\partial \bar{V}_{\text{ion}}^{\text{loc}}(\mathbf{r})}{\partial \mathbf{u}_{a,i}} = -i \sum_{\mathbf{G}} \left(v_a^{\text{SR}}(\mathbf{G}) + \bar{v}_a^{\text{LR}}(\mathbf{G}) \right) G_i e^{-i\mathbf{G}\cdot\mathbf{d}_a} e^{i\mathbf{G}\cdot\mathbf{r}}. \tag{5.3.24}$$

The effect of the derivative in reciprocal space is basically to bring down a factor $-iG_i$ from the exponential. The corresponding force is then calculated in reciprocal space:

$$-\int_\Omega n(\mathbf{r}) \frac{\partial \bar{V}_{\text{ion}}^{\text{loc}}(\mathbf{r})}{\partial \mathbf{u}_{a,i}} d\mathbf{r} = i\Omega \sum_{\mathbf{G}} n^*(\mathbf{G}) \left(v_a^{\text{SR}}(\mathbf{G}) + \bar{v}_a^{\text{LR}}(\mathbf{G}) \right) G_i e^{-i\mathbf{G}\cdot\mathbf{d}_a}. \tag{5.3.25}$$

The gate and the barrier have indirect contributions to this term. Indeed, they have an effect on $n(\mathbf{r})$, via their presence in the self-consistent KS potential.

The second term in Eq. (5.3.23) is the force from the other ions. It is found by derivation of the ion-ion interaction energy. We only treat the LR contribution, because it is the only one that needs to be cut off:

$$-\frac{\partial E_{\text{i-i}}^{\text{LR}}}{\partial \mathbf{u}_{a,i}} = -\frac{\partial}{\partial \mathbf{u}_{a,i}} \left(\frac{\Omega}{2} \sum_{\mathbf{G}} n_{\text{ion}}^*(\mathbf{G}) \bar{\Phi}^{\text{LR}}(\mathbf{G}) \right) \tag{5.3.26}$$

$$= -\frac{1}{\Omega} \sum_{\mathbf{G}} \bar{v}_c(\mathbf{G}) e^{-|\mathbf{G}|^2/4\eta} Z_a G_i \sum_{a'} Z_{a'} \sin(\mathbf{d}_{a'} - \mathbf{d}_a). \tag{5.3.27}$$

The third term is the direct contribution of the electrostatic force applied by the gate to the ions. Depending on doping, it can be repulsive or attractive:

$$\mathbf{F}_{a,i}^{\text{g-i}} = -\frac{\partial E_{\text{g-i}}}{\partial \mathbf{u}_{a,i}} = +Z_a 2\pi e^2 n_{dop} \text{ sign}(d_{a,z} - z_{\text{g}}). \tag{5.3.28}$$

The barrier applies no direct force on the ions $\mathbf{F}_{a,i}^{\text{b-i}} = \mathbf{0}$. The ions effectively never see the barrier potential (they could if the barrier was smoother). However, the barrier can act on the ground-state electronic density $n(\mathbf{r})$ which in turn acts on the ions. For example, if the system is too close from the barrier, the repulsive effect of the barrier will show in the self-consistent cycles, shifting the electrons away from the barrier. The first term in Eq. (5.3.23) will thus include a force that tends to push the ions away from the barrier, with the electrons. The barrier is then essential to relax the forces, arriving at an equilibrium between the attraction from the gate and repulsion from the barrier. This is represented in Fig. 5.9. For large material-barrier distances, the force tends to the attraction from the gate, and the total energy is linear. In that case, we have checked that the total force on the ions is the force between two charged plates, Eq. (5.1.17).

$$\sum_a \mathbf{F}_{a,z} = S \times 2\pi e^2 n_{dop}^2 \text{ sign}(z_{\text{g}}). \tag{5.3.29}$$

For small material-barrier distances, as the system gets too close to the barrier, there is a sharper increase of the force and the total energy.

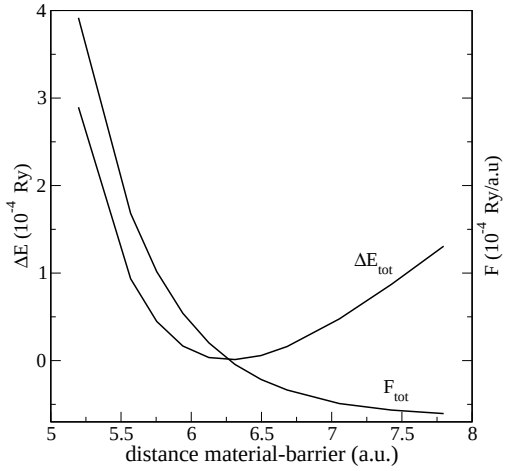

Figure 5.9: Total energy (variation from relaxed position) and forces as a function of the distance between the barrier and the 2D material. The gate is moved with the barrier $z_{\rm g} = z_{\rm b1} - 0.02c$ where c is the interlayer distance $c \approx 37$ a.u. The position of the second barrier is such that it covers the unphysical region $z_{\rm b2} = z_{\rm g} + 0.5c$. The 2D material is graphene doped at a Fermi level of +0.5 eV. The relaxed material-barrier distance is found to be around 6.26 a.u.

5.3.4 Phonons and EPC

To calculate the phonon dispersion and electron-phonon interactions, as shown in App. A, we need to calculate the response of the electronic density to a phonon perturbation. In essence, the linear response of the system involves derivatives of the previous potentials and energies. Once the previous framework is set up, we just have to apply the Coulomb cutoff to the derivatives consistently.

Dynamical matrix

In practice, the dynamical matrix is given by the following integrals on the unit cell:

$$\begin{aligned}\mathcal{D}_{a,i,a',j} \times \sqrt{M_a M_{a'}} = &\int_\Omega d\mathbf{r} \frac{\partial^2 \bar{V}_{\rm ion}(\mathbf{r})}{\partial \mathbf{u}_{a,i}(\mathbf{q}) \partial \mathbf{u}_{a',j}(\mathbf{q})} n(\mathbf{r}) \\ &+ \int_\Omega d\mathbf{r} \left(\frac{\partial \bar{\mathcal{V}}_{\rm ion}(\mathbf{r})}{\partial \mathbf{u}_{a,i}(\mathbf{q})} \right)^* \left(\frac{\partial n(\mathbf{r})}{\partial \mathbf{u}_{a',j}(\mathbf{q})} e^{-i\mathbf{q}\cdot\mathbf{r}} \right) \\ &+ \mathcal{D}^{\rm i-i}_{a,i,a',j}\end{aligned} \tag{5.3.30}$$

The first term can readily be computed from the quantities obtained in the ground-state calculation. It is computed in reciprocal space as:

$$\begin{aligned}&\int_\Omega d\mathbf{r} \frac{\partial^2 \bar{V}^{\rm loc}_{\rm ion}(\mathbf{r})}{\partial \mathbf{u}_{a,i}(\mathbf{q}) \partial \mathbf{u}_{a',j}(\mathbf{q})} n(\mathbf{r}) = \\ &\quad - \delta_{a,a'} \Omega \sum_{\mathbf{G}} \left(v^{\rm SR}_a(\mathbf{q}+\mathbf{G}) + \bar{v}^{\rm LR}_a(\mathbf{q}+\mathbf{G}) \right) G_i G_j \Re \left(n^*(\mathbf{G}) e^{-i\mathbf{G}\cdot\mathbf{d}_a} \right).\end{aligned} \tag{5.3.31}$$

where $\Re(x)$ gives the real part of x.

The last term comes from the second derivative of the ion-ion interaction $E_{\text{i-i}}$ with respect to a phonon displacement. The contribution from $E_{\text{i-i}}^{\text{SR}}$ does not change. The LR part $E_{\text{i-i}}^{\text{LR}}$ yields the following contribution to the dynamical matrix:

$$\begin{aligned}\mathcal{D}_{a,i,a',j}^{\text{i-i,LR}} =& \frac{1}{\Omega} \sum_{\mathbf{G},\mathbf{q}+\mathbf{G}\neq 0} \bar{v}_c(\mathbf{q}+\mathbf{G}) e^{-|\mathbf{q}+\mathbf{G}|^2/4\eta} Z_a Z_{a'} (\mathbf{q}+\mathbf{G})_i (\mathbf{q}+\mathbf{G})_j e^{i(\mathbf{q}+\mathbf{G})\cdot(\mathbf{d}_a - \mathbf{d}_{a'})} \\ & - \frac{1}{\Omega} \sum_{\mathbf{G}\neq 0} \bar{v}_c(\mathbf{G}) e^{-|\mathbf{G}|^2/4\eta} Z_a \mathbf{G}_i \mathbf{G}_j \left(\sum_{a''} Z_{a''} \cos(\mathbf{G}(\mathbf{d}_a - \mathbf{d}_{a''})) \right) \delta_{a,a'}.\end{aligned} \tag{5.3.32}$$

The second term is computed as expressed in Eq. (5.3.30), that is, via numerical integration over the unit cell in real space. The quantities inside the integral are computed during the calculation of the electronic density response to the perturbed KS potential, presented in the following.

Perturbed KS potential

The linear electronic density response is found by solving a self-consistent system involving the effective perturbation, that is the derivative of the KS potential with respect to a phonon displacement $\frac{\partial \bar{\mathcal{V}}_{\text{KS}}(\mathbf{r}_p,z)}{\partial \mathbf{u}_{a,i}(\mathbf{q})}$, Eq. (A.2.7) (the notation "$\bar{\mathcal{V}}$" indicates lattice periodic functions, see App. A). The first term is the perturbation of the external potential. The phonons only bring a direct perturbation to the potentials in which the ions are involved. This means the perturbed external potential contains only the contribution from the ionic potential. The Fourier transform of the derivative of the local part of the ionic potential has non-zero components at wave vectors $\mathbf{q}+\mathbf{G}$:

$$\frac{\partial \bar{\mathcal{V}}_{\text{ion}}^{\text{loc}}(\mathbf{q}+\mathbf{G})}{\partial \mathbf{u}_{a,i}(\mathbf{q})} = -i \left(v_a^{\text{SR}}(\mathbf{q}+\mathbf{G}) + \bar{v}_a^{\text{LR}}(\mathbf{q}+\mathbf{G}) \right) (\mathbf{q}+\mathbf{G})_i e^{-i(\mathbf{q}+\mathbf{G})\cdot\mathbf{d}_a}, \tag{5.3.33}$$

where the Fourier components of the long-range part of the local pseudopotential are similar to Eq. (5.3.8):

$$\bar{v}_a^{\text{LR}}(\mathbf{q}+\mathbf{G}) = -\frac{Z_s}{\Omega} \bar{v}_c(\mathbf{q}+\mathbf{G}) e^{-|\mathbf{q}+\mathbf{G}|^2/4}. \tag{5.3.34}$$

The perturbed ionic potential of Eq. (5.3.33) (along with the non-local part that is computed as in the original 3D code), is Fourier transformed and inserted in the second term of the dynamical matrix Eq. (5.3.30).

The remaining long-range potential to cut off is the Hartree potential generated by the density response, computed in reciprocal space:

$$\frac{\partial \bar{\mathcal{V}}_{\text{H}}(\mathbf{q}+\mathbf{G})}{\partial \mathbf{u}_{a,i}(\mathbf{q})} = \bar{v}_c(\mathbf{q}+\mathbf{G}) \frac{\partial n(\mathbf{q}+\mathbf{G})}{\partial \mathbf{u}_{a,i}(\mathbf{q})}. \tag{5.3.35}$$

The density response, solution of the self-consistent system corresponding to the effective perturbation $\frac{\partial \mathcal{V}_{\text{KS}}(\mathbf{r}_p,z)}{\partial \mathbf{u}_{a,i}(\mathbf{q})}$ is inserted in the second term of the dynamical matrix Eq. (5.3.30).

EPC

We already have all the quantities to calculate the EPC.

$$g_{\mathbf{k}+\mathbf{q},s,\mathbf{k},s',\nu} = \sum_{a,i} \mathbf{e}^{a,i}_{\mathbf{q},\nu} \sqrt{\frac{\hbar}{2M_a\omega_{\mathbf{q},\nu}}} \langle \mathbf{k}+\mathbf{q},s| \frac{\partial \bar{\mathcal{V}}_{\mathrm{KS}}(\mathbf{r})}{\partial \mathbf{u}_{a,i}(\mathbf{q})} |\mathbf{k},s'\rangle. \tag{5.3.36}$$

Those EPC matrix elements can be screened via the induced part of the effective KS perturbation (Hartree and exchange-correlation). The Hartree part of the screening is then that of a 2D material. The gate and the barrier have no direct effect in the KS perturbation. Note that they are absent from this section. However, they broke the symmetry of the ground-state. In particular, the electronic distribution is not centered on the ions' plane anymore. We will study the consequences of their presence in the following section.

5.4 Results in graphene

In this section we present some results demonstrating that our implementation of the 2D Coulomb cutoff is operational. We will show that the predicted peculiarities of the FET setup can indeed be simulated. We perform calculations for graphene doped in the FET setup. The following results can be described as preliminary from the point of view of applications. Presently, some work remains to be done to determine with more confidence the setup that should be used for comparison with experiment. With the ability to simulate the FET comes many new degrees of freedom, the most influential probably being the barriers. As will be shown, the presence of one or two barriers, their nature and their positions play an important role. As of yet, we have not determined the right method to choose the corresponding parameters. This section should thus be considered as a demonstration of principle and a first estimation rather than a attempt to reproduce experimental data. We will show that we now have all the tools to model an experimental FET setup.

We first show that we can simulate the finite frequency of the ZA phonons at $\mathbf{\Gamma}$. We then simulate the screened deformation potential of graphene in the FET setup. Finally, we show the emergence of a non-zero linear coupling with ZA phonons.

5.4.1 Finite frequency for ZA phonons at $\mathbf{\Gamma}$

We would like to be able to simulate the emergence of a finite ZA phonon frequency at $\mathbf{\Gamma}$ when graphene is enclosed between two barriers. We use a setup in which this finite frequency would be important. We put the graphene sheet between two barriers separated by a relatively small distance of ≈ 9.2 Å. Roughly, this is twice the experimental distance between graphene and a SiO_2 substrate. However, the equilibrium distances between graphene and the substrate or the dielectric depend on the details of the interactions between those materials. It is possible to simulate the main consequences of the presence of a substrate and dielectric with potential barriers. However, the distance between graphene and the barriers on the one hand and between graphene and its substrate/dielectric on the other hand might very well be different. The choice of the graphene-barrier distance is thus rather arbitrary.

We plot the KS potential, total energy per unit cell, and out-of-plane forces on the atoms of the unit cell in the upper panel of Fig. ∗.9. The barriers are placed at z_{b1} and $z_{b2} = -z_{b1}$, such that $z_{b2} - z_{b1} \approx 9.2$ Å. As the graphene sheet is displaced between the two barriers, the total energy presents a minimum. This minimum occurs when the ions are at a position that is slightly closer to the barrier on the opposite side of the gate. This suggest a strong effect of the barriers on the electrons. Since the barriers are relatively close to each other, they force the electron density to be in between them, and the effect of the gate is negligible. Indeed, since we are considering electron-doping here, the electrons should be attracted by the gate and thus shifted left. But the barriers are so close to each other that the electronic density is forced to be essentially centered around $z = 0$. The ions are not subject to any direct force from the barriers, but they are attracted by the electrons toward the middle, and slightly repulsed by the positively charged gate. This is why they end up shifted slightly to the right. Around its minimum, the energy is approximately quadratic. The force is then linear. We have numerically checked the corresponding relation:

$$\sum_a \mathbf{F}_{a,i} = \frac{\partial E_{\text{tot}}}{\partial z_{\text{ions}}}. \tag{5.4.1}$$

We then calculate the phonons in this system and get the dispersion in the lower panel of Fig. ∗.9 for the acoustic phonons at small momenta. The dispersion of the in-plane modes is essentially unaffected by the cutoff or the presence of the gate and barriers. For neutral graphene (without gate or barriers), the use of the 2D Coulomb cutoff seems to induce a slight increase of the ZA frequencies. However, numerical accuracy for such small momenta and energies is of the order of the disagreement between the two dispersions. In contrast, the large shift in the dispersion of the ZA phonons in the double barrier setup cannot be attributed to numerical errors. We observe in this case a rather flat dispersion, with $\omega(\mathbf{\Gamma}) \approx 2.0905$ THz, ≈ 70 cm^{-1}. This value is consistent with the derivatives of the total energy and forces.

$$\omega^2_{\mathbf{\Gamma},ZA} = \frac{1}{2M}\frac{\partial^2 E_{\text{tot}}}{\partial z^2_{\text{ions}}} \tag{5.4.2}$$

$$= \frac{1}{2M}\sum_a \frac{\partial \mathbf{F}_{\text{a,z}}}{\partial \mathbf{u}_{a,z}}. \tag{5.4.3}$$

5.4.2 Screening

We discuss here the screening of the deformation potential. We have seen that the original 3D code leads to some spurious screening from the periodic images for the 3D deformation potential $\alpha^{\text{3D}}(q)$. We have calculated the bare deformation potential with the static-strain method. We have managed to simulate the response of an isolated 2D graphene sheet to a single wavelength perturbing potential in chapter 4. From this we have inferred the static dielectric function of graphene $\epsilon_{2D}(q)$. This provided us with an estimation of the screened deformation potential via the relation $\frac{\alpha^{\text{bare}}}{\epsilon_{2D}(q)}$.

We are now in a position to compute directly the screened deformation potential of single layer graphene doped in the FET setup, $\alpha^{\text{2D}}(q)$. We compare the results of this

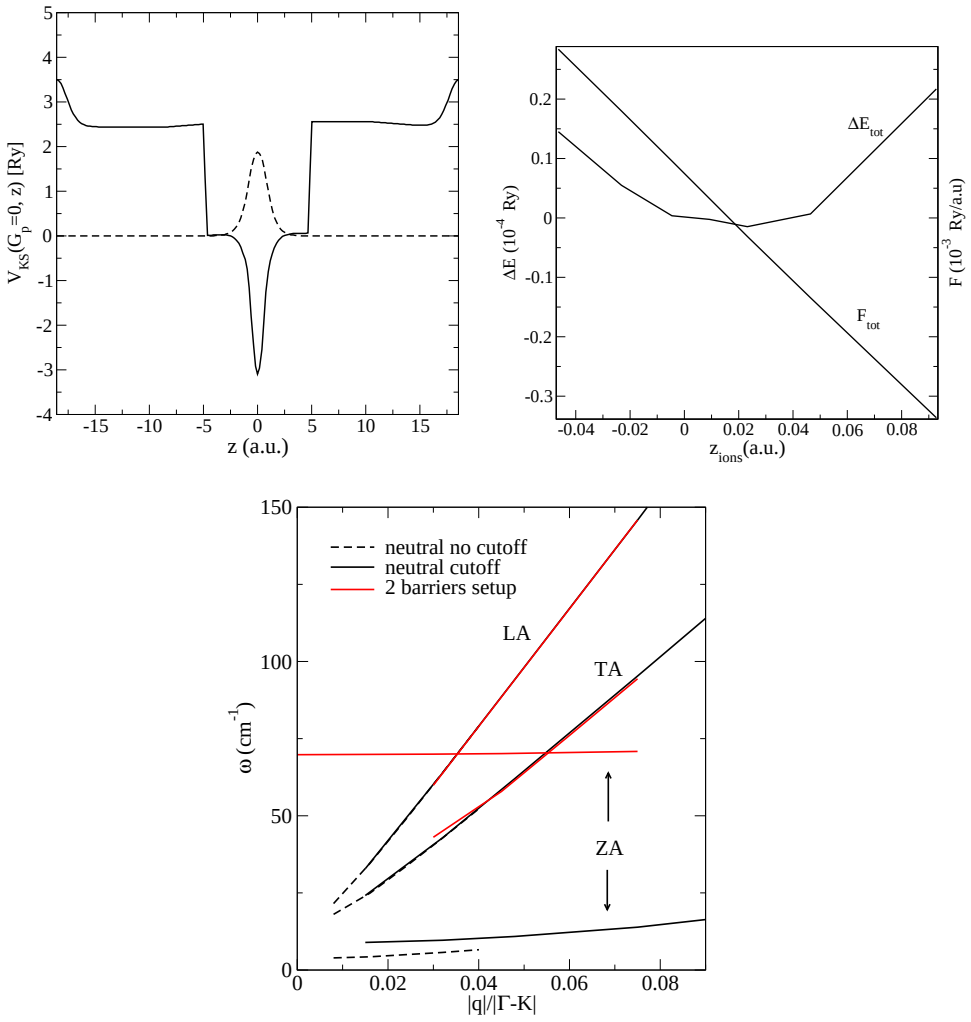

Figure 5.10: On the top left is the KS potential of the simulated system. The dashed line represents the electronic density, in arbitrary units. The 2D material is graphene doped at a Fermi level of 0.5 eV. On the top right are the corresonding total energy (variation from relaxed position) and force as a function of the position of graphene between the two barriers. Below is the dispersion of the acoustic phonons of graphene in the FET setup, enclosed between two potential barriers. For comparison, we added the dispersions in the case of neutral graphene calculated with or without the Coulomb cutoff.

method to the values of $\frac{\alpha^{\text{bare}}}{\epsilon_{2D}(q)}$ in Fig. 5.11, and observe a significant difference. There are several possible sources for this discrepancy. When we computed $\epsilon_{2D}(q)$ in chapter 4, we used a simple single-wavelength perturbing potential, adequate for the definition of $\epsilon_{2D}(q)$. Assuming that $\alpha(q) = \frac{\alpha^{\text{bare}}}{\epsilon_{2D}(q)}$ then amounts to consider that the deformation potential contribution to the phonon perturbation is equivalent to a single-wavelength

perturbing potential. In truth, the phonon perturbation is more complicated. In particular, for a phonon of momentum $\mathbf{q}$, it has local fields components at $\mathbf{q}+\mathbf{G}$. We don't know how important those local fields components are and how they would be screened. Also, we computed the value of the bare perturbation potential with the static strain method, that is at $\mathbf{q}=\mathbf{0}$. Assuming $\alpha(q)=\frac{\alpha^{\text{bare}}}{\epsilon_{2D}(q)}$ implies using this same constant at finite $\mathbf{q}$. It is possible that the bare perturbation in itself includes a dependency on $\mathbf{q}$. Finally, the presence of an out-of-plane electric field could have an influence on the bare deformation potential. In light of those remarks, it is not so

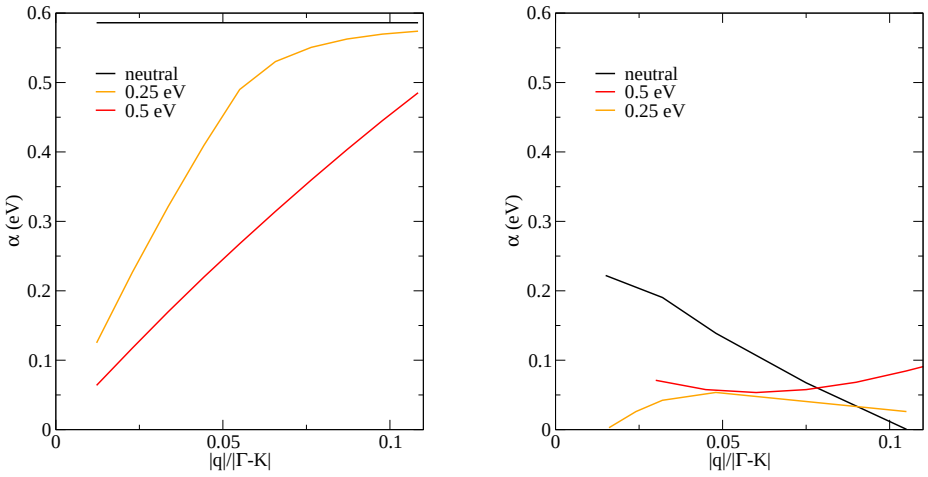

Figure 5.11: On the left, the screened deformation potential is calculated as $\frac{\alpha^{\text{bare}}}{\epsilon_{2D}(q)}$ where $\epsilon_{2D}(q)$ is the analytical expression of the screening function of graphene studied in the previous chapter. On the right, the screened deformation potential of graphene in the FET setup is computed directly in DFPT using our implementation of the 2D Coulomb cutoff. This is done for several doping levels ε_F (0, 0.25 and 0.5 eV).

surprising that $\alpha^{\text{2D}}(q)\neq\frac{\alpha^{\text{bare}}}{\epsilon_{2D}(q)}$. Presently, we have not investigated the discrepancy further. An idea for further investigation would be to disable the screening of the phonon perturbation to study the bare deformation potential at finite $\mathbf{q}$. Another idea would be to manipulate the phonon perturbation and study the effects of its $\mathbf{q}+\mathbf{G}$ components. Those are interesting leads to pursue in general. However, a common feature of all the results for the screened deformation potential in graphene is that it is quite small and negligible in comparison with the gauge field [3]. For now, we will settle for this conclusion. Investigating the screening of the deformation potential further does not seem essential for graphene applications. It would be more interesting to investigate in a different material, where a deformation potential would dominate the EPC. Another interesting phenomenon to study in graphene is the coupling between electrons and remote phonons from the substrate. Since screening plays an crucial role in this interaction, it is essential to be able to eliminate interactions between periodic images. Those simulations are feasible with the implementation presented here, since we can simulate a 2D material consisting of graphene and a few layers of substrate

[3] We have checked that the gauge field is unchanged by the 2D Coulomb cutoff.

(h-BN for example). Overall, there are many interesting calculations left to do. For now, we finish this chapter with the coupling of electrons to ZA phonons in graphene.

5.4.3 Finite coupling to out-of-plane phonons

We now wish to demonstrate the emergence of a finite coupling to linear order of the electrons with the out-of-plane acoustic phonons. For this we use the minimal setup that makes sense from the point of view of DFT simulations. Namely, we use a gate and a single barrier on the same side to relax the forces in the out-of-plane direction. In practice, there is a second potential barrier on the other side at the limit of the physical region, but it is far enough from the system to be ignored. Graphene is doped at a Fermi level of $\varepsilon_F = 0.5$ eV. We obtain the results of Fig. 5.12. Those g^2_{ZA} values

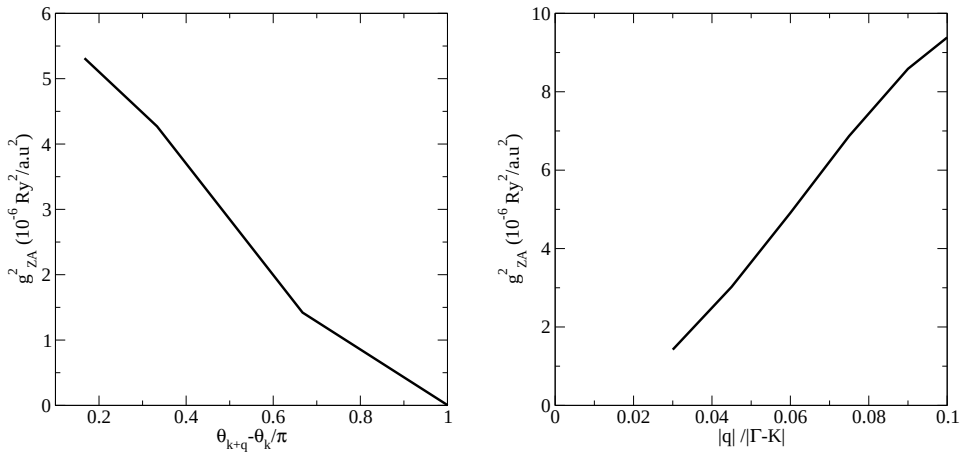

Figure 5.12: Emergence of a non-zero value of EPC matrix elements $g^2_{\mathrm{ZA}} \equiv g^2_{\mathbf{k}+\mathbf{q},\pi,\mathbf{k},\pi,\mathrm{ZA}}$ for the ZA phonons in graphene.

are small in comparison with the gauge field. The coupling with the ZA phonons is of the order of the screened deformation potential. As simulated here, the contribution of the ZA phonons to the scattering would then be negligible. However, in different gate/barrier setups, it might be much more significant. The important advance here is that the coupling is not zero. With the original 3D code, in the case of neutral or "jellium-doped" graphene, g^2_{ZA} is numerical noise, with values of the order of 10^{-26} $\mathrm{Ry}^2\mathrm{a.u.}^{-2}$. Here, values of the order of 10^{-6} $\mathrm{Ry}^2\mathrm{a.u.}^{-2}$ and the general angular and $|\mathbf{q}|$ dependency of g^2_{ZA} clearly indicate that we are getting more than numerical noise. The 2D Coulomb cutoff thus enables the simulation of the coupling to linear order to ZA phonons in graphene. Still, this first estimation of the coupling seems to indicate that it can be neglected in graphene. Similar conclusions can be drawn concerning the coupling to out-of-plane optical phonons ZO.

Summary

- 3D PBC are not adequate for 2D materials in the FET setup.
- 2D Coulomb cutoff enables the simulation of the FET setup.
- 2D Coulomb cutoff implemented in QE for energy, forces, phonons and EPC.
- Emergence of finite $\omega_{\mathbf{\Gamma},ZA}$ with two barriers.
- Screened deformation potential in the FET setup stays negligible.
- Emergence of a finite yet negligible linear coupling with ZA/ZO phonons.

Chapter 6

Solution to Boltzmann equation for phonon-limited resistivity in graphene

We conclude the thesis with the application of our EPC model to the phonon-limited resistivity of graphene. Given the general enthusiasm concerning the use of graphene in prospective electronic devices, accurate models and precise understanding of its transport properties are essential. Intrinsic contributions to resistivity are of particular interest because they set an ideal limit for technological improvements to reach. As the fabrication methods improve, intrinsic contributions begin to dominate the temperature dependence of transport measurements [86, 87]. The measured resistivity can now be compared with numerical approaches to the intrinsic resistivity.

The dominant contribution to the intrinsic resistivity of graphene comes from phonons. Some partial (i.e. including only a restricted set of phonon modes) transport models were developed analytically [88, 89] to predict the qualitative behavior of acoustic phonon scattering below room-temperature. The low-temperature $\propto T^4$ behavior was theoretically predicted [24, 89] and experimentally verified [87], as was the linear behavior in the equipartition regime. Those behaviors are interesting expressions of the unique Dirac Cone structure of graphene and the peculiarity of electron and phonon dynamics in 2D. Around room-temperature, a remarkable change of behavior in the temperature-dependent resistivity indicates a strong contribution from a scattering source other than acoustic phonons, often attributed to remote optical phonons from the substrate [86].

In those models, the calculated resistivity fell well below experiments, due to a lack of completeness and consistency of the EPC and transport models. Preliminary to the model presented in this chapter, we participated in the developments of Ref. [28]. In this work, it was shown that by calculating the resistivity in the framework of the Allen model [90] and including estimations of EPC parameters at the GW level [23], a better agreement with experiments could be achieved in the low temperature ($T < 270$ K), high doping regime where acoustic phonon scattering dominates. We also noticed a surprisingly important contribution of intrinsic optical phonons around room temperature. Although their energy is much higher than thermal energy, we found that

their coupling to electrons is much stronger than that of acoustic phonons. This called for further investigation of this contribution at higher temperatures ($T > 270$ K).

In order to model transport correctly at higher temperatures, we go one step beyond in the transport model. We overcome the approximations involved in the Allen model by solving directly the Boltzmann equation with full inclusion of acoustic and optical phonon modes. Furthermore we compare our numerical results to experimental data in a larger range of temperatures and electron densities. Finally, we detail the derivation of approximated solutions to the Boltzmann equation and check their validity against the full solution.

6.1 Boltzmann transport theory

In this section we present a numerical solution to the Boltzmann transport equation for phonon-limited transport in graphene. The general method presented here is well known in carrier transport theory and has been applied to some extent to graphene [26, 88, 91, 92, 89, 93]. The central addition to those previous works resides in the treatment of a more complete EPC model, and a numerical solution involving very few approximations. The initial steps are repeated in an effort to clarify the assumptions involved.

A carrier current is created by applying an in-plane electric field $\mathbf{E}$. This has the effect of changing the electronic distribution $f(\mathbf{k})$. The notation of the latter has slightly changed because here, contrary to the rest of the thesis, the occupation of a state depends on both its energy and the direction of the associated momentum $\mathbf{k}$. In the steady state regime, the new distribution favors states with electron momenta in the opposite direction of the electric field, thus creating a net current $\mathbf{j}$. We are interested in the current in the direction of the electric field that we choose to be the $\mathbf{x}$-axis, used as a reference for angles in our model. This is simply a practical choice, the following results do not depend on it. Throughout this work, the resistivity is to be understood as the diagonal part of the resistivity tensor $\rho = \rho_{xx}$. It is given by [3]:

$$\frac{1}{\rho} = \frac{\mathbf{j}\cdot\mathbf{x}}{|\mathbf{E}|} = \frac{2e}{|\mathbf{E}|}\int_{BZ}\frac{d\mathbf{k}}{(2\pi)^2} f(\mathbf{k})\mathbf{v}(\mathbf{k})\cdot\mathbf{x} \tag{6.1.1}$$

The integral is made over the Brillouin zone with a factor 2 for spin degeneracy, e is the elementary charge, $\mathbf{v}(\mathbf{k})$ is the carrier velocity of state $|\mathbf{k}\rangle$, and $\mathbf{x}$ is the Cartesian coordinate basis vector. In the framework of linear response theory, we are interested in the response of $f(\mathbf{k})$ to the first order in electric field [94, 95, 96]. We study graphene moderately doped with electrons, such that we can consider only the π^* band ($s = 1$). Within the Dirac cone model, we assume $\varepsilon_{\mathbf{k}} = \hbar v_F|\mathbf{k}|$ and $\mathbf{v}(\mathbf{k}) = v_F\frac{\mathbf{k}}{|\mathbf{k}|}$. We then separate the norm and angular dependency of $\mathbf{k}$ in $f(\mathbf{k}) = f(\varepsilon_{\mathbf{k}}, \theta_{\mathbf{k}})$ and consider the first order expansion:

$$f(\varepsilon_{\mathbf{k}},\theta_{\mathbf{k}}) = f^{(0)}(\varepsilon_{\mathbf{k}}) + f^{(1)}(\varepsilon_{\mathbf{k}}, \theta_{\mathbf{k}}) \tag{6.1.2}$$

where $f^{(1)}$ is proportional to the electric field, and $f^{(0)}$ is the equilibrium Fermi-Dirac distribution, which has no angular dependency. Due to graphene symmetries, the two Dirac cones of the Brillouin zone give the same contribution to Eq. (6.1.1). Multiplying

by a factor 2 for valley degeneracy, performing the dot product, and using f, Eq. (6.1.1) becomes:

$$\frac{1}{\rho} = \frac{4e}{|\mathbf{E}|}\int_{\mathbf{K}} \frac{d\mathbf{k}}{(2\pi)^2} f^{(1)}(\varepsilon_{\mathbf{k}}, \theta_{\mathbf{k}}) v_F \cos(\theta_{\mathbf{k}}) \tag{6.1.3}$$

where the integral is now carried out within a circular region around $\mathbf{K}$. It is clear that the zeroth order term gives no contribution due to the angular integral, and that we have to look for $f^{(1)} \propto \cos(\theta_{\mathbf{k}})$.

We now use Boltzmann transport equation to obtain the energy dependency of $f^{(1)}$. A key quantity is the collision integral $\left(\frac{\partial f}{\partial t}\right)_{\text{coll}}(\mathbf{k})$ describing the rate of change in the occupation of the electronic state $|\mathbf{k}\rangle$ due to scattering. Assuming that the electronic distribution is spatially uniform, out-of-equilibrium but in steady state, the change of the occupation function triggered by the electric field must be compensated by the change due to collisions [3]:

$$-\frac{e\mathbf{E}}{\hbar}\cdot\frac{\partial f}{\partial \mathbf{k}} = \left(\frac{\partial f}{\partial t}\right)_{\text{coll}}(\mathbf{k}) \tag{6.1.4}$$

Using Fermi golden rule, the collision integral is:

$$\left(\frac{\partial f}{\partial t}\right)_{\text{coll}}(\mathbf{k}) = \sum_{\mathbf{k}'} \left\{P_{\mathbf{k}'\mathbf{k}} f(\mathbf{k}')(1-f(\mathbf{k})) - P_{\mathbf{k}\mathbf{k}'} f(\mathbf{k})(1-f(\mathbf{k}'))\right\} \tag{6.1.5}$$

Here, $\mathbf{k}$ belongs to a circular region around $\mathbf{K}$. The momentum of the scattered states $\mathbf{k}'$ is i) around $\mathbf{K}$ for intra-valley scattering modes; ii) around the other Dirac cone $\mathbf{K}'$ in case of inter-valley scattering. The quantity $P_{\mathbf{k}\mathbf{k}'}$ is the scattering probability from state $|\mathbf{k}\rangle$ to $|\mathbf{k}'\rangle$. It satisfies the detailed balance condition, namely:

$$P_{\mathbf{k}'\mathbf{k}} f^{(0)}(\varepsilon_{\mathbf{k}'})(1-f^{(0)}(\varepsilon_{\mathbf{k}})) = P_{\mathbf{k}\mathbf{k}'} f^{(0)}(\varepsilon_{\mathbf{k}})(1-f^{(0)}(\varepsilon_{\mathbf{k}'})) \tag{6.1.6}$$

The scattering probability $P_{\mathbf{k}\mathbf{k}'}$ is composed of two terms,

$$P_{\mathbf{k}\mathbf{k}'} = P_{\mathbf{k}\mathbf{k}',\text{I}} + \sum_{\nu} P_{\mathbf{k}\mathbf{k}',\nu} \tag{6.1.7}$$

where $P_{\mathbf{k}\mathbf{k}',\text{I}}$ is the impurity scattering probability and $P_{\mathbf{k}\mathbf{k}',\nu}$ is due to the electron-phonon scattering of the ν^{th} phonon branch.

In the Born approximation, the impurity scattering probability is

$$P_{\mathbf{k}\mathbf{k}',\text{I}} = \frac{2\pi}{\hbar}\frac{1}{N} n_i |\langle \mathbf{k}|H_i|\mathbf{k}'\rangle|^2 \delta(\varepsilon_{\mathbf{k}} - \varepsilon_{\mathbf{k}'}) \tag{6.1.8}$$

where H_i is the electron-impurity interaction Hamiltonian, n_i the impurity density and N is the number of unit cells. When needed for comparison with experiment, we use existing methods [93, 97, 98] to fit charged and short-range impurity densities on the low temperature resistivity measurements. The electron-phonon scattering probability is given by

$$\begin{aligned} P_{\mathbf{k},\mathbf{k}+\mathbf{q},\nu} = \frac{2\pi}{\hbar}\frac{1}{N}|g_{\mathbf{k}+\mathbf{q},\mathbf{k},\nu}|^2 \times \\ \left\{n_{q,\nu}\delta(\varepsilon_{\mathbf{k}+\mathbf{q}} - \varepsilon_{\mathbf{k}} - \hbar\omega_{\mathbf{q},\nu}) + (n_{q,\nu}+1)\delta(\varepsilon_{\mathbf{k}+\mathbf{q}} - \varepsilon_{\mathbf{k}} + \hbar\omega_{\mathbf{q},\nu})\right\} \end{aligned} \tag{6.1.9}$$

where $\mathbf{k}+\mathbf{q}=\mathbf{k}'$, $g_{\mathbf{k}+\mathbf{q},\mathbf{k},\nu}$ is the electron-phonon matrix element introduced in Eq. (2.2.5) and $n_{q,\nu}$ is the Bose-Einstein equilibrium occupation of mode ν with phonon-momentum $\mathbf{q}$ and phonon frequency $\omega_{\mathbf{q},\nu}$.

By Replacing Eq. (6.1.2) in Eq. (6.1.5), using Eq. (6.1.6) and keeping only first order terms we obtain

$$-\frac{e\mathbf{E}}{\hbar}\cdot\frac{\partial f}{\partial \mathbf{k}}=\sum_{\mathbf{k}'}P_{\mathbf{k}\mathbf{k}'}\frac{1-f^{(0)}(\varepsilon_{\mathbf{k}'})}{1-f^{(0)}(\varepsilon_{\mathbf{k}})}\Big(f^{(1)}(\varepsilon_{\mathbf{k}'},\theta_{\mathbf{k}'})\frac{f^{(0)}(\varepsilon_{\mathbf{k}})(1-f^{(0)}(\varepsilon_{\mathbf{k}}))}{f^{(0)}(\varepsilon_{\mathbf{k}'})(1-f^{(0)}(\varepsilon_{\mathbf{k}'}))}-f^{(1)}(\varepsilon_{\mathbf{k}},\theta_{\mathbf{k}})\Big) \tag{6.1.10}$$

We first consider the left-hand side of Eq. (6.1.10) and, looking for a solution that is first order in the electric field, we have:

$$-\frac{e\mathbf{E}}{\hbar}\cdot\frac{\partial f}{\partial \mathbf{k}}=-F\cos(\theta_{\mathbf{k}})\hbar v_F\frac{\partial f^{(0)}}{\partial\varepsilon}(\varepsilon_{\mathbf{k}}) \tag{6.1.11}$$

with $F=\frac{e|\mathbf{E}|}{\hbar}$. In the right-hand side of Eq. (6.1.10) we adopt [95] the following ansatz for $f^{(1)}(\varepsilon_{\mathbf{k}},\theta_{\mathbf{k}})$:

$$f^{(1)}(\varepsilon_{\mathbf{k}},\theta_{\mathbf{k}})=F\tau(\varepsilon_{\mathbf{k}})\cos(\theta_{\mathbf{k}})\hbar v_F\frac{\partial f^{(0)}}{\partial\varepsilon}(\varepsilon_{\mathbf{k}}) \tag{6.1.12}$$

and verify that it solves Eq. (6.1.10). We need to find $\tau(\varepsilon_{\mathbf{k}})$, which captures the energy dependency of $f^{(1)}$. This auxiliary variable has the dimension of time. The time $\tau(\varepsilon_{\mathbf{k}})$ depends on the perturbation and has a meaning only in the the framework studied here, namely the steady state of a distribution under an external electric field. It is different from the relaxation time from relaxation time approximation and from the scattering time as can be measured by angle resolved photoemission spectroscopy.

By replacing Eqs. (6.1.11) and (6.1.12) in Eq. (6.1.10) and dividing both members by $\cos(\theta_{\mathbf{k}})$ (we can ignore the case $\cos(\theta_{\mathbf{k}})=0$, for which everything is zero), we obtain the following equation, as in Refs. [94, 96, 95]:

$$1=\sum_{\mathbf{k}'}P_{\mathbf{k}\mathbf{k}'}\frac{1-f^{(0)}(\varepsilon_{\mathbf{k}'})}{1-f^{(0)}(\varepsilon_{\mathbf{k}})}\left(\tau(\varepsilon_{\mathbf{k}})-\tau(\varepsilon_{\mathbf{k}'})\frac{\cos(\theta_{\mathbf{k}'})}{\cos(\theta_{\mathbf{k}})}\right) \tag{6.1.13}$$

We then parametrize $\mathbf{k}$-space in energy (equivalent to norm through $\varepsilon=\hbar v_F|\mathbf{k}|$). On an energy grid of step $\Delta\varepsilon$, Eq. (6.1.13) can be written:

$$\sum_{\varepsilon'}\mathcal{M}_{\varepsilon,\varepsilon'}\tau(\varepsilon')=1 \tag{6.1.14}$$

where $\varepsilon=\hbar v_F|\mathbf{k}|$, $\varepsilon'=\hbar v_F|\mathbf{k}'|$ and the matrix $\mathcal{M}$ is defined in appendix E.1. The time τ can then be obtained by numerical inversion of the matrix $\mathcal{M}$ (see App. E.1 for more details).

It is worthwhile to recall that, due to the additivity of the scattering probabilities in Eq. (6.1.7), the matrix $\mathcal{M}$ involves a sum over impurities and different phonon branches, namely $\mathcal{M}=\mathcal{M}_{\mathrm{I}}+\sum_\nu\mathcal{M}_\nu$. Strictly speaking, the time τ is obtained from the inversion of the global matrix $\mathcal{M}$ and not from the sum of the inverse of the matrices $\mathcal{M}_\nu$ and $\mathcal{M}_{\mathrm{I}}$. The latter is equivalent to applying Matthiessen's rule, which is an approximation (see Sec. 6.4).

From the time τ we obtain the distribution function. Inserting it into Eq. (6.1.1), the electrical resistivity is found by evaluating the following integral numerically:

$$\frac{1}{\rho} = \frac{e^2 v_F^2}{2} \int d\varepsilon \mathrm{DOS}(\varepsilon)\tau(\varepsilon) \left(-\frac{\partial f^{(0)}}{\partial \varepsilon}(\varepsilon) \right) \tag{6.1.15}$$

Where $\mathrm{DOS}(\varepsilon_{\mathbf{k}}) = \frac{2|\varepsilon_{\mathbf{k}}|}{\pi(\hbar v_F)^2}$ is the total density of states per unit area of graphene, valley and spin degeneracy included.

6.2 EPC included in the transport model

To compute the intrinsic resistivity of graphene, we accounted for the following sources of scattering:

- impurities
- gauge field contribution of the acoustic in-plane phonons at $\mathbf{\Gamma}$ (β_A)
- Optical in-plane phonons at $\mathbf{\Gamma}$ (β_O)
- Optical in-plane mode at $\mathbf{K}$ (β_K)

For those contributions we use the EPC parameters evaluated within the GW approximation in Sec. 3.3.3. As will be discussed later, the contribution to the resistivity of each phonon mode is proportional to the squared ratio of the EPC parameter and the Fermi velocity. For the phonon modes at $\mathbf{\Gamma}$, the Fermi velocity renormalization is exactly compensated by the electron-phonon coupling renormalization. The GW corrections thus has no effect on their contributions resistivity. The A_1' mode, on the other hand, is renormalized more strongly than the Fermi velocity. Therefore, we have to choose relevant values of the renormalization for both the Fermi velocity and β_K. Given the experimental measurements of high-temperature resistivity available for comparison with our model, we will need a value of β_K only in a short range of doping close to neutrality ($0.12 \rightarrow 0.21$eV). In our resistivity simulations we will use the +46% renormalization of β_K obtained at neutrality by Ref. [35]. We then choose the corresponding +20% renormalization of the Fermi velocity, relevant at low doping. The coupling to phonons modes at $\mathbf{\Gamma}$ (β_A, β_O) are renormalized by +20%, as the Fermi velocity.

We neglect the coupling to out-of-plane phonons at $\mathbf{\Gamma}$, as well as the contribution from the screened deformation potential. Overall, the matrix elements $g_{\mathbf{k+q},\mathbf{k},\nu}$ of the neglected couplings are found to be three orders of magnitude smaller than those we account for.

6.3 Results

On general grounds, three different regimes are present in our calculations. These three regimes depend on three energy scales: i) the Fermi energy ε_F is the reference energy around which initial and scattered states are situated; ii) the phonon energy

Table 6.1: Sources of the experimental data used in this section. Experiment I and II correspond to Ref. [87] and Ref. [86] respectively. Combining those two experiments provides us with a wide range of temperature and doping conditions. PEO stands for poly(ethylene)oxide.

Experiment	I	II
Temp. range (K)	$4 \sim 250$	$14 \sim 480$
Doping range (eV)	$0.36 \sim 1.01$	$0.09 \sim 0.21$
Gate dielectric	PEO	SiO_2

$\hbar\omega$ is the energy difference between initial and scattered states; iii) the temperature k_BT sets the interval on which electronic and phonon occupations vary. Comparing $\hbar\omega$ to ε_F indicates how much the density of states changes during a scattering process. Comparing $\hbar\omega$ to k_BT indicates phonon occupations and the change of electronic occupations. Based on those observations, we have:

- *Bloch-Grüneisen* (BG) regime ($0K < T \lesssim 0.15 \times T_{BG}$, $T_{BG} = 2\hbar v_{TA/LA} k_F/k_B$). At these temperatures, k_BT is small compared to the energy of optical phonons. Those modes are not occupied and do not contribute. In contrast, the acoustic modes contribute since k_BT is of the order of $\hbar\omega_{\mathbf{q},\mathrm{TA/LA}}$. Moreover, the occupation of initial states $f(\varepsilon_{\mathbf{k}})$ and scattered states $f(\varepsilon_{\mathbf{k}} \pm \hbar\omega_{\mathbf{q},\mathrm{TA/LA}})$ are significantly different. Finally, as $\hbar\omega_{\mathbf{q},\mathrm{TA/LA}} << \varepsilon_F$, quantities other than occupation, such as the density of states, can be considered constant. In this regime, the resistivity has a $\propto T^4$ dependency due to acoustic phonons.

- *Equipartition* (EP) regime ($0.15 \times T_{BG} \lesssim T \lesssim 0.15 \times \hbar\omega_{A_1'}/k_B \approx 270\mathrm{K}$): optical phonons still do not contribute. As $\hbar\omega_{\mathbf{q},\mathrm{TA/LA}} << k_BT << \varepsilon_F$ the scattering by acoustic phonons can be approximated as elastic, including in the occupations of initial and final states. The resulting resistivity is then linear in temperature.

- *High temperature* (HT) regime ($T \gtrsim 0.15 \times \hbar\omega_{A_1'}/k_B \approx 270\mathrm{K}$): the elastic approximation for acoustic phonons holds, but the three energy scales are comparable in the case of optical phonons. In this case, no reasonable approximation can be made globally. The optical phonon participation is characterized by a strongly increasing resistivity at a temperature around 15% of the phonon energy. Due to their lower energy and stronger coupling, the contribution of optical A_1' phonons is more pronounced than LO/TO phonons.

Our calculated resistivity is compared with experimental data in Fig. 6.1. Experimental data are from the references cited in Table 6.1. In those experiments, the FET setup is used. The computational parameters are summarized in Table 6.2.

Below room temperature, Fig. 6.1a, the comparison between theory and experiment is meaningful only above $\varepsilon_F \gtrsim 0.14$ eV. Indeed, when approaching the Dirac point [46], the electron density tends to zero and resistivity diverges. One has to adopt

Table 6.2: Numerical values of parameters used in resistivity calculations. The effective sound velocity v_{A} is defined in Eq. (6.4.5).

Parameter	symbol	Value
Acoustic gauge field (GW)	β_A	4.32 eV
Acoustic gauge field (fitted)	β_A	4.97 eV
Optical gauge field (GW)	β_O	11.4 eV/Å
A_1' EPC parameter (GW)	β_K	13.9 eV/Å
A_1' EPC parameter (fitted)	β_K	see Fig. 6.3
Lattice parameter	b	2.46 Å
Unit-cell area	S	5.24 Å^2
Sound velocity TA	v_{TA}	13.6 km.s^{-1}
Sound velocity LA	v_{LA}	21.4 km.s^{-1}
Effective sound velocity	v_{A}	16.23 km.s^{-1}
LO/TO phonon energy	$\hbar\omega_{\mathrm{LO/TO}}$	0.20 eV
A_1' phonon energy	$\hbar\omega_{\mathrm{A}_1'}$	0.15 eV
Carbon atom mass	M	12.0107 u
Mass density	$\mu_S = 2M/S$	7.66 kg/m^2
Fermi Velocity (GW)	v_F	1.00 10^6 ms^{-1}

a model with non-homogenous electron density [99] to obtain a finite resistivity, such that the Fermi energy is ill-defined. Temperature-dependent screening of impurity scattering as well as temperature-dependent chemical potential shift [47] also play a role in this regime. Those issues are not treated in our model. At sufficiently high doping, the temperature behavior in the BG and EP regimes is well reproduced, despite an overall underestimation. The doping-dependency of the resistivity is limited to the BG ($\rho \propto T^4$) regime. The upper boundary of this regime increases with doping, since $T_{BG} \propto k_F$. Above $\sim 0.15 \times T_{BG}$, in the EP regime, the slope of the resistivity is essentially doping independent. This confirms that the deformation potential term can be neglected, since its screening would induce such a dependency.

In the HT regime, Fig. 6.1b, the underestimation is globally more pronounced. The increase of experimental resistivity around room temperature is steeper than the theoretical one. A strong doping dependency of the experimental curves appear. The agreement with the simulations improves as the system is doped far away from the Dirac point. This discrepancy is usually attributed to remote-phonon scattering from the SiO_2 substrate [86]. This effect is missing in our calculations as the substrate is not included. Moreover, we found no experimental data on other substrates for those temperatures. It follows that substrate-dependent sources of scattering cannot be ruled out in the HT regime. However, we would like to point out that based on the observation that the contribution of optical phonons seems to appear at a temperature $\approx 0.15 \times \hbar\omega_\nu$, we expect intrinsic optical phonons to be better candidates than the relatively low-energy remote phonons proposed in Ref. [86]. The optical A_1' mode at **K** does induce a sudden increase of resistivity, and the temperature at which this occurs is in very good agreement with experiment. The increasing discrepancy between theory

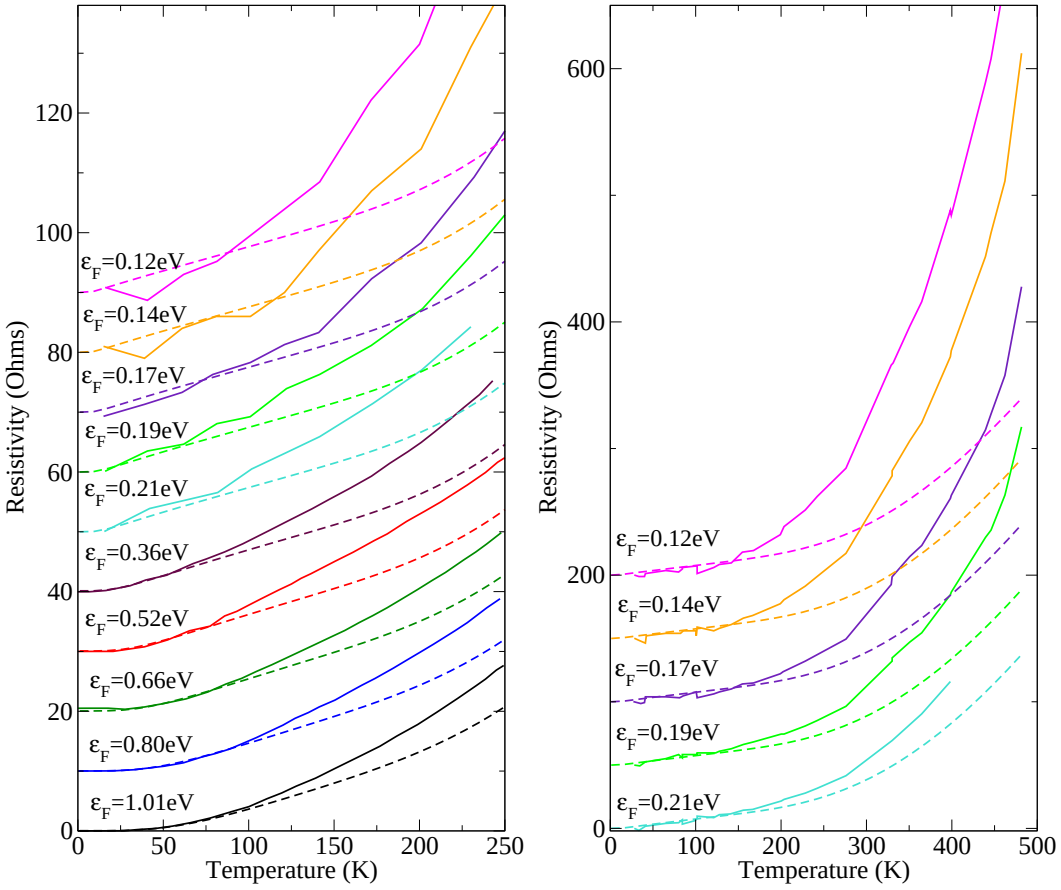

(a) BG and EP (b) HT

Figure 6.1: Comparison of experimental data (plain lines) and the numerical solution of the Boltzmann equation (dashed lines) in the Bloch-Grüneisen and Equipartition regimes(a) and in the HT regime(b), for several doping levels ranging from $\varepsilon_F = 0.12$ eV to $\varepsilon_F = 1.01$ eV. Experimental data are from Refs. [86] ($0.12 \rightarrow 0.21$ eV) and [87] ($0.36 \rightarrow 1.01$ eV). For each curve, the residual resistivity was subtracted, then a fictitious residual resistivity was added for clarity of the plot (different values were used in the two plots). Though their value has no absolute sense, the fictitious residual resistivities are ordered as the real ones.

and experiment in the magnitude of resistivity at lower doping could be explained by the fact that the EPC parameter β_K corresponding to the A_1' mode is renormalized by electron-electron interactions [35]. This renormalization decreases the larger the electron-doping of graphene, and tends to the DFT value at high doping.

We then fit the value of β_A for acoustic modes on experimental data in the EP regime. We find that an increase of the electron-phonon coupling of the acoustic modes of 15% leads to an excellent agreement with experimental data in the BG and EP regimes, as shown in Fig. 6.2a. We found an equivalent agreement for resistivity measurements of graphene on h-BN [9] or on SiO_2 with HfO_2 gate dielectric [100], thus ruling out any significant contribution from substrate dependent sources of scattering

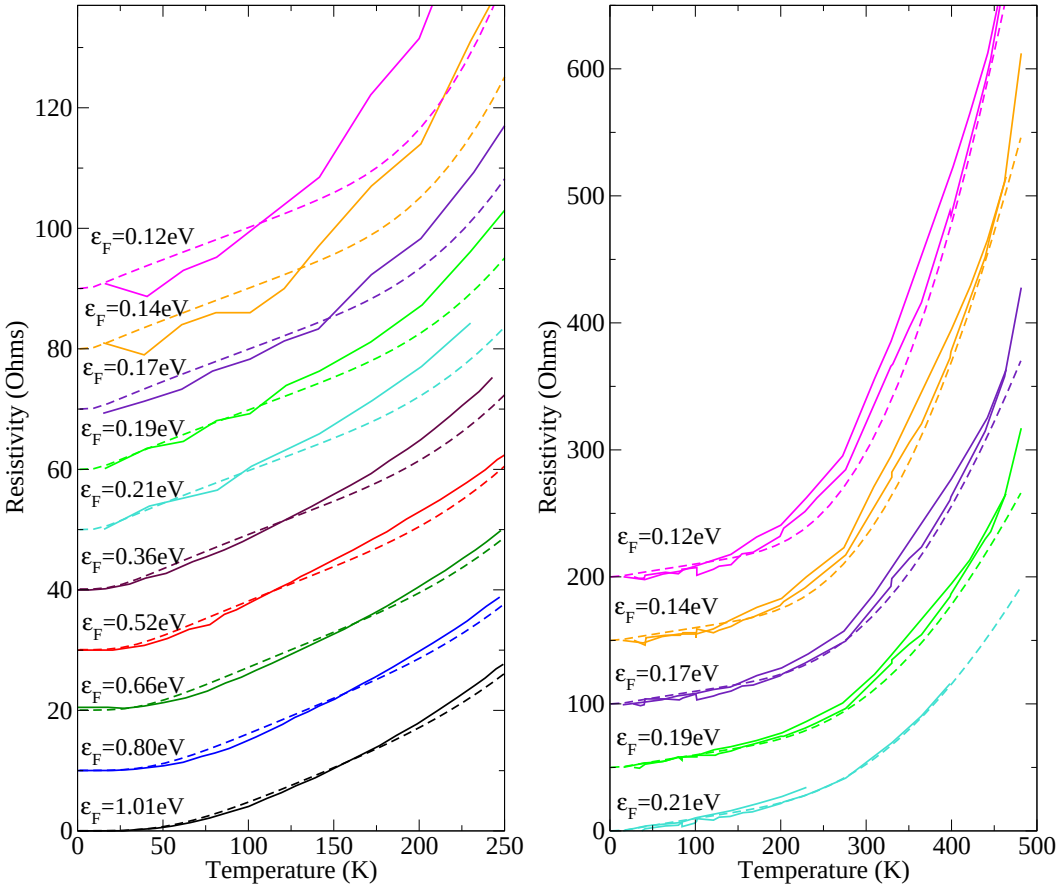

(a) BG and EP (b) HT

Figure 6.2: Results presented as in Fig. 6.1, with fitted values for β_A (see Table 3.1) and β_K (see Fig. 6.3) in the simulations. Experimental data from a different sample are added in plain lines in Fig. 6.2b to show that the sample-to-sample discrepancy when approaching the Dirac point is of the same order as the disagreement with the fitted numerical model.

(other than charged and short-range impurities) in the BG and EP regimes. We then conclude that the solution of the Boltzmann equation based on DFT and GW (the two methods are equivalent here) electron-phonon coupling parameters and bands explains fairly well the low-temperature regime (BG and EP), although DFT seems to underestimate the coupling to acoustic modes by 15%, or the resistivity by $\approx 30\%$. On closer inspection (see Sec. 6.4 and App. E.2), the resistivity in the EP regime is proportional to $\frac{\beta_A^2}{v_A^2}$ where v_A is the effective sound velocity given in Table 6.2 and defined in Eq. (6.4.5). An overestimation of v_A could also explain the 30% underestimation of the resistivity. This discrepancy might also be partly due to some other $\propto T$ contribution from processes ignored here, such as impurity scattering with temperature-dependent screening [47]. Finally, it could be due to the coupling to ZA phonons in a FET setup. Although our very first estimation of the latter gave negligible results in the previous

chapter, this coupling is very sensible to the details of graphene's environment. Some improvements of our model for the FET setup (replacing the potential barriers by a material for example), could reveal some non-negligible coupling with ZA phonons. In any case, defining an effective parameter β_A with the fitted value found here is sufficient to describe low temperature resistivity in a relatively large range of doping levels.

Within such a picture, we fit the optical β_K parameter as a function of doping. The fitted values of β_K are plotted in Fig. 6.3, along with GW and DFT values. Near the Dirac point, the fitted coupling parameter increases substantially more than previous estimates [35] at the GW level, but it seems to approach the DFT value at high doping. We then plot the resistivity with the fitted β_A and β_K, and find a good agreement with experiments on Fig. 6.2b. As mentioned, the increase of the fitted β_K could be due to a renormalization from electron-electron interactions. A small doping, computing reliable estimates for this renormalization within the GW approximation is quite a challenge. Indeed, large **k**-point grids are necessary to sample the small Fermi surfaces. Thus, the reliability of the GW β_K is questionable at small doping. The increase of the fitted β_K could also represent the effect of the *screened* coupling to remote phonons. Such contribution would give a similar behavior as a function of doping. Due to screening, the simulation of the coupling to remote phonons is affected by the presence of periodic images. The implementation of the previous chapter enables the correct simulation of this kind of coupling. We intend to perform the corresponding calculations soon.

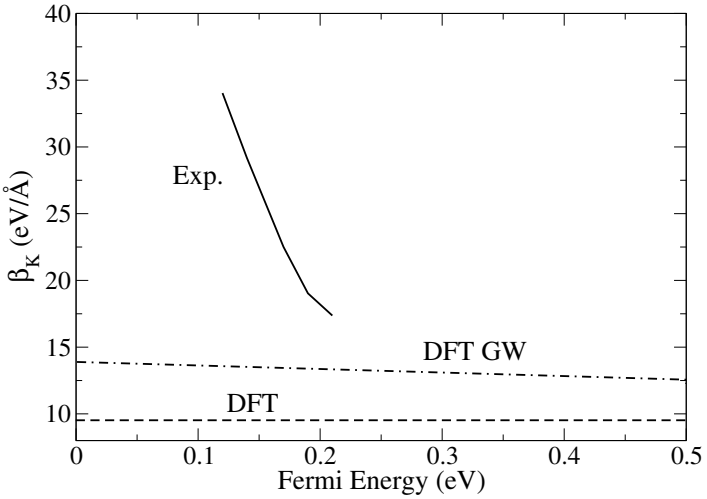

Figure 6.3: The parameter β_K fitted on experimental results as a function of Fermi energy is compared to the DFT LDA and DFT GW values. The DFT GW values are from Ref. [35].

6.4 Approximated solutions

In this section we seek a compromise between analytical simplicity and numerical accuracy. We review some of the approximations often made in transport models, and check their validity against the full numerical solution presented in Sec. 6.1. Fitted EPC parameters are used in the resistivity calculations.

6.4.1 Semi-analytical approximated solution

The first essential step is to derive an analytical expression of the time $\tau_\nu(\varepsilon_\mathbf{k})$ for each phonon branch. We first rewrite equation (6.1.13) as:

$$\frac{1}{\tau(\varepsilon_\mathbf{k})} = \sum_{\mathbf{k}'} P_{\mathbf{k}\mathbf{k}'} \frac{1-f^{(0)}(\varepsilon_{\mathbf{k}'})}{1-f^{(0)}(\varepsilon_\mathbf{k})} \times \Big(1 - \frac{\tau(\varepsilon_{\mathbf{k}'})\cos(\theta_{\mathbf{k}'})}{\tau(\varepsilon_\mathbf{k})\cos(\theta_\mathbf{k})}\Big) \tag{6.4.1}$$

For the doping level considered here, impurity scattering is essentially constant on the energy scale of the phonon energies. When this type of scattering dominates, the approximation $\tau(\varepsilon_{\mathbf{k}'}) \approx \tau(\varepsilon_\mathbf{k})$ becomes reasonable. We can simplify $\tau(\varepsilon_\mathbf{k})$ on the right-hand side of Eq. (6.4.1) and write:

$$\frac{1}{\tau(\varepsilon_\mathbf{k})} = \sum_\nu \frac{1}{\tau_\nu(\varepsilon_\mathbf{k})} \tag{6.4.2}$$

In other words, Matthiessen's rule [101] can be applied. With mild restrictions on the form of the angular dependency of the scattering probability, one can then use the following expression for the times τ_ν [37, 89]:

$$\frac{1}{\tau_\nu(\varepsilon_\mathbf{k})} \approx \sum_{\mathbf{k}'} P_{\mathbf{k}\mathbf{k}',\nu} \frac{1-f^{(0)}(\varepsilon_{\mathbf{k}'})}{1-f^{(0)}(\varepsilon_\mathbf{k})} \Big(1 - \cos(\theta_{\mathbf{k}'} - \theta_\mathbf{k})\Big) \tag{6.4.3}$$

A solution of Eq. (6.4.3) can now be carried out for different times separately by using phonon-specific approximations. Details can be found in App. E.2. We present here a solution that is relatively simple, yet very close to the complete one in a large range of temperature. For the sum of TA and LA acoustic phonons, labeled by the index $\mathrm{A} \equiv \mathrm{TA} + \mathrm{LA}$, we use the time derived in the EP and HT regime:

$$\left(\frac{1}{\tau_\mathrm{A}(\varepsilon_\mathbf{k})}\right)_{\mathrm{EP,HT}} = \frac{2\beta_A^2 k_B T}{\mu_S \hbar v_\mathrm{A}^2} \frac{\varepsilon_\mathbf{k}}{(\hbar v_F)^2} \tag{6.4.4}$$

where $\mu_S = 2M/S$ is the mass density per unit area of graphene. The full derivation can be found in App. E.3. The effective sound velocity for the sum of TA and LA contributions v_A is such that:

$$\frac{2}{v_\mathrm{A}^2} = \frac{1}{v_\mathrm{TA}^2} + \frac{1}{v_\mathrm{LA}^2} \tag{6.4.5}$$

For the sum of LO and TO phonons, labeled by $\mathrm{O} \equiv \mathrm{LO} + \mathrm{TO}$, we use no other approximation than the constant phonon dispersion ($\hbar\omega_\mathrm{LO} = \hbar\omega_\mathrm{TO} = \hbar\omega_\mathrm{O} = 0.20$ eV) and find the expression given in Eq. (E.2.5) of App. E.2. The same approximation is made for Optical A_1' phonons at $\mathbf{K}$ ($\hbar\omega_{\mathrm{A}_1'} = 0.15$ eV) and we find the expression

given in Eq. (E.2.6) of App. E.2. Finally, impurity scattering can be easily included knowing the residual resistivity $\rho_{\mathrm{I}}(T=0) = \rho(T=0)$:

$$\frac{1}{\tau_{\mathrm{I}}(\varepsilon_{\mathbf{k}})} = \frac{1}{\tau_{\mathrm{I}}(\varepsilon_F)} = \frac{e^2 v_F^2}{2} DOS(\varepsilon_F)\rho_I(T=0) \tag{6.4.6}$$

Defining $\tau = \left(\sum_\nu \frac{1}{\tau_\nu}\right)^{-1}$, and numerically evaluating the integral in Eq. (6.1.15) we obtain the results shown in Fig. 6.4 that are only weakly different from the solution of the complete Boltzmann equation. The low temperature BG regime ($\rho \propto T^4$) is not reproduced because of the quasi-elastic approximation made to obtain Eq. (6.4.4). However, a more complicated yet analytical expression for τ_{A} in the BG regime is given in App. E.2 and yields better results. In the EP regime, both solutions are equivalent. The effects of the $\tau(\varepsilon_{\mathbf{k}'}) \approx \tau(\varepsilon_{\mathbf{k}})$ approximation are seen only slightly in the high temperature regime, when optical A_1' phonons dominate the resistivity. It is thus a good and useful approximation, since it allows a separate treatment of each contributions and the use of Matthiessen's rule. Furthermore, inspecting the times τ_ν validates the statement made in Sec. 3.3.3, namely that the contribution to resistivity from each phonon is proportional to the squared ratio of the EPC parameter and the Fermi velocity.

6.4.2 Additivity of resistivities

As shown in Sec. 6.4.1, in the presence of impurities, it is possible to define independent times τ_ν for each mode. Then from each time τ_ν, the resistivity ρ_ν of a given mode is obtained via the use of Eq. (6.1.15). It is then tempting to sum the resistivities to obtain the total resistivity. However, the energy integral of Eq. (6.1.15) should be carried on the total time τ, found by adding the *inverse* times of each modes under Matthiessen's rule. For the resistivities to be additive, it is required that

$$\tau = \left(\sum_\nu \frac{1}{\tau_\nu}\right)^{-1} \approx \sum_\nu \left(\frac{1}{\tau_\nu}\right)^{-1} \tag{6.4.7}$$

which is rarely valid, as demonstrated in Fig. 6.5. An important consequence is that care needs to be taken when the resistivity due to impurities (the so called residual resistivity) is subtracted from the overall resistivity to isolate the intrinsic contributions. This approach is justified only if the time τ_{I} corresponding to impurities is such that $1/\tau_{\mathrm{I}} >> 1/\tau_{\mathrm{A}} + 1/\tau_{\mathrm{A}_1'} + 1/\tau_{\mathrm{O}}$. In general, this is not the case and impurity scattering has a more subtle effect than just shifting the total resistivity by ρ_{I} as shown in Fig. 6.5. Throughout this work, we include impurity scattering and then subtract the residual resistivity. This procedure is convenient but one must keep in mind that what remains is not the theoretical intrinsic resistivity. Both are plotted in Fig. 6.5, as well as Allen's method [90] used in Ref. [28]. The latter overestimates the resistivity.

At low temperature, and in the EP regime, the process of adding the residual resistivity $\rho_{\mathrm{I}}(T=0)$ and the acoustic resistivity ρ_A is justified and allows one to access directly the magnitude of the gauge field parameter β_A. Indeed, when only impurities and acoustic phonons contribute and if $\tau_{\mathrm{I}} << \tau_{\mathrm{A}}$, the corresponding resistivities are

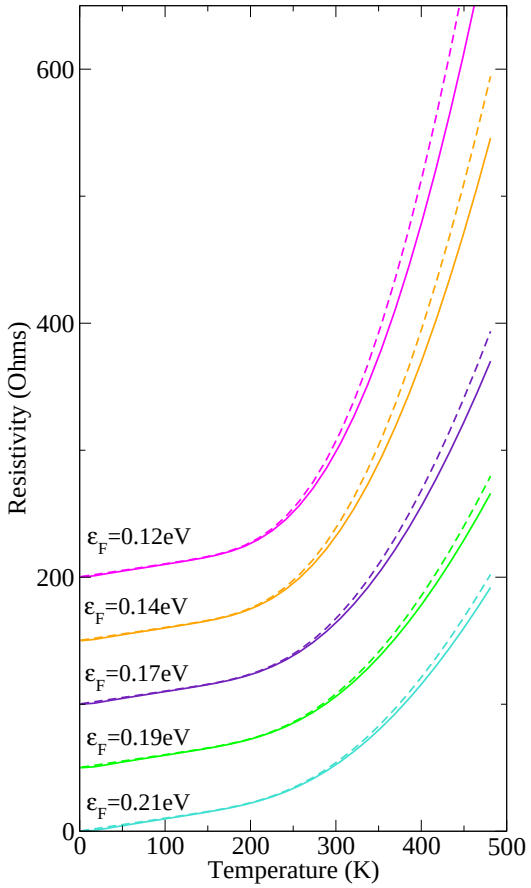

Figure 6.4: Comparison between the full Boltzmann transport solution (plain lines) and the semi-analytical solution with the $\tau(\varepsilon_{\mathbf{k}}) \approx \tau(\varepsilon_{\mathbf{k}'})$ approximation made and the expressions of τ_ν given in Sec. 6.4.1 (dotted lines). Fitted EPC parameters were used. Residual resistivity was included in the transport simulation then subtracted for the plots. A fictitious residual resistivity was then added for clarity.

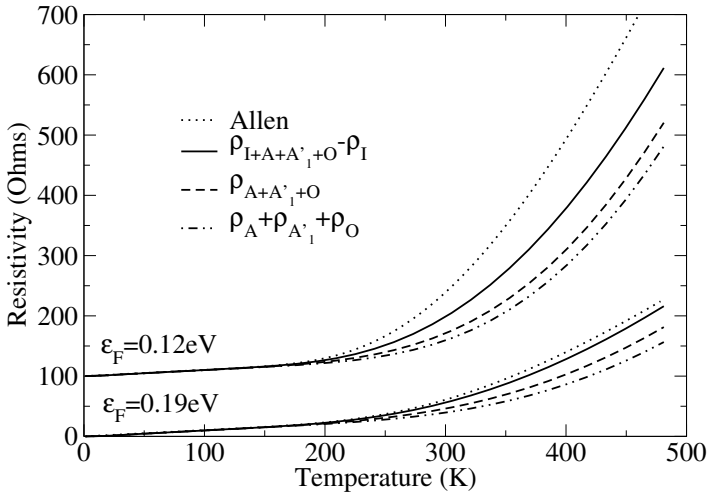

Figure 6.5: Comparison of various methods for the simulation of graphene's resistivity. The complete solution to Boltzmann equation (including impurities) to which we subtract the residual resistivity $\rho_{\mathrm{I+A+A'_1+O}} - \rho_{\mathrm{I}}$ gives the result closer to experimental conditions. The Boltzmann solution including only phonon contributions $\rho_{\mathrm{A+A'_1+O}}$ corresponds to the theoretical intrinsic resistivity. The resistivity made up of the sum of independently derived resistivities is $\rho_{\mathrm{A}}+\rho_{\mathrm{A'_1}}+\rho_{\mathrm{O}}$. Allen's method, used in Ref. [28], overestimates the resistivity. Only at low temperature are those methods equivalent.

additive. Moreover, in the EP regime, ρ_{A} has the simple expression (see appendix E.3 for detailed derivation):

$$\rho_A \approx \frac{2\pi\beta_A^2 k_B T}{e^2\hbar v_F^2 \mu_S v_{\mathrm{A}}^2} \tag{6.4.8}$$

It is clear that the slope of the resistivity is determined by v_{A}^2 and β_A^2. Once the sound velocities are known, it is then possible to extract β_A directly from transport measurements. We expect this parameter to be very close to the amplitude of the synthetic vector potential [102]. One must be careful when comparing the result of such measurement to other values in literature. As noted in Ref. [91], different EPC models bring different pre-factors in Eq. (6.4.8). For example, the magnitude of the deformation potential D in Ref. [89] is defined such that a similar equation is obtained, but $D \equiv 2\beta_A$.

Summary

- Development of numerical solution to Boltzmann transport in graphene.
- Predominant role of acoustic phonons below room-temperature is confirmed.
- EP regime dominated by doping-independent acoustic gauge field β_A.
- Experimental low-T transport reproduced with 15% increase of β_A.
- A_1' mode is the dominant intrinsic contribution at high-T.
- Remote phonons could also contribute to high-T resistivity.
- Thorough survey of approximated solutions to resistivity.
- Indications for experimental extraction of acoustic gauge field.

Conclusion

This work starts with an effort to clarify, improve and quantify existing models for the coupling of electrons to in-plane acoustic phonon modes. By diagonalizing the density-functional dynamical matrix at finite phonon momenta, we develop a model for graphene's in-plane acoustic phonon modes beyond the set of strictly longitudinal and transverse phonon modes. With the support of *ab initio* simulations, we demonstrate that inserting those phonon modes into the most general symmetry-based model of electron-phonon interactions is essential to obtain numerically accurate values for the acoustic gauge field parameter.

In order to calculate the coupling to acoustic modes in the GW approximation, we develop the static strain method, similar to the frozen phonon scheme used for optical modes. We interpret the zero-momentum limit of an acoustic phonon as a static strain of the unit cell. We then extract acoustic coupling parameters from band structure calculations performed on strained graphene. Using this method within the GW approximation, we confirm that the acoustic gauge field is renormalized by electron-electron interactions as the Fermi velocity. The unscreened acoustic gauge field is the main contribution to the coupling of electrons with acoustic phonons. The other contribution, the deformation potential, is screened. However, the values of the screened deformation potential obtained using standard plane-wave density-functional theory calculations are wrong. Indeed, 3D periodic boundary conditions imply the presence of periodic images of the graphene sheet, which leads to some spurious screening. As for the static strain method, it only gives an estimation for the *bare* deformation potential. We then naturally proceed to the study of the screening properties of graphene.

The definition of the dielectric function depends on dimensionality. After clarifying the formalism for screening in two dimensional frameworks, we review previous analytical derivations of the screening properties of graphene. We highlight the approximations involved in those derivations and propose a method based on density-functional theory to overcome them. We compute the electronic density response to a perturbing potential and implement the 2D Coulomb cutoff to prevent screening from the periodic images. We show that cutting off the Coulomb interactions between periodic images is essential to recover the screening properties of an isolated layer. Applied to graphene, our method leads to an inverse dielectric function that is very close to the analytical form for $|\mathbf{q}| \leq 2k_F$, and is smaller by $\approx 10\%$ for $|\mathbf{q}| > 2k_F$, where $\mathbf{q}$ is an in-plane wave vector and k_F is the Fermi wave vector. Overall, the Dirac cone model in a strictly 2D framework, in the zero temperature limit, using random phase aproximation and neglecting local fields gives a quite accurate and simple analytical expression for the static dielectric function of graphene. Smearing effects are negligible at room

temperature and exchange-correlation effects within the local density approximation are also quite small. Neglecting the local fields amounts to an $\approx 8\%$ underestimation of the inverse dielectric function above $2k_F$. The largest error comes from the Dirac cone model for the band structure. This model remains an excellent approximation in the $|\mathbf{q}| \leq 2k_F$ regime, as long as the Fermi level lies in the region where the bands are linear. In the $|\mathbf{q}| > 2k_F$ regime, however, the Dirac cone model leads to a $\approx 16\%$ overestimation of the inverse dielectric function due to the contribution of interband processes probing states beyond the Dirac cones. This overestimation compensates the local fields effects and the analytical model ends up overestimating the simulated inverse dielectric function by $\approx 10\%$ above $2k_F$.

Using the value of the bare deformation potential and the simulated screening function of graphene, we estimate the screened deformation potential and note that it is one order of magnitude smaller that the acoustic gauge field. Thus, the unscreened gauge field remains the dominating contribution for the coupling of electrons to the *in-plane* acoustic phonons.

The ability to simulate 2D materials in a field effect setup within the plane-wave density-functional framework is essential to study *out-of-plane* phonons and their coupling to electrons. We first describe the typical potential profile of the field effect setup. We then show that 3D periodic boundary conditions, as used in standard plane-wave density-functional theory, raise serious issues for its simulation. We then show how the 2D Coulomb cutoff technique can solve those issues. We detail the implementation of the 2D Coulomb cutoff for the ground state and linear response of 2D systems in the density-functional theory code Quantum ESPRESSO. This implementation includes the calculation of the total energy, forces, phonons and electron-phonon coupling in 2D materials. We apply the method to graphene and demonstrate the benefits of the implementation by simulating mechanisms specific to the field effect setup. We show the emergence of a finite frequency for out-of-plane acoustic phonons in the limit of small momenta when the 2D material is blocked between two repulsive barriers. We show that out-of-plane phonons can couple linearly to electrons for graphene doped in the field effect setup, in contrast with the case of neutral or jellium-doped graphene. In the preliminary estimation performed here, the coupling with ZA and ZO phonons is found to be small compared to the acoustic gauge field and the coupling to in-plane optical modes. The method also enables the calculation of the screened deformation potential within density-functional theory without spurious screening from the periodic images. The screened deformation potential obtained with this method remains negligible compared to the acoustic gauge field.

We then developed a numerical solution to the complete Boltzmann transport equation including contributions from acoustic and optical phonon branches. Comparison to experiment confirms the role of acoustic phonons in the low temperature regime of resistivity. In the equipartition regime, the resistivity is proportional to the squared ratio of the acoustic gauge field parameter over the effective sound velocity (the harmonic mean of the squared LA and TA sound velocities). The slope of the resistivity as a function of temperature is then doping and substrate independent. We found that increasing the acoustic gauge field parameter by 15% with respect to the GW value leads to an excellent agreement with experiment. In the high temperature regime, scattering by intrinsic A_1' optical phonon modes at $\mathbf{K}$ could account for the strong increase

in resistivity. However, a doping-dependent renormalization of the corresponding coupling parameter is necessary, and this renormalization is much stronger than existing estimate within GW. The role of remote-phonon scattering at high temperature was not ruled out. If remote-phonons are indeed involved, their screening plays an important role and needs to be modeled and simulated accurately. We verified the validity of approximations commonly used when solving the Boltzmann transport equation. An approximate yet accurate semi-analytical solution is proposed. Finally, partial analytic solutions were derived in order to extract the numerical parameter (gauge field parameter) that relates the synthetic vector potential to strain directly from transport measurements.

The interactions with out-of-plane intrinsic phonons and with remote phonons are among the interesting mechanisms to explore further in graphene. Our implementation of the 2D Coulomb cutoff in Quantum ESPRESSO is the adequate tool to study those interactions. The solution to Boltzmann transport equation and the static strain method require some analytical work that is specific to each material. However, the processes can be adapted to other 2D materials. The 2D Coulomb cutoff was implemented in a general manner and is readily applicable to other 2D materials. The corresponding codes can be used to compute the ground-state density, total energy, bands, static screening function, phonon dispersions and electron-phonon coupling of isolated and gate-doped 2D materials. We expect that the computational methods developed in this thesis can be exploited for numerous applications other than graphene.

Appendices

Chapter A

Computational Methods

In this appendix we introduce the computational methods used in the thesis. A recapitulative diagram is given in Fig. A.1.

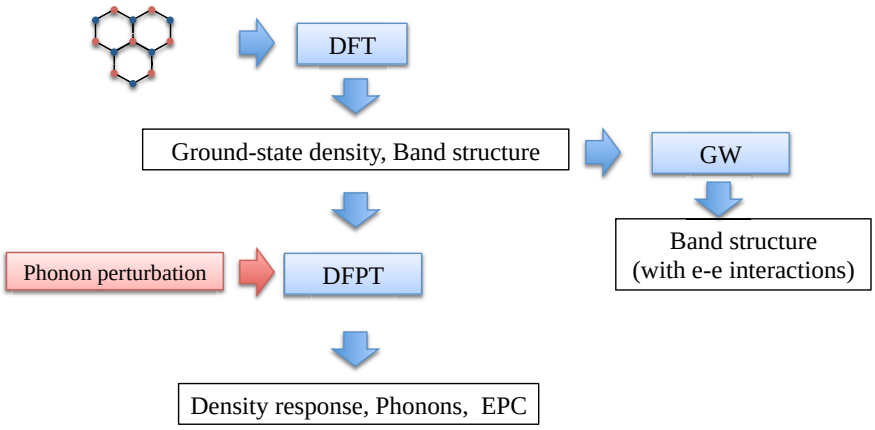

Figure A.1: Schematic of the main computational methods used in this work. The DFT and DFPT calculations are performed with the Quantum ESPRESSO package [38]. The GW calculations were carried out by C-H. Park on the BerkeleyGW package [39].

The general framework is that of density-functional theory (DFT) [103]. Density-functional theory can be used in several contexts. In this work, the term DFT will always imply the context of the Kohn-Sham (KS) equations [77], Bloch plane waves [18] and pseudopotentials [104]. The DFT calculations were performed using the Quantum ESPRESSO (QE) code [38].

The first Hohenberg-Kohn theorem [103] states that all the properties of the ground-state of a system are determined by its electron density. In other words, a theory (such as DFT) that gives us the electronic density is sufficient to obtain the physical properties of the system. In particular, the energy of the system of electrons can be expressed as a functional of the density:

$$\mathcal{E}_{\text{elec}}[n] = \mathcal{E}_{\text{kin}}[n] + \mathcal{E}_{\text{ext}}[n] + \mathcal{E}_{\text{H}}[n] + \mathcal{E}_{\text{XC}}[n] \tag{A.0.1}$$

where the different contributions are functionals for the kinetic energy of the electrons, the energy of the electrons in an external field (e.g. the ions), the Hartree energy and exchange-correlation (XC) energy. A potential $V[n] = \frac{\delta \mathcal{E}[n]}{\delta n}$ can be associated to each of those energy functionals.

To find the electronic density, DFT maps a complex interacting electron system onto the simpler problem of free electrons moving in an effective potential, the Kohn-Sham (KS) potential [77]. The KS potential $V_{\mathrm{KS}}(\mathbf{r})$, where $\mathbf{r} = (x,y,z)$ is a space variable, is the sum of three potentials:

$$V_{\mathrm{KS}}(\mathbf{r}) = V_{\mathrm{ext}}(\mathbf{r}) + V_{\mathrm{H}}(\mathbf{r}) + V_{\mathrm{XC}}(\mathbf{r}). \tag{A.0.2}$$

For a 2D material in the ground state, without any perturbation, the external potential V_{ext} is simply the potential generated by the ions of the lattice, computed using the pseudopotentials. The remaining potentials V_{H} and V_{XC} are functionals of the electronic density. V_{H} is the Hartree potential, accounting for the classical Coulomb repulsion between electrons. The KS potential also includes, to some extent, a contribution from the more quantum mechanical nature of electron-electron interactions in the form of the exchange-correlation potential V_{XC}. The QE code solves the KS equations, which are the Schrödinger equations for a system of free electrons in the effective KS potential. This process is achieved in reciprocal space thanks to the plane-wave formalism, and yields the KS electronic density. Since the KS potential determines the solution for the density which in turn generates part of the KS potential (Hartree and XC terms), this approach leads to a self-consistent problem. When self-consistency is reached, the ground-state density $n(\mathbf{r})$ is found. That is the only physical observable defining the density functionals. It is also possible to extract the band energies and the Bloch wave functions from the solution of the KS equations. However, it should be noted that those quantities have no strict physical meaning in principle [105]. Nevertheless, they usually represent a good single-particle representation of the system.

The major approximation of DFT comes from the fact that the exact functional giving all the contributions from electron-electron correlations to the energy is unknown. We only have approximate forms of $\mathcal{E}_{\mathrm{XC}}$ and the corresponding potential V_{XC}. DFT is known to be limited to treat electron correlations. Computational methods based on the GW approximation allows one to compute corrections to the DFT results. In those kind of calculations, represented in Fig.A.1, we start from the electronic density, wave functions and band energies obtained in DFT and compute corrections that electron-electron interactions might bring to the energies of the Bloch states. Other methods, such as Quantum Monte Carlo, go beyond those corrections and allow one to compute wave functions more similar to those of interacting electrons, as opposed to the non-interacting Bloch waves used in DFT. Still, DFT is computationally much cheaper than these methods, and works very well in a great number of situations. This is our main tool for simulations. In graphene, we evaluate corrections from electron-electron interactions within the GW approximation when necessary.

Density-functional perturbation theory (DFPT) [19, 20, 21] allows one to calculate the linear response of the ground state energy to a certain perturbation. An example of perturbation are phonons. Of course, the response is that of the fictive system on which the real system is mapped. Its validity relies on the linear response assumption and the approximations related to the exchange-correlation part of the DFT functional used in

the calculations. We will see that phonon dispersions can be inferred from the second derivative of the total energy with respect to the displacement of ions. The second derivative of the total energy can be calculated with the first-order perturbations of the KS potential and electronic density, such that it is accessible in linear response theory. EPC stems from the linear order perturbation of the effective KS potential by phonons. DFPT, as implemented in the QE phonon code, will be used to simulate phonons and their interactions with electrons.

Although we present a few calculations within the GW approximation, DFT and DFPT remain the central methods that we use and develop in this work. The basic formalism of those methods, as implemented in the QE code, is presented in the following.

A.1 DFT

In this section we introduce the quantities that can be calculated in DFT. We give the most straightforward expressions for a generic 3D-periodic material. The following description is obviously very far from exhaustive. The aim is simply to set the notations and provide definitions for the quantities mentioned in the main text of the thesis. For more details, we refer the reader to the literature cited in the above introduction. The lattice vectors are noted $\mathbf{R}$, the internal coordinate of atom a is $\mathbf{d}_a$. The reciprocal lattice vectors $\mathbf{G}$ are such that $e^{i\mathbf{G}\cdot\mathbf{R}} = 1$.

A.1.1 Potentials

The central potential in the self-consistent process is the KS potential of Eq. (A.0.2). It contains:

- V_{ext}: the principal contribution to V_{ext} is the potential generated by the ions V_{ion} calculated via the pseudopotentials. For the purpose of this thesis, we consider only the local part of V_{ion}, written as:

$$V_{\text{ion}}^{\text{loc}}(\mathbf{r}) = \sum_{\mathbf{R},a} v_a(\mathbf{r} - \mathbf{R} - \mathbf{d}_a) \tag{A.1.1}$$

  where v_a is the pseudopotential associated to atom a. We can put other contributions into V_{ext}, but in this appendix $V_{\text{ext}} = V_{\text{ion}}$.

- V_{H}: the Hartree potential is given by:

$$V_{\text{H}}(\mathbf{r}) = e^2 \int d\mathbf{r}' \frac{n(\mathbf{r}')}{|\mathbf{r} - \mathbf{r}'|}, \tag{A.1.2}$$

  Here, and whenever there is no specified interval, the integrals are carried out over the entire space spanned by the corresponding variable.

- V_{XC}: the exchange-correlation potential is based on the local density approximation [22] (LDA).

We also have to mention the potential $\Phi(\mathbf{r})$ which is the potential generated by the ions used to compute ion-ion interactions. Although it is generated by the same source as V_{ion}, it is not calculated via the pseudopotentials. To generate this potential, the ions are modeled by a collection of point charges. This potential is defined as:

$$\Phi(\mathbf{r}) = {\sum_{\mathbf{R}',a}}' \frac{e^2 Z_{a'}}{|\mathbf{r} - \mathbf{R}' - \mathbf{d}'_a|} \tag{A.1.3}$$

where the prime on the sum excludes the $\{\mathbf{R} = \mathbf{R}', a = a'\}$ case if $\mathbf{r} = \mathbf{R} + \mathbf{d}_a$.

A.1.2 Total Energy

What we call the total energy of the system is the clamped-ions energy or the Born-Oppenheimer energy surface [11]:

$$\mathcal{E}_{\text{tot}} = \mathcal{E}_{\text{kin}} + \mathcal{E}_{\text{XC}} + \mathcal{E}_{\text{H}} + \mathcal{E}_{\text{ext}} + \mathcal{E}_{\text{i-i}} \tag{A.1.4}$$

where

$$\mathcal{E}_{\text{kin}} = -\frac{\hbar^2}{2m_e} \sum_{\mathbf{k},s} f(\varepsilon_{\mathbf{k},s}) \langle \psi_{\mathbf{k},s} | \nabla^2 | \psi_{\mathbf{k},s} \rangle \tag{A.1.5}$$

$$\mathcal{E}_{\text{H}} = \frac{1}{2} \int n(\mathbf{r}) V_{\text{H}}(\mathbf{r}) d\mathbf{r} \tag{A.1.6}$$

$$\mathcal{E}_{\text{ext}} = \int n(\mathbf{r}) V_{\text{ext}}(\mathbf{r}) d\mathbf{r} \tag{A.1.7}$$

$$\mathcal{E}_{\text{i-i}} = \frac{1}{2} \sum_{\mathbf{R},a} Z_a \Phi(\mathbf{R} + \mathbf{d}_a) \tag{A.1.8}$$

and $\mathcal{E}_{\text{XC}}$ is the exchange-correlation energy. For any of the above quantity $\mathcal{E}$, one can define the corresponding energy per unit cell $E = \mathcal{E}/N$ where N is the number of unit cells. This is often more useful in practice, since the system is infinite, as are the energies $\mathcal{E}$.

A.1.3 Forces

To calculate the force on atom a in direction i, we compute the derivative of the total energy per unit cell with respect to a displacement $\mathbf{u}_{a,i}$ of this atom in this direction, and take the value at $\mathbf{u}_{a,i} = 0$. Using the Hellmann-Feynman theorem [106, 107], the force acting on ion a, in direction i is given by:

$$\mathbf{F}_{a,i} = -\frac{\partial E_{\text{tot}}}{\partial \mathbf{u}_{a,i}} \tag{A.1.9}$$

$$= -\int_{\Omega} n(\mathbf{r}) \frac{\partial V_{\text{ext}}(\mathbf{r})}{\partial \mathbf{u}_{a,i}} d\mathbf{r} - \frac{\partial E_{\text{i-i}}}{\partial \mathbf{u}_{a,i}}, \tag{A.1.10}$$

where the integral is carried over the volume of the unit cell Ω. Here and in the following, the notation $\frac{\partial}{\partial \mathbf{u}_{a,i}}$ represents the value of the derivative at zero displacement. The first term is the contribution from the electrons, the second from the ions. The forces can be computed as soon as we have solved the ground state, since there are only known quantities and their derivatives.

A.2 DFPT

DFPT enables the computation of the linear response of the ground state to given perturbation. In the case of the QE phonon code, those perturbations are phonons.

A.2.1 Phonons

We can simulate the response of the system to a phonon perturbation within DFPT. A phonon perturbation of momentum $\mathbf{q}$ is represented by a collection of displacements $\mathbf{u}_{a,i}(\mathbf{R})$ of atom a in Cartesian direction i:

$$\mathbf{u}_{a,i}(\mathbf{R}) = \mathbf{u}_{a,i}(\mathbf{q})e^{i\mathbf{q}\cdot\mathbf{R}} \tag{A.2.1}$$

where $\mathbf{u}_{a,i}(\mathbf{q})$ is the Fourier transform of $\mathbf{u}_{a,i}(\mathbf{R})$. The phonon frequencies are obtained from the second derivative of the total energy of the crystal $\mathcal{E}_{\text{tot}}$ (not the energy of a unit cell) via the matrix of the interatomic force constants defined as [21]:

$$\begin{aligned}\mathbf{C}_{ai,a'j}(\mathbf{R}-\mathbf{R}') &= \frac{\partial^2 \mathcal{E}_{\text{tot}}}{\partial \mathbf{u}_{a,i}(\mathbf{R})\partial \mathbf{u}_{a',j}(\mathbf{R}')} \\ &= \mathbf{C}^{ion}_{ai,a'j}(\mathbf{R}-\mathbf{R}') + \mathbf{C}^{elec}_{ai,a'j}(\mathbf{R}-\mathbf{R}')\end{aligned} \tag{A.2.2}$$

In this particular context, it does not make sense to talk about energy per unit cell. Indeed, the energy is not lattice periodic because of the phonon perturbation. There are two contributions, one from the electrons, one from the ions:

$$\mathbf{C}^{elec}_{ai,a'j}(\mathbf{R}-\mathbf{R}') = \int \frac{\partial^2 V_{\text{ext}}(\mathbf{r})}{\partial \mathbf{u}_{a,i}(\mathbf{R})\partial \mathbf{u}_{a',j}(\mathbf{R}')} n(\mathbf{r})d\mathbf{r} + \int \frac{\partial V_{\text{ext}}(\mathbf{r})}{\partial \mathbf{u}_{a,i}(\mathbf{R})} \frac{\partial n(\mathbf{r})}{\partial \mathbf{u}_{a',j}(\mathbf{R}')} d\mathbf{r} \tag{A.2.3}$$

$$\mathbf{C}^{ions}_{ai,a'j}(\mathbf{R}-\mathbf{R}') = \frac{\partial^2 \mathcal{E}_{i-i}}{\partial \mathbf{u}_{a,i}(\mathbf{R})\partial \mathbf{u}_{a',j}(\mathbf{R}')} \tag{A.2.4}$$

The first term of Eq. (A.2.3) and Eq. (A.2.4) are simply the second derivatives of quantities we already know. The second term of Eq. (A.2.3), however, contains the linear response of the electronic density to a phonon perturbation. This quantity can be calculated within DFPT. A phonon perturbation translates into a periodic perturbation of the potential generated by the ions, that is a periodic perturbation of V_{ext}:

$$\frac{\partial V_{\text{ext}}(\mathbf{r})}{\partial \mathbf{u}_{a,i}(\mathbf{q})} = \frac{\partial V_{\text{ion}}(\mathbf{r})}{\partial \mathbf{u}_{a,i}(\mathbf{q})} \tag{A.2.5}$$

where we now work with the (single-component) Fourier transform of the phonon perturbation $\mathbf{u}_{a,i}(\mathbf{q})$. The phonon perturbation triggers the linear response of the electronic density:

$$\frac{\partial n(\mathbf{r})}{\partial \mathbf{u}_{a,i}(\mathbf{q})}, \tag{A.2.6}$$

which is found by solving a new set of equations, involving the linear perturbation to the KS potential:

$$\frac{\partial \mathcal{V}_{\mathrm{KS}}(\mathbf{r})}{\partial \mathbf{u}_{a,i}(\mathbf{q})} = \frac{\partial \mathcal{V}_{\mathrm{ext}}(\mathbf{r})}{\partial \mathbf{u}_{a,i}(\mathbf{q})} + \frac{\partial \mathcal{V}_{\mathrm{H}}(\mathbf{r})}{\partial \mathbf{u}_{a,i}(\mathbf{q})} + \frac{\partial \mathcal{V}_{\mathrm{XC}}(\mathbf{r})}{\partial \mathbf{u}_{a,i}(\mathbf{q})} \tag{A.2.7}$$

where the $\mathcal{V}$ notation indicates that we take the lattice-periodic part of the perturbations:

$$\frac{\partial V(\mathbf{r})}{\partial \mathbf{u}_{a,i}(\mathbf{q})} = \frac{\partial \mathcal{V}(\mathbf{r})}{\partial \mathbf{u}_{a,i}(\mathbf{q})} e^{i\mathbf{q}\cdot\mathbf{r}}. \tag{A.2.8}$$

The last two terms of Eq. (A.2.7) are generated by the density response Eq. (A.2.6). We thus have a new self-consistent system to solve. Once self-consistency is reached, we can calculate the dynamical matrix $\mathcal{D}$ which is the Fourier transform of the matrix of the force constants:

$$\mathcal{D}_{a,i,a',j}(\mathbf{q}) = \frac{1}{\sqrt{M_a M_{a'}}} \sum_{\mathbf{R}} \mathbf{C}_{ai,a'j}(\mathbf{R}) e^{i\mathbf{q}\cdot\mathbf{R}} \tag{A.2.9}$$

where M_a is the mass of atom a, and we have used translational invariance to express the matrix of the force constant as a function of the generic lattice vector $\mathbf{R}$. The eigenvalue problem:

$$\omega^2(\mathbf{q})\mathbf{u}_{a,i}(\mathbf{q}) = \sum_{a',j} \mathcal{D}_{a,i,a',j}(\mathbf{q})\mathbf{u}_{a,i}(\mathbf{q}) \tag{A.2.10}$$

gives the frequencies $\omega_{\mathbf{q},\nu}$ ($\omega^2_{\mathbf{q},\nu}$ being the eigenvalues) and eigenvectors $\mathbf{e}_{\mathbf{q},\nu}$ of mode ν at momentum $\mathbf{q}$.

A.2.2 EPC

The electron-phonon interaction matrix elements are obtained from the derivative of the KS potential as follows:

$$g_{\mathbf{k}+\mathbf{q},s,\mathbf{k},s',\nu} = \sum_{a,i} \mathbf{e}^{a,i}_{\mathbf{q},\nu} \sqrt{\frac{\hbar}{2M_a\omega_{\mathbf{q},\nu}}} \langle \mathbf{k}+\mathbf{q},s| \frac{\partial \mathcal{V}_{\mathrm{KS}}(\mathbf{r})}{\partial \mathbf{u}_{a,i}(\mathbf{q})} |\mathbf{k},s'\rangle \tag{A.2.11}$$

Chapter B

Electron-phonon coupling in the tight-binding model of graphene

In this appendix, we detail the derivation of the tight-binding (TB) Hamiltonian model for the electronic structure and the EPC in graphene. Although not detailed, parts of those calculations were carried out in Refs. [27, 14, 24, 28]. Even if we go beyond this model in the main text, the TB model is useful to get a formal understanding of EPC.

B.1 Low-energy, two nearest neighbors TB Hamiltonian

Omitting on-site energy, the TB Hamiltonian reads:

$$\mathcal{H}^{\mathrm{TB}} = -\sum_{1^{\mathrm{st}}\mathrm{n.n.}} t_1 |\mathbf{R},a\rangle\langle\mathbf{R}',a'| - \sum_{2^{\mathrm{nd}}\mathrm{n.n.}} t_2 |\mathbf{R},a\rangle\langle\mathbf{R}',a'| \tag{B.1.1}$$

where t_1 and t_2 are the first and second neighbor hopping integrals, respectively. Using the following basis:

$$|\mathbf{K}+\mathbf{k},a\rangle = \frac{1}{\sqrt{N}} \sum_{\mathbf{R}} e^{i(\mathbf{K}+\mathbf{k})\cdot(\mathbf{R}+\mathbf{d}_a)} |\mathbf{R},a\rangle, \tag{B.1.2}$$

the two nearest neighbor TB Hamiltonian yields:

$$\langle \mathbf{K}+\mathbf{k},a|\mathcal{H}^{\mathrm{TB}}|\mathbf{K}+\mathbf{k},a'\rangle = \mathcal{H}^{\mathrm{TB}}_{\mathbf{K}}(\mathbf{k}) = \begin{pmatrix} g(\mathbf{k}) & h(\mathbf{k}) \\ h^*(\mathbf{k}) & g(\mathbf{k}) \end{pmatrix}, \tag{B.1.3}$$

where the "star" notation indicates complex conjugates and

$$h(\mathbf{k}) = -t_1 \sum_{l=1,3} e^{(\mathbf{K}+\mathbf{k})\cdot\mathbf{C}^{\mathbf{1}}_{\mathbf{l}}} \quad , \quad g(\mathbf{k}) = -t_2 \sum_{l=1,6} e^{(\mathbf{K}+\mathbf{k})\cdot\mathbf{C}^{\mathbf{2}}_{\mathbf{l}}}. \tag{B.1.4}$$

The vectors $\mathbf{C}^{\mathbf{j}}_{\mathbf{l}}$ connect atom 1 to its l j^{th} nearest neighbors. For $\mathbf{k} \ll \mathbf{K}$, one gets:

$$\mathcal{H}^{\mathrm{TB}}_{\mathbf{K}}(\mathbf{k}) = \begin{pmatrix} 3t_2 & \frac{3b_0}{2} t_1 (k_x - ik_y) \\ \frac{3b_0}{2} t_1 (k_x + ik_y) & 3t_2 \end{pmatrix}, \tag{B.1.5}$$

where b_0 is the interatomic distance. Up to a redefinition of the zero for energies, this is similar to the Hamiltonian of Eq. (2.1.1), with:

$$\hbar v_F = \frac{3b_0}{2} t_1 \tag{B.1.6}$$

B.2 Derivation of EPC from the TB Hamiltonian

In the following we derive the TB electron-phonon interaction Hamiltonian. The TB Hamiltonian is separated in first and second nearest neighbors contributions as follows:

$$\mathcal{H}_1^{\mathrm{TB}} = -\sum_{1^{\mathrm{st}}\mathrm{n.n.}} t_1 |\mathbf{R},a\rangle\langle\mathbf{R}',a'| \tag{B.2.1}$$

$$\mathcal{H}_2^{\mathrm{TB}} = -\sum_{2^{\mathrm{nd}}\mathrm{n.n.}} t_2 |\mathbf{R},a\rangle\langle\mathbf{R}',a'| \tag{B.2.2}$$

B.2.1 First nearest neighbors contribution

We start by calculating the derivative $\Delta\mathcal{H}_{1,1}^{\mathrm{TB}}$ of the first nearest neighbors term of the TB Hamiltonian with respect to a phonon displacement $\mathbf{e}^1_{\mathbf{q},\tilde{\nu}}$ of atom 1.

$$\Delta\mathcal{H}_{1,1}^{\mathrm{TB}} = \frac{\partial}{\partial \mathbf{e}^1_{\mathbf{q},\tilde{\nu}}} \left(-\sum_{1^{\mathrm{st}}\mathrm{n.n.}} t_1 |\mathbf{R},a\rangle\langle\mathbf{R}',a'| \right) = \sum_{1^{\mathrm{st}}\mathrm{n.n.}} \eta_1 \frac{\mathbf{C}^{\mathbf{1}}_{\mathbf{l}} \cdot \mathbf{e}^1_{\mathbf{q},\tilde{\nu}}}{b_0} |\mathbf{R},a\rangle\langle\mathbf{R}',a'| \tag{B.2.3}$$

where $\eta_1 = \frac{\partial t_1}{\partial b_0}$, and $-\eta_1 \frac{\mathbf{C}^{\mathbf{1}}_{\mathbf{l}} \cdot \mathbf{e}^1_{\mathbf{q},\tilde{\nu}}}{b_0}$ is the variation of the hopping parameter when atom 1 moves by $\mathbf{e}^1_{\mathbf{q},\tilde{\nu}}$. The minus sign is because the hopping parameter increases when the distance decreases. A similar expression is obtained for a displacement of atom 2, with a minus sign because the vectors connecting atom 2 to its neighbors are opposite:

$$\Delta\mathcal{H}_{1,2}^{\mathrm{TB}} = \frac{\partial}{\partial \mathbf{e}^2_{\mathbf{q},\tilde{\nu}}} \left(-\sum_{1^{\mathrm{st}}\mathrm{n.n.}} t_1 |\mathbf{R},a\rangle\langle\mathbf{R}',a'| \right) = -\sum_{1^{\mathrm{st}}\mathrm{n.n.}} \eta_1 \frac{\mathbf{C}^{\mathbf{1}}_{\mathbf{l}} \cdot \mathbf{e}^2_{\mathbf{q},\tilde{\nu}}}{b_0} |\mathbf{R},a\rangle\langle\mathbf{R}',a'| \tag{B.2.4}$$

Now we calculate the corresponding matrix elements $\langle \mathbf{K}+\mathbf{k}+\mathbf{q},a|\Delta\mathcal{H}^{\mathrm{TB}}_{1,a''}|\mathbf{K}+\mathbf{k},a'\rangle$. Only off-diagonal ($a \neq a'$) matrix elements are non-zero since the first neighbors of atom a are necessarily from the other sublattice. For $a=1$, $a'=2$ and $a''=1$, we get:

$$\langle \mathbf{K}+\mathbf{k}+\mathbf{q},1|\Delta\mathcal{H}_{1,1}^{\mathrm{TB}}|\mathbf{K}+\mathbf{k},2\rangle = \frac{1}{N} \sum_{1^{\mathrm{st}}\mathrm{n.n.}} \eta_1 \frac{\mathbf{C}^{\mathbf{1}}_{\mathbf{l}} \cdot \mathbf{e}^1_{\mathbf{q},\tilde{\nu}}}{b_0} e^{-i(\mathbf{K}+\mathbf{k}+\mathbf{q})\cdot(\mathbf{R}+\mathbf{d}_1)} e^{i(\mathbf{K}+\mathbf{k})\cdot(\mathbf{R}'+\mathbf{d}_2)} \tag{B.2.5}$$

$$= \frac{1}{N} \sum_{\mathbf{R},l} \eta_1 \frac{\mathbf{C}^{\mathbf{1}}_{\mathbf{l}} \cdot \mathbf{e}^1_{\mathbf{q},\tilde{\nu}}}{b_0} e^{-i\mathbf{q}\cdot(\mathbf{R}+\mathbf{d}_1)} e^{i(\mathbf{K}+\mathbf{k})\cdot\mathbf{C}^{\mathbf{1}}_{\mathbf{l}}} \tag{B.2.6}$$

It is now convenient to extract the phase factor from the phonon eigenvector $\mathbf{e}^a_{\mathbf{q},\tilde{\nu}} = \bar{\mathbf{e}}^a_{\mathbf{q},\tilde{\nu}} e^{i\mathbf{q}\cdot(\mathbf{R}+\mathbf{d_a})}$ such that we end up with the same contribution from each cell:

$$\langle \mathbf{K}+\mathbf{k}+\mathbf{q},1|\Delta\mathcal{H}^{\mathrm{TB}}_{1,1}|\mathbf{K}+\mathbf{k},2\rangle = \frac{1}{N}\sum_{\mathbf{R},l}\eta_1 \frac{\mathbf{C_l^1}\cdot\bar{\mathbf{e}}^1_{\mathbf{q},\tilde{\nu}}}{b_0} e^{i(\mathbf{K}+\mathbf{k})\cdot\mathbf{C_l^1}} \tag{B.2.7}$$

$$= \sum_l \frac{\eta_1}{b_0} e^{i(\mathbf{K}+\mathbf{k})\cdot\mathbf{C_l^1}} \mathbf{C_l^1}\cdot\bar{\mathbf{e}}^1_{\mathbf{q},\tilde{\nu}} \tag{B.2.8}$$

$$= \mathbf{h}'(\mathbf{k})\cdot\bar{\mathbf{e}}^1_{\mathbf{q},\tilde{\nu}} \tag{B.2.9}$$

We introduce the vector function $\mathbf{h}'(\mathbf{k}) = \sum_l \frac{\eta_1}{b_0} e^{i(\mathbf{K}+\mathbf{k})\cdot\mathbf{C_l^1}}\mathbf{C_l^1}$. The prime notation in $\mathbf{h}'$ is loosely used for its resemblance to a derivative of the function $h(\mathbf{k})$ used before. By following the same process of eliminating the phonon phase factors, we get:

$$\langle \mathbf{K}+\mathbf{k}+\mathbf{q},2|\Delta\mathcal{H}^{\mathrm{TB}}_{1,1}|\mathbf{K}+\mathbf{k},1\rangle = \mathbf{h}'^*(\mathbf{k}+\mathbf{q})\cdot\bar{\mathbf{e}}^1_{\mathbf{q},\tilde{\nu}} \tag{B.2.10}$$

$$\langle \mathbf{K}+\mathbf{k}+\mathbf{q},1|\Delta\mathcal{H}^{\mathrm{TB}}_{1,2}|\mathbf{K}+\mathbf{k},2\rangle = -\mathbf{h}'(\mathbf{k}+\mathbf{q})\cdot\bar{\mathbf{e}}^2_{\mathbf{q},\tilde{\nu}} \tag{B.2.11}$$

$$\langle \mathbf{K}+\mathbf{k}+\mathbf{q},2|\Delta\mathcal{H}^{\mathrm{TB}}_{1,2}|\mathbf{K}+\mathbf{k},1\rangle = -\mathbf{h}'^*(\mathbf{k})\cdot\bar{\mathbf{e}}^2_{\mathbf{q},\tilde{\nu}} \tag{B.2.12}$$

B.2.2 Second nearest neighbors contribution

Now we calculate $\Delta\mathcal{H}^{\mathrm{TB}}_{2,a''}$. This yields non-zero matrix elements $\langle \mathbf{K}+\mathbf{k}+\mathbf{q},a|\Delta\mathcal{H}^{\mathrm{TB}}_{2,a''}|\mathbf{K}+\mathbf{k},a'\rangle$ only when $a = a' = a''$, since the 2$^{\mathrm{nd}}$ nearest neighbors of an atom of type a are of type a as well, and those must move to give a non-zero contribution.

$$\Delta\mathcal{H}^{\mathrm{TB}}_{2,a} = \frac{\partial}{\partial\mathbf{e}^a_{\mathbf{q},\tilde{\nu}}}\left(-\sum_{2^{\mathrm{nd}}\mathrm{n.n.}} t_2|\mathbf{R},a\rangle\langle\mathbf{R}',a|\right) \tag{B.2.13}$$

$$= \sum_{2^{\mathrm{nd}}\mathrm{n.n.}} \eta_2 \frac{\mathbf{C_l^2}\cdot\mathbf{e}^a_{\mathbf{q},\tilde{\nu}}}{\sqrt{3}b_0}\left(1-e^{i\mathbf{q}\cdot(\mathbf{R}'-\mathbf{R})}\right)|\mathbf{R},a\rangle\langle\mathbf{R}',a| \tag{B.2.14}$$

$$\tag{B.2.15}$$

where $\eta_2 = \frac{\partial t_2}{\partial b_0}$. Again, the phonon phase factor cancel in the matrix elements, and we get the same contribution from every cell:

$$\langle \mathbf{K}+\mathbf{k}+\mathbf{q},a|\Delta\mathcal{H}^{\mathrm{TB}}_{2,a}|\mathbf{K}+\mathbf{k},a\rangle = \sum_l \eta_2 \frac{\mathbf{C_l^2}\cdot\bar{\mathbf{e}}^a_{\mathbf{q},\tilde{\nu}}}{\sqrt{3}b_0}\left(1-e^{i\mathbf{q}\cdot\mathbf{C_l^2}}\right)e^{i(\mathbf{K}+\mathbf{k})\cdot\mathbf{C_l^2}} \tag{B.2.16}$$

$$= \mathbf{g}'(\mathbf{k},\mathbf{q})\cdot\bar{\mathbf{e}}^a_{\mathbf{q},\tilde{\nu}} \tag{B.2.17}$$

with $\mathbf{g}'(\mathbf{k},\mathbf{q}) = \sum_l \frac{\eta_2}{\sqrt{3}b_0}\left(1-e^{i\mathbf{q}\cdot\mathbf{C_l^2}}\right)e^{i(\mathbf{K}+\mathbf{k})\cdot\mathbf{C_l^2}}\mathbf{C_l^2}$

B.3 First order expansion at small wave vectors

By summing the above contributions, we can write the TB EPC matrix $\Delta\mathcal{H}^{\mathrm{TB}}_{\mathbf{q},\tilde{\nu}}$ in the pseudo-spinor basis:

$$\Delta\mathcal{H}^{\mathrm{TB}}_{\mathbf{q},\tilde{\nu}} = \begin{pmatrix} \mathbf{g}'(\mathbf{k},\mathbf{q})\cdot\bar{\mathbf{e}}^1_{\mathbf{q},\tilde{\nu}} & \mathbf{h}'(\mathbf{k})\cdot\bar{\mathbf{e}}^1_{\mathbf{q},\tilde{\nu}} - \mathbf{h}'(\mathbf{k}+\mathbf{q})\cdot\bar{\mathbf{e}}^2_{\mathbf{q},\tilde{\nu}} \\ \mathbf{h}'^*(\mathbf{k}+\mathbf{q})\cdot\bar{\mathbf{e}}^1_{\mathbf{q},\tilde{\nu}} - \mathbf{h}'^*(\mathbf{k})\cdot\bar{\mathbf{e}}^2_{\mathbf{q},\tilde{\nu}} & \mathbf{g}'(\mathbf{k},\mathbf{q})\cdot\bar{\mathbf{e}}^2_{\mathbf{q},\tilde{\nu}} \end{pmatrix} \tag{B.3.1}$$

We are interested in the small vector limit of EPC. We develop the function $\mathbf{h}'$ at first order in $\mathbf{k}$:

$$\mathbf{h}'(\mathbf{k}) = \mathbf{h}'(\mathbf{0}) + \mathbf{k}\cdot\nabla_{\mathbf{k}}\mathbf{h}'|_{\mathbf{k}=\mathbf{0}} \tag{B.3.2}$$

$$= \sum_l \frac{\eta_1}{b_0} e^{i\mathbf{K}\cdot\mathbf{C_l^1}}\mathbf{C_l^1} + \mathbf{k}\cdot\sum_l \frac{i\eta_1}{b_0}\mathbf{C_l^1} e^{i\mathbf{K}\cdot\mathbf{C_l^1}}\mathbf{C_l^1} \tag{B.3.3}$$

with $\mathbf{K} = (2/3,0)\frac{2\pi}{b}$, $\mathbf{C_1^1} = (0,-1/\sqrt{3})b$, $\mathbf{C_2^1} = (1/2,1/2\sqrt{3})b$, and $\mathbf{C_2^1} = (-1/2,1/2\sqrt{3})b$, we get:

$$\mathbf{h}'(\mathbf{0}) = \frac{3\eta_1}{2}\begin{pmatrix} i \\ -1 \end{pmatrix} \tag{B.3.4}$$

$$\nabla_{\mathbf{k}}\mathbf{h}'|_{\mathbf{k}=\mathbf{0}} = \frac{3i\eta_1 b_0}{4}\begin{pmatrix} -1 & i \\ i & 1 \end{pmatrix} \tag{B.3.5}$$

The function $\mathbf{g}'$ is developed at first orders in $\mathbf{k}$ and $\mathbf{q}$:

$$\mathbf{g}'(\mathbf{k}) = \mathbf{g}'(\mathbf{0},\mathbf{0}) + \mathbf{k}\cdot\nabla_{\mathbf{k}}\mathbf{g}'|_{\mathbf{k}=\mathbf{0},\mathbf{q}=\mathbf{0}} + \mathbf{q}\cdot\nabla_{\mathbf{q}}\mathbf{g}'|_{\mathbf{k}=\mathbf{0},\mathbf{q}=\mathbf{0}} \tag{B.3.6}$$

$$\mathbf{g}'(\mathbf{0},\mathbf{0}) = \mathbf{0} \tag{B.3.7}$$

$$\nabla_{\mathbf{k}}\mathbf{g}'|_{\mathbf{k}=\mathbf{0}} = \mathbf{0} \tag{B.3.8}$$

$$\nabla_{\mathbf{q}}\mathbf{g}'|_{\mathbf{q}=\mathbf{0}} = -\sum_l \frac{i\eta_2}{\sqrt{3}b_0}\mathbf{C_l^2} e^{i\mathbf{K}\cdot\mathbf{C_l^2}}\mathbf{C_l^2} \tag{B.3.9}$$

with $\mathbf{K} = (2/3,0)\frac{2\pi}{b}$, $\mathbf{C_1^2} = (1,0)b$, $\mathbf{C_2^2} = (1/2,\sqrt{3}/2)b$, $\mathbf{C_3^2} = (-1/2,\sqrt{3}/2)b$, $\mathbf{C_4^2} = (-1,0)b$, $\mathbf{C_5^2} = (-1/2,-\sqrt{3}/2)b$, $\mathbf{C_3^2} = (1/2,-\sqrt{3}/2)b$, we get:

$$\nabla_{\mathbf{q}}\mathbf{g}'|_{\mathbf{q}=\mathbf{0}} = \frac{3\sqrt{3}i\eta_2 b_0}{2}\begin{pmatrix} 1 & 0 \\ 0 & 1 \end{pmatrix} \tag{B.3.10}$$

We now have all the elements to express the EPC matrix for the canonical acoustic and optical phonon modes.

B.4 EPC matrix in the TB model

B.4.1 Optical phonons

For the optical phonons, we have $\bar{\mathbf{e}}^2_{\mathbf{q},\tilde{O}} = -\bar{\mathbf{e}}^1_{\mathbf{q},\tilde{O}}$. This implies that the lowest order in $\mathbf{q}$ is zero, in the off-diagonal elements. We neglect all higher orders.

$$\Delta\mathcal{H}^{\mathrm{TB}}_{\mathbf{q},\tilde{O}} = \begin{pmatrix} 0 & 2\mathbf{h}'(\mathbf{0})\cdot\bar{\mathbf{e}}^1_{\mathbf{q},\tilde{O}} \\ 2\mathbf{h}'^*(\mathbf{0})\cdot\bar{\mathbf{e}}^1_{\mathbf{q},\tilde{O}} & 0 \end{pmatrix} \tag{B.4.1}$$

The scalar product is easiest in the $\frac{1}{|\mathbf{q}|}\{\mathbf{q},\mathbf{q}_\perp\}$ basis. For this, we have to rotate the vectors in the $\{\mathbf{x},\mathbf{y}\}$ by an angle $-\theta_{\mathbf{q}}$, that is multiplying them from the left by the rotation matrix:

$$R = \begin{pmatrix} \cos(\theta_{\mathbf{q}}) & \sin(\theta_{\mathbf{q}}) \\ -\sin(\theta_{\mathbf{q}}) & \cos(\theta_{\mathbf{q}}) \end{pmatrix} \tag{B.4.2}$$

$$2\mathbf{h}'(\mathbf{0}) \cdot \bar{\mathbf{e}}^1_{\mathbf{q},\tilde{O}} = 2\frac{3\eta_1}{2} e^{i\theta_{\mathbf{q}}} \begin{pmatrix} i \\ -1 \end{pmatrix} \cdot \frac{1}{\sqrt{2}} \begin{pmatrix} Q_{\widetilde{\mathrm{LO}}} \\ Q_{\widetilde{\mathrm{TO}}} \end{pmatrix} \tag{B.4.3}$$

$$= i\frac{3\eta_1}{\sqrt{2}} e^{i\theta_{\mathbf{q}}} (Q_{\widetilde{\mathrm{LO}}} + iQ_{\widetilde{\mathrm{TO}}}) \tag{B.4.4}$$

$$2\mathbf{h}'^*(\mathbf{0}) \cdot \bar{\mathbf{e}}^1_{\mathbf{q},\tilde{O}} = -i\frac{3\eta_1}{\sqrt{2}} e^{-i\theta_{\mathbf{q}}} (Q_{\widetilde{\mathrm{LO}}} - iQ_{\widetilde{\mathrm{TO}}}) \tag{B.4.5}$$

$$\Delta\mathcal{H}^{\mathrm{TB}}_{\mathbf{q},\tilde{O}} = i \times \begin{pmatrix} 0 & \frac{3\eta_1}{\sqrt{2}} e^{i\theta_{\mathbf{q}}} (Q_{\widetilde{\mathrm{LO}}} + iQ_{\widetilde{\mathrm{TO}}}) \\ -\frac{3\eta_1}{\sqrt{2}} e^{-i\theta_{\mathbf{q}}} (Q_{\widetilde{\mathrm{LO}}} - iQ_{\widetilde{\mathrm{TO}}}) & 0 \end{pmatrix} \tag{B.4.6}$$

The matrix has of course the same form as the one derived from symmetry considerations in Sec. 2.2. However, it is less general. The particularity of the TB model is that the magnitude of the matrix elements are related to the derivative of the hopping integral. We can associate the parameters from both model by writing:

$$\tilde{\beta_O} \equiv \frac{3\eta_1}{\sqrt{2}}. \tag{B.4.7}$$

One should keep in mind that $\tilde{\beta_O}$ is much more general than its TB counterpart, as discussed in Sec. 3.2. Similar calculations for the coupling to the optical mode A'_1 at $\mathbf{K}$ can be carried out and we find that:

$$\beta_K \equiv \tilde{\beta_O} \equiv \frac{3\eta_1}{\sqrt{2}}. \tag{B.4.8}$$

B.4.2 Acoustic phonons

For the acoustic phonons, we have $\bar{\mathbf{e}}^2_{\mathbf{q},\tilde{A}} = \bar{\mathbf{e}}^1_{\mathbf{q},\tilde{A}}$. This implies that the lowest order in $\mathbf{q}$ is one, in the off-diagonal and diagonal elements. We neglect all higher orders.

$$\Delta\mathcal{H}^{\mathrm{TB}}_{\mathbf{q},\tilde{A}} = \begin{pmatrix} \mathbf{q} \cdot \nabla_{\mathbf{q}}\mathbf{g}'|_{\mathbf{q}=\mathbf{0}} \cdot \bar{\mathbf{e}}^1_{\mathbf{q},\tilde{A}} & -\mathbf{q} \cdot \nabla_{\mathbf{k}}\mathbf{h}'|_{\mathbf{k}=\mathbf{0}} \cdot \bar{\mathbf{e}}^1_{\mathbf{q},\tilde{A}} \\ \mathbf{q} \cdot \nabla_{\mathbf{k}}\mathbf{h}'^*|_{\mathbf{k}=\mathbf{0}} \cdot \bar{\mathbf{e}}^1_{\mathbf{q},\tilde{A}} & \mathbf{q} \cdot \nabla_{\mathbf{q}}\mathbf{g}'|_{\mathbf{q}=\mathbf{0}} \cdot \bar{\mathbf{e}}^2_{\mathbf{q},\tilde{A}} \end{pmatrix}$$

With:

$$\mathbf{q} \cdot \nabla_{\mathbf{q}}\mathbf{g}'|_{\mathbf{q}=\mathbf{0}} \cdot \bar{\mathbf{e}}^a_{\mathbf{q},\tilde{\nu}} = \frac{3\sqrt{3}i\eta_2 b_0}{2} \mathbf{q} \cdot \bar{\mathbf{e}}^a_{\mathbf{q},\tilde{\nu}} \tag{B.4.9}$$

$$= \frac{3\sqrt{3}i\eta_2 b_0}{2\sqrt{2}} |\mathbf{q}| Q_{\widetilde{LA}} \tag{B.4.10}$$

and

$$-\mathbf{q}\cdot\nabla_{\mathbf{k}}\mathbf{h}'|_{\mathbf{k}=\mathbf{0}}\cdot\bar{\mathbf{e}}^{1}_{\mathbf{q},\tilde{A}} = -\frac{3i\eta_1 b_0}{4}\mathbf{q}\cdot R\begin{pmatrix}-1 & i\\ i & 1\end{pmatrix}R^T\cdot\bar{\mathbf{e}}^{1}_{\mathbf{q},\tilde{A}} \tag{B.4.11}$$

$$= \frac{3i\eta_1 b_0}{4\sqrt{2}}e^{-2i\theta_{\mathbf{q}}}|\mathbf{q}|(Q_{\widetilde{LA}} - iQ_{\widetilde{TA}}) \tag{B.4.12}$$

$$\mathbf{q}\cdot\nabla_{\mathbf{k}}\mathbf{h}'^{*}|_{\mathbf{k}=\mathbf{0}}\cdot\bar{\mathbf{e}}^{1}_{\mathbf{q},\tilde{A}} = \frac{3i\eta_1 b_0}{4\sqrt{2}}e^{2i\theta_{\mathbf{q}}}|\mathbf{q}|(Q_{\widetilde{LA}} + iQ_{\widetilde{TA}}) \tag{B.4.13}$$

$$\Delta\mathcal{H}^{\mathrm{TB}}_{\tilde{A}} = i|\mathbf{q}|\times\begin{pmatrix}\frac{3\sqrt{3}\eta_2 b_0}{2\sqrt{2}}Q_{\widetilde{LA}} & \frac{3\eta_1 b_0}{4\sqrt{2}}e^{-2i\theta_{\mathbf{q}}}(Q_{\widetilde{LA}} - iQ_{\widetilde{TA}})\\ \frac{3\eta_1 b_0}{4\sqrt{2}}e^{2i\theta_{\mathbf{q}}}(Q_{\widetilde{LA}} + iQ_{\widetilde{TA}}) & \frac{3\sqrt{3}\eta_2 b_0}{2\sqrt{2}}Q_{\widetilde{LA}}\end{pmatrix} \tag{B.4.14}$$

Again, the EPC matrix has the same form as in 2.2, and we can associate the following parameters:

$$\tilde{\beta_A} \equiv \frac{3\eta_1 b_0}{4\sqrt{2}} \tag{B.4.15}$$

$$\alpha^{\mathrm{bare}} \equiv \frac{3\sqrt{3}\eta_2 b_0}{4\sqrt{2}} \tag{B.4.16}$$

once more keeping in mind that the validity of those relations is limited to the validity of the of the two-nearest-neighbors TB model. Also, the bare deformation potential is used because screening is absent from the TB model.

Chapter C

Derivation of the suceptibility

In this appendix we detail the derivation of the analytical independent particle susceptibility $\tilde{\chi}^0(\mathbf{q}_p)$:

$$\tilde{\chi}^0(\mathbf{q}_p) = \frac{1}{\pi^2}\int_{\mathbf{K}} d^2\mathbf{k} \sum_{s,s'} |\langle \mathbf{k},s|\mathbf{k}+\mathbf{q}_p,s'\rangle|^2 \frac{f(\varepsilon_{\mathbf{k},s}) - f(\varepsilon_{\mathbf{k}+\mathbf{q}_p,s'})}{\varepsilon_{\mathbf{k},s} - \varepsilon_{\mathbf{k}+\mathbf{q}_p,s'}}. \tag{C.0.1}$$

Similar derivations were performed by the authors of Refs. [63, 64, 65, 66, 67, 68, 69]. Since very few details were given, we deem useful to give some more details here. Note that there might be more efficient ways to perform the following derivations.

Since we are working in a strictly 2D framework, there is no ambiguity about the fact that $\mathbf{q}_p$ is in-plane and we drop the "p" index. In the Dirac cone model, we sum over the π ($s=+1$) and π^* ($s=-1$) bands:

$$\begin{aligned}\tilde{\chi}^0(|\mathbf{q}|) = \frac{1}{2\pi^2}\int_{\mathbf{K}} d^2\mathbf{k}\Big[&(1+\cos(\theta_{\mathbf{k},\mathbf{k}+\mathbf{q}}))\frac{f^+_{\mathbf{k}} - f^+_{\mathbf{k}+\mathbf{q}}}{\varepsilon_{\mathbf{k}} - \varepsilon_{\mathbf{k}+\mathbf{q}}} + (1+\cos(\theta_{\mathbf{k},\mathbf{k}+\mathbf{q}}))\frac{f^-_{\mathbf{k}} - f^-_{\mathbf{k}+\mathbf{q}}}{-\varepsilon_{\mathbf{k}} + \varepsilon_{\mathbf{k}+\mathbf{q}}} \\ &+ (1-\cos(\theta_{\mathbf{k},\mathbf{k}+\mathbf{q}}))\frac{f^+_{\mathbf{k}} - f^-_{\mathbf{k}+\mathbf{q}}}{\varepsilon_{\mathbf{k}} + \varepsilon_{\mathbf{k}+\mathbf{q}}} + (1-\cos(\theta_{\mathbf{k},\mathbf{k}+\mathbf{q}}))\frac{f^-_{\mathbf{k}} - f^+_{\mathbf{k}+\mathbf{q}}}{-\varepsilon_{\mathbf{k}} - \varepsilon_{\mathbf{k}+\mathbf{q}}}\Big]\end{aligned} \tag{C.0.2}$$

where we set $\varepsilon_{\mathbf{k}} = |\varepsilon_{\mathbf{k},s}| = \hbar v_F|\mathbf{k}|$, $f^+_{\mathbf{k}} = f(\varepsilon_{\mathbf{k},+1})$, and $\theta_{\mathbf{k},\mathbf{k}+\mathbf{q}} = \theta_{\mathbf{k}} - \theta_{\mathbf{k}+\mathbf{q}}$ to simplify notations. As indicated in [69], it is convenient to separate $\tilde{\chi}^0(|\mathbf{q}_p|) = \tilde{\chi}^0_+(|\mathbf{q}_p|) + \tilde{\chi}^0_-(|\mathbf{q}_p|)$ as follows:

$$\tilde{\chi}^0_+(|\mathbf{q}|) = \frac{1}{2\pi^2}\int d^2\mathbf{k}\Big[(1+\cos(\theta_{\mathbf{k},\mathbf{k}+\mathbf{q}}))\frac{f^+_{\mathbf{k}} - f^+_{\mathbf{k}+\mathbf{q}}}{\varepsilon_{\mathbf{k}} - \varepsilon_{\mathbf{k}+\mathbf{q}}} + (1-\cos(\theta_{\mathbf{k},\mathbf{k}+\mathbf{q}}))\frac{f^+_{\mathbf{k}} + f^+_{\mathbf{k}+\mathbf{q}}}{\varepsilon_{\mathbf{k}} + \varepsilon_{\mathbf{k}+\mathbf{q}}}\Big] \tag{C.0.3}$$

$$\tilde{\chi}^0_-(|\mathbf{q}|) = -\frac{1}{2\pi^2}\int d^2\mathbf{k}\Big[(1+\cos(\theta_{\mathbf{k},\mathbf{k}+\mathbf{q}}))\frac{f^-_{\mathbf{k}} - f^-_{\mathbf{k}+\mathbf{q}}}{\varepsilon_{\mathbf{k}} - \varepsilon_{\mathbf{k}+\mathbf{q}}} + (1-\cos(\theta_{\mathbf{k},\mathbf{k}+\mathbf{q}}))\frac{f^-_{\mathbf{k}} + f^-_{\mathbf{k}+\mathbf{q}}}{\varepsilon_{\mathbf{k}} + \varepsilon_{\mathbf{k}+\mathbf{q}}}\Big] \tag{C.0.4}$$

Let us start with $\tilde{\chi}^0_-(|\mathbf{q}|)$. The first term is obviously zero for electron doping (and at

zero temperature), but we must keep it in order to rearrange the integral as follows:

$$\tilde{\chi}^0_-(|\mathbf{q}|) = -\frac{1}{2\pi^2}\int d^2\mathbf{k}\Big[f^-_{\mathbf{k}}\left(\frac{1+\cos(\theta_{\mathbf{k},\mathbf{k+q}})}{\varepsilon_{\mathbf{k}}-\varepsilon_{\mathbf{k+q}}}+\frac{1-\cos(\theta_{\mathbf{k},\mathbf{k+q}})}{\varepsilon_{\mathbf{k}}+\varepsilon_{\mathbf{k+q}}}\right) + f^-_{\mathbf{k+q}}\left(\frac{1-\cos(\theta_{\mathbf{k},\mathbf{k+q}})}{\varepsilon_{\mathbf{k}}+\varepsilon_{\mathbf{k+q}}}-\frac{1+\cos(\theta_{\mathbf{k},\mathbf{k+q}})}{\varepsilon_{\mathbf{k}}-\varepsilon_{\mathbf{k+q}}}\right)\Big] \tag{C.0.5}$$

By extracting a common denominator for all the fractions, we find:

$$\tilde{\chi}^0_-(|\mathbf{q}|) = -\frac{1}{\pi^2}\int d^2\mathbf{k}\frac{1}{\varepsilon^2_{\mathbf{k}}-\varepsilon^2_{\mathbf{k+q}}}\Big[f^-_{\mathbf{k}}\left\{\varepsilon_{\mathbf{k}}+\varepsilon_{\mathbf{k+q}}\cos(\theta_{\mathbf{k},\mathbf{k+q}})\right\} - f^-_{\mathbf{k+q}}\left\{\varepsilon_{\mathbf{k+q}}+\varepsilon_{\mathbf{k}}\cos(\theta_{\mathbf{k},\mathbf{k+q}})\right\}\Big] \tag{C.0.6}$$

There is a kind of symmetry between $\mathbf{k}$ and $\mathbf{k}+\mathbf{q}$. We are going to exploit this symmetry by noticing that:

$$|\mathbf{k}+\mathbf{q}|\cos(\theta_{\mathbf{k},\mathbf{k+q}}) = |\mathbf{k}| + |\mathbf{q}|\cos(\theta_{\mathbf{k}}) \tag{C.0.7}$$

$$|\mathbf{k}|\cos(\theta_{\mathbf{k},\mathbf{k+q}}) = |\mathbf{k}+\mathbf{q}| - |\mathbf{q}|\cos(\theta_{\mathbf{k+q}}) \tag{C.0.8}$$

where the angles $\theta_{\mathbf{k}}$ and $\theta_{\mathbf{k+q}}$ are measured from the direction of $\mathbf{q}$. We now write:

$$\tilde{\chi}^0_-(|\mathbf{q}|) = -\frac{1}{\pi^2}\int d^2\mathbf{k}\frac{1}{\varepsilon^2_{\mathbf{k}}-\varepsilon^2_{\mathbf{k+q}}}\Big[f^-_{\mathbf{k}}\left\{2\varepsilon_{\mathbf{k}}+\hbar v_F|\mathbf{q}|\cos(\theta_{\mathbf{k}})\right\} - f^-_{\mathbf{k+q}}\left\{2\varepsilon_{\mathbf{k+q}}-\hbar v_F|\mathbf{q}|\cos(\theta_{\mathbf{k+q}})\right\}\Big] \tag{C.0.9}$$

Using a change of variable $\mathbf{k}+\mathbf{q}\to\mathbf{k}$ in the second term and using $\varepsilon_{\mathbf{k}} = \hbar v_F|\mathbf{k}|$ we obtain:

$$\tilde{\chi}^0_-(|\mathbf{q}|) = -\frac{1}{\pi^2\hbar v_F}\int d^2\mathbf{k} f^-_{\mathbf{k}}\left[\frac{2|\mathbf{k}|+|\mathbf{q}|\cos(\theta_{\mathbf{k}})}{|\mathbf{k}|^2-|\mathbf{k}+\mathbf{q}|^2}+\frac{2|\mathbf{k}|-|\mathbf{q}|\cos(\theta_{\mathbf{k}})}{|\mathbf{k}|^2-|\mathbf{k}-\mathbf{q}|^2}\right] \tag{C.0.10}$$

$$= -\frac{1}{\pi^2\hbar v_F}\int d^2\mathbf{k} f^-_{\mathbf{k}}\left[\frac{2|\mathbf{k}|+|\mathbf{q}|\cos(\theta_{\mathbf{k}})}{-|\mathbf{q}|^2-2|\mathbf{k}||\mathbf{q}|\cos(\theta_{\mathbf{k}})}+\frac{2|\mathbf{k}|-|\mathbf{q}|\cos(\theta_{\mathbf{k}})}{-|\mathbf{q}|^2+2|\mathbf{k}||\mathbf{q}|\cos(\theta_{\mathbf{k}})}\right] \tag{C.0.11}$$

$$= \frac{1}{2\pi^2\hbar v_F}\int d|\mathbf{k}|d\theta_{\mathbf{k}} f^-_{\mathbf{k}}\left[\frac{\frac{2|\mathbf{k}|}{|\mathbf{q}|}+\cos(\theta_{\mathbf{k}})}{\frac{|\mathbf{q}|}{2|\mathbf{k}|}+\cos(\theta_{\mathbf{k}})}+\frac{-\frac{2|\mathbf{k}|}{|\mathbf{q}|}+\cos(\theta_{\mathbf{k}})}{-\frac{|\mathbf{q}|}{2|\mathbf{k}|}+\cos(\theta_{\mathbf{k}})}\right] \tag{C.0.12}$$

Changing variables shows that the two terms give the same contribution to the integral. We have to calculate:

$$\tilde{\chi}^0_-(|\mathbf{q}|) = \frac{1}{\pi^2\hbar v_F}\int d|\mathbf{k}| f^-_{\mathbf{k}}\left(\int d\theta_{\mathbf{k}}\frac{\frac{2|\mathbf{k}|}{|\mathbf{q}|}+\cos(\theta_{\mathbf{k}})}{\frac{|\mathbf{q}|}{2|\mathbf{k}|}+\cos(\theta_{\mathbf{k}})}\right) \tag{C.0.13}$$

We first perform the angular integral. It is of the form:

$$I_1 = \int_{-\pi}^{\pi} d\theta\frac{a+\cos(\theta)}{a^{-1}+\cos(\theta)} \tag{C.0.14}$$

$$\tag{C.0.15}$$

We substitute $u = \tan(\theta/2)$ and $du = \frac{1}{2}\sec^2(\theta/2)$ and transform $\sin(\theta) = \frac{2u}{1+u^2}$, $\cos(\theta) = \frac{1-u^2}{1+u^2}$, $d\theta = \frac{2du}{1+u^2}$:

$$I_1 = \int_{-\infty}^{\infty} du \frac{2\left(a + \frac{1-u^2}{1+u^2}\right)}{(1+u^2)\left(1/a + \frac{1-u^2}{1+u^2}\right)} \tag{C.0.16}$$

$$= 2\int_{-\infty}^{\infty} du \frac{1}{(1+u^2)} + \frac{(a^2-1)}{(1+u^2)+a(1-u^2)} \tag{C.0.17}$$

$$= 2\left(\left[\tan^{-1}(u)\right]_{-\infty}^{\infty} + \frac{a^2-1}{1+a}\int_{-\infty}^{\infty} du \frac{1}{1+\frac{1-a}{1+a}u^2}\right) \tag{C.0.18}$$

The first term gives $\left[\tan^{-1}(u)\right]_{-\infty}^{\infty} = \pi$. The solution of the remaining integral depends on the sign of the prefactor of u^2, and therefore on $a = \frac{2|\mathbf{k}|}{|\mathbf{q}|}$. If $|\mathbf{k}| < |\mathbf{q}|/2$, we have:

$$\frac{a^2-1}{1+a}\int_{-\infty}^{\infty} du \frac{1}{1+\frac{1-a}{1+a}u^2} = -\pi\sqrt{1-a^2} \tag{C.0.19}$$

If $|\mathbf{k}| \geq |\mathbf{q}|/2$, we have:

$$\frac{a^2-1}{1+a}\int_{-\infty}^{\infty} du \frac{1}{1-\frac{a-1}{1+a}u^2} = 0 \tag{C.0.20}$$

Thus, coming back to $\tilde{\chi}^0_-(|\mathbf{q}|)$:

$$\tilde{\chi}^0_-(|\mathbf{q}|) = \frac{2}{\pi\hbar v_F}\int_0^{\infty} d|\mathbf{k}| f^-_{\mathbf{k}} - \frac{2}{\pi\hbar v_F}\int_0^{|\mathbf{q}|/2} d|\mathbf{k}| f^-_{\mathbf{k}}\sqrt{1-(2|\mathbf{k}|/|\mathbf{q}|)^2} \tag{C.0.21}$$

The derivation of $\tilde{\chi}^0_+(|\mathbf{q}|)$ is very similar:

$$\tilde{\chi}^0_+(|\mathbf{q}|) = -\frac{2}{\pi\hbar v_F}\int_0^{\infty} d|\mathbf{k}| f^+_{\mathbf{k}} + \frac{2}{\pi\hbar v_F}\int_0^{|\mathbf{q}|/2} d|\mathbf{k}| f^+_{\mathbf{k}}\sqrt{1-(2|\mathbf{k}|/|\mathbf{q}|)^2} \tag{C.0.22}$$

Setting the density of states to zero at the Dirac point, we have:

$$\frac{2}{\pi\hbar v_F}\int_0^{\infty} d|\mathbf{k}| = \mathrm{DOS}(\varepsilon_\mathrm{F} = 0) = 0 \tag{C.0.23}$$

For $\varepsilon_F \geq 0$, this gives:

$$\tilde{\chi}^0_-(|\mathbf{q}|) = -\frac{2}{\pi\hbar v_F}\int_0^{|\mathbf{q}|/2} d|\mathbf{k}| f^-_{\mathbf{k}}\sqrt{1-(2|\mathbf{k}|/|\mathbf{q}|)^2} \tag{C.0.24}$$

$$\tilde{\chi}^0_+(|\mathbf{q}|) = -\mathrm{DOS}(\varepsilon_F) + \frac{2}{\pi\hbar v_F}\int_0^{|\mathbf{q}|/2} d|\mathbf{k}| f^+_{\mathbf{k}}\sqrt{1-(2|\mathbf{k}|/|\mathbf{q}|)^2} \tag{C.0.25}$$

$$\tilde{\chi}^0(|\mathbf{q}|) = -\mathrm{DOS}(\varepsilon_F) + \frac{2}{\pi\hbar v_F}\int_0^{|\mathbf{q}|/2} d|\mathbf{k}| (f^+_{\mathbf{k}} - f^-_{\mathbf{k}})\sqrt{1-(2|\mathbf{k}|/|\mathbf{q}|)^2} \tag{C.0.26}$$

Chapter D

2D Coulomb cutoff at $\mathrm{G} = 0$

D.1 Treatment of divergent $\mathrm{G} = 0$ terms in the 3D QE code

In this section we highlight some practical issues arising in the implementation of a plane-wave DFT code and review the general idea behind their resolution in the standard QE code. We focus on the specific treatment of the individually divergent $\mathbf{G} = 0$ terms in the potentials and energy contributions. We refer to App. A and the references cited therein for a more global description of plane-wave DFT. More details on the issues approached here can be found in Ref. [18].

We consider the simulation of a 2D material using the plane-wave code of the QE package. In truth, we are discussing the simulation of a 3D-periodic material made of periodic images of the 2D system. We first consider a neutral system for which both the 2D system and the 3D-periodic system are well defined. The structure of the KS potential entails the separation of the material into two subsystems corresponding to ions and electrons. The electrons interact with the ions via the ionic potential, and with themselves via the Hartree interaction. For the purpose of this discussion, we can ignore the exchange-correlation potential. The two subsystems are treated quite differently. The ionic potential is computed from the pseudopotentials only once at the beginning of the calculation. For the electrons, the central quantity is the electron density, the Hartree potential being computed for the purpose of constructing the KS potential. The electron density and the Hartree potential are re-computed at each iteration of the self-consistent process. The computation of the potentials of the two subsystems is done separately.

The issue is that the subsystems are not physically well defined when taken individually. They roughly consist in the infinite periodic repetition of charged planes in vacuum. Such subsystems are unphysical because their charge, potentials and energies are diverging. In practice, this translates into a finite average charge in the unit cell, that is to say a non-zero $\mathbf{G} = 0$ component of the Fourier transform of either the ionic or electronic charge distribution. Via the diverging Coulomb interaction at small momenta, the $\mathbf{G} = 0$ terms of the potential and energy contribution associated with each subsystem is divergent. As long as the total system is globally neutral, it can be shown that those divergences cancel each other when summed in the KS potential and total energy [18, 19]. Yet we do need to compute finite potentials and energy contributions

for each subsystem.

This practical issue is easily treated at the potential level, since every potential is defined up to a constant. In the QE code, the simple convention of setting the average ($\mathbf{G} = 0$ term) of each potential to zero is chosen. At the potential level, this process can be interpreted as the addition of the so-called "jellium background", a uniform distribution of charges compensating for the charges of the subsystems. Each subsystem plus its jellium is then neutral, and the potentials are finite. For a neutral 2D material, since the charges of the subsystems – ions and electrons – are equal and opposite, so are their respective jellium backgrounds. Hence, when the subsystems are added, the jellium backgrounds cancel each other and the correct KS potential is recovered.

The separation into subsystems also applies at the energy level. The $\mathbf{G} = 0$ terms of the energy contributions associated with the ion-electron, electron-electron and ion-ion interactions are individually diverging. It can be shown, however, that their sum is finite in the case of a neutral system. At the energy level, the interpretation of the treatment of the $\mathbf{G} = 0$ divergences is more complex than the jellium picture used for the potentials. The general idea is to compute combinations of the individually divergent $\mathbf{G} = 0$ energy terms to form finite contributions [18]. Those finite contributions are then added to the total energy that we would obtain in a jellium picture by setting all the $\mathbf{G} = 0$ terms to zero. In any case, the idea that every contribution must be treated consistently remains.

Let us now consider the simulation of a doped 2D material. The 3D-periodic system made of periodic images of the charged 2D system has divergent potential and total energy. At the potential level, the use of a compensating jellium for the ionic and Hartree potentials implicitly takes care of this divergence. Indeed, as for a neutral system, each subsystem is defined with its own compensating jellium background. Due to the doping, however, those jellium backgrounds are not equal and opposite, and they do not cancel each other in the total KS potential. What the code effectively simulate is then the potential of a doped 2D material bathed in a remaining jellium background to compensate the doping. This situation could be labeled as a "jellium-induced doping", and is evidently very different from gate-induced doping. At the energy level, the divergent term that should appear because of the addition of the doping charges is dropped, and the meaning of the total energy becomes somewhat obscure.

In order to simulate the potential of a 2D material doped within the FET setup, we effectively eliminate the jellium. This implies modifying the treatment of the $\mathbf{G} = 0$ divergences. This treatment must be consistent for every potential and energy contribution.

D.2 Treatment of the $\mathrm{G} = 0$ singularities in the 2D code

D.2.1 $\mathrm{G} = 0$ value of the Coulomb interaction

The treatment of the $\mathbf{G} = 0$ terms with a 2D Coulomb cutoff is developed in Ref. [74], where the authors show that one should consistently separate all potentials into short-range and long-range contributions and use the following value for the $\mathbf{G} \to 0$

limit of the cutoff Coulomb interaction on the long-range parts:

$$\bar{v}_c(\mathbf{G} \to 0) = -2\pi e^2 l_z^2 \tag{D.2.1}$$

The following is an attempt at justifying this recommendation. Note that we use the notation $\mathbf{G} \to 0$ to distinguish this value from the value $\bar{v}_c(\mathbf{G} = 0) = 0$ used in our implementation. The potential $V(\mathbf{r}_p, z)$ generated by a generic 2D distribution $m(\mathbf{r}_p, z)$ via the cutoff Coulomb interaction is written:

$$V(\mathbf{r}_p, z) = e^2 \int_{\text{plane}} \int_{-l_z}^{+l_z} \frac{m(\mathbf{r}'_p, z')}{\sqrt{|\mathbf{r}'_p - \mathbf{r}_p|^2 + (z' - z)^2}} d\mathbf{r}'_p dz' \tag{D.2.2}$$

By changing variables and exploiting the in-plane periodicity of $m(\mathbf{r}_p, z)$, it can be shown that the planar average of the potential $V(\mathbf{G}_p = 0, z)$ reads:

$$V(\mathbf{G}_p = 0, z) = e^2 \int_{\text{plane}} \int_{-l_z}^{+l_z} \frac{\langle m \rangle_p(z')}{\sqrt{|\mathbf{r}_p|^2 + (z' - z)^2}} d\mathbf{r}_p dz' \tag{D.2.3}$$

This can be written as :

$$V(\mathbf{G}_p = 0, z) = \int_{-l_z}^{+l_z} \langle m \rangle_p(z') \;\; \bar{v}_c(\mathbf{G}_p = 0, |z - z'|) \; dz' \tag{D.2.4}$$

with

$$\bar{v}_c(\mathbf{G}_p = 0, |z|) = e^2 \int_{\text{plane}} \frac{1}{\sqrt{|\mathbf{r}_p|^2 + z^2}} d\mathbf{r}_p \tag{D.2.5}$$

$$= e^2 \int_{\text{plane}} \left[\frac{1}{|\mathbf{r}_p|} + \frac{1}{\sqrt{|\mathbf{r}_p|^2 + z^2}} - \frac{1}{|\mathbf{r}_p|} \right] d\mathbf{r}_p \tag{D.2.6}$$

$$= e^2 \int_{\text{plane}} \frac{d\mathbf{r}_p}{|\mathbf{r}_p|} - 2\pi e^2 |z| \tag{D.2.7}$$

The first term of the above equation is the one that gives the diverging behavior in the potential of a charged plane. However, this term vanishes as soon as the 2D system is globally neutral within the cutoff because it does not depend on z. If we replace m by a distribution n_{tot} that would be the sum of the distributions of the electrons, ions and gate, we get:

$$\int_{-l_z}^{+l_z} \langle m \rangle_p(z') \left(e^2 \int_{\text{plane}} \frac{d\mathbf{r}_p}{|\mathbf{r}_p|} \right) dz' = \left(e^2 \int_{\text{plane}} \frac{d\mathbf{r}_p}{|\mathbf{r}_p|} \right) \int_{-l_z}^{+l_z} \langle n_{\text{tot}} \rangle_p(z') dz' = 0 \tag{D.2.8}$$

We can thus drop this term. The definition of the $\bar{v}_c(\mathbf{G} \to 0)$ is then found by Fourier transform along the third direction (as in Eq. (5.2.9)):

$$\bar{v}_c(\mathbf{G} \to 0) = \frac{1}{c} \int_{-l_z}^{+l_z} \left(-2\pi e^2 |z| \right) dz \tag{D.2.9}$$

$$= -2\pi e^2 l_z^2 \tag{D.2.10}$$

D.2.2 Implementation

We now show why we can further simplify the process and use $\bar{v}_c(\mathbf{G} = 0) = 0$ in our implementation. The exchange-correlation and barrier contributions to the potentials and energies are ignored here because they bring no divergence. We refer the reader to App. A and the main text for definitions of the potentials and energies. Since we are talking about cutoff quantities, the following concerns the long-range part of the potentials and the corresponding contributions to energy when the long-range/short-range separation is done. In order to simplify the argument, we do not make the distinction in the notation. In the following, the "tilde" quantities are those defined using the value $\bar{v}_c(\mathbf{G} \to 0) = -2e^2\pi l_z^2$ recommended in Ref. [74]. Here is how we define the potentials in our implementation:

$$\begin{aligned}
\bar{V}_{\mathrm{H}}(\mathbf{r}) &= \tilde{V}_{\mathrm{H}}(\mathbf{r}) - \bar{v}_c(\mathbf{G} \to 0) n(\mathbf{G} = 0) \\
\bar{V}_{\mathrm{ion}}(\mathbf{r}) &= \tilde{V}_{\mathrm{ion}}(\mathbf{r}) + \bar{v}_c(\mathbf{G} \to 0) n_{\mathrm{ion}}(\mathbf{G} = 0) \\
\bar{V}_{\mathrm{gate}}(\mathbf{r}) &= \tilde{V}_{\mathrm{gate}}(\mathbf{r}) + \bar{v}_c(\mathbf{G} \to 0) \frac{n_{\mathrm{dop}}}{c} \\
\bar{\Phi}(\mathbf{r}) &= \tilde{\Phi}(\mathbf{r}) - \bar{v}_c(\mathbf{G} \to 0) n_{\mathrm{ion}}(\mathbf{G} = 0)
\end{aligned} \tag{D.2.11}$$

Defined this way, the $\mathbf{G} = 0$ value of our potentials is zero (at least for the long-range part in the case of $\bar{V}_{\mathrm{ion}}$ and $\bar{\Phi}$). Note that if we sum $\bar{V}_{\mathrm{H}}$, $\bar{V}_{\mathrm{ion}}$ and $\bar{V}_{\mathrm{gate}}$, we find that $\bar{V}_{\mathrm{KS}} = \tilde{V}_{\mathrm{KS}}$, which is essential. The potentials give the following energies:

$$\begin{aligned}
E_{\mathrm{H}} &= \tilde{E}_{\mathrm{H}} - \frac{\Omega}{2}(n_{\mathrm{ion}}(0) + \frac{n_{\mathrm{dop}}}{c})^2 \bar{v}_c(\mathbf{G} \to 0) \\
E_{\mathrm{ext}}^{\mathrm{ion}} &= \tilde{E}_{\mathrm{ext}}^{\mathrm{ion}} + \Omega(n_{\mathrm{ion}}(0) + \frac{n_{\mathrm{dop}}}{c}) n_{\mathrm{ion}}(\mathbf{G} = 0) \bar{v}_c(\mathbf{G} \to 0) \\
E_{\mathrm{ext}}^{\mathrm{gate}} &= \tilde{E}_{\mathrm{ext}}^{\mathrm{gate}} + \Omega(n_{\mathrm{ion}}(\mathbf{G} = 0) + \frac{n_{\mathrm{dop}}}{c}) \frac{n_{\mathrm{dop}}}{c} \bar{v}_c(\mathbf{G} \to 0) \\
E_{\mathrm{i-i}} &= \tilde{E}_{\mathrm{i-i}} - \frac{\Omega}{2} n_{\mathrm{ion}}^2(\mathbf{G} = 0) \bar{v}_c(\mathbf{G} \to 0) \\
E_{\mathrm{g-i}} &= \tilde{E}_{\mathrm{g-i}} - \Omega \frac{n_{\mathrm{dop}}}{c} n_{\mathrm{ion}}(\mathbf{G} = 0) \bar{v}_c(\mathbf{G} \to 0) \\
E_{\mathrm{g-g}} &= \tilde{E}_{\mathrm{g-g}} - \frac{\Omega}{2} \left(\frac{n_{\mathrm{dop}}}{c} \right)^2 \bar{v}_c(\mathbf{G} \to 0)
\end{aligned} \tag{D.2.12}$$

where, once again, we have that all the $\mathbf{G} = 0$ contributions to the energy are zero, and that $E_{\mathrm{tot}} = \tilde{E}_{\mathrm{tot}}$, if we sum all the contributions. The process described above is equivalent to setting $\bar{v}_c(\mathbf{G} = 0)$ to zero, and it gives the same KS potential and total energy as using $\bar{v}_c(\mathbf{G} \to 0) = -2\pi e^2 l_z^2$. It also mimics the method adopted to treat the $\mathbf{G} = 0$ divergences in the original code.

Chapter E

Boltzmann transport equation

E.1 Numerical Solution to Boltzmann transport equation

Eq. (6.1.13) can be written as a matrix-vector product of the kind $\sum_{\varepsilon'} \mathcal{M}_{\varepsilon,\varepsilon'}\tau(\varepsilon') = 1$, with $\mathcal{M} = \mathcal{M}_{\mathrm{I}} + \sum_{\nu} \mathcal{M}_{\nu}$ where $\mathcal{M}_{\mathrm{I}}$ is just a diagonal matrix containing the inverse relaxation times for impurity scattering obtained using existing methods [93, 97, 98] and

$$[\mathcal{M}_{\nu}]_{\varepsilon,\varepsilon'} = \sum_{\theta'} \frac{|\varepsilon'|\Delta\theta'}{(2\pi\hbar v_F)^2} P_{\nu}(\varepsilon,\theta,\varepsilon',\theta') \frac{1-f^{(0)}(\varepsilon')}{1-f^{(0)}(\varepsilon)} \left(\delta_{\varepsilon,\varepsilon'} - \frac{\cos(\theta')}{\cos(\theta)}\right) \tag{E.1.1}$$

where angular variables have been discretized with step $\Delta\theta'$ to perform numerical integrals, $\theta = \theta_{\mathbf{k}}$ and $\theta' = \theta_{\mathbf{k}'}$. The scattering probability $P_{\nu}(\varepsilon,\theta,\varepsilon',\theta')$ is the equivalent of Eq. (6.1.9), defined in a way more suitable for the numerical integration:

$$P_{\nu}(\varepsilon,\theta,\varepsilon',\theta') = \frac{2\pi}{\hbar} S|g_{\mathbf{k}+\mathbf{q},\mathbf{k},\nu}|^2 \left\{ n_{q,\nu}\delta_{\varepsilon',\varepsilon+\hbar\omega_{\mathbf{q},\nu}} + (n_{q,\nu}+1)\delta_{\varepsilon',\varepsilon_{\mathbf{k}}-\hbar\omega_{\mathbf{q},\nu}} \right\} \tag{E.1.2}$$

We represent the matrix $[\mathcal{M}_{\nu}]_{\varepsilon,\varepsilon'}$ by discretizing the energy bands with $N_{\mathcal{M}} = 8000$ energy points on a scale of $E_{\mathcal{M}} = 4\hbar\omega_{\mathrm{A}_1'}$ around ε_F, such that $\Delta\varepsilon = \frac{E_{\mathcal{M}}}{N_{\mathcal{M}}}$. We sum over matrices associated with each phonon branch. The sum of scattering probabilities $P_{\mathrm{LO}}+P_{\mathrm{TO}}$ being isotropic, the corresponding matrix is diagonal. On the contrary, P_{TA}, P_{LA} and $P_{A_1'}$ have angular dependencies such that the term $\frac{\cos(\theta')}{\cos(\theta)}$ does not integrate to zero and give rise to off-diagonal terms.

The number of off-diagonal terms in the matrix $[\mathcal{M}_{\nu}]_{\varepsilon,\varepsilon'}$ depends of the energy conservation in the scattering probability, Eq. (6.1.9). In the small $|\mathbf{q}|$ limit and for optical A_1' having constant long-wavelength phonon dispersion, each energy conservation in Eq. (6.1.9) is satisfied for only one value of ε at fixed phonon momentum. Thus, the matrix $\left[\mathcal{M}_{\mathrm{A}_1'}\right]_{\varepsilon,\varepsilon'}$ has only 2 off-diagonal terms for each ε. The energy parametrization is such that the energies $\varepsilon \pm \hbar\omega_{\mathrm{A}_1'}$ are on the grid.

In the case of acoustic phonons, the linear phonon dispersion $\hbar\omega_{\mathbf{q},\nu} = v_{\nu}|\mathbf{q}|$ implies that the energy conservation in Eq. (6.1.9) is satisfied by a larger subset of ε' values for each ε. $[\mathcal{M}_{\mathrm{TA,LA}}]_{\varepsilon,\varepsilon'}$ is thus a band matrix. However, the distance from the diagonal is given by the magnitude of the phonon frequency, and since $\hbar\omega_{\mathbf{q},\mathrm{TA/LA}} \lesssim$

$\hbar\omega_{2k_F,\mathrm{LA}} = 2\frac{v_{\mathrm{LA}}}{v_F}\varepsilon_F << \hbar\omega_{\mathrm{A}'_1}$, the band is very narrow compared to the width of the full matrix. For the acoustic modes only, we made the approximation that all off-diagonal terms can be summed up and concentrated into the diagonal term, which is equivalent to neglecting [89] the variation of $\tau(\varepsilon)$ on the energy scale $\hbar\omega_{2k_F,\mathrm{TA/LA}}$. This approximation is discussed in App. E.2 concerning the acoustic phonons in the BG regime. It is not equivalent to the elastic approximation, as in this case, we do not constrain $\varepsilon = \varepsilon'$ in the calculation of each term in Eq. (E.1.1).
Matrix inversion of the 8000×8000 $\mathcal{M}$ matrix gives the time $\tau(\varepsilon)$.

E.2 Relaxation times

In this appendix, the $\tau(\varepsilon_{\mathbf{k}'}) \approx \tau(\varepsilon_{\mathbf{k}})$ approximation is made, such that each phonon mode can be treated separately. Some phonon-specific approximations can then be made to simplify the calculation of each τ_ν. In the following the indices A and O designate the summed contributions of acoustic (TA/LA) and optical (LO/TO) phonons, respectively.

E.2.1 Acoustic phonons in the BG regime

The variation of τ_{A} on the scale $\hbar\omega_{\mathbf{q},\mathrm{TA/LA}}$ is neglected [89]. Since $\hbar\omega_{\mathbf{q},\mathrm{TA/LA}} \ll \varepsilon_F$, the initial and final states can be considered to be on the same iso-energetic line at $\varepsilon = \varepsilon_F$, which simplifies the angular part of the calculus. However, the variation of the electronic occupation must be included because $\hbar\omega_{\mathbf{q},\mathrm{TA/LA}}$ is of the order of k_BT. The following expression of τ_{A} is found, with $\nu = \mathrm{TA,LA}$:

$$\left(\frac{1}{\tau_{\mathrm{A}}(\varepsilon_{\mathbf{k}})}\right)_{\mathrm{BG}} = \sum_{\mathbf{k}'} \frac{2\pi}{\hbar}\frac{1}{N}\sum_{\nu} |g_{\mathbf{k}',\mathbf{k},\nu}|^2 \frac{1-f^{(0)}(\mathbf{k}')}{1-f^{(0)}(\mathbf{k})}(1-\cos(\theta_{\mathbf{k}'}-\theta_{\mathbf{k}})) \tag{E.2.1}$$
$$\times \left\{ n_{|\mathbf{k}'-\mathbf{k}|\nu}\delta(\varepsilon_{\mathbf{k}'} - \varepsilon_{\mathbf{k}} - \hbar\omega_{|\mathbf{k}-\mathbf{k}'|,\nu}) + (n_{|\mathbf{k}-\mathbf{k}'|\nu}+1)\delta(\varepsilon_{\mathbf{k}'} - \varepsilon_{\mathbf{k}} + \hbar\omega_{|\mathbf{k}-\mathbf{k}'|,\nu}) \right\}$$

where $\mathbf{k}' = \mathbf{k} + \mathbf{q}$.

E.2.2 Acoustic phonons in the EP and HT regimes

The quasi-elastic approximation is valid. The phonon occupation can be approximated as $n_{q,\mathrm{TA/LA}} \approx \hbar\omega_{\mathbf{q},\mathrm{TA/LA}}/(k_BT)$, since $k_BT >> \hbar\omega_{\mathbf{q},\mathrm{TA/LA}}$. We use the following expression of $\tau_\nu(\varepsilon_{\mathbf{k}})$, easily deduced from Eq. (6.4.3) in the elastic case:

$$\frac{1}{\tau_\nu(\varepsilon_{\mathbf{k}})} = \sum_{\mathbf{k}'} P_{\mathbf{k}\mathbf{k}',\nu}\Big(1-\cos(\theta_{\mathbf{k}'}-\theta_{\mathbf{k}})\Big) \quad \text{(Elastic)} \tag{E.2.2}$$

The cosine in the scattering probabilities $P_{\mathbf{k}\mathbf{k}',\mathrm{TA/LA}}$ times the cosine in the above equation integrates to zero, so that $\frac{1}{\tau_{\mathrm{A}}(\varepsilon_{\mathbf{k}})} = \sum_{\nu=\mathrm{TA,LA}}\sum_{\mathbf{k}'} P_{\mathbf{k}\mathbf{k}',\nu}$. We finally obtain:

$$\left(\frac{1}{\tau_{\mathrm{A}}(\varepsilon_{\mathbf{k}})}\right)_{\mathrm{EP,HT}} = \frac{2\beta_A^2 k_B T}{\mu_S \hbar v_{\mathrm{A}}^2}\frac{\varepsilon_{\mathbf{k}}}{(\hbar v_F)^2} \tag{E.2.3}$$

Where v_{A} is the effective sound velocity defined in Eq. (6.4.5), and μ_S is the mass density defined in Table. 6.2.

E.2.3 Optical LO/TO phonons

The scattering probability made by the sum of LO and TO branches ($P_{\mathbf{k}\mathbf{k}',\mathrm{LO}}+P_{\mathbf{k}\mathbf{k}',\mathrm{TO}}$) is isotropic. We can use a simplified form of Eq. (6.4.1) in the isotropic case:

$$\frac{1}{\tau_\nu(\varepsilon_\mathbf{k})} = \sum_{\mathbf{k}'} P_{\mathbf{k}\mathbf{k}',\nu} \frac{1-f^{(0)}(\varepsilon_{\mathbf{k}'})}{1-f^{(0)}(\varepsilon_\mathbf{k})} \quad \text{(Isotropic)} \tag{E.2.4}$$

We obtain the following expression, with $\hbar\omega_{\mathrm{LO}} = \hbar\omega_{\mathrm{TO}} = \hbar\omega_{\mathrm{O}} = 0.20$ eV, and $n_{\mathrm{LO}} = n_{\mathrm{TO}} = n_{\mathrm{O}} = n(\hbar\omega_{\mathrm{O}})$:

$$\begin{aligned}\frac{1}{\tau_{\mathrm{O}}(\varepsilon_\mathbf{k})} =& \frac{\beta_O^2}{\mu_S\omega_{\mathrm{O}}} \frac{1}{(\hbar v_F)^2} \{ n_{\mathrm{O}} |\varepsilon_\mathbf{k} + \hbar\omega_{\mathrm{O}}| \frac{1-f^{(0)}(\varepsilon_\mathbf{k}+\hbar\omega_{\mathrm{O}})}{1-f^{(0)}(\varepsilon_\mathbf{k})} \\ &+ (n_{\mathrm{O}}+1)|\varepsilon_\mathbf{k} - \hbar\omega_{\mathrm{O}}| \frac{1-f^{(0)}(\varepsilon_\mathbf{k}-\hbar\omega_{\mathrm{O}})}{1-f^{(0)}(\varepsilon_\mathbf{k})} \}\end{aligned} \tag{E.2.5}$$

E.2.4 Optical A_1' phonons

As mentioned before, a difficulty encountered with optical A_1' phonons at **K** is the change in the EPC matrix element for interband scattering. Since we consider only electron doping, interband scattering occurs only in case of phonon emission. We find the general expression of $\tau_{\mathrm{A}_1'}$ to be, with $\hbar\omega_{\mathrm{A}_1'} = 0.15$ eV and $n_{\mathrm{A}_1'} = n(\hbar\omega_{\mathrm{A}_1'})$:

$$\begin{aligned}\frac{1}{\tau_{\mathrm{A}_1'}(\varepsilon_\mathbf{k})} =& \frac{\beta_K^2}{\mu_S\omega_{\mathrm{A}_1'}} \frac{1}{(\hbar v_F)^2} \times \left\{ \frac{3}{2} n_{\mathrm{A}_1'} |\varepsilon_\mathbf{k} + \hbar\omega_{\mathrm{A}_1'}| \frac{1-f^{(0)}(\varepsilon_\mathbf{k}+\hbar\omega_{\mathrm{A}_1'})}{1-f^{(0)}(\varepsilon_\mathbf{k})} \right. \\ &\left. + (n_{\mathrm{A}_1'}+1) \left(|\varepsilon_\mathbf{k} - \hbar\omega_{\mathrm{A}_1'}| + \frac{1}{2}(\varepsilon_\mathbf{k} - \hbar\omega_{\mathrm{A}_1'}) \right) \frac{1-f^{(0)}(\varepsilon_\mathbf{k}-\hbar\omega_{\mathrm{A}_1'})}{1-f^{(0)}(\varepsilon_\mathbf{k})} \right\}\end{aligned} \tag{E.2.6}$$

E.3 Derivation of acoustic phonon resistivity in EP regime

In the EP regime, we can consider scattering by acoustic phonons (ν = TA,LA) to be elastic:

$$\frac{1}{\tau_{\mathrm{A}}(\varepsilon_\mathbf{k})} = \sum_{\mathbf{k}'} P_{\mathbf{k}\mathbf{k}',\mathrm{A}} \Big(1 - \cos(\theta_{\mathbf{k}'} - \theta_\mathbf{k}) \Big) \tag{E.3.1}$$

with

$$P_{\mathbf{k}\mathbf{k}',\mathrm{A}} = \frac{2\pi}{\hbar} \frac{1}{N} \sum_{\nu=\mathrm{TA,LA}} |g_{\mathbf{k},\mathbf{k}',\nu}|^2 \{ n_{|\mathbf{k}'-\mathbf{k}|\nu} \delta(\varepsilon_{\mathbf{k}'} - \varepsilon_\mathbf{k} - \hbar\omega_{|\mathbf{k}-\mathbf{k}'|,\nu}) \tag{E.3.2}$$

$$+ (n_{|\mathbf{k}-\mathbf{k}'|\nu}+1) \delta(\varepsilon_{\mathbf{k}'} - \varepsilon_\mathbf{k} + \hbar\omega_{|\mathbf{k}-\mathbf{k}'|,\nu}) \} \tag{E.3.3}$$

By neglecting the phonon frequency in the delta functions we obtain:

$$P_{\mathbf{k}\mathbf{k}',\mathrm{A}} \approx \frac{2\pi}{\hbar} \frac{1}{N} \sum_{\nu=\mathrm{TA,LA}} |g_{\mathbf{k},\mathbf{k}',\nu}|^2 \delta(\varepsilon_{\mathbf{k}'} - \varepsilon_\mathbf{k}) \{ 2n_{|\mathbf{k}-\mathbf{k}'|\nu} + 1 \} \tag{E.3.4}$$

$$\approx \frac{2\pi}{\hbar} \frac{1}{N} \sum_{\nu=\mathrm{TA,LA}} \frac{\beta_A^2 k_B T}{\mu_S S v_\nu^2} (1 \pm \cos 3(\theta_{\mathbf{k}'} + \theta_\mathbf{k})) \delta(\varepsilon_{\mathbf{k}'} - \varepsilon_\mathbf{k}) \tag{E.3.5}$$

where $|\mathbf{k}-\mathbf{k}'| = |\mathbf{q}|$ and the angular expressions are simplified because $\mathbf{k}'$ and $\mathbf{k}$ are on a iso-energetic line. The $\pm$ sign corresponds to LA and TA respectively. We made the approximation $n_{|\mathbf{q}|,\mathrm{TA/LA}} \approx \frac{k_B T}{\hbar\omega_{\mathbf{q},TA/LA}}$, since $k_B T >> \hbar\omega_{\mathbf{q},TA/LA}$.

Thus we have:

$$\frac{1}{\tau_{\mathrm{A}}(\varepsilon_{\mathbf{k}})} \approx \sum_{k'} \frac{2\pi}{\hbar}\frac{1}{N}\sum_{\nu=\mathrm{TA,LA}} \frac{1}{\mu_S S v_\nu^2}\beta_A^2 k_B T(1 \pm \cos 3(\theta_{\mathbf{k}'}+\theta_{\mathbf{k}})) \tag{E.3.6}$$
$$\times\, \delta(\varepsilon_{\mathbf{k}'}-\varepsilon_{\mathbf{k}})(1-\cos(\theta_{\mathbf{k}'}-\theta_{\mathbf{k}}))$$

$$\frac{1}{\tau_{\mathrm{A}}(\varepsilon_{\mathbf{k}})} \approx \sum_{\nu=\mathrm{TA,LA}} \frac{\beta_A^2 k_B T}{\mu_S \hbar v_\nu^2}\frac{1}{(\hbar v_F)^2}\int \frac{|\varepsilon_{\mathbf{k}'}| d\varepsilon_{\mathbf{k}'} d\theta_{\mathbf{k}'}}{(2\pi)}(1 \pm \cos 3(\theta_{\mathbf{k}'}+\theta_{\mathbf{k}})) \tag{E.3.7}$$
$$\times\, \delta(\varepsilon_{\mathbf{k}'}-\varepsilon_{\mathbf{k}})(1-\cos(\theta_{\mathbf{k}'}-\theta_{\mathbf{k}}))$$

$$\frac{1}{\tau_{\mathrm{A}}(\varepsilon_{\mathbf{k}})} \approx \sum_{\nu=\mathrm{TA,LA}} \frac{\beta_A^2 k_B T}{\mu_S \hbar v_\nu^2}\frac{|\varepsilon_{\mathbf{k}}|}{(\hbar v_F)^2}\int \frac{d\theta_{\mathbf{k}'}}{(2\pi)}(1 \pm \cos 3(\theta_{\mathbf{k}'}+\theta_{\mathbf{k}}))(1-\cos(\theta_{\mathbf{k}'}-\theta_{\mathbf{k}})) \tag{E.3.8}$$

$$\frac{1}{\tau_{\mathrm{A}}(\varepsilon_{\mathbf{k}})} \approx \frac{2\beta_A^2 k_B T}{\mu_S \hbar v_{\mathrm{A}}^2}\frac{|\varepsilon_{\mathbf{k}}|}{(\hbar v_F)^2} \tag{E.3.9}$$

Doing the usual approximation valid at low temperature:

$$\frac{1}{\rho} = \frac{e^2 v_F^2}{2}\int d\varepsilon DOS(\varepsilon)\tau(\varepsilon)\left(-\frac{\partial f^{(0)}}{\partial\varepsilon}(\varepsilon)\right) \tag{E.3.10}$$
$$\approx \frac{e^2 v_F^2}{2} DOS(\varepsilon_F)\tau(\varepsilon_F) \approx \frac{e^2 v_F^2 |\varepsilon_F|}{\pi(\hbar v_F)^2}\tau(\varepsilon_F) \tag{E.3.11}$$

we obtain:

$$\rho_A \approx \frac{\pi(\hbar v_F)^2}{e^2 v_F^2 |\varepsilon_F|}\frac{1}{\tau(\varepsilon_F)} \approx \frac{2\pi\beta_A^2 k_B T}{e^2 \hbar v_F^2 \mu_S v_{\mathrm{A}}^2} \tag{E.3.12}$$

Chapter *

Résumé

Malgré de nombreux arguments contre la stabilité des matériaux 2D à température ambiante, André Geim et Konstantin Novoselov sont parvenus à produire du graphène en 2004. Les propriétés uniques de cette monocouche de carbone ont d'abord été étudiées par P.R. Wallace, en 1947. Pendant des dizaines d'années, plusieurs théoriciens se sont intéressés au graphène en tant que réalisation de la physique des fermions de Dirac en matière condensée. À l'époque, cependant, on ne pensait pas pouvoir observer le graphène en lui-même. Plutôt que la découverte d'un nouveau matériau, c'est l'*isolation* et la *caractérisation* du graphène qui ont valu le prix Nobel Nobel de physique 2010 à Geim et Novoselov.

La dimensionalité est un paramètre critique dans l'étude des propriétés des matériaux. Elle définit souvent les caractéristiques et particularités des transitions de phase, qu'elle soient structurelles, électroniques, magnétiques ou autres. Bien que les théoriciens travaillaient déjà en deux dimensions, l'*isolation* du graphène ouvra la porte des matériaux 2D aux expérimentateurs. Ceci permit à la physique de la matière condensée de bénéficier de l'échange fondamental entre théorie et expérience en deux dimensions.

La capacité à contrôler et *caractériser* les propriétés d'un matériau est tout aussi importante que le matériau lui-même. Une composante cruciale de la technique de caractérisation employée par Geim et Novoselov est l'utilisation de l'effet de champ. L'idée d'utiliser un champ électrique pour moduler les propriétés électroniques d'un matériau fût introduite par Julius Lilienfeld en 1925, mais il faudra quelques décennies pour que John Atalla et Dawon Kahng fabriquent la première version opérationnelle de ce que nous appelons aujourd'hui le transistor à effet de champ. L'effet de champ se révéla être d'une importance capitale pour la technologie d'aujourd'hui puisque le transistor à effet de champ est devenu le composant élémentaire de la plupart des systèmes électroniques que nous utilisons.

L'intérêt de l'effet de champ réside dans sa capacité à induire des changements notoires dans les propriétés électroniques du matériau cible en variant sa densité de porteurs de charges. C'est pourquoi les transistors à effet de champ modernes sont principalement constitués de semi-conducteurs plutôt que de métaux ou semi-métaux comme le graphite. En effet, il suffit d'induire une densité de porteurs relativement faible dans les semi-conducteurs pour engendrer une transition entre un comportement isolant et conducteur. Dans les métaux ou semi-métaux épais, l'intensité typique des champs électriques que l'on trouve dans les transistors à effet de champ s'avère

trop faible pour induire une densité de porteurs mobiles significative comparée à la densité intrinsèquement présente. L'effet du champ électrique est alors trop faible pour être exploité. Durant son discours d'acceptation du prix Nobel, Geim indique que ses recherches sur les fines couches de graphites furent en partie motivées par l'observation potentielle de l'effet de champ dans des matériaux autres que les semi-conducteurs. Pour cela, il était nécessaire d'augmenter la *densité* des porteurs de charge induite dans le graphite. Plutôt que d'essayer d'augmenter le *nombre* de charges, son ambition était de réduire l'épaisseur du graphite, et donc le *volume* dans lequel les charges sont induites. D'une certaine façon, l'élimination d'une dimension spatiale et l'utilisation de l'effet de champ furent un moyen d'explorer une autre dimension du graphite semi-métallique, à savoir sa structure électronique.

Pour des raisons d'ordre plus technologique, l'industrie du semi-conducteur a toujours été impliquée dans la course vers de plus fins matériaux et la réduction de leur taille en général. L'isolation du graphène marque l'atteinte de la limite ultime de cette course ainsi que l'accès à une nouvelle catégorie de matériaux. Le temps qui sépare les travaux de Geim et Novoselov sur le graphène et leur récompense par le prix Nobel est remarquablement court. Ce fût également le cas pour la réalisation du premier transistor en 1947 par Bardeen, Brattain et Shockley et le prix Nobel correspondant en 1956. Ceci résulte de l'impact considérable et immédiat que ces travaux ont eu sur la science et la technologie. Etant donné l'importance des transistors de nos jours, on peut s'attendre à un grand succès pour les matériaux 2D. En un peu plus d'une décennie, une quantité impressionnante de travaux de recherche ont été réalisés sur les matériaux 2D. Leur sensibilité au stimulations externes (champs électriques ou magnétiques, lumière, température, contraintes, etc...) invite à de nombreuses applications dans les composants électroniques, capteurs, panneaux solaires, batteries, thermoélectriques, et bien d'autres. Pour d'autres champs d'application jusque là moins développés, comme la spintronique, l'informatique quantique ou la supraconductivité, les matériaux 2D pourraient être l'élément déclencheur d'avancées considérables.

Le transport électronique joue un rôle prépondérant dans un grand nombre de ces applications. Il est alors essentiel de développer de bons modèles et d'identifier les différents facteurs susceptibles d'agir sur le transport afin d'améliorer les performances des matériaux. Le transport est aussi une technique de caractérisation courante, utilisée pour observer les signatures de diverses phénomènes. L'interaction électron-phonon et l'écrantage font partie des concepts à considérer lorsque l'on parle de transport. Dans les composants électroniques, la diffusion des électrons par les phonons détériore la capacité d'un matériau à conduire les électrons. L'interaction électron-phonon peut alors être un facteur limitant. Dans le contexte de la supraconductivité conventionnelle, au contraire, cette interaction est l'élément moteur du mécanisme physique. Dans tous les cas, cette interaction est omniprésente en matière condensée, et son étude est essentielle pour la physique fondamentale et appliquée. L'écrantage est un aspect important et complexe du comportement collectif des électrons d'un matériau. Ce terme désigne la capacité des électrons à atténuer un champ électrique extérieur via une réponse collective engendrée par l'interaction coulombienne à longue portée. En tant que réponse à un champ électrique, l'écrantage influe sur la réponse des électrons à un champ perturbateur, et en particulier sur le couplage électron-phonon. Ce phénomène dépend de la dimensionalité et requiert une modélisation soigneuse. Beaucoup reste à compren-

dre concernant la spécificité du transport, l'interaction électron-phonon et l'écrantage dans les matériaux 2D.

Les simulations *ab initio*, en complément de l'expérience, peuvent aider à la compréhension des propriétés électroniques et structurelles des matériaux. Bien souvent, la reproduction de résultats expérimentaux par la simulation implique une bonne compréhension des mécanismes physiques mis en jeu. En amont de l'expérience, les simulations *ab initio* permettent de prédire et d'explorer les matériaux 2D, indiquant ainsi le chemin à suivre aux recherches expérimentales et appliquées.

Cette thèse fait suite à la constatation d'un écart quantitatif entre simulations et mesures expérimentales concernant la résistivité associée à la diffusion des électrons par les phonons dans le graphène. Malgré une interprétation théorique qualitativement satisfaisante, les travaux numériques sous-estiment largement l'expérience. Ceci indique d'éventuels défauts ou lacunes dans les modèles et simulations *ab initio* de l'interaction électron-phonon du graphène.

Afin de réaliser des simulations plus fidèles des interactions électron-phonon dans les matériaux 2D, il a été nécessaire d'améliorer les méthodes *ab initio* existantes fondées sur la théorie de la fonctionnelle de la densité avec ondes planes. Ces méthodes furent initialement développées pour la simulation de matériaux périodiques dans les trois dimensions. Malgré leurs nombreux succès dans ce contexte, ces méthodes ne sont pas adaptées à la simulation de matériaux 2D. En particulier, elles ne permettent pas la simulation correcte de l'écrantage et de l'effet de champ. Puisque ces deux mécanismes ont un effet sur l'interaction électron-phonon, il est important de développer leur simulation pour les matériaux 2D. De manière plus générale, ces deux sujets font l'objet de nombreux débats et leur importance dépasse largement le cadre des interactions électron-phonon. En effet, l'écrantage peut être impliqué dans tous les types de réponse électronique alors que l'effet de champ est utilisé dans la plupart des mesures expérimentales de résistivité et dans de nombreuses applications. Afin de simuler correctement les effets de l'écrantage et l'effet de champ sur le couplage électron-phonon, nous avons modifié les méthodes *ab initio* existantes. Ces nouvelles méthodes numériques nous ont permis d'établir des modèles quantitatifs de l'interaction électron-phonon dans le graphène. Nous avons amélioré les modèles qualitatifs et quantifié *ab initio* les paramètres en jeu. La résistivité du graphène peut ensuite être calculée en introduisant les interactions électron-phonon dans un modèle de transport électronique, qu'il faut alors résoudre. Souvent, des approximations sont utilisées pour pouvoir résoudre les équations analytiquement. Afin de relaxer ces approximations, nous avons implémenté une solution numérique plus précise.

Un objectif direct de ce travail est l'amélioration de la compréhension du couplage électron-phonon et de son influence sur le transport électronique dans le graphène. Au delà de l'application au graphène, un objectif moins direct mais tout aussi important est de fournir de nouvelles méthodes numériques pour la simulation des matériaux 2D en général.

Dans le premier chapitre, on introduit les concepts de matière condensée au centre de cette thèse. Ce premier chapitre étant général et dépourvu de résultats nouveaux, il ne sera pas résumé ici. Dans le chapitre 2, on présente et améliore les modèles analytiques des électrons, des électrons (dans le plan), et de leurs interactions dans le graphène. Dans le chapitre 3, on évalue *ab initio* les paramètres apparaissant dans

le modèle de couplage électron-phonon. Dans le chapitre 4, on présente une méthode numérique fondée sur la théorie de la fonctionnelle de la densité pour calculer les propriétés d'écrantage des matériaux 2D. Cette méthode est appliquée au graphène et les résultats sont comparés aux modèles analytiques. Dans le chapitre 5, on se concentre sur la spécificité des configurations du type transistor à effet de champ et les implications pour l'interaction électron-phonon. On détaille les modifications apportées au code *ab initio* pour permettre la simulation de matériaux 2D dans de telles configurations. La méthode est ensuite appliquée au graphène. Enfin, dans le chapitre 6, on développe une solution numérique à l'équation de Boltzmann pour le transport d'électron en présence de phonons. On simule la résistivité du graphène et on la compare aux mesures expérimentales.

∗.1 Chapitre 2: Modèlisation analytique du couplage électron-phonon dans le graphène

Cette étude commence par un travail de clarification, amélioration et quantification du modèle de couplage entre les électrons et les phonons dans le plan. La modélisation du couplage électron-phonon passe d'abord par celle des électrons et des phonons. Parmi ceux-ci, on se concentre sur les électrons et phonons pertinents, c'est-à-dire ceux qui jouent un rôle dans le transport électronique. Les électrons pertinents ont des énergies $|\varepsilon| < 1$ eV, où les énergies sont mesurées par rapport à l'énergie de Fermi dans le cas du graphène neutre. Les phonons pertinents sont les modes LA, TA, LO et TO proches du point $\mathbf{\Gamma}$ ("L" pour longitudinal, "T" pour transverse, "A" pour acoustique, "O" pour optique), et le mode optique A_1' proche du point $\mathbf{K}$. On peut montrer que les phonons hors plan ne se couplent pas linéairement aux électrons dans le cas du graphène isolé ou en présence d'un champ électrique hors plan symétrique. Il peut y avoir un couplage pour une configuration de type transistor à effet de champ, mais cette situation n'est pas modélisée analytiquement. Le couplage des électrons aux phonons hors plan n'est considéré que dans le chapitre 5, lorsque l'on simule l'effet de champ. Pour les modèles analytiques, on se restreint donc au couplage avec les modes LA, TA, LO, TO et A_1'. Les modèles de couplage avec les modes optiques, déjà considérablement développés dans la littérature [14, 34, 35, 27], sont présentés et vérifiés dans le texte principal. Pour ce résumé, on se concentre sur les développements accomplis lors de cette thèse, qui concernent principalement la modélisation du couplage aux modes acoustiques.

électrons. La structure électronique du graphène est représentée par des cônes de Dirac, soit une dispersion linéaire $\varepsilon_{\mathbf{k},s} = \pm\hbar v_F|\mathbf{k}|$ où $\varepsilon_{\mathbf{k},s}$ est l'énergie associée à l'état électronique de vecteur d'onde $\mathbf{k}$ dans la bande s, et v_F est la vitesse de Fermi. La structure de bande obtenue dans le cadre de la théorie de la fonctionnelle de la densité (DFT) coïncide avec ce modèle pour des états électroniques d'énergie $\varepsilon = \pm 0{,}5$ eV, voir Fig. ∗.1. En dehors de ce domaine, la structure de bande DFT est plus complexe. Cependant, le modèle des cônes de Dirac fourni un support analytique suffisant à l'interprétation de nos résultats numériques.

Phonons. La dispersion des phonons du graphène est donnée Fig. ∗.2. Les modes strictement optiques ou acoustiques et strictement longitudinaux ou transverses, appelés ici modes canoniques, sont souvent utilisés pour modéliser analytiquement les

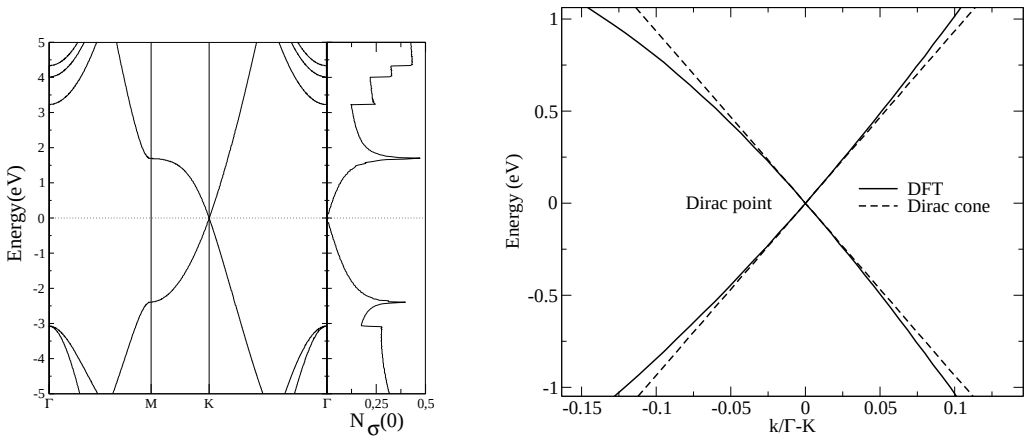

Figure ∗.1: Sur la gauche est représentée la structure de bande du graphène obtenue en DFT, accompagnée de sa densité d'états. Sur la droite, on compare le modèle des cônes de Dirac avec la structure de bande DFT pour des énergies $\varepsilon_{\mathbf{k},s} = \pm 1$ eV autour du point de Dirac.

modes LA, TA, LO et TO. En réalité et dans le cadre de la DFT, les modes de phonons du graphène (et tout autre réseau 2D qui ne soit pas parfaitement tétragonal) sont un mélange de ces modes canoniques [25, 26, 16]. En diagonalisant la matrice dynamique à des vecteurs de phonons $\mathbf{q}$ proches de zéro mais finis, on quantifie ce mélange et on établit un modèle analytique approché plus satisfaisant que les modes canoniques. Pour les phonons acoustiques, les conséquences de ce mélange sur le couplage électron-phonon s'avèrent importantes.

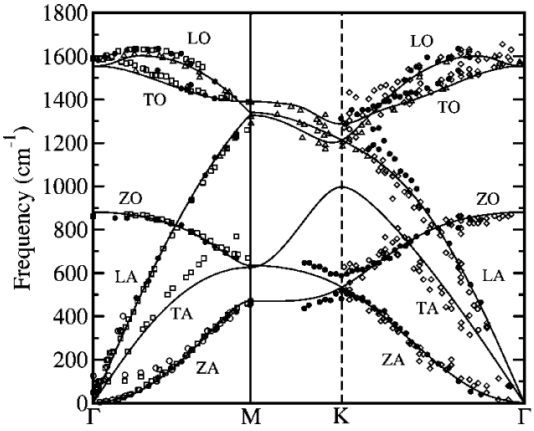

Figure ∗.2: Dispersion des phonons du grahène, d'après Ref. [13]. Les lignes continues representent la dispersion DFT, les symboles sont des données expérimentales.

Couplage électron-phonon (EPC). On utilise le modèle le plus général pour l'Hamiltonien d'interaction électron-phonon, établi à partir d'arguments symétriques

[16], auquel on ajoute l'effet de l'écrantage. Le couplage avec les phonons acoustiques est constitué de deux type de termes, représentés Fig. ∗.3:

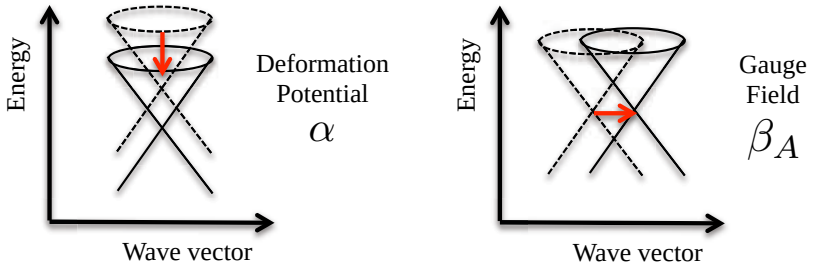

Figure ∗.3: Représentation schématique des contributions de types potentiel de déformation et champ de jauge pour le couplage des électrons aux phonons acoustiques dans le plan.

- les termes de type "champ de jauge" [24], associés au paramètre β_A, déplacent le cône de Dirac dans la zone de Brillouin sans changer l'énergie du point de Dirac. En tant que tel, ces termes ne modifient pas la charge globale et ne sont pas écrantés. Pour un feuillet de graphène soumis à une déformation uni-axiale, ce type de termes correspond à l'amplitude du potentiel vecteur, le "champs de jauge synthétique" [31, 32, 16], qui apparait dans la perturbation de l'Hamiltonien. En présence d'un champ de contrainte non-uniforme, l'effet de ce potentiel vecteur est similaire à celui d'un champ magnétique effectif [33].
- Les termes de type "potentiel de déformation", associés au paramètre α, déplacent le cône de Dirac en énergie, sans changer la position du point de Dirac dans l'espace réciproque. Comme ces termes engendrent une variation de la charge locale, ils sont écrantés par les électrons. Dans un feuillet de graphène soumis à des déformations, ces termes correspondent à l'amplitude du potentiel scalaire, ou " champ électrique synthétique" [31, 16], généré par une variations de la surface de la maille unitaire.

L'incorporation des fonctions d'ondes électroniques (associés aux cônes de Dirac) et des modes de phonons dans le modèle d'interaction permet l'obtention des éléments de matrice EPC, qui représentent la probabilité pour qu'un mode de phonon donné diffuse un électron d'un état électronique à un autre. L'utilisation du modèle de phonons DFT plutôt que les phonons canoniques mène à une renormalisation du paramètre de couplage de type champ de jauge.

∗.2 Chapitre 3: Evaluation des paramètres par calculs *ab initio*

Comme pour les modèles analytiques, l'évaluation *ab initio* des paramètres de couplage aux phonons optiques est amplement couverte dans la littérature [14, 34, 35, 27]. Les calculs *ab initio* de ces paramètres sont simplement vérifiés et présentés dans le texte principal. Les développements effectués au cours de cette thèse concernent majoritairement les phonons acoustiques et sont résumé ici.

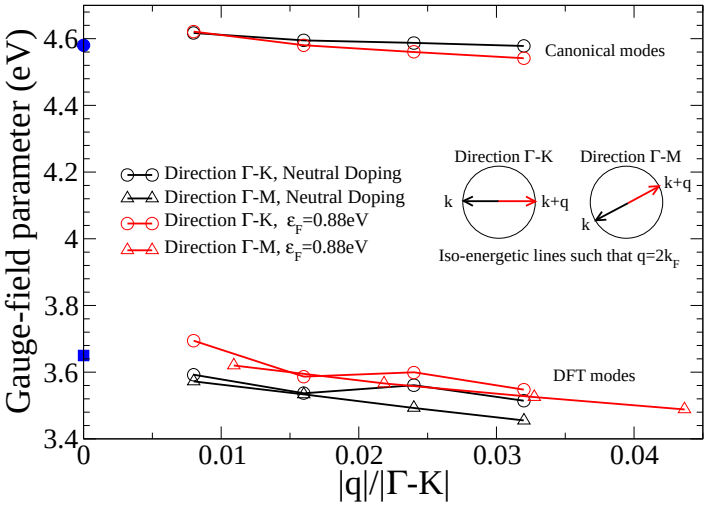

Figure ∗.4: Calculs DFT du paramètre associé au couplage de type champ de jauge, en fonction de la norme du vecteur d'onde des phonons. Les calculs sont réalisés dans différentes directions, à différents dopages, et pour les deux ensembles de modes de phonons canoniques et DFT. Les variations négligeables en fonction du dopage confirment que le champ de jauge n'est pas écranté. La variation significative du résultat en fonction de l'utilisation des modes canoniques ou DFT souligne l'importance de la modélisation du mélange des modes canoniques dans les modes DFT. Les point et carré bleus représentent les valeurs des paramètres trouvées avec la méthode des déformations statiques.

On utilise la DFT en perturbation [19, 20, 21] pour calculer directement le couplage électron-phonon. Cette méthode, de par sa flexibilité, permet la vérification des modèles analytiques. On vérifie les dépendances en angles et en la norme du vecteur de phonon du modèle analytique des éléments de matrice du couplage électron-phonon, voir Fig. ∗.4. Une attention particulière est également accordée aux conséquences numériques des développements apportés au modèle analytique, à savoir le mélange des modes de phonon canoniques dans les modes DFT et l'écrantage du potentiel de déformation. On trouve une variation d'environ 30% dans l'amplitude du couplage de champ jauge lorsqu'on perturbe le système avec les modes canoniques ou DFT, comme on le voit dans la Fig. ∗.4. Numériquement, une modélisation correcte des phonons acoustiques et du mélange des modes canoniques est donc essentielle.

La simulation de l'écrantage du potentiel de déformation est un défi majeur. Dans le cadre de la DFT avec des ondes planes, on ne peut que simuler des systèmes avec des conditions aux bords périodiques dans les trois dimensions. La simulation d'un matériau 2D comme le graphène implique alors la présence d'images périodiques du système 2D. Les électrons de ces images périodiques apportent un écrantage supplémentaire par rapport à celui d'un système 2D isolé. Ainsi, nos calculs DFT confirment

l'écrantage du potentiel de déformation, mais les valeurs numériques du potentiel de déformation écranté ne sont pas valables du fait de la présence d'images périodiques. Le traitement de l'écrantage en DFT est traité dans le chapitre suivant.

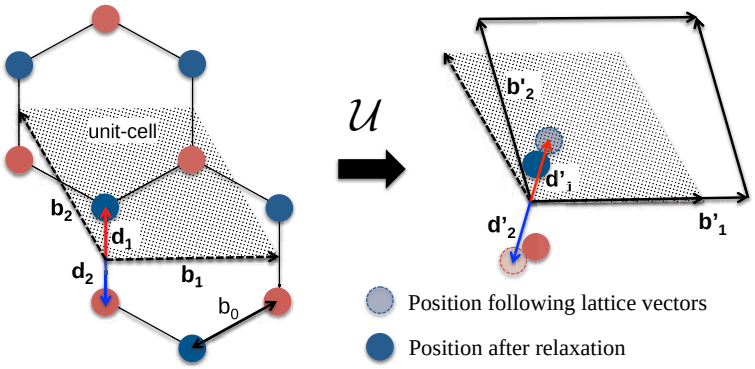

Figure ∗.5: Déformation statique de la maille unitaire. La transformation des vecteurs de la maille est donnée par le tenseur des déformations $\mathcal{U}$. Une fois la maille déformé, on doit relaxer les positions internes des atomes.

D'autre part, le calcul direct du couplage électron-phonon en DFT présente une autre limite: le traitement approximatif des interactions électrons-électrons. Un des apports de cette thèse réside dans le développement de méthodes permettant d'évaluer le couplage aux phonons acoustiques dans l'approximation GW. Les méthodes dites "GW" traitent les interactions électrons-électrons de manière plus poussée que la DFT. Cependant, elles ne permettent que le calcul des énergies des états électroniques, et pas le calcul direct du couplage électron-phonon comme la DFT en perturbation. Pour calculer les couplages électron-phonon dans l'approximation GW, on associe la limite en $|\mathbf{q}| \to 0$ d'un phonon acoustique à une déformation statique du graphène comme celle représentée Fig. ∗.5. Un phonon strictement acoustique correspond à une déformation de la maille alors qu'un phonon strictement optique correspond à une variation des coordonnées internes des atomes. Un mode acoustique DFT étant un mélange de phonons strictement acoustiques ou optiques, il correspond à une déformation de la maille accompagnée d'une relaxation des coordonnées internes des atomes. Lors d'une telle déformation, l'Hamiltonien du graphène est perturbé par des potentiels scalaires et vecteurs qui peuvent être reliés aux couplages électron-phonon. Les perturbations apportées à l'Hamilonien du graphène déformé sont celles présentées dans la section précédente, à savoir des déplacements des cônes de Dirac dans l'espace réciproque (champ de jauge) ou en énergie (potentiel de déformation). Il suffit alors d'étudier la structure de bande du graphène déformé pour en déduire les paramètres EPC. Cette procédure peut être réalisée dans le cadre de la DFT, mais aussi dans l'approximation GW. Grâce à cette méthode, on observe la renormalisation du paramètre de jauge par les interactions électrons-électrons et on confirme que cette renormalisation suit celle de la vitesse de Fermi, soit une augmentation d'environ 20% du paramètre de jauge. Le paramètre de type champ de jauge est la contribution principale du couplage avec les phonons acoustiques. Sa valeur numérique et celles des autres paramètres de couplages sont résumées dans la table ∗.1. Il n'y a pas d'écrantage dans la méthode

Table ∗.1: Paramètres de couplage électron-phonon, calculés par différentes méthodes. β_A est le paramètre de couplage de type champ de jauge pour les phonons acoustiques DFT. $\tilde{\beta_A}$ est le paramètre obtenu pour les modes acoustiques canoniques. α^{bare} correspond au potentiel de déformation non-écranté. β_O et β_K sont les paramètres associés au couplage avec les modes LO/TO et A_1' respectivement. Les différentes méthodes sont : (i) DFPT EPC: calcul direct du paramètre dans le cadre de la DFT. Cette méthode ne donne pas accès au potentiel de déformation non-écranté α^{bare}. (ii) $|\mathbf{q}| = 0$: calcul "à moment de phonon nul" via les déformations statiques, dans le cadre de la DFT. Les paramètres acoustiques sont obtenus en calculant l'amplitude des potentiels scalaires et vecteurs engendrés par les déformations. Les paramètres optiques ont été obtenu avec la méthode des "frozen phonons" dans la référence [34]. (iii)TB-DFT: résultats provenant de l'évaluation en DFT des paramètres du modèle liaison forte de l'EPC [28]. (iv) Calculs GW. Pour les phonons à $\mathbf{\Gamma}$, la renormalisation est de 20%, comme la vitesse de Fermi. Pour le mode A_1', les résultats sont extraits de la référence [35]. (v) Exp: paramètres obtenus en ajustant la solution numérique de l'équation de Boltzmann sur l'expérience, voir chapitre 6.

	DFPT EPC	$\|\mathbf{q}\| = 0$	TB-DFT [28]	GW	Exp
$\tilde{\beta_A}$ (eV)	4,60	4,58	3,58	5,52	–
β_A (eV)	3,60	3,64	–	4,32	4,97
α^{bare}(eV)	–	2,96	3,25	–	–
$\beta_O = \tilde{\beta_O}$ (eV/Å)	9,5	9,5	10,08	11,39	11,39
β_K (eV/Å)	9,5	9,5	10,08	$12{,}5 \sim 14$	$17 \sim 40$

des déformations statiques. Par conséquent, on ne peut qu'obtenir une valeur du potentiel de déformation nue ("bare"), c'est à dire non-écrantée. Cette valeur nue n'est pas renormalisée par les interactions électrons-électrons. Nous n'avons toujours pas de valeur fiable pour le potentiel de déformation écranté. Cependant, avec la valeur nue et la fonction d'écrantage du graphene, on peut en obtenir une estimation. La prochaine étape est donc naturellement l'étude de l'écrantage dans le graphène.

∗.3 Chapitre 4: Écrantage statique dans le graphène

Le phénomène d'écrantage et le formalisme associé dépendent fortement de la dimensionalité. Le premier objectif est donc de clarifier ce que nous cherchons à calculer. Plusieurs cas de figure sont détaillés dans le texte principal. Le cas d'un matériau 3D périodique fait office de référence et point de départ. On traite ensuite le cas d'un matériau strictement 2D en considérant une densité électronique d'épaisseur infiniment petite, cadre dans lequel on se place généralement pour effectuer des développements analytiques. Puis on traite le cas plus réaliste d'un matériau 2D d'épaisseur fini. Enfin, on considère un matériau 2D d'épaisseur fini et répété dans la troisième direction, ce qui est effectivement simulé dans le cadre de la DFT avec les ondes planes. L'objectif

est de comparer les résultats des travaux analytiques avec les simulations DFT. Pour ceci, on doit prendre soin de déterminer les conditions dans lesquelles les fonctions diélectriques dans ces deux situations sont formellement équivalentes. En particulier, l'élimination de l'écrantage superflu provenant des images périodiques en DFT est essentielle pour simuler un matériau 2D isolé tel qu'il est étudié analytiquement. On

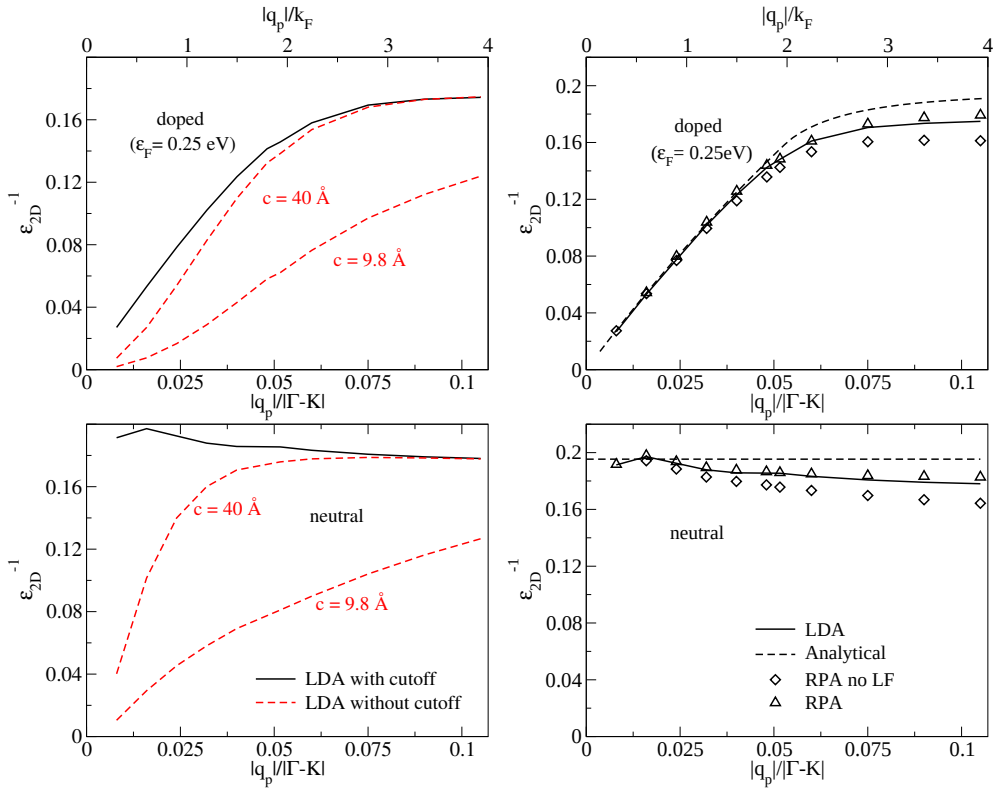

Figure ∗.6: À gauche, on trace la fonction diélectrique inverse du graphène calculée en DFT ("LDA") avec et sans troncature ("cutoff") des interactions coulombiennes entre les images périodiques, et pour du graphène neutre et dopé. $\mathbf{q}_p$ est le vecteur d'onde de la pertrubation. La variable $|\mathbf{q}_p|/|\mathbf{\Gamma}-\mathbf{K}|$ est adimensionnelle, et $|\mathbf{\Gamma}-\mathbf{K}| \approx 1{,}7$ Å^{-1} est la distance entre les points $\mathbf{\Gamma}$ et $\mathbf{K}$ de la zone de Brillouin. On fait varier l'espacement entre les images périodiques (c) pour souligner le fait que le résultat en dépend en l'absence de troncature. À droite, on compare la méthode DFT et les résultats analytiques ("Analytical"). Voir le texte principal pour la signification des autres méthodes.

examine le modèle analytique [63, 64, 65, 66, 67, 68, 69] de la fonction d'écrantage statique du graphène. On souligne plus particulièrement les approximations qui y sont rattachées, à savoir le cadre de travail strictement 2D, l'utilisation du modèle des cônes de Dirac, l'approximation des phases aléatoires, et le moyennage du champ induit sur la maille élémentaire. On développe une méthode DFT pour relaxer ces approximations. On implémente la réponse électronique à un potentiel perturbatif périodique et on propose la troncature du potentiel coulombien [73, 74, 40] induit par les électrons entre les images périodiques pour éliminer l'écrantage superflu. On montre que la

troncature est nécessaire pour retrouver les propriétés d'écrantage d'un matériau 2D isolé, ce que l'on peut voir sur la Fig. ∗.6.

La méthode DFT avec troncature est appliquée au graphène neutre et dopé et la comparaison des résultats à ceux du modèle analytique dans la Fig. ∗.6 révèlent un bon accord général. Les approximations mentionnées plus haut semblent donc être un moyen simple et efficace d'obtenir la fonction diélectrique du graphène. Plus précisément, la fonction diélectrique inverse du graphène simulée est très proche de l'expression analytique pour $|\mathbf{q}| \leq 2k_F$ (k_F étant le vecteur d'onde de Fermi, et $\mathbf{q}$ le vecteur d'onde de la perturbation), et $\approx 10\%$ plus faible pour $|\mathbf{q}| > 2k_F$. On trouve que la température a un effet négligeable, ainsi que le potentiel d'échange et corrélation dans le cadre de l'approximation de la densité locale (LDA). La source principale des $\approx 10\%$ de différence entre les deux méthodes est l'utilisation des cônes de Dirac pour modéliser la structure de bande.

A partir de la valeur du potentiel de déformation nu et de la fonction diélectrique du graphène (on peut alors utilisé l'expression analytique de cette dernière), on estime que le potentiel de déformation écranté est au plus un ordre de grandeur plus petit que le potentiel de jauge. Le couplage avec les phonons acoustiques dans le plan est donc bien dominé par le champ de jauge.

∗.4 Chapitre 5: Quantum ESPRESSO 2D

La simulation DFT de matériaux 2D dans une configuration de type transistor à effet de champ est essentielle pour étudier les phonons hors plan et leur couplage aux électrons. Le principe de fonctionnement d'un transistor à effet de champ est représenté Fig. ∗.7. Le matériau 2D est posé sur un substrat isolant. Au dessus du matériau 2D sont déposés un diélectrique isolant puis une grille conductrice. L'application d'une différence de potentiel entre le matériau 2D et la grille permet d'établir un champ électrique au sein du diélectrique, perpendiculaire au plan du matériau 2D. Ceci s'accompagne d'une accumulation de charges de part et d'autre du diélectrique, dans la grille et le matériau 2D. Ce dispositif est très souvent utilisé pour doper, ou charger le matériau. C'est le caractère asymétrique du champ électrique hors plan, fini d'un côté du matériau 2D, zéro de l'autre, qui fait la particularité de cette configuration. Pour simuler un matériau 2D dans de telles conditions, on simplifie le système de manière à rendre compte des effets de la grille et du diélectrique sans forcément simuler les atomes et électrons qui les constituent. La grille est représentée par un plan de charge homogène et strictement 2D (infiniment fin), alors que le diélectrique est remplacé par une simple barrière de potentiel. L'objectif est de retrouver le modèle du profil de potentiel du transistor à effet de champ Fig. ∗.8.

Les conditions aux bords périodiques 3D sont nécessairement respectée dans un programme DFT utilisant des ondes planes. Dans ce cadre, on simule toujours le système 3D-périodique constitué de l'ensemble des images périodiques du système 2D que l'on veut simuler. On voudrait que chaque image périodique soit exactement équivalente au système 2D, ce qui n'est pas possible dans l'implémentation standard de la DFT avec ondes planes. En effet, l'apparition d'un moment dipolaire hors plan dans ce système est incompatible avec les conditions au bords périodiques 3D [78,

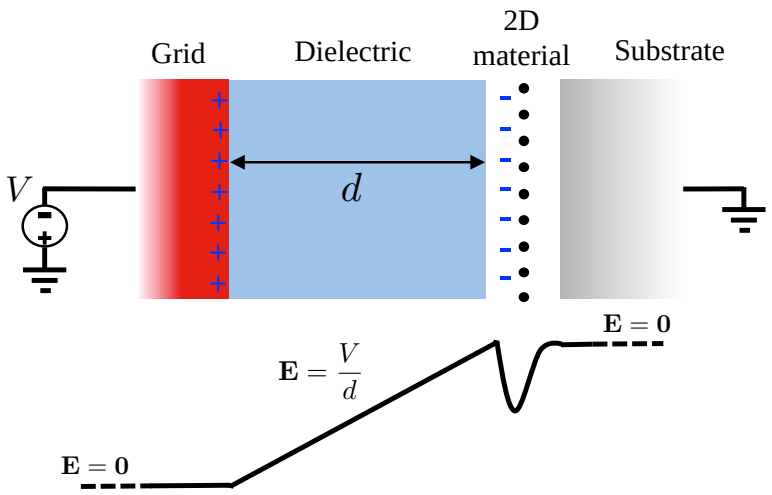

Figure ∗.7: On schématise le principe physique de l'effet de champ. Les points noirs symbolisent les atomes d'un matériau 2D monocouche. Ici, on représente un dopage positif. Des électrons sont ajoutés au matériaux 2D, des trous sont ajoutés à la grille.

79, 80]. Ceci est facilement compris lorsque l'on remarque que la valeur du potentiel électrostatique est différente d'un côté à l'autre du système (à gauche et à droite des systèmes des Figs. ∗.7 et ∗.8). Certaines méthodes ont été proposées pour remédier à cette problématique [78, 79, 80, 82]. Ces méthodes on été appliquées au cas de transistors à effet de champ avec des matériaux 2D [12, 81, 83]. Cependant, elles ne permettent pas le calcul de l'état perturbé et donc des phonons.

On développe ici la technique de troncature des interactions coulombiennes [73, 74, 40] entre les images périodiques pour tous les potentiels présents en DFT. On montre alors que l'on peut éliminer les liens physiques entre les images périodiques tout en respectant mathématiquement les conditions aux bords périodiques. On détaille l'implémentation de cette troncature dans le code DFT Quantum ESPRESSO [38]. Ces modifications permettent alors de calculer l'énergie totale, les forces, les phonons, et les interactions électron-phonon dans les systèmes 2D, en particulier dans une configuration type transistor à effet de champ.

On applique ensuite cette méthode au graphène et on démontre son intérêt en simulant des mécanismes propres au transistor à effet de champ. On observe une énergie finie pour les phonons acoustiques hors plan dans la limite des longueurs d'ondes infinies. On montre également qu'en présence d'un champ électrique hors plan asymétrique, les phonons hors plan (acoustiques et optiques) se couplent linéairement aux électrons. Une première estimation de ces couplages donne des valeurs qui restent négligeables devant les autres types de couplage déjà considérés pour les phonons dans le plan. Comme discuté dans le texte principal, cependant, il n'est pas exclu qu'une modélisation plus réaliste du diélectrique révèle de plus importants couplages. Enfin, on calcule directement le potentiel de déformation écranté pour du graphène dans un transistor à effet de champ. Celui-ci est différent de la valeur obtenue en divisant la valeur du potentiel de déformation nu (obtenu par la méthode des déformations) par la fonction diélectrique du graphène. Ceci montre qu'il reste des choses à comprendre

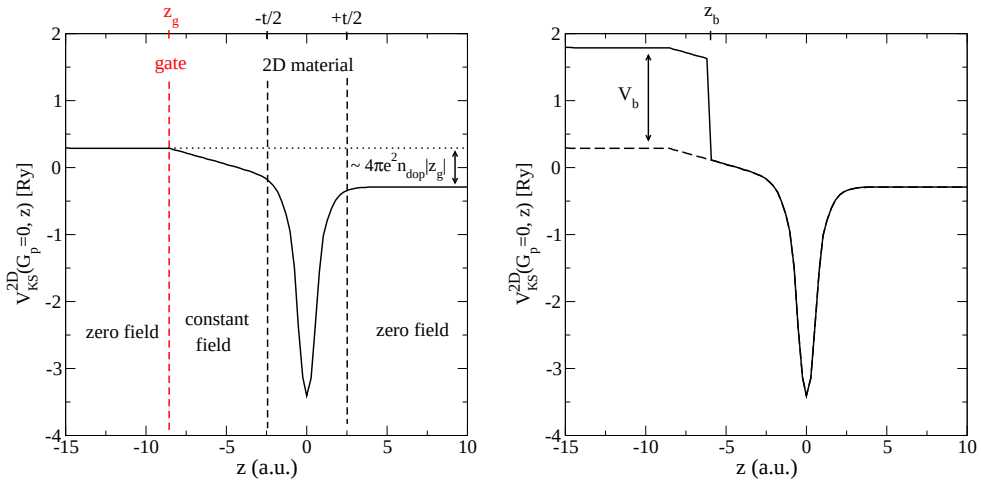

Figure ∗.8: Profil type du potentiel électrostatique dans notre modèle de transistor à effet de champ. Sur la gauche, seuls le matériau 2D et la grille sont présents. Sur la droite, on ajoute une barrière de potentiel pour simuler le diélectrique.

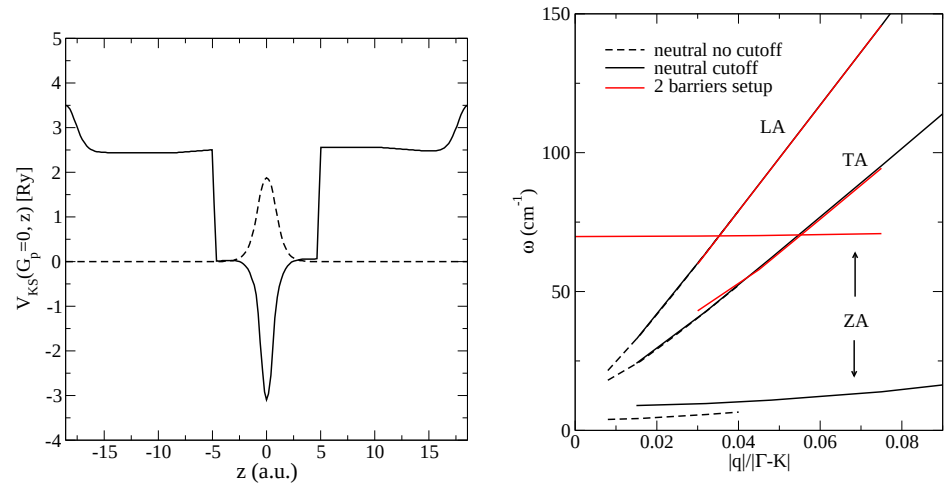

Figure ∗.9: Sur la gauche on représente le potentiel d'un système où le matériau 2D est dopé et enfermé entre deux barrières de potentiel. La ligne pointillée représente la densité électronique, en unités arbitraires. À droite, en rouge, on trace la dispersion des phonons acoustiques de ce système. Pour fournir une référence, on trace en noir les dispersions obtenues pour du graphène neutre, sans barrières, avec et sans troncature ("cutoff") des interactions coulombiennes.

concernant l'écrantage des couplages électron-phonon en 2D. Quoi qu'il en soit, les valeurs obtenues restent négligeables devant le champ de jauge.

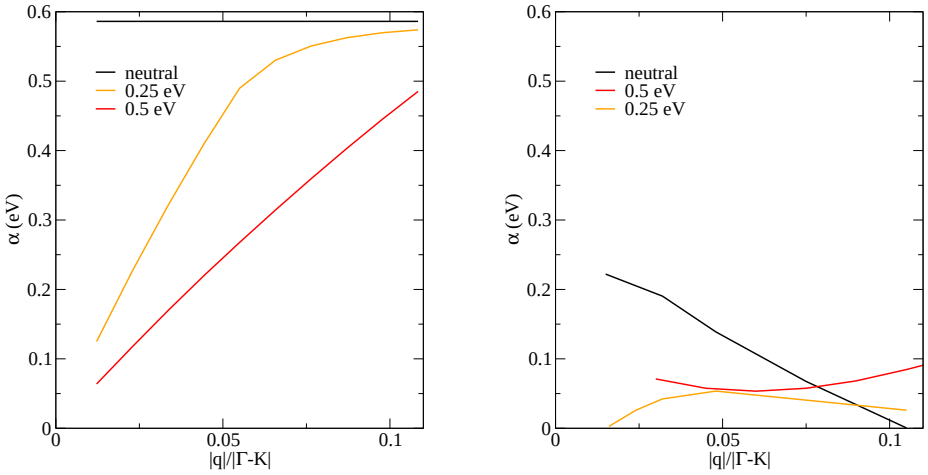

Figure ∗.10: Sur la gauche, on trace le rapport du potentiel de déformation non-écranté sur la fonction diélectrique du graphène. Sur la droite, on trace le potentiel de déformation écranté obtenu dans la configuration transistor à effet de champ. Ceci est fait pour différents dopages avec des énergies de Fermi ε_F de 0, 0,25 et 0,5 eV.

∗.5 Chapitre 6: Résistivité du graphène

Dans le dernier chapitre, on développe une solution numérique à l'équation de Boltzmann pour le transport électronique dans le graphène, en prenant en compte la diffusion par les phonons LA, TA, LO, TO et A_1'. Cette solution numérique permet de relaxer diverses approximations souvent utilisées pour obtenir des expressions analytiques de la résistivité du graphène [88, 89]. La comparaison des résultats de cette méthode avec les mesures expérimentales [86, 87] confirme le rôle prédominant des phonons acoustiques à basse température (en dessous de la température ambiante). Dans le régime d'équipartition, la résistivité est proportionnelle à la température. La pente est proportionnelle au carré du rapport du paramètre associé au champ de jauge sur la vitesse du son effective (la moyenne harmonique des carrés des vitesses du son associées aux modes LA et TA). Cette pente est alors indépendante du dopage ou de la nature du substrat. On montre qu'une augmentation de 15% du paramètre de champ de jauge par rapport à la valeur *ab initio* GW permet un excellent accord quantitatif avec l'expérience. Plusieurs hypothèses peuvent être émises pour expliquer ce désaccord de 15%. Quoi qu'il en soit, le désaccord est assez faible pour affirmer la domination du champ de jauge dans la diffusion des électrons par les phonons acoustiques. Autour de la température ambiante, une forte augmentation de la résistivité en fonction de la température apparait. Dans l'interprétation des données expérimentales, celle-ci est souvent attribuée au couplage à distance avec les phonons optiques du substrat. Il n'existe cependant pas de simulation *ab initio* pour confirmer la contribution dominante d'un tel couplage. D'autre part, nos simulations révèlent un fort couplage avec les phonons optiques A_1'. Ces phonons intrinsèques engendrent un augmentation notable de la résistivité à partir d'une température qui est en accord avec ce que l'on observe

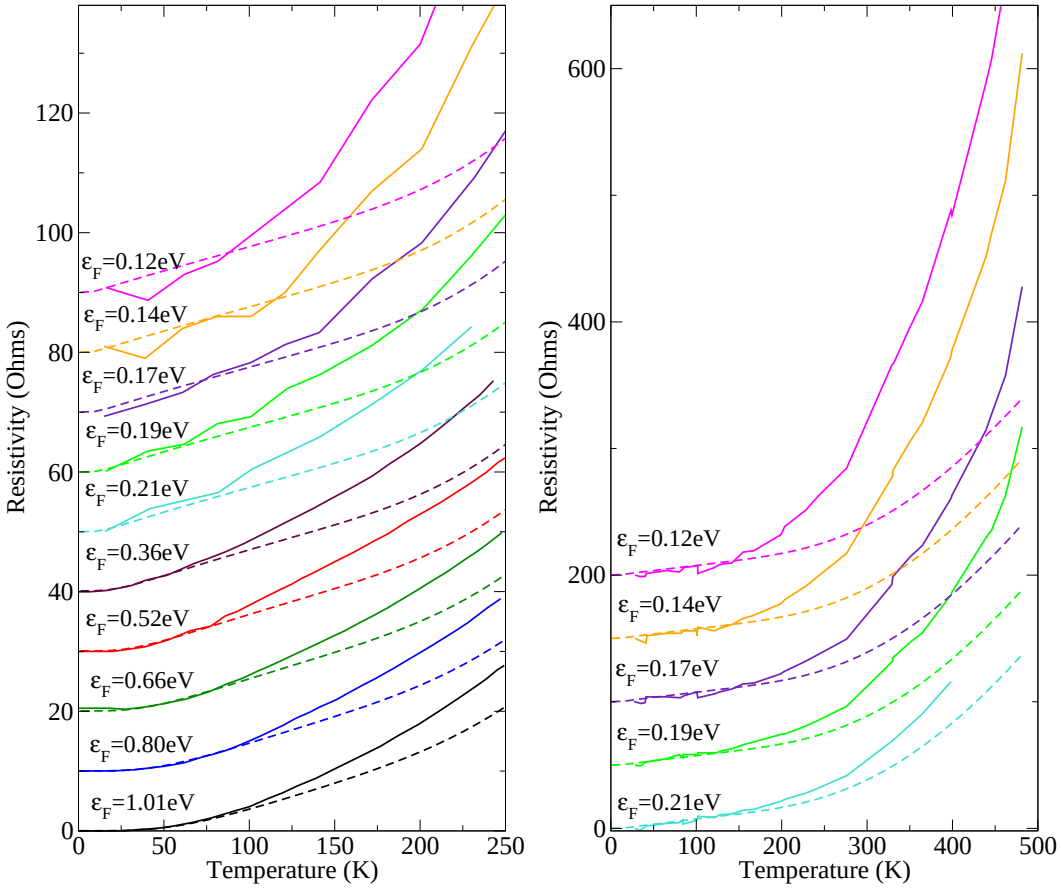

(a) BG and EP (b) HT

Figure ∗.11: Comparaison des mesures expérimentales (lignes continues) et de la solution numérique (lignes pointillées) dans les régimes (a) basses températures et (b) hautes températures, pour différents dopages.

expérimentalement. Cependant, on doit effectuer un ajustement du paramètre de couplage correspondant qui dépend du dopage pour obtenir un bon accord numérique entre simulations et expériences. Il existe plusieurs explications possibles pour ce désaccord. On peut remettre en cause la validité des valeurs du paramètre non-ajusté que l'on utilise. Celui-ci a été calculé [35] dans le cadre de l'approximation GW, mais ces calculs sont très délicats pour les dopages considérés (du fait de la difficulté d'échantillonner de petites surface de Fermi). Les phonons optiques intrinsèques hors plan pourraient aussi contribuer d'une manière similaire. Enfin, le substrat n'étant pas présent dans nos simulations, les phonons du substrat n'ont pas été écarté. Soulignons que ces derniers seraient écrantés, et qu'une correcte simulation de leur écrantage serait nécessaire pour évaluer leur contribution à la résistivité quantitativement.

On met également à profit la solution numérique pour examiner la validité des diverses approximations communément utilisées dans les modèles analytiques de transport. On propose une solution semi-numérique facile à implémenter en gardant une précision satisfaisante. Finalement, on propose des solutions analytiques partielles qui

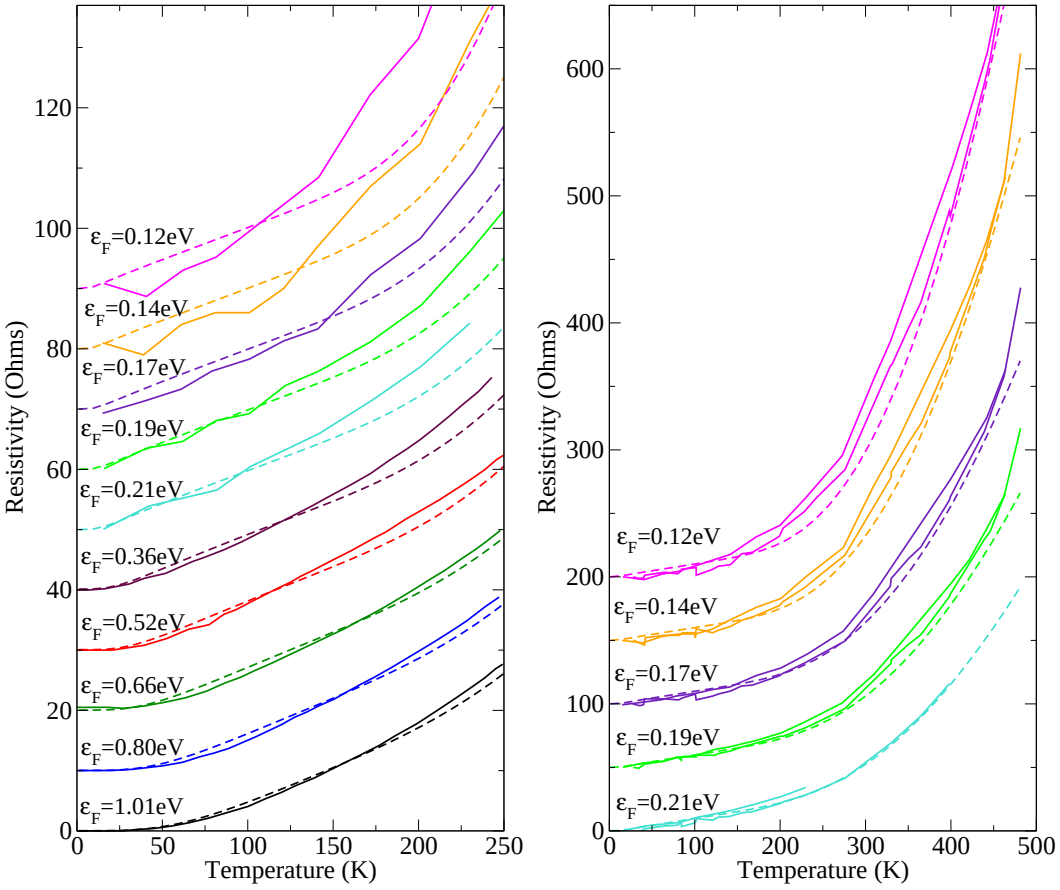

(a) BG and EP (b) HT

Figure ∗.12: Résultats présentés comme sur la figure précédente, avec des paramètres de couplages fittés, voir tableau ∗.1.

permettent d'extraire des données expérimentales le paramètre de couplage associé au champ de jauge.

∗.6 Perspectives

L'interaction des électrons avec les phonons intrinsèques hors plan et avec les phonons du substrat sont parmi les mécanismes qu'il serait intéressant d'étudier plus amplement. Notre développement du programme Quantum ESPRESSO avec troncature des interactions coulombienne entre les images périodiques est l'outil adapté à ces études. La solution numérique de l'équation de Boltzmann ainsi que la méthode des déformations statiques demandent un travail analytique spécifique au matériau étudié. Cependant, ces méthodes peuvent être adapté à d'autre matériaux que le graphène. La troncature des interactions coulombienne, quant à elle, a été implémentée de manière générale et est d'hors et déjà applicable à d'autres matériaux. Les programmes correspondant peuvent être utilisés pour calculer la densité électronique, l'énergie totale,

les bandes, la fonction diélectrique statique, les dispersions de phonons, et le couplage électron-phonon pour tous les matériaux 2D dans une configuration de type transistor à effet de champ. On espère que les méthodes développées au cours de cette thèse pourront être utile à de nombreuses applications au delà du transport électronique dans le graphène.

Bibliography

[1] H. Bruus and K. Flensberg, *Many-body quantum theory in condensed matter physics: an introduction*, August (Oxford University Press, Oxford, 2002).

[2] G. Grimvall, *The electron-phonon interaction in metals* (North-Holland Publishing Company, Amsterdam, New-York, Oxford, 1981).

[3] N. W. Ashcroft and N. D. Mermin, *Solid State Physics* (Brooks Cole, Belmont (USA), 1976).

[4] G. Giuliani and G. Vignale, *Quantum theory of the electron liquid* (Cambridge University Press, 2005).

[5] K. S. Novoselov, A. K. Geim, S. V. Morozov, D. Jiang, Y. Zhang, S. V. Dubonos, I. V. Grigorieva, and A. A. Firsov, "Electric field effect in atomically thin carbon films." Science **306**, 666–9 (2004).

[6] Y. Zhang, Y.-W. Tan, H. L. Stormer, and P. Kim, "Experimental observation of the quantum Hall effect and Berry's phase in graphene." Nature **438**, 201–4 (2005).

[7] K. S. Novoselov, A. K. Geim, S. V. Morozov, D. Jiang, M. I. Katsnelson, I. V. Grigorieva, S. V. Dubonos, and A. A. Firsov, "Two-dimensional gas of massless Dirac fermions in graphene." Nature **438**, 197–200 (2005).

[8] B. Radisavljevic, A. Radenovic, J. Brivio, V. Giacometti, and A. Kis, "Single-layer MoS2 transistors." Nature nanotechnology **6**, 147–50 (2011).

[9] C. R. Dean, A. F. Young, I. Meric, C. Lee, L. Wang, S. Sorgenfrei, K. Watanabe, T. Taniguchi, P. Kim, K. L. Shepard, and J. Hone, "Boron nitride substrates for high-quality graphene electronics." Nature nanotechnology **5**, 722–6 (2010).

[10] J. T. Ye, Y. J. Zhang, R. Akashi, M. S. Bahramy, R. Arita, and Y. Iwasa, "Superconducting dome in a gate-tuned band insulator." Science (New York, N.Y.) **338**, 1193–6 (2012).

[11] M. Born and R. Oppenheimer, "Zur quantentheorie der molekeln," Annalen der Physik (1927).

[12] T. Brumme, M. Calandra, and F. Mauri, "Electrochemical doping of few-layer ZrNCl from first principles: Electronic and structural properties in field-effect configuration," Physical Review B **89**, 245406 (2014).

[13] N. Mounet and N. Marzari, "First-principles determination of the structural, vibrational and thermodynamic properties of diamond, graphite, and derivatives," Physical Review B **71**, 205214– (2005).

[14] S. Piscanec, M. Lazzeri, F. Mauri, A. C. Ferrari, and J. Robertson, "Kohn anomalies and electron-phonon interactions in graphite," Physical Review Letters **93**, 185503 (2004).

[15] P. B. Allen and M. L. Cohen, "Superconductivity and Phonon Softening," Physical Review Letters **29**, 1593–1596 (1972).

[16] J. L. Manes, "Symmetry-based approach to electron-phonon interactions in graphene," Physical Review B **76**, 045430 (2007).

[17] E. Engel and R. Dreizler, "Density functional theory," (Springer, Berlin, 2011).

[18] J. Ihm, A. Zunger, and M. L. Cohen, "Momentum-space formalism for the total energy of solids," Journal of Physics C: Solid State Physics **12**, 4409–4422 (1979).

[19] M. T. Yin and M. L. Cohen, "Theory of lattice-dynamical properties of solids: Application to Si and Ge," Physical Review B **26**, 3259–3272 (1982).

[20] S. Baroni, S. De Gironcoli, and A. Dal Corso, "Phonons and related crystal properties from density-functional perturbation theory," Reviews of Modern Physics **73**, 515–562 (2001).

[21] P. Giannozzi, S. De Gironcoli, P. Pavone, and S. Baroni, "Ab initio calculation of phonon dispersions in semiconductors," Physical Review B **43** (1991).

[22] J. P. Perdew and A. Zunger, "Self-interaction correction to density-functional approximations for many-electron systems," Physical Review B **23**, 5048–5079 (1981).

[23] L. Hedin, "New Method for Calculating the One-Particle Green's Function with Application to the Electron-Gas Problem," Physical Review **139**, A796–A823 (1965).

[24] L. Pietronero, S. Strässler, H. R. Zeller, and M. J. Rice, "Electrical conductivity of a graphite layer," Physical Review B **22**, 904–910 (1980).

[25] L. M. Woods and G. D. Mahan, "Electron-phonon effects in graphene and armchair (10,10) single-wall carbon nanotubes," Physical Review B **61**, 10651–10663 (2000).

[26] H. Suzuura and T. Ando, "Phonons and electron-phonon scattering in carbon nanotubes," Physical Review B **65**, 235412 (2002).

[27] P. Venezuela, M. Lazzeri, and F. Mauri, "Theory of double-resonant Raman spectra in graphene: intensity and line shape of defect-induced and two-phonon bands," Physical Review B **84**, 035433 (2011).

[28] C.-H. Park, N. Bonini, T. Sohier, G. Samsonidze, B. Kozinsky, M. Calandra, F. Mauri, and N. Marzari, "Electron-Phonon Interactions and the Intrinsic Electrical Resistivity of Graphene." Nano letters **14**, 1113–1119 (2014).

[29] A. H. Castro Neto, F. Guinea, N. M. R. Peres, K. S. Novoselov, and A. Geim, "The electronic properties of graphene," Reviews of Modern Physics **81**, 109–162 (2009).

[30] S. Das Sarma, S. Adam, E. H. Hwang, and E. Rossi, "Electronic transport in two-dimensional graphene," Reviews of Modern Physics **83**, 407–470 (2011).

[31] F. von Oppen, F. Guinea, and E. Mariani, "Synthetic electric fields and phonon damping in carbon nanotubes and graphene," Physical Review B **80**, 075420–(2009).

[32] M. Vozmediano, M. I. Katsnelson, and F. Guinea, "Gauge fields in graphene," Physics Reports **496**, 109–148 (2010).

[33] F. Guinea, A. K. Geim, M. I. Katsnelson, and K. S. Novoselov, "Generating quantizing pseudomagnetic fields by bending graphene ribbons," Physical Review B **81**, 035408 (2010).

[34] M. Lazzeri, C. Attaccalite, L. Wirtz, and F. Mauri, "Impact of the electron-electron correlation on phonon dispersion: Failure of LDA and GGA DFT functionals in graphene and graphite," Physical Review B **78**, 081406 (2008).

[35] C. Attaccalite, L. Wirtz, M. Lazzeri, F. Mauri, and A. Rubio, "Doped graphene as tunable electron-phonon coupling material." Nano letters **10**, 1172–6 (2010).

[36] K. M. Borysenko, J. T. Mullen, E. A. Barry, S. Paul, Y. G. Semenov, J. M. Zavada, M. B. Nardelli, and K. W. Kim, "First-principles analysis of electron-phonon interactions in graphene," Physical Review B **81**, 121412 (2010).

[37] K. Kaasbjerg, K. S. Thygesen, and K. W. Jacobsen, "Unraveling the acoustic electron-phonon interaction in graphene," Physical Review B **85**, 165440 (2012).

[38] P. Giannozzi, S. Baroni, N. Bonini, M. Calandra, R. Car, C. Cavazzoni, D. Ceresoli, G. L. Chiarotti, M. Cococcioni, I. Dabo, A. Dal Corso, S. De Gironcoli, S. Fabris, G. Fratesi, R. Gebauer, U. Gerstmann, C. Gougoussis, A. Kokalj, M. Lazzeri, L. Martin-Samos, N. Marzari, F. Mauri, R. Mazzarello, S. Paolini, A. Pasquarello, L. Paulatto, C. Sbraccia, S. Scandolo, G. Sclauzero, A. P. Seitsonen, A. Smogunov, P. Umari, and R. M. Wentzcovitch, "QUANTUM ESPRESSO: a modular and open-source software project for quantum simulations of materials." Journal of physics. Condensed matter : an Institute of Physics journal **21**, 395502 (2009).

[39] J. Deslippe, G. Samsonidze, D. A. Strubbe, M. Jain, M. L. Cohen, and S. G. Louie, "BerkeleyGW: A massively parallel computer package for the calculation of the quasiparticle and optical properties of materials and nanostructures," Computer Physics Communications **183**, 1269–1289 (2012).

[40] S. Ismail-Beigi, "Truncation of periodic image interactions for confined systems," Physical Review B **73**, 233103 (2006).

[41] M. S. Hybertsen and S. G. Louie, "Electron correlation in semiconductors and insulators: Band gaps and quasiparticle energies," Physical Review B **34**, 5390–5413 (1986).

[42] S.-M. Choi, S.-H. Jhi, and Y.-W. Son, "Effects of strain on electronic properties of graphene," Physical Review B **81**, 081407 (2010).

[43] D. M. Basko and I. L. Aleiner, "Interplay of Coulomb and electron-phonon interactions in graphene," Physical Review B **77**, 41409 (2008).

[44] M. I. Katsnelson, "Nonlinear screening of charge impurities in graphene," Physical Review B **74**, 201401 (2006).

[45] M. M. Fogler, D. S. Novikov, and B. I. Shklovskii, "Screening of a hypercritical charge in graphene," Physical Review B **76**, 233402 (2007).

[46] S. Das Sarma and E. H. Hwang, "Density-dependent electrical conductivity in suspended graphene: Approaching the Dirac point in transport," Physical Review B **87**, 035415 (2013).

[47] E. H. Hwang and S. Das Sarma, "Screening-induced temperature-dependent transport in two-dimensional graphene," Physical Review B **79**, 165404 (2009).

[48] T. Sohier, M. Calandra, C.-H. Park, N. Bonini, N. Marzari, and F. Mauri, "Phonon-limited resistivity of graphene by first-principles calculations: Electron-phonon interactions, strain-induced gauge field, and Boltzmann equation," Physical Review B **90**, 125414 (2014).

[49] S. Fratini and F. Guinea, "Substrate-limited electron dynamics in graphene," Physical Review B **77**, 195415 (2008).

[50] V. N. Kotov, B. Uchoa, V. M. Pereira, F. Guinea, and a. H. Castro Neto, "Electron-Electron Interactions in Graphene: Current Status and Perspectives," Reviews of Modern Physics **84**, 1067–1125 (2012).

[51] S. Lebègue and O. Eriksson, "Electronic structure of two-dimensional crystals from ab initio theory," Physical Review B **79**, 115409 (2009).

[52] S. Adler, "Quantum Theory of the Dielectric Constant in Real Solids," Physical Review **126**, 413–420 (1962).

[53] R. Pick, M. Cohen, and R. Martin, "Microscopic Theory of Force Constants in the Adiabatic Approximation," Physical Review B **1**, 910–920 (1970).

[54] S. Sinha, R. Gupta, and D. Price, "Microscopic theory of dielectric screening and lattice dynamics. I. Local-field corrections and dielectric constants," Physical Review B **9**, 2564–2572 (1974).

[55] A. Baldereschi and E. Tosatti, "Mean-value point and dielectric properties of semiconductors and insulators," Physical Review B **17**, 4710–4717 (1978).

[56] R. Car and A. Selloni, "Local-Field Effects in the Screening of Impurities in Silicon," Physical Review Letters **42**, 1365–1368 (1979).

[57] M. S. Hybertsen and S. G. Louie, "Model dielectric matrices for quasiparticle self-energy calculations," Physical Review B **37**, 2733–2736 (1988).

[58] R. Resta and A. Baldereschi, "Dielectric matrices and local fields in polar semiconductors," Physical Review B **23**, 6615–6624 (1981).

[59] R. Resta, "Local-field effects and phonon screening in polar semiconductors," Physical Review B **27**, 3620–3630 (1983).

[60] S. Baroni and R. Resta, "Ab initio calculation of the macroscopic dielectric constant in silicon," Physical Review B **33**, 7017–7021 (1986).

[61] M. S. Hybertsen and S. G. Louie, "Ab initio static dielectric matrices from the density-functional approach. I. Formulation and application to semiconductors and insulators," Physical Review B **35**, 5585–5601 (1987).

[62] M. S. Hybertsen and S. G. Louie, "Ab initio static dielectric matrices from the density-functional approach. II. Calculation of the screening response in diamond, Si, Ge, and LiCl," Physical Review B **35**, 5602–5610 (1987).

[63] K. Shung, "Dielectric function and plasmon structure of stage-1 intercalated graphite," Physical Review B **34**, 979–993 (1986).

[64] E. V. Gorbar, V. P. Gusynin, V. A. Miransky, and I. A. Shovkovy, "Magnetic field driven metal-insulator phase transition in planar systems," Physical Review B **66**, 045108 (2002).

[65] T. Ando, "Screening Effect and Impurity Scattering in Monolayer Graphene," Journal of the Physics Society Japan **75**, 074716 (2006).

[66] B. Wunsch, T. Stauber, F. Sols, and F. Guinea, "Dynamical polarization of graphene at finite doping," New Journal of Physics **8**, 318–318 (2006).

[67] Y. Barlas, T. Pereg-Barnea, M. Polini, R. Asgari, and A. H. MacDonald, "Chirality and Correlations in Graphene," Physical Review Letters **98**, 236601 (2007).

[68] X.-F. Wang and T. Chakraborty, "Collective excitations of Dirac electrons in a graphene layer with spin-orbit interactions," Physical Review B **75**, 033408 (2007).

[69] E. H. Hwang and S. Das Sarma, "Dielectric function, screening, and plasmons in two-dimensional graphene," Physical Review B **75**, 205418– (2007).

[70] M. van Schilfgaarde and M. I. Katsnelson, "First-principles theory of nonlocal screening in graphene," Physical Review B **83**, 081409 (2011).

[71] B. Kozinsky and N. Marzari, "Static Dielectric Properties of Carbon Nanotubes from First Principles," Physical Review Letters **96**, 166801 (2006).

[72] B. Kozinsky, "Dielectric response and interactions in low-dimensional carbon materials from first principles calculations," Ph.D. thesis, Massachusetts Institute of Technology, Cambridge, Massachusetts, USA (2007).

[73] M. R. Jarvis, I. D. White, R. W. Godby, and M. C. Payne, "Supercell technique for total-energy calculations of finite charged and polar systems," Physical Review B **56**, 14972–14978 (1997).

[74] C. A. Rozzi, D. Varsano, A. Marini, E. K. U. Gross, and A. Rubio, "Exact Coulomb cutoff technique for supercell calculations," Physical Review B **73**, 205119 (2006).

[75] D. J. Mowbray, "Theoretical electron energy loss spectroscopy of isolated graphene," physica status solidi (b) **251**, 6 (2014).

[76] S. Baroni, P. Giannozzi, and A. Testa, "Green's-function approach to linear response in solids," Physical Review Letters **58**, 1861–1864 (1987).

[77] W. Kohn and L. J. Sham, "Self-Consistent Equations Including Exchange and Correlation Effects," Physical Review **140**, A1133–A1138 (1965).

[78] J. Neugebauer and M. Scheffler, "Adsorbate-substrate and adsorbate-adsorbate interactions of Na and K adlayers on Al(111)," Physical Review B **46**, 16067–16080 (1992).

[79] L. Bengtsson, "Dipole correction for surface supercell calculations," Physical Review B **59**, 12301–12304 (1999).

[80] B. Meyer and D. Vanderbilt, "Ab initio study of BaTiO 3 and PbTiO 3 surfaces in external electric fields," Physical Review B **63**, 205426 (2001).

[81] T. Brumme, M. Calandra, and F. Mauri, "First-principles theory of field-effect doping in transition-metal dichalcogenides: Structural properties, electronic structure, Hall coefficient, and electrical conductivity," Physical Review B **91**, 155436 (2015).

[82] M. Otani and O. Sugino, "First-principles calculations of charged surfaces and interfaces: A plane-wave nonrepeated slab approach," Physical Review B **73**, 115407 (2006).

[83] Y.-P. Wang and H.-P. Cheng, "First-principles simulations of a graphene-based field-effect transistor," Physical Review B **91**, 245307 (2015).

[84] T. Sohier, M. Calandra, and F. Mauri, "Density-functional calculation of static screening in two-dimensional materials: The long-wavelength dielectric function of graphene," Physical Review B **91**, 165428 (2015).

[85] P. P. Ewald, "Die Berechnung optischer und elektrostatischer Gitterpotentiale," Annalen der Physik **369**, 253–287 (1921).

[86] J. J.-H. Chen, C. Jang, S. Xiao, M. Ishigami, and M. S. Fuhrer, "Intrinsic and extrinsic performance limits of graphene devices on SiO2," Nature Nanotechnology **3**, 206–209 (2008).

[87] D. K. Efetov and P. Kim, "Controlling Electron-Phonon Interactions in Graphene at Ultrahigh Carrier Densities," Physical Review Letters **105**, 256805 (2010).

[88] R. S. Shishir and D. K. Ferry, "Intrinsic mobility in graphene." Journal of physics. Condensed matter : an Institute of Physics journal **21**, 232204 (2009).

[89] E. H. Hwang and S. Das Sarma, "Acoustic phonon scattering limited carrier mobility in two-dimensional extrinsic graphene," Physical Review B **77**, 115449 (2008).

[90] P. B. Allen, "New Method for Solving Boltzmann's equation for electrons in metals," Physical Review B **17**, 3725 (1978).

[91] V. Perebeinos and P. Avouris, "Inelastic scattering and current saturation in graphene," Physical Review B **81**, 195442 (2010).

[92] E. Mariani and F. von Oppen, "Temperature-dependent resistivity of suspended graphene," Physical Review B **82**, 195403 (2010).

[93] E. H. Hwang, S. Adam, and S. Das Sarma, "Carrier Transport in Two-Dimensional Graphene Layers," Physical Review Letters **98**, 186806 (2007).

[94] B. Nag, "Electron Transport in Compound Semiconductors," Springer Series in Solid-State Sciences **11** (1980).

[95] T. Kawamura and S. Das Sarma, "Phonon-scattering-limited electron mobilities in AlxGa1-xAs/GaAs heterojunctions," Physical Review B **45**, 3612–3627 (1992).

[96] P. K. Basu and B. R. Nag, "Lattice scattering mobility of a two-dimensional electron gas in GaAs," Physical Review B **22**, 4849–4852 (1980).

[97] E. H. Hwang and S. Das Sarma, "Single-particle relaxation time versus transport scattering time in a two-dimensional graphene layer," Physical Review B **77**, 195412– (2008).

[98] A. Barreiro, M. Lazzeri, J. Moser, F. Mauri, and A. Bachtold, "Transport Properties of Graphene in the High-Current Limit," Physical Review Letters **103**, 76601 (2009).

[99] J. Martin, N. Akerman, G. Ulbricht, T. Lohmann, J. H. Smet, K. von Klitzing, and A. Yacoby, "Observation of electron–hole puddles in graphene using a scanning single-electron transistor," Nature Physics **4**, 144–148 (2007).

[100] K. Zou, X. Hong, D. Keefer, and J. Zhu, "Deposition of High-Quality HfO_{2} on Graphene and the Effect of Remote Oxide Phonon Scattering," Physical Review Letters **105**, 126601 (2010).

[101] A. Matthiessen and C. Vogt, "On the Influence of Temperature on the Electric Conducting-power of Alloys," Philosophical Transactions of the Royal Society of London **154**, 167–200 (1864).

[102] T. Low and F. Guinea, "Strain-induced pseudomagnetic field for novel graphene electronics." Nano letters **10**, 3551–4 (2010).

[103] P. Hohenberg and W. Kohn, "Inhomogeneous Electron Gas," Physical Review **136**, B864–B871 (1964).

[104] J. C. Phillips and L. Kleinman, "New Method for Calculating Wave Functions in Crystals and Molecules," Physical Review **116**, 287–294 (1959).

[105] W. Kohn, A. D. Becke, and R. G. Parr, "Density Functional Theory of Electronic Structure," The Journal of Physical Chemistry **100**, 12974–12980 (1996).

[106] R. P. Feynman, "Forces in Molecules," Physical Review **56**, 340–343 (1939).

[107] H. Hellmann, "Einfuhrung in die Quantumchemie," Franz Deutsche, Leipzig (1937).

Thibault SOHIER **22/09/2015**

Sujet : Électrons et phonons dans le graphène: couplage electron-phonon, écrantage et transport dans une configuration type transistor à effet de champ

Résumé : Comprendre le transport électronique dans les cristaux bidimensionnels est un enjeu conceptuel majeur pour la nanoélectornique de demain. Dans cette thèse, on développe des méthodes *ab initio* pour étudier l'interaction électron-phonon, l'écrantage et le transport dans le graphène. Pour surpasser les limites des méthodes *ab initio* en ondes planes, à l'origine destinées aux matériaux périodiques en trois dimensions, on tronque l'interaction coulombienne dans la troisième dimension, isolant ainsi le système bidimensionnel de ses images périodiques. Ceci est réalisé au sein de la théorie de la fonctionnelle de la densité en perturbation, afin de calculer la réponse de la densité de charge et le spectre des phonons dans un cadre bidimensionnel.

On utilise ces méthodes pour obtenir un modèle quantitatif du couplage électron-phonon dans le graphène pour une configuration de type transistor à effet de champ. Le couplage aux phonons acoustiques est dominé par le champ de jauge non-écranté, que nous calculons en incluant l'effet des interactions électron-électron au niveau GW. Nos simulations des propriétés d'écrantage statiques du graphene valident les modèles analytiques et montrent que le potentiel de déformation est fortement écranté, de sorte que sa contribution à la diffusion des électrons par les phonons acoustiques est négligeable. On montre également que le couplage avec les phonons hors-plan est faible mais fini. On obtient la contribution de la diffusion par les phonons à la résistivité en résolvant l'équation de Boltzmann pour le transport. En dessous de la température ambiante, nos résultats confirment le rôle des phonons acoustiques et une augmentation de 15% du paramètre de jauge *ab initio* permet un excellent accord avec l'expérience. Au dessus de la température ambiante, on dénote l'importance des phonons optiques intrinsèques.

Mots clés : graphène, transistor à effet de champ, ab initio, théorie de la fonctionnelle de la densité, couplage électron-phonon, champ de jauge, potentiel de déformation, écrantage, transport, équation de Boltzmann, troncature de l'interaction coulombienne, images périodiques

Thibault SOHIER **22/09/2015**

Subject : Electrons and phonons in graphene: electron-phonon coupling, screening and transport in the field effect setup

Abstract : Understanding the transport properties of two-dimensional crystals doped by field effect is a conceptual milestone for tomorrow's nanoelectronics. In this thesis we develop first-principles methods to investigate electron-phonon interactions, screening and phonon-limited transport in graphene. To overcome the limitations of existing plane-wave *ab initio* packages, originally devised for three-dimensional periodic solids, we truncate the Coulomb interaction in the third direction and isolate the 2D system from its periodic images. This is implemented in density-functional perturbation theory to calculate charge density responses and phonon spectra in a two-dimensional framework.

We use those methods to develop a quantitative model of electron-phonon coupling for graphene in the field effect transistor configuration. We find that the coupling of electrons to acoustic phonons is dominated by the unscreened gauge field, which we compute with full inclusion of electron-electron interactions at the GW level. Our simulations of the static screening properties of graphene validate analytical models and reveal that the deformation potential is strongly screened, such that its contribution to acoustic phonon scattering is negligible. We find a small but finite linear coupling with out-of-plane phonons. By solving the Boltzmann transport equation we obtain the phonon-limited resistivity. Below room temperature, our results confirm the role of acoustic phonons and a 15% increase of the *ab initio* gauge field parameter leads to an excellent quantitative agreement with experiment. Above room-temperature, we point to the importance of the coupling with intrinsic optical phonons.

Keywords : graphene, field effect transistor, ab initio, density-functional theory, electron-phonon coupling, gauge field, deformation potential, screening, Boltzmann transport, Coulomb cutoff, periodic images